Influences of Calcium and Oxygen on Retinal Metabolism

Celia Bisbach

A dissertation
submitted in partial fulfillment of the
requirements for the degree of

Doctor of Philosophy

University of Washington
2021

Reading Committee:
James Hurley, Chair
Susan Brockerhoff
Yasemin Sancak

Program Authorized to Offer Degree:
Biochemistry

University of Washington

Abstract

Influences of Calcium and Oxygen on Retinal Metabolism

Celia Bisbach

Chair of the Supervisory Committee:

James Hurley

Biochemistry

Photoreceptors require an excessive amount of energy to carry out their function, yet their access to the nutrients and oxygen which could facilitate efficient ATP production is restricted by neighboring retinal pigment epithelial (RPE) cells. This dissertation investigates the metabolic adaptations made by both photoreceptors and RPE which allow both cell types to coexist in a competitive environment, with a focus on understanding the independent influences of mitochondrial Ca^{2+} uptake and O_2 tension. Highly specialized photoreceptors in the retina use Ca^{2+} as a second messenger to transduce light to a chemical signal, yet we find that mitochondrial Ca^{2+} uptake mediated by the Mitochondrial Ca^{2+} Uniporter is quite dispensable for photoreceptor metabolism and function. Instead, we find that photoreceptor metabolism appears to be programmed by the basal hypoxic niche they normally reside in, which causes photoreceptors produce succinate by non-canonical reversal of succinate dehydrogenase. This succinate is exported from retinas by Monocarboxylate Transporter 1 (MCT1) and is capable of being imported and oxidized by eyecup tissue, which has ample access to O_2 in the eye. Transport of succinate between tissues may be more widespread than previously thought, as we also uncover evidence that succinate can be oxidized in cerebellum, kidney, liver, and brown adipose tissue.

Table of Contents

Acknowledgements

This dissertation was completed in the labs of Dr. James Hurley and Dr. Susan Brockerhoff, who are both excellent mentors with diverse and complementary strengths. Jim showed me how to be creative, both when coming up with hypotheses and designing experiments to test them. Sue showed me how to systematically approach and plan out a project while always keeping the big picture in mind. Both Jim and Sue are kind and supportive mentors who always gave me the freedom to pursue my own ideas and allowed me to grow as a scientist. It has been an overwhelmingly positive experience to complete my PhD under their instruction.

I am lucky that Jim and Sue have fostered an excellent lab environment which attracts great people to work with. I was very fortunate to work closely with Rachel Hutto during my rotation and my first three years as a graduate student. I learned so much from Rachel about how to plan experiments and critically interpret results, and I could not have asked for a better first role model and friend in the lab. I also feel very lucky that Dan Hass appeared in the lab during my fourth year. Working with Dan taught me that you need to be your own “reviewer number 2” when trying to interpret your results, meaning you should be the harshest critic of your data and do that extra experiment to test your hypothesis rather than wait for someone else to point out a flaw. Dan also helped me overcome one of my weaknesses by encouraging me to discuss and think about the results of each experiment before blindly rushing forward to test a new idea. Whitney Cleghorn and Kristine Tsantilas were both very generous with their time and effort, both in terms of mentoring junior lab members and keeping common lab resources up and running. Michelle Giarmarco’s excitement about science and the Hurley and Brockerhoff labs is one of the things that drew me to the UW Biochemistry graduate program in the first place. Finally, I need to give a special thank you to Dan Hass and Brian Robbings for providing extra experimental assistance during a 3-month period during which I couldn’t walk due to a broken leg. I can’t overstate how much they both helped the project (and me) move forward during what was a difficult time.

There are several scientific mentors who were formative prior to my graduate career. First and foremost is Saja Fakhraldeen, who invested countless hours in mentoring me while I was an undergraduate. Saja gave me a solid foundation on how to think critically and work carefully, and I can only really appreciate the extent of her effort after mentoring undergraduates myself. Andreas Gerondopoulos, Ildiko Kasza, Caroline Alexander, Bill Sugden, and Francis Barr also invested their time and resources in helping me develop as a scientist.

I am fortunate to have made two excellent friends in the UW Biochemistry Graduate program in Ha Van Dang and Inez Pranoto. Ha always pushes my limits and makes sure any idea I have (scientific or not) is supported by evidence, while Inez is endlessly supportive, funny, and positive.

Finally, thank you to my partner Spencer Buyansky, who happily moved across the country with me and who has supported me through the challenging times of graduate school (and enjoyed the good times with me as well). Spencer (and of course our dog Pesto) are the best reminders that a failed experiment is not the end of the world.

Chapter 1: Introduction

Organisms on earth have not always been able to see. The first living cell probably appeared a few billion years ago, totally blind and with few attributes other than the ability to replicate (Knoll et al., 2016). Over millions of years, the complexity of organisms increased, and some genetic mistakes led to the formation of light-sensitive patches on the surface of these ancient animals. Even though these light-sensitive patches could do nothing but distinguish between the presence and absence of light, they conferred a significant survival advantage to those who possessed them. Over hundreds of thousands of generations, evolution transformed the light-sensitive patches into a complex and sensitive organ (Land, 2019).

While our ancient ancestors could barely distinguish light from dark, today our complex vertebrate eyes allow us to read the tiny print in a newspaper (or this thesis), see the broad range of colors and varied light intensities of a sunset, and detect even a slight movement in the periphery of our visual field. There is an obvious practical benefit to understanding how the vertebrate eye works, as knowledge about how a healthy eye operates can be used to develop treatments for blindness-causing diseases. Beyond the practical, there is a secondary driver behind studying vision: curiosity about how a collection of cells can accomplish this remarkable function.

Tight control of intracellular Ca^{+2} is critical for vision

The functional tissue in the vertebrate eye is the neural retina, and photoreceptors are the light-detecting cells of the retina (**Figure 1.1A**). Photoreceptor activity is controlled by changes in the fluxes and levels of second-messenger cations, mainly Na^+ and Ca^{2+} (**Figure 1.1B**). In outer segments, there is a steady influx of Na^+ and Ca^{2+} during darkness which is cleared upon exposure to light, causing the cell to hyperpolarize. At the synapse, there is a similar influx of Ca^{2+} which is inhibited upon light-induced hyperpolarization. Subsequent clearance of synaptic Ca^{2+} then blocks synaptic neurotransmitter release, which transduces the signal of light to downstream neurons (Kolb et al., 2012).

Ca^{2+} also plays a critical role in the process of light adaptation. The activities of several proteins in the phototransduction cascade and their regulators (such as guanylyl cyclase, cyclic nucleotide gated (CNGs) channels, guanylyl cyclase activating proteins, and recoverin) are modulated by Ca^{2+}. The general outcome of this regulation is that photoreceptors become less sensitive in bright light when Ca^{2+} is low. This allows a photoreceptor to more effectively detect light over a wider range of intensities (Fain et al., 2001; Nakatani and Yau, 1988).

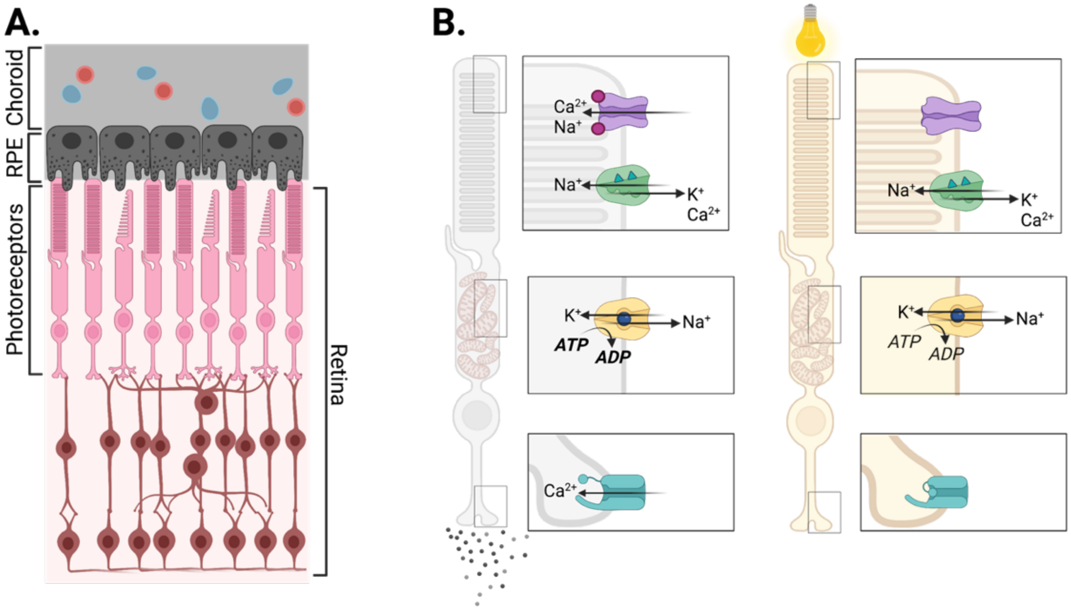

Figure 1.1: Retinal and Photoreceptor morphology and physiology

(A) Architecture of the vertebrate eye. (**B)** Cartoon of cation fluxes in light and dark photoreceptors. In darkness, cyclic-nucleotide gated channels (cNGCs, purple) on the plasma membrane outer segment allow an influx of Ca^{2+} and Na^{2+} which keep the cell depolarized. Depolarization maintains voltage gated Ca^{2+} channels (teal) at the synapse in an open position, allowing for an influx of synaptic Ca^{2+} that triggers release of neurotransmitter which communicate the “dark” state of the photoreceptor to downstream neurons. When a photon strikes the photoreceptor outer segment, it triggers a signaling cascade which causes cNGCs to close, shutting off the inward flux of Ca^{2+} and Na^{+}. The plasma membrane Na^{+}/K^{+}, Ca^{2+} exchanger (NCKX, green) remains operational and clears outer segment Ca^{2+}, while the Na^{+}/K^{+} ATPase (yellow) clears Na^{2+}. Clearance of Ca^{2+} and Na^{+} hyperpolarize the photoreceptor, which triggers closure of the synaptic voltage-gated Ca^{2+} channels. Synaptic Ca^{2+} is cleared by plasma membrane Ca^{2+} ATPases, and decreased synaptic Ca^{2+} inhibits the release of neurotransmitter-filled synaptic vesicles, signaling the presence of light.

Mitochondria reside between Ca^{2+} domains in photoreceptors

Given that intracellular Ca^{2+} plays a central role in phototransduction, transmission, and light adaptation, it is of interest to understand all factors which could modulate it. While the majority of intracellular Ca^{2+} is thought to be cleared through plasma membrane transporters in photoreceptors, organelles such as the endoplasmic reticulum and mitochondria might also contribute to Ca^{2+} buffering (Szikra and Krizaj, 2007). Mitochondrial localization in photoreceptors varies from species to species. In species with vascular retinas such as mouse, rat, and human, mitochondria are found mainly in the cell body but also at the synapse. In species with avascular retinas such as zebrafish, mitochondria reside only in the cell body (Stone et al., 2008).

The population of mitochondria that exists in the cell body between the outer segment and synaptic Ca^{2+} domains is of particular interest as they have been hypothesized to play a role in buffering Ca^{2+} between these domains. Studies in salamander photoreceptors have shown that the outer segment and synaptic Ca^{2+} domains are well-compartmentalized, can operate independently of one another, and that mitochondria can take up synaptic Ca^{2+} (Krizaj and Copenhagen, 1998). Cone mitochondria clusters in retinal slices from zebrafish also have the ability to buffer both outer segment and synaptic Ca^{2+} (Giarmarco et al., 2017a). These experiments show that photoreceptor mitochondria have the capacity to take up Ca^{2+} in a way that could insulate these Ca^{2+} domains. **Despite this, the extent that mitochondrial Ca^{2+} uptake functionally modulates any aspect of phototransduction or transmission in a living animal has not yet been established.**

Mitochondrial Ca^{2+} uptake can alter metabolism and function in different tissues

Mitochondrial Ca^{2+} uptake has been observed for over 50 years (DeLuca and Engstrom, 1961). However, determination of the identity of the pore forming Mitochondrial Calcium Uniporter (MCU) 10 years ago allowed for the importance of mitochondrial Ca^{2+} uptake in living organisms to be tested directly for the first time (Baughman et al., 2011; De

Stefani et al., 2011). Since then, it has become clear that the role played by MCU in different tissues is highly context dependent. This is exemplified by comparing the severity of metabolic phenotypes in a panel of tissue-specific MCU$^{-/-}$ models. For example, brown adipose tissue is unaffected by loss of MCU, liver and cultured cortical neurons exhibit a degree of metabolic remodeling, and heart and skeletal muscle exhibit both metabolic remodeling and an inability to meet energy demands during times of high energy consumption (Flicker et al., 2019; Gherardi et al., 2018; Kwong et al., 2015; Luongo et al., 2015; Mammucari et al., 2015a; Nichols et al., 2016; Tomar et al., 2019) The compensatory metabolic remodeling that occurs among affected tissues can also be very different. MCU$^{-/-}$ muscle accumulates hyperphosphorylated PDH and as a result upregulates fatty acid oxidation (Gherardi et al., 2018; Mammucari et al., 2015a; Pan et al., 2013). In contrast, MCU$^{-/-}$ livers accumulate fatty acids via an AMPK-dependent mechanism (Tomar et al., 2019). **Given the diverse consequences of MCU deficiency in other tissues, the role MCU plays in modulating photoreceptor metabolism and physiology must be tested and interpreted in the context of basal photoreceptor metabolism.**

Photoreceptors have high energy demands and are glycolytic

Roughly 80% of cone ellipsoids and 60% of rod ellipsoids are devoted to housing mitochondria in macaque, with a similar pattern observed in mouse (Hoang et al., 2002; Perkins et al., 2003). Given their abundance of mitochondria, it is surprising that studies performed on isolated retinas from several species show that >70% of glucose consumed by retinas is converted to lactate (**Table 1.1**) (Ames et al., 1992; Cohen and Noell, 1960; Wang et al., 1997b, 1997a; Winkler, 1995; Winkler et al., 2008). Photoreceptors are capable of increasing their reliance on oxidative metabolism in darkness when their energy demands

	Dark	*Light*
Ground Squirrel	94%	96%
Rabbit	89%	80%
C57Bl6/J Mouse	71%	54%
AIPL1$^{-/-}$ Mouse	5%	n.d.
Pig (outer retina)	n.d.	61%
Pig (inner retina)	n.d.	20%
Cat (outer retina)	n.d.	78%
Rat	n.d.	90%

Table 1.1: The percentage of glucose carbons which are converted to lactate by retinas from a variety of species. *AIPL1$^{-/-}$* mice are a model of Leber's congenital amaurosis and exhibit complete loss of photoreceptors due to degeneration. Data from mouse models provided by Daniel Hass.

are highest (Ames et al., 1992; Linsenmeier, 1986; Winkler, 1981). Intracellular Ca^{2+} levels are also at their highest in darkness, and it is known that at least three TCA cycle dehydrogenases are stimulated by Ca^{2+} (Denton, 2009; Denton et al., 1972, 1980; McCormack et al., 1990). **However, it is not yet known if mitochondrial Ca^{2+} uptake is required to stimulate these Ca^{2+}-sensitive dehydrogenases for dark-associated energy demands to be met.**

The architecture of the eye demands that the retina and retinal pigment epithelium use specialized metabolic fuels to meet their energy needs

When considering how a photoreceptor makes sufficient ATP to sustain activity, nutrient and oxygen availability should also be kept in mind. In the vertebrate retina, light must pass through a layer of inner-retinal neurons prior to striking the light-sensitive photoreceptors. To avoid scattering this light, obstructions in the light path such as blood vessels need to be kept to a minimum. This means that photoreceptors obtain almost all the nutrients and oxygen they consume from the choriocapillaris (**Figure1.1A**).

A metabolite traveling from the choriocapillaris to the photoreceptor layer must first cross Bruch’s membrane and the retinal pigment epithelial (RPE) cells. Metabolites passively diffuse through Bruch’s membrane, but RPE cells form tight junctions and create a legitimate barrier that metabolites must be transported across. Since photoreceptors consume an unusually high amount of glucose and produce huge quantities of lactate, there must be a high degree of flux of these metabolites between photoreceptors, RPE, and choroidal blood supply. This is supported by the polarized expression of glucose and monocarboxylate transporters on both the apical and basal surface of the RPE and photoreceptors (Ban and Rizzolo, 2000; Chidlow et al., 2005; Han et al., 2020; Hsu and Molday, 1991; Philp et al., 2001, 2003; Sánchez-Chávez et al., 2012). Additional ex vivo experiments contribute evidence to a model where glucose passes through RPE cells mostly unconsumed to reach the photoreceptors, where it is metabolized to lactate and released. RPE cells then import and oxidize the lactate

(Kanow et al., 2017). In addition to lactate, RPE cells can use mitochondrial fuels such as glutamine, proline, and fatty acids (Adijanto et al., 2014; Du et al., 2016a; Xu et al., 2020; Yam et al., 2019). **Given the diverse range of fuels RPE cells are capable of oxidizing, it is likely they rely on additional, undiscovered fuels.**

Oxygen tension differs dramatically between the RPE and retina

Reliance of the RPE on oxidative metabolism is facilitated by their nearly unlimited supply of O_2. O_2 tension is highest in the choriocapillaris and RPE, falls steeply at the photoreceptor layer, and remains low in the rest of the retina (Linsenmeier, 1986, 2004; Linsenmeier and Yancey, 1989; Linsenmeier and Zhang, 2017; Yu and Cringle, 2006; Yu et al., 2000, 2005). It remains a point of debate whether the low levels of O_2 observed in the retina are due to depletion by the RPE or the photoreceptor mitochondria. Regardless, the result is that RPE mitochondria exist in an O_2 maximum while photoreceptor mitochondria reside in an O_2 minimum.

Oxygen is the terminal electron acceptor in the conventional electron transport chain (ETC). This means that O_2 scarcity can create a metabolic pileup capable of influencing any upstream reaction. This is readily seen in cases of acute hypoxia (such as during a heart attack, stroke, or forced oxygen deprivation) when the TCA cycle metabolite succinate accumulates (Chouchani et al., 2014; Hochachka et al., 1975). It is widely accepted that this accumulation is related to the fact that Coenzyme Q (CoQ) becomes overly reduced in hypoxia because it is unable to deposit its electrons onto O_2. However, whether succinate accumulates because SDH can no longer deposit

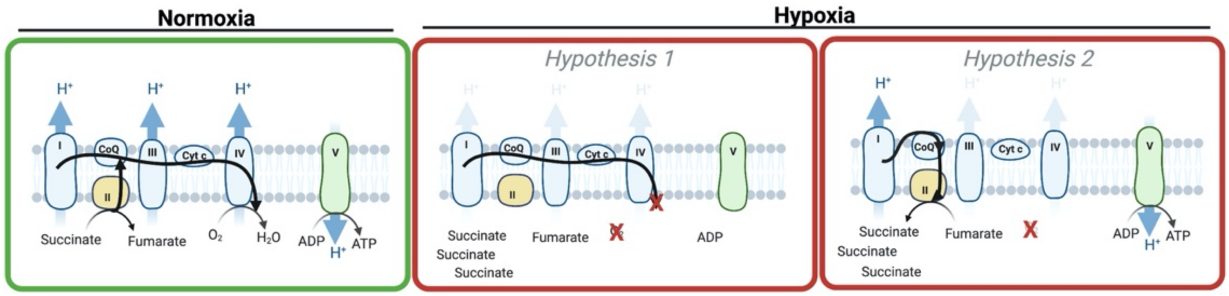

Figure 1.2: Possible pathways of succinate production during hypoxia

electrons from succinate into the reduced CoQ pool (*hypothesis 1*), or if succinate accumulates because it is newly produced as a result of reduced CoQ depositing electrons onto fumarate via reversal of the conventional SDH reaction (*hypothesis 2*) is still hotly debated (**Figure 1.2**) (Chinopoulos, 2019; Chouchani et al., 2014; Zhang et al., 2018). Furthermore, research efforts geared toward understanding the metabolic impact of low O_2 have focused on understanding the consequences of transient ischemia on cells and tissues. **The influence a permanent hypoxic niche might have on the basal metabolic program of a healthy tissue like the retina remains largely unexplored.**

Understanding how Ca^{2+} and low oxygen regulate photoreceptor metabolism and function

The broad goal of this dissertation is to gain a greater understanding of how photoreceptors and retinal pigment epithelial cells make energy, with a focus on filling the specific gaps in knowledge emphasized above.

First, we asked if photoreceptor mitochondrial Ca^{2+} uptake plays an important role in enhancing mitochondrial ATP production, and if mitochondrial Ca^{2+} uptake might alter cytosolic Ca^{2+} levels to a degree which modulates the photoresponse. To test this hypothesis, we generated animal models with overexpression or deletion of MCU and asked how photoreceptor metabolism and function changed. Overexpression of MCU results in altered TCA cycle activity and more rapid recovery of the photoresponse, providing a proof-of-principal model that mitochondrial Ca^{2+} buffering can regulate both cytosolic and mitochondrial photoreceptor functions. In parallel to these exciting findings, we noted that they were obtained only after ~100-fold overexpression of MCU and that endogenous MCU is expressed at very low levels in photoreceptors. This underscored the need for validation of the importance of mitochondrial Ca^{2+} uptake in photoreceptors using MCU knock-out animals. Surprisingly, although mitochondria from MCU KO zebrafish had reduced rapid Ca^{2+} uptake, they still maintained some ability to take up Ca^{2+} and had no metabolic or physiological defects. This led us to conclude that while mitochondrial Ca^{2+} uptake can influence photoreceptor metabolism and physiology if it is enhanced, MCU normally plays no role in mediating functionally important Ca^{2+} uptake in photoreceptors.

While conducting experiments to test the role of MCU-mediated mitochondrial Ca^{2+} uptake on metabolism, we observed flux through some unexpected metabolic pathways in wild-type retinas. These observations were consistent with the hypothesis that low oxygen in retinas might regulate their metabolism. We first observed that retinas produce and export large amounts of succinate, and that this succinate is produced through non-canonical reversal of succinate dehydrogenase. This caused us to wonder if another cell type in the eye was capable of metabolizing succinate, and we found that eyecups (containing RPE cells and choroidal endothelial cells) import and oxidize succinate. Succinate cannot cross plasma membranes and it is thought that most healthy cells do not import or export succinate. However, we validated that succinate transit in the eye is legitimately transport mediated and that MCT1 facilitates retinal succinate export, while an unidentified transporter (and not MCT1) facilitates eyecup succinate import.

Chapter 2: Increasing Ca^{2+} in photoreceptor mitochondria alters metabolites and accelerates light recovery

Introduction

Maintenance of Ca^{2+} homeostasis is critical for photoreceptor function and survival. Photoreceptors rely on Ca^{2+} as a second messenger for recovery from transient light signals, adaptation to constant illumination, and neurotransmission (Barnes and Kelly, 2002; Nakatani and Yau, 1988). This cytosolic Ca^{2+} can be buffered by mitochondria, and in photoreceptors the precise localization of mitochondria to the ellipsoid can protect the cell body from the cytosolic Ca^{2+} that accumulates in the outer segment in darkness (Krizaj and Copenhagen, 1998; Szikra and Krizaj, 2007),(Giarmarco et al., 2017b). Uptake of Ca^{2+} into mitochondria can also influence their energetic output (Glancy and Balaban, 2012). However, metabolic responses to changes in mitochondrial Ca^{2+} can vary from tissue to tissue (Griffiths and Rutter, 2009).

Ca^{2+} import into the mitochondrial matrix occurs via the mitochondrial Ca^{2+} uniporter complex (MCU complex), comprised of a multimer of the pore-forming protein MCU and many associated regulatory proteins (Baughman et al., 2011; De Stefani et al., 2011, 2015). The protein EMRE is necessary for MCU function in vertebrates, while MICU proteins (MICU1-3) tune Ca^{2+} uptake through the uniporter complex (Patron et al., 2018; Perocchi et al., 2010a; Plovanich et al., 2013a; Sancak et al., 2013a). This degree of regulation, along with the variability of modulator expression across tissues, implies that the activity of the MCU complex is attuned to cellular needs and critical in the interplay between optimal function and prolonged survival. To investigate the relationship between mitochondrial Ca^{2+} and photoreceptor physiology, we generated zebrafish models of cone-specific MCU overexpression (MCU OE) to test how cones respond to the increase of this key modulator of mitochondrial Ca^{2+}.

Results

Retinas express very low levels of MCU

We developed a custom antibody against the purified N-terminus of zebrafish MCU and validated its specificity with a global zebrafish MCU knock-out (MCU KO, **Figure 2.1A**). MCU protein expression is high in brain, lower in the heart, and lowest in the retina (**Figure 2.1A**). Retina resembles heart when MCU is normalized to mitochondrial proteins cytochrome oxidase (MTCO1) and succinate dehydrogenase (SDH) (**Figure 2.1B**). However, transcript expression of the MCU regulators MICU1, MICU2, and MICU3 resembles brain more than heart (**Figure 2.1C**).

Our antibody was not suitable for IHC of endogenous MCU, so we used the pde6c$^{-/-}$ zebrafish model of cone-specific degeneration to estimate MCU expression in cones. In this model, cones degenerate and rod photoreceptors populate the retina (Stearns et al., 2007). Cones have more mitochondrial volume than rods (Hoang et al., 2002; Winkler et al., 2008). Without cones, there are fewer mitochondrial membrane proteins but no significant loss of MCU signal (**Figure 2.1D,E**). This shows that cone mitochondria must have less MCU than other neurons.

We established a stable transgenic line that uses MCU-T2A-RFP under control of the promoter for cone transducin (“*gnat2”* or “TαCP”) to overexpress zebrafish MCU in cone mitochondria (**Figure 2.2A**). Because of the T2A sequence, cones overexpressing MCU (MCU OE) also express cytosolic RFP (Kim et al., 2011). MCU expression in MCU OE retinas is 102 ± 5 -fold higher than normal (**Figure 2.2B,C**). The overexpressed MCU localizes to cone mitochondria (**Figure 2.2D**).

Ca^{2+} influx depends on MCU and its regulators, so we investigated whether MCU OE increases the steady-state concentration of free Ca^{2+} in cone mitochondria. We used *gnat2*:mito-GCaMP3 fish, which express the Ca^{2+} sensor GCaMP3 in cone mitochondria (Giarmarco et al., 2017b). Mito-GCaMP3 fluorescence in the mitochondrial clusters of live zebrafish larvae is 4.4 fold higher (median, Q1: 3.4, Q3: 6.06 fold) in

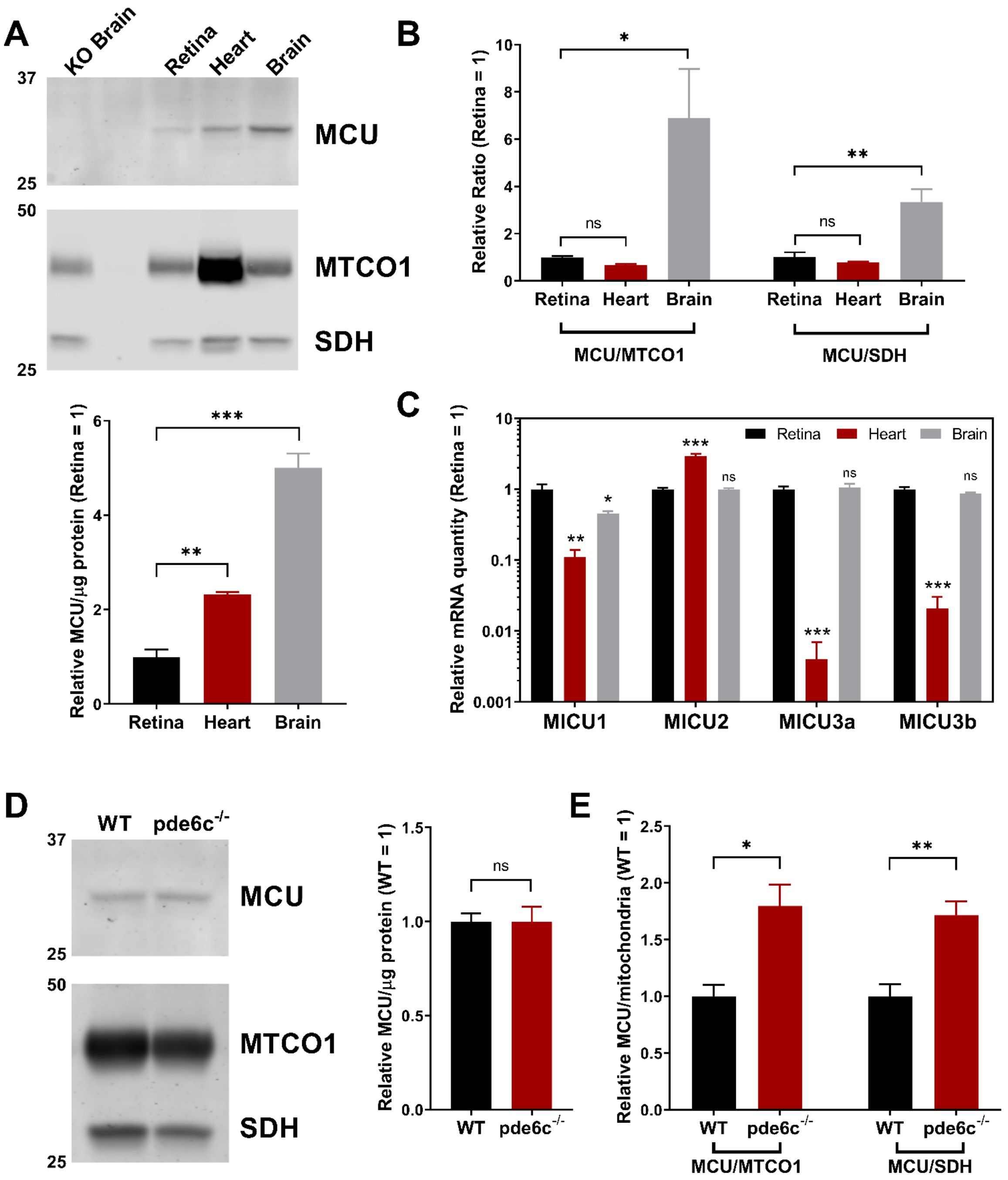

Figure 2.1: MCU expression is limited in the retina, particularly in cones.

(A) Western blot of zebrafish tissue lysate, enriched for mitochondrial proteins and probed for MCU, mitochondrial cytochrome oxidase (MTCO1), and succinate dehydrogenase (SDH). Samples were pooled from either 4 retinas, 2 hearts, or 1 brain and performed with n=3 replicates of each pool. Each lane contains 8 µg of protein. Values normalized to retina tissue. Bars = standard error. $^{**}p<0.01$, $^{***}p<0.001$ using ANOVA followed by Dunnett post-hoc test (comparison to retina). **(B)** Within each lane from the gel in A, the ratios of MCU signal to the mitochondrial proteins MTCO1 and SDH were determined. Values were normalized relative to retina tissue. Bars = standard error. $^{*}p<0.05$, $^{**}p<0.01$ using ANOVA followed by Dunnett post-hoc test (comparison to retina).

(Figure 2.1 continued)

(C) qRT-PCR quantification of relative mRNA of MICU proteins (relative to reference gene *Ef1α* and/or *b2m*, see methods) across retina, heart, and brain tissues. Bars = standard error. *$p<0.05$, **$p<0.01$, ***$p<0.001$ and ns = not significant using ANOVA followed by Dunnett post-hoc test (comparison to retina). **(D)** Retinal lysate, enriched for mitochondrial proteins, of WT and pde6c$^{-/-}$ cone deficient retinas. Each lane is from mitochondrial-enriched lysate of two pooled retinas from a single fish, n=4 fish. 30 µg of protein were loaded in each lane. Ns = not significant using Welch's t-test. **(E)** Relative quantification of the ratio MCU to mitochondrial proteins MTCO1 and SDH in WT and pde6c$^{-/-}$ cone deficient retinas from the gel shown in D. *$p<0.05$, **$p<0.01$ using Welch's t-test.

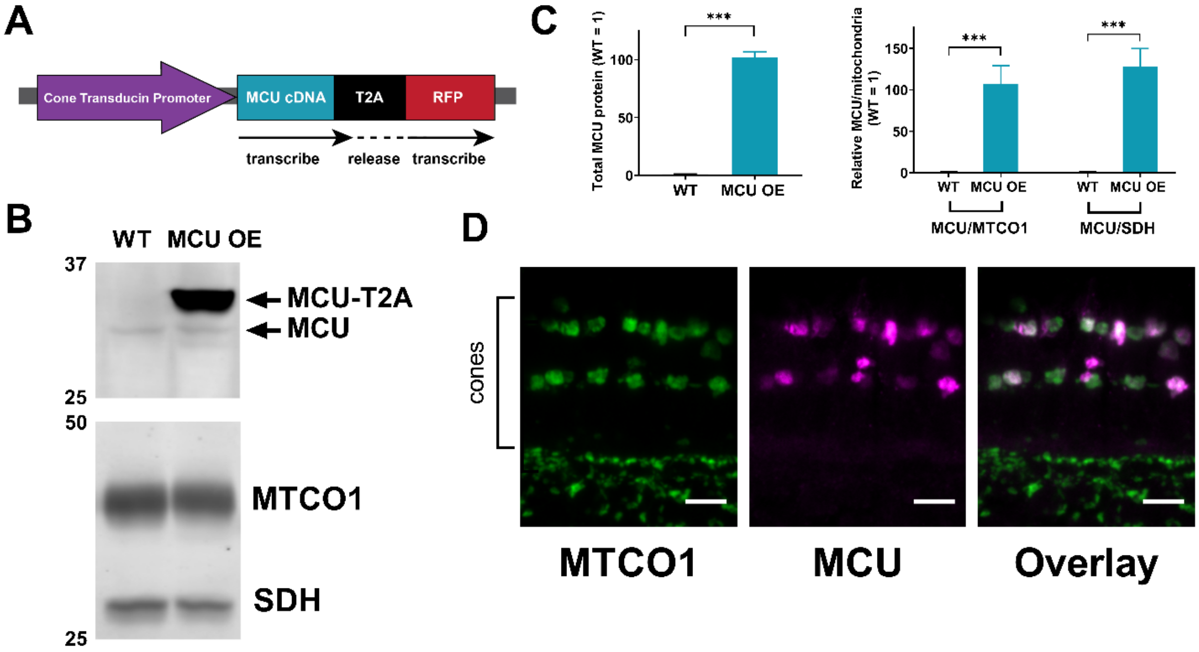

Figure 2.2: Successful generation of a cone-specific MCU overexpression zebrafish model.

(A) Schematic of MCU OE construct. The cone transducin promoter (TαCP, *gnat2*) drives expression of zebrafish MCU cDNA in all cone subtypes. The MCU cDNA is tagged with a T2A sequence followed by RFP. The T2A sequence causes ribosomes to stall and release the nascent MCU polypeptide with some added peptides from the T2A sequence before translating the RFP separately. Thus, RFP is present in the cytosol of cones with MCU overexpression. **(B)** Retinal lysate, enriched for mitochondrial proteins, of WT and MCU OE retinas. Blot was probed with antibodies for MCU, MTCO1, and SDH. 8 µg of protein was loaded per well. Each lane is from mitochondrial-enriched lysate of two pooled retinas from a single fish, n=4 fish. **(C)** Quantification of relative MCU signal as a function of protein concentration and relative to other mitochondrial markers from the gel in B. Both exogenous and endogenous MCU were used for total MCU quantification in the MCU OE retina. ***$p<0.001$ using Welch's t-test. **(D)** Immunohistochemistry of a larval zebrafish retina expressing the MCU construct in A using MCU and mitochondrial cytochrome oxidase (MTCO1) antibodies. Scale bar = 5 µm.

MCU OE compared to WT siblings (**Figure 2.3A**). We next prepared *ex vivo* retinal slices of *gnat2*:mito-GCaMP3 zebrafish, measuring the baseline mito-GCaMP3 fluorescence (F_0), the maximum fluorescence (F_{max}) by addition of ionomycin to the media containing 2 mM Ca^{2+}, and the minimum fluorescence (F_{min}) by addition of 5 mM EGTA to chelate Ca^{2+} (**Figure 2.3B**). Comparing (F_0 - F_{min}) to (F_{max} - F_{min}) indicated that baseline GCaMP3 is at 20 ± 1% of maximum fluorescence in WT mitochondria and 48 ± 2% of maximum in MCU OE mitochondria. Using these measurements and a K_D of 345 nM for the blinding of Ca^{2+} to GCaMP3 (ref (Chen et al., 2013)), the baseline free $[Ca^{2+}]_{mito}$ in WT mitochondria is 80.0 nM (median, with Q1: 67.1, Q3: 110.5 nM) and in MCU OE mitochondria is 320.6 nM (median, with Q1: 223.9, Q3: 509.0 nM) (**Figure 2.3C, equation in legend**).

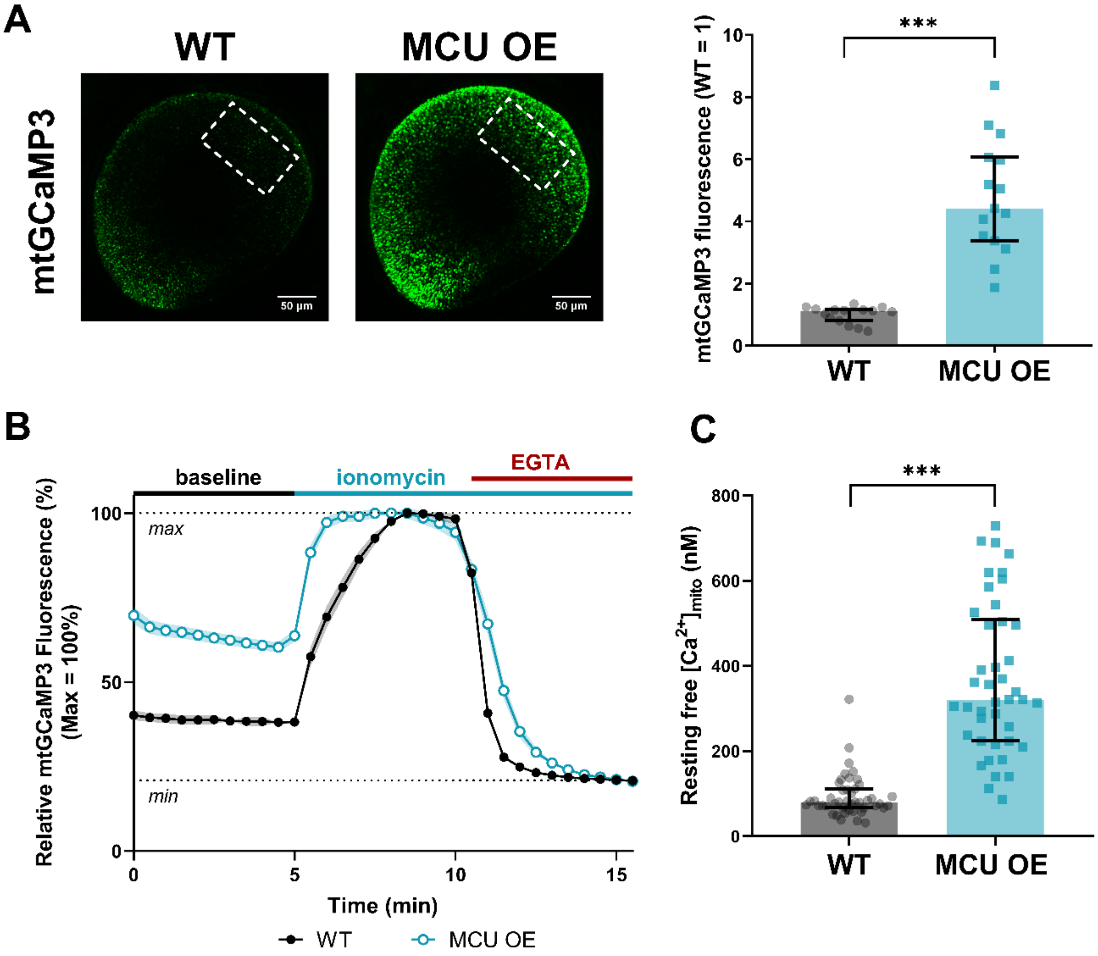

Figure 2.3: Overexpression of MCU in cones raises basal [Ca^{2+}] in the mitochondrial matrix. **(A)** Total cone mitochondrial clusters in a larval zebrafish eye expressing *gnat2*:mtGCaMP3, a

(Figure 2.3 continued)

mitochondrial Ca^{2+} sensor (green). Dotted outlines demarcate the region of the eye used for fluorescence quantification. Reporting the median with bars = interquartile range, n=15 larvae for both WT and MCU OE. ***p<0.001 using Mann-Whitney test. **(B)** Relative mito-GCaMP3 fluorescence of cone mitochondrial clusters in adult retinal slices of *gnat2:*mtGCaMP3 fish (WT or MCU OE) collected between 3 and 6 months of age. Baseline fluorescence was first assayed in the presence of KRB buffer containing 2 mM $CaCl_2$, then ionomycin (5 μM) was added to the slice to allow 2 mM Ca^{2+} entry into the mitochondria to saturate the probe. Next, EGTA (5 mM) was added to the solution (keeping [ionomycin] constant) to chelate Ca^{2+} and establish the minimum GCaMP3 fluorescence signal. n= 45 mitochondrial clusters (3 fish) for WT and n=42 mitochondrial clusters (3 fish) for MCU OE. Fish were between 3-5 months of age and slices were imaged every 30 s. Shaded region = standard error. **(C)** Approximation of resting free [Ca^{2+}] in mitochondrial clusters assayed in B. Approximations used the equation $[Ca^{2+}] = K_D \times \frac{\theta}{1-\theta}$, where $\theta = \frac{F_0 - F_{min}}{F_{max} - F_{min}}$. We used the previously reported K_D of GCaMP3 (345 nM, from ref 57) as an approximation for our calculation. Reporting the median with bars = interquartile range and ***p<0.001 using Mann-Whitney test.

Retinas with MCU overexpressing cones have altered isocitrate dehydrogenase (IDH) and α-ketoglutarate (α-KGDH) dehydrogenase activity

The enhanced resting Ca^{2+} levels in MCU OE cones allowed us to determine how altered mitochondrial Ca^{2+} content and structure affect cone metabolism. Zebrafish retinas are cone-dominant; quantification of the data in **Figure 2.1D** shows cones have ~40% of the mitochondrial mass in a zebrafish retina (MTCO1 and SDH in cone-deficient retinas are present at 56 ± 4% and 58 ± 5% of WT levels, n = 4). Thus, analysis of whole retinas provides valuable information regarding changes to mitochondrial metabolism in cones.

In vitro studies have shown that Ca^{2+} lowers the K_m of isocitrate dehydrogenase (IDH) and α-ketoglutarate dehydrogenase (α-KGDH) for their substrates (Denton, 2009; McCormack and Denton, 1979). We sought to determine if MCU OE in cones alters the activities of these enzymes. Cones rely on glucose as a fuel, so we incubated 4-month old WT and MCU OE retinas in U-^{13}C-glucose and used gas chromatography-mass spectrometry (GC-MS) to quantify ^{13}C-labeled TCA cycle metabolites **(Figure 2.4A)**.

Steady-state levels of m2 citrate and m2 isocitrate are lower in MCU OE retinas than control retinas (**Figure 2.4B**). After the α-ketoglutarate dehydrogenase (α-KGDH) reaction this relationship reverses. The steady state levels of m2 succinate, m2 fumarate, m2 malate, and m2 aspartate all are high in MCU OE retinas. This is consistent with both IDH and α-KGDH being stimulated by Ca^{2+} in MCU OE retinas. Ca^{2+} stimulation of IDH lowers its K_m for isocitrate, meaning it is more active at lower concentrations and thus able to deplete isocitrate pools. Increased IDH activity in isolation would cause m2 α-ketoglutarate accumulation, but instead we observe similar steady-state levels of m2 α-ketoglutarate in MCU OE and WT retinas and begin to observe an accumulation of metabolites only downstream of α-KGDH. This suggests that MCU OE retinas also have enhanced α-KGDH activity which prevents the buildup of α-ketoglutarate and leads to increased production of downstream metabolites. This shift in steady-state levels also is reflected in the total (sum of unlabeled and all isotopomers) metabolite levels **(Figure 2.5E)**. Additional metabolite data is included in the supplemental material **(2.5A, B, D, E)**.

Glucose is a physiologically relevant fuel for photoreceptors, but it does not allow for IDH and α-KGDH activity to be observed in isolation because the two are intrinsically linked in the TCA cycle. To confirm that α-KGDH is stimulated by Ca^{2+} in MCU OE cones, we bypassed IDH and fueled α-KGDH directly with U-^{13}C-glutamine **(Figure 2.4C)**. MCU OE retinas fueled with U-^{13}C-glutamine for 15 minutes accumulate higher levels of metabolites downstream of α-KGDH **(Figure 2.4D,** glutamine titration in **Figure 2.5F**). These observations confirm that Ca^{2+} enhances α-KGDH activity in cones.

It has been reported both *in vitro* and *in vivo* that Ca^{2+} can boost PDH activity by stimulating PDP1c, a subunit of the phosphatase that converts inactive phosphorylated PDH to active unphosphorylated PDH (Denton, 2009; Denton et al., 1972). We hypothesized MCU OE cones would have a lower ratio of phosphorylated/total PDH due to increased mitochondrial Ca^{2+}, but instead it is very slightly increased (1.12 ± 0.04-fold higher in MCU OE retinas, $p < 0.05$ using Welch's t-test) **(Figure 2.5C)**.

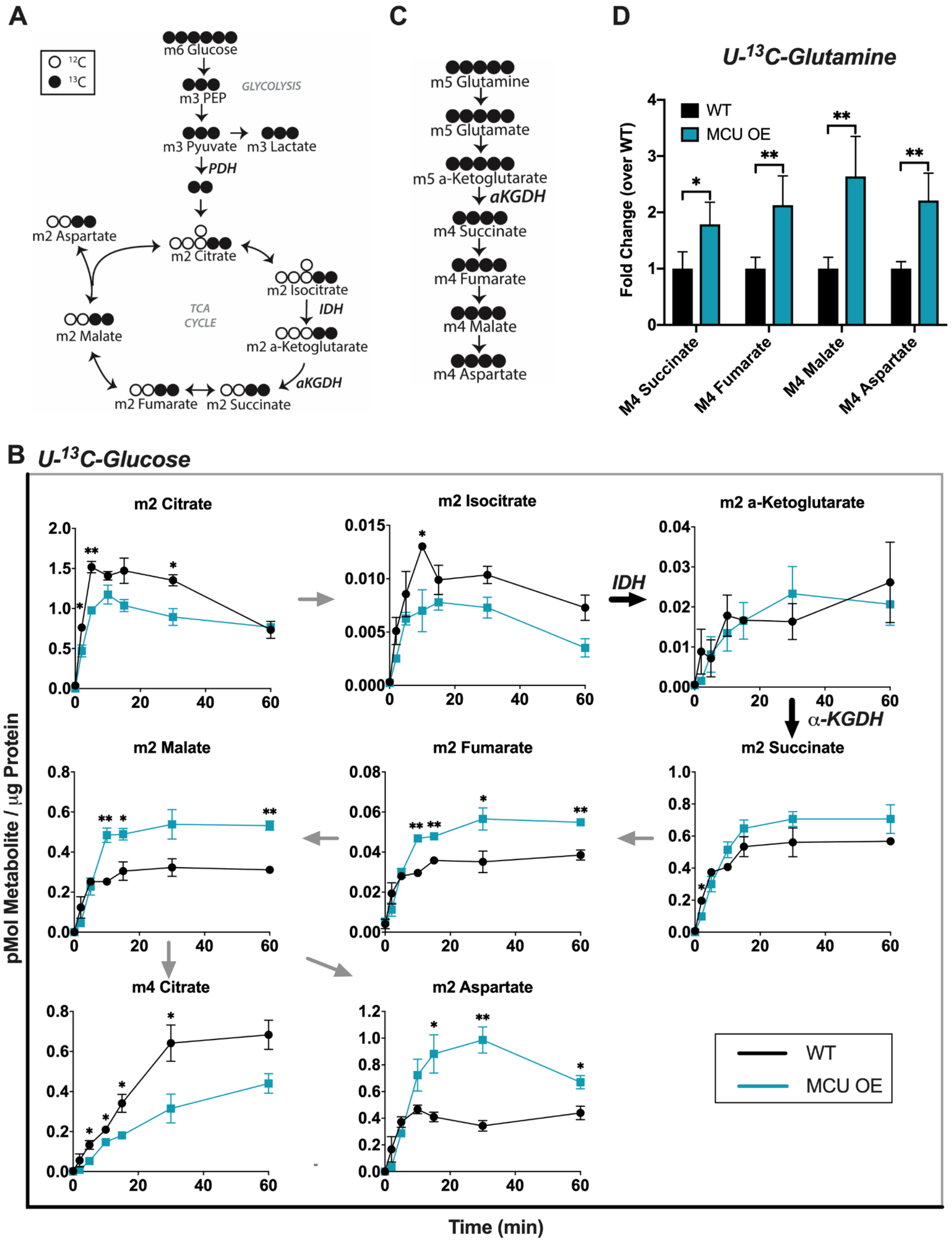

Figure 2.4: ^{13}C-Glucose and ^{13}C-Glutamine reveal changes to TCA cycle metabolites in MCU OE retinas consistent with faster rates of α-KGDH and IDH.

(A) Diagram showing how labelled carbons from U-^{13}C-glucose are incorporated through glycolysis and the first round of the TCA cycle. Shaded = labeled carbon, empty = unlabeled carbon. **(B)** Levels of isotopomers in WT and MCU OE retinas supplied with U-^{13}C-glucose. ‘m’ signifies the number of ^{13}C-labeled carbons in each metabolite. ‘m2’ TCA cycle metabolites are made from one round of the TCA cycle. Data points represent averages from n=3 retinas from 3 different fish. Fish were 4 months of age. *p<0.05, **p<0.01 using Welch’s t-test. **(C)** Diagram showing how labelled carbons from U-^{13}C-glutamine are incorporated into α-ketoglutarate and downstream metabolites. Shaded = labeled carbon, empty = unlabeled carbon. **(D)** Levels of isotopomers in WT and MCU retinas supplied with 2 mM ^{13}C-glutamine for 15 minutes. Data points represent averages from n=3 retinas from 3 different fish. Fish were 4 months of age. *p<0.05, **p<0.01 using Welch’s t-test.

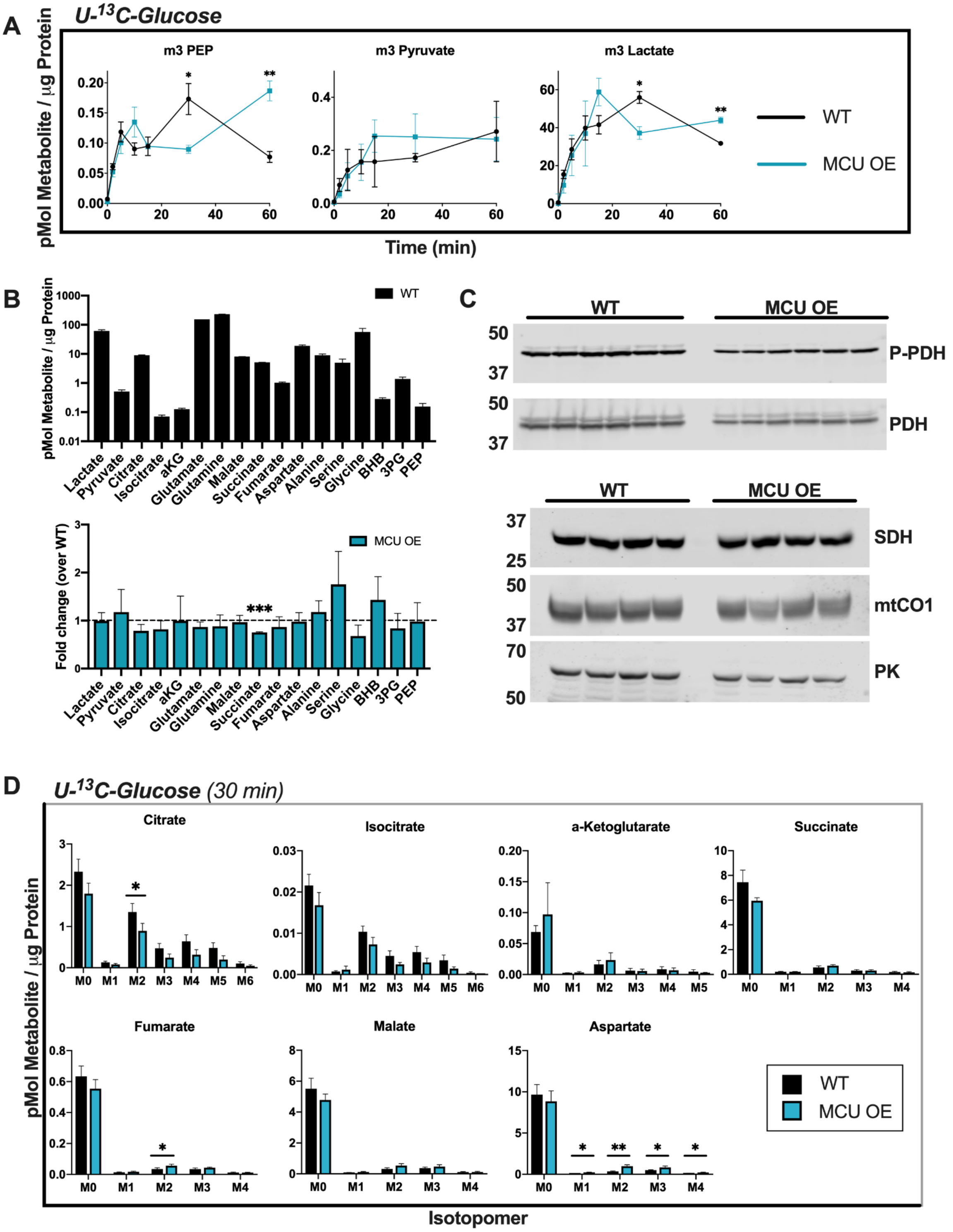

Figure 2.5: Further metabolic characterization of MCU OE retinas.

(A) Glycolytic intermediates from WT and MCU OE retinas supplied with ^{13}C-glucose. We observed no trends of altered glycolytic flux over time between WT and MCU OE retinas. $^*p<0.05$, $^{**}p<0.01$ using Welch's t-test. **(B)** Total metabolite levels in freshly dissected WT zebrafish retinas and relative levels of these metabolites in MCU OE retinas. (BHB: β-hydroxybutyrate, 3PG: 3-phosphoglycerate, PEP: phosphoenolpyruvate). **(C)** Top: Immunoblot showing P-PDH and total PDH expression in WT

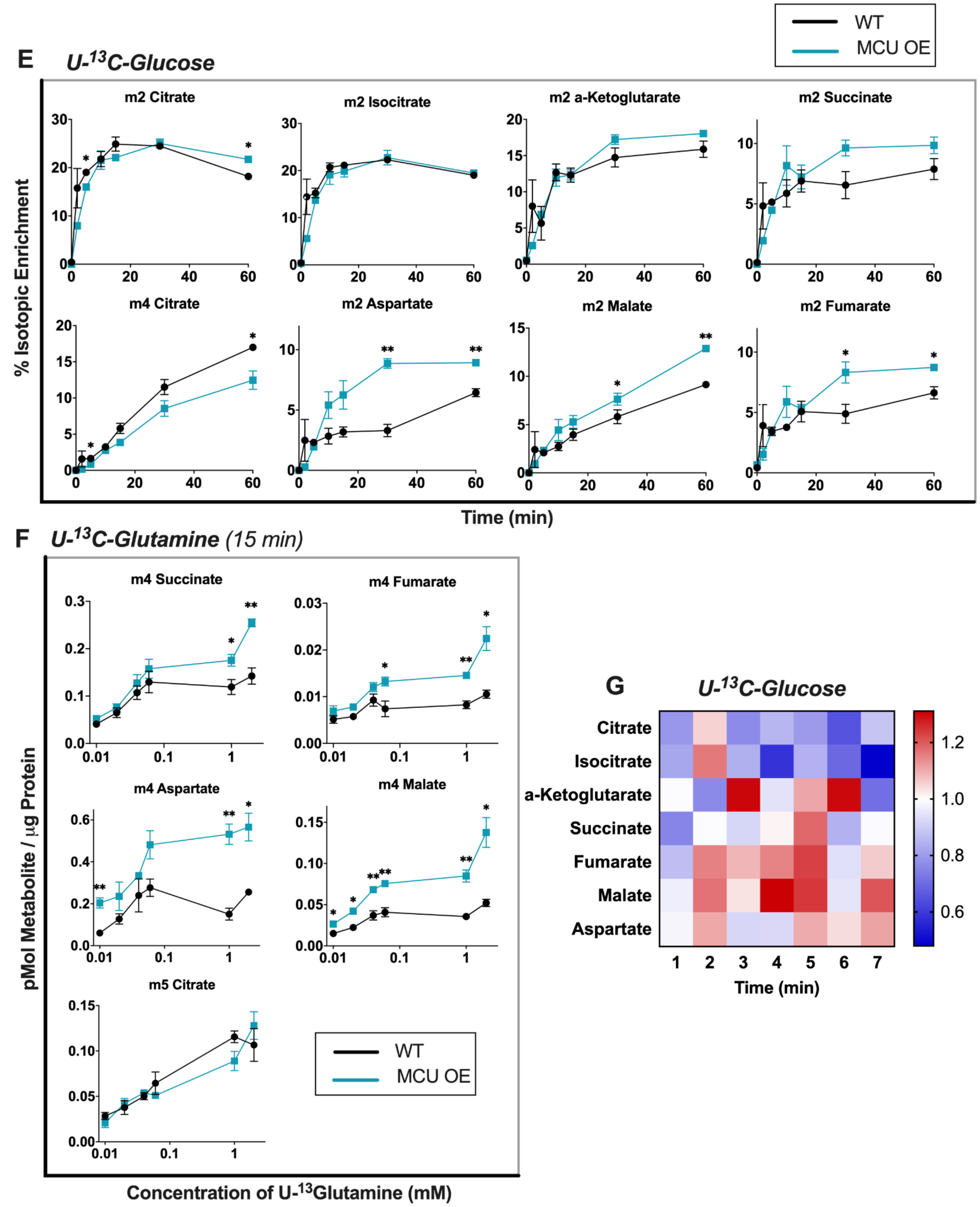

(Figure 2.5 continued)

and MCU OE retinas. n=6 WT and 6 MCU OE retinas from 3 different fish. The P-PDH/PDH ratio is 1.12 ± 0.04-fold higher in MCU OE retinas, $p<0.05$ using Welch's t-test. Bottom: Immunoblot of MTCO1, SDH, and Pyruvate Kinase (PK) in WT and MCU OE retinas. We observed that expression of every protein we probed for (PDH, SDH, mtCO1 and pyruvate kinase) was slightly lower in MCU OE

(Figure 2.5 continued)

retinas, even when the same amount of protein lysate was loaded. We hypothesize that this is because in MCU OE retinas, MCU and RFP comprise a greater fraction of the total amount of protein, meaning that other proteins comprise a smaller fraction of the total amount of protein when the same amount is loaded in a lane. n=4 WT and 4 MCU OE retinas from 4 different fish. **(D)** Distribution of isotopomers in WT and MCU OE retinas fed with U-^{13}C-Glucose for 30 min. **(E)** Isotopic enrichment (µg isotopomer/µg total metabolite) of WT and MCU OE retinas supplied with U-13C-Glucose. Since total citrate and isocitrate pools are depleted (see supplemental figure 5G), isotopic enrichment of m2 citrate and m2 isocitrate appear unchanged in MCU OE retinas. **(F)** Titration of WT and MCU OE retinas supplied with ^{13}C-glutamine (0.1, 0.2, 0.4, 0.6, 1, and 2 mM) for 15 minutes. m5 citrate (produced from reductive carboxylation) is included to show that only metabolites directly downstream of α-KGDH are produced at higher levels in MCU OE cones. Data points represent averages from n=3 retinas from 3 different fish. $^{*}p<0.05$, $^{**}p<0.01$ using Welch's t-test. **(G)** Heat map showing altered distribution of total levels of TCA cycle metabolite in MCU OE retinas fed with U-^{13}C-Glucose. At most time points, total levels of citrate and isocitrate are decreased in MCU OE retinas, while total levels of metabolites downstream of α-KGDH are increased.

Overexpression of MCU in cones reduces cytosolic Ca^{2+} transients and alters their phototransduction kinetics

Cytosolic Ca^{2+} plays a key role in phototransduction, so we assessed whether this was altered in MCU OE models. We first tested if MCU OE cones could clear cytosolic Ca^{2+} transients faster than in their WT counterparts. We pre-incubated retinal slices from *gnat2*:GCaMP3 fish in a 0 mM Ca^{2+} solution, then introduced a bolus of 5 mM $CaCl_2$ and monitored clearance of cytosolic Ca^{2+} from the cell body (**Figure 2.6A**). MCU OE cones clear Ca^{2+} from the cell body cytosol 2.3 ± 0.1 times faster than their WT siblings, as determined by the decay constant of a single exponential fit (**Figure 2.6B, Figure 2.7A**). The peak fold change in cone cell body GCaMP3 fluorescence in response to the Ca^{2+} bolus is lower in MCU OE compared to their WT siblings (**Figure 6C**). To determine whether these changes are due to Ca^{2+} uptake via MCU, we incubated MCU OE retinal slices in the MCU inhibitor Ru360. Ru360 treatment partially but significantly restores the WT kinetics (**Figure 2.6A-C**). The incompleteness of the effect may be attributed to other buffering mechanisms affected by MCU overexpression (such as the ER), insufficient permeability of Ru360 into cells, or an abundance of MICU1 which can block Ru360 binding to MCU (Paillard et al., 2018).

Cytosolic Ca^{2+} in photoreceptor outer segments regulates the gain of phototransduction, light response recovery kinetics and light adaptation (Makino et al., 2004; Mendez et al., 2001; Sakurai et al., 2011, 2015). Efficient clearance of Ca^{2+} from the outer segment in response to light is critical for rapid recovery of the photoresponse (see ref (Vinberg et al., 2018) for review), so we asked whether overexpressing MCU in cones accelerates recovery. Using an *ex vivo* ERG technique to measure pharmacologically isolated cone photoreceptor responses, we found that the initial phase of photoresponse recovery following light flashes is accelerated by MCU overexpression (**Figure 2.6D**). This is more apparent in the dim flash responses, which have a shorter time to half-maximum in MCU OE retinas (**Figure 2.6E**). At the age tested (7 months) the maximal response amplitude (R_{max}) is somewhat decreased in MCU OE retinas (**Figure 2.7B**). However, the dim flash responses normalized to R_{max} have larger amplitude in MCU cones compared to WT, suggesting an increased gain of phototransduction (**Figure 2.6D, Figure 2.7C**). To evaluate this, we determined a parameter called the amplification constant (A) using a model introduced by Lamb and Pugh (Lamb and Pugh Jr, 1992). We found a significant increase in A in MCU OE retinas, consistent with increased gain of phototransduction activation reactions **(Figure 2.7D)**.

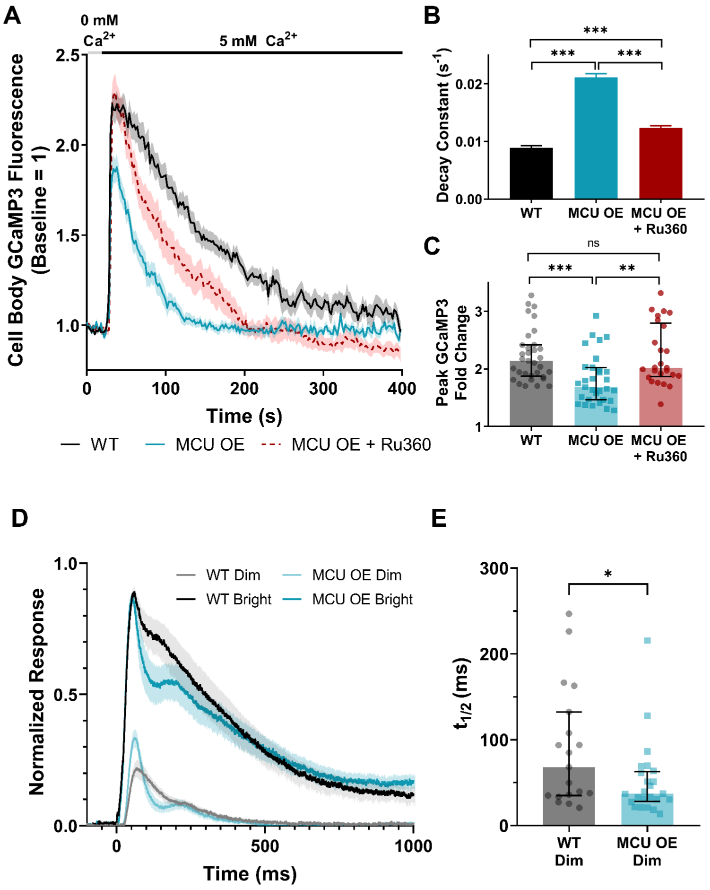

Figure 2.6: Overexpression of MCU in cones reduces cytosolic Ca^{2+} transients and alters their phototransduction kinetics.

(A) Isolated retinas from *gnat2*:GCaMP3 fish pre-incubated in 0 mM Ca^{2+} for 10 min then

(Figure 2.6 continued)

subjected to a 5 mM Ca^{2+} bolus (black bar). Fish used were WT, MCU OE, or MCU OE retinas preincubated in Ru360 (100 μM) and maintained throughout the experiment. N=33 cells (7 fish) for WT, n=31 cells (7 fish) for MCU OE, n=26 cells (3 fish) for MCU OE + Ru360. Fish were between 3-5 months of age and slices were imaged every 2s. Shaded region = standard error. **(B)** Decay constant of Ca^{2+} clearance for experiments shown in A. Bars = standard error. ***$p<0.001$ using ANOVA followed by Tukey post-hoc test. **(C)** Peak GCaMP3 fluorescence fold-change from baseline for experiments shown in A. The median is reported and bars = interquartile range. WT: median=2.14, Q1=1.87, Q3=2.42. MCU OE: median=1.68, Q1=1.46, Q3=2.02. MCU OE + Ru360: median=2.02, Q1=1.87, Q3=2.80. **$p<0.01$, ***$p<0.001$ using Kruskal-Wallis followed by Dunn post-hoc test. **(D)** The normalized *ex vivo* a-wave response isolated using DL-AP4 (40 μM) and CNQX (40 μM). Each retina response is normalized to R$_{max}$, the maximum response at the brightest light intensity. Bright flash stimulus intensity is 800,457 photons μm^{-2} and 20ms in duration. N=19 retinas (11 fish) for WT siblings, n=24 retinas (14 fish) for MCU OE. Fish were 7 months of age. Shaded region = standard error. **(E)** Time to half maximum of the individual responses to a dim stimulus flash from data shown in D. Dim flash stimulus intensity is 2144 photons μm^{-2} and 5ms in duration. The median is reported and bars = interquartile range. WT: median=68.1 s, Q1=34.9, Q3=132.4. MCU OE: median=37.1 s, Q1=28.2, Q3=63.0 *$p<0.05$ using Mann-Whitney test.

The median is reported and bars = interquartile range. WT: median=2.14, Q1=1.87, Q3=2.42. MCU OE: median=1.68, Q1=1.46, Q3=2.02. MCU OE + Ru360: median=2.02, Q1=1.87, Q3=2.80. **$p<0.01$, ***$p<0.001$ using Kruskal-Wallis followed by Dunn post-hoc test. **(D)** The normalized *ex vivo* a-wave response isolated using DL-AP4 (40 μM) and CNQX (40 μM). Each retina response is normalized to R$_{max}$, the maximum response at the brightest light intensity. Bright flash stimulus intensity is 800,457 photons μm^{-2} and 20ms in duration. N=19 retinas (11 fish) for WT siblings, n=24 retinas (14 fish) for MCU OE. Fish were 7 months of age. Shaded region = standard error. **(E)** Time to half maximum of the individual responses to a dim stimulus flash from data shown in D. Dim flash stimulus intensity is 2144 photons μm^{-2} and 5ms in duration. The median is reported and bars = interquartile range. WT: median=68.1 s, Q1=34.9, Q3=132.4. MCU OE: median=37.1 s, Q1=28.2, Q3=63.0 *$p<0.05$ using Mann-Whitney test.

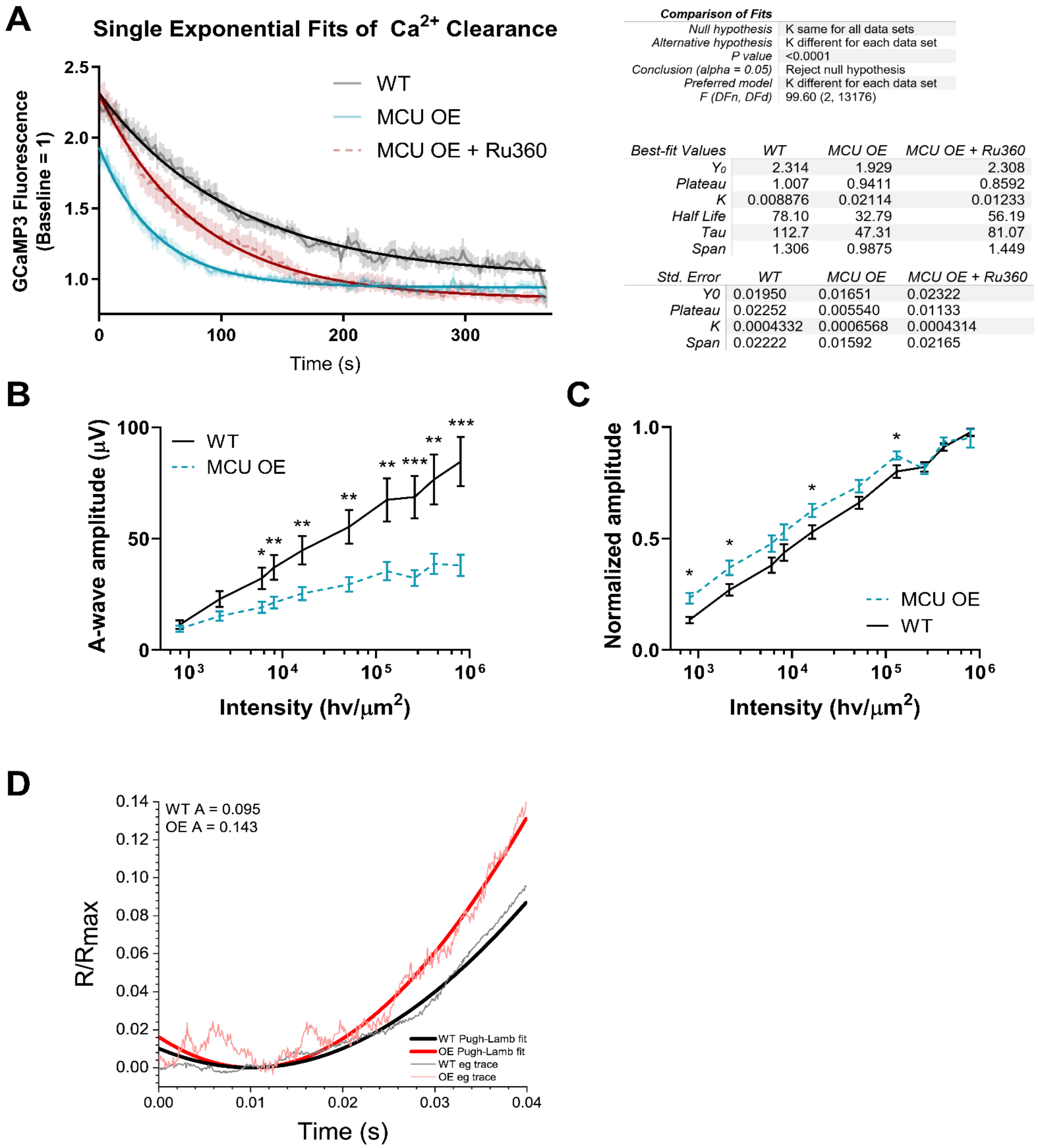

Comparison of Fits	
Null hypothesis	K same for all data sets
Alternative hypothesis	K different for each data set
P value	<0.0001
Conclusion (alpha = 0.05)	Reject null hypothesis
Preferred model	K different for each data set
F (DFn, DFd)	99.60 (2, 13176)

Best-fit Values	*WT*	*MCU OE*	*MCU OE + Ru360*
Y_0	2.314	1.929	2.308
Plateau	1.007	0.9411	0.8592
K	0.008876	0.02114	0.01233
Half Life	78.10	32.79	56.19
Tau	112.7	47.31	81.07
Span	1.306	0.9875	1.449

Std. Error	*WT*	*MCU OE*	*MCU OE + Ru360*
Y0	0.01950	0.01651	0.02322
Plateau	0.02252	0.005540	0.01133
K	0.0004332	0.0006568	0.0004314
Span	0.02222	0.01592	0.02165

Figure 2.7: Fitting of Ca^{2+} clearance data and other ERG parameters.

(A) Truncated Ca^{2+} clearance data used for fitting with a one-phase exponential decay function (least squares fit) in GraphPad Prism 8.0.1. The fitted exponentials are shown by a solid, dark line. No constraints were included for Y_0 or the plateau, $K > 0$. K is different for each data set, with $p < 0.0001$. Descriptive statistics of the fit included in table. **(B)** Absolute amplitude of the isolated a-wave response to varying intensity light of WT and MCU OE retinas for experiments shown in Figure 4D. Bars = standard error. $^*p<0.05$ using Welch's t-test. **(C)** Amplitude of a-wave responses in WT and MCU OE retinas normalized to the maximum response for experiments shown in Figure 4D. Bars = standard error. $^*p<0.05$ using Welch's t-test. **(D)** Lamb-Pugh model fits to ex-vivo ERG dim flash responses normalized to R_{max} of example WT and OE retinas, with original response traces in pale red/grey. WT mean A = 0.0128 $\mu m^2 s^{-2}$ ± 0.0143, n= 16 retinas. MCU OE mean A = 0.18278 $\mu m^2 s^{-2}$ ± 0.0217, n= 23 retinas. $^*p<0.05$ using Welch's t test.

Discussion

The key findings of our study are 1) metabolic and physiologic functions of cones are influenced by enhanced mitochondrial Ca^{2+} influx, and 2) MCU is expressed at very low levels in cone photoreceptors.

Mitochondrial Ca^{2+} uptake can alter phototransduction kinetics

Mitochondria can act as a barrier between the Ca^{2+} pools in the outer segment and the rest of the cell (Giarmarco et al., 2017b). Their proximity to the outer segment raises the possibility that they could influence Ca^{2+} in the outer segment, where Ca^{2+} clearance is essential to promote photoresponse recovery and adaptation. Clearance of outer segment Ca^{2+} is thought to be accomplished primarily by plasma membrane Na^+/Ca^{2+}, K^+ exchangers, but cones lacking these can respond to light, light-adapt, and degenerate rather slowly, suggesting that there is an additional pathway that clears Ca^{2+} from cone outer segments (Vinberg and Kefalov, 2018; Vinberg et al., 2017). Survival of MCU OE cones allowed us to investigate the capacity for mitochondria to influence the photoresponse, and we report that faster clearance of cytosolic Ca^{2+} is accompanied by accelerated photoresponse recovery. This indicates that mitochondrial Ca^{2+} uptake in photoreceptors can contribute to Ca^{2+} clearance from the outer segment and modulate the kinetics of the photoreceptor response to light. Similarly, delayed rod photorecovery is observed in human patients with malfunctioning mitochondria (Cooper et al., 2002).

MCU overexpression enhances IDH and α-KGDH activity

The perturbations to mitochondrial structure and localization in MCU OE cones could cause Ca^{2+}-independent changes to mitochondrial metabolism. However, TCA cycle metabolites are not globally decreased and MCU OE retinas have unaltered glycolytic activity, suggesting they are not compensating for decreased mitochondrial metabolic function. Instead of disrupting mitochondrial metabolism, MCU overexpression specifically alters the steady-state levels of TCA cycle metabolites, consistent with enhanced activities of the Ca^{2+}-sensitive enzymes IDH and α-KGDH.

The highest levels of intracellular free Ca^{2+} in photoreceptors occur in darkness, when energy demand and O_2 consumption are greatest. Ca^{2+} could play an important role in stimulating increased TCA cycle activity in photoreceptors in darkness (Krizaj and Copenhagen, 2002; Okawa et al., 2008). Rod photoreceptors in mouse retinas accumulate higher levels of TCA cycle metabolites downstream of α-KGDH in darkness than in light (Du et al., 2016b). Here, we report a similar accumulation of downstream metabolites in MCU OE cones. We also note that enhanced IDH and α-KGDH activities deplete upstream pools of citrate and isocitrate. MCU OE retinas do not increase citrate production in response to a decrease in the steady-state level of citrate, suggesting that TCA cycle activity in cones is limited either by pyruvate entry into mitochondria or by acetyl-CoA production.

An increase in the P-PDH/total PDH ratio is a common metabolic phenotype in MCU KO tissues (Mammucari et al., 2018). However, we did not find evidence for Ca^{2+} stimulation of PDH phosphatase in cones. Since the P-PDH/total PDH ratio also does not decrease when MCU is overexpressed in muscle cells, it is possible that changes in mitochondrial bioenergetics resulting from increased mitochondrial Ca^{2+} feed into the complex regulation of PDH (Mammucari et al., 2015b). For example, stimulation of α-KGDH and IDH activity may result in higher NADH levels in MCU OE cones, which in turn stimulates PDH kinase to balance increased PDP1c activity.

Overall, we observe specific changes to metabolism and phototransduction kinetics that are consistent with enhanced mitochondrial Ca^{2+} uptake in MCU overexpressing cones. This provides evidence that mitochondrial buffering of cytosolic Ca^{2+} has the capacity to modulate photoreceptor activity. However, these results were obtained after nearly 100-fold overexpression of MCU and we found that cones actually express low levels of endogenous MCU. This raises the question of whether the minimal amount of MCU present in wild-type cones is sufficient to facilitate the degree of Ca^{2+} uptake that would be required to see an effect on cone function. The hypothesis that endogenous MCU modulates photoreceptor metabolism and physiology will be explored in **chapter 3** of this thesis.

Acknowledgements

This chapter contains findings that are reported in a Cell Death and Differentiation publication and are part of a larger project that was spearheaded by Rachel Hutto. The authors who contributed to this work are Celia M. Bisbach (CMB), Rachel A. Hutto (RAH), Daniel C. Brock (DCB) Fatima Abbas (FA), Whitney M. Cleghorn (WMC), James B. Hurley (JBH), and Susan E. Brockerhoff (SEB). CMB, RAH, JBH, and SEB conceptualized and designed experiments. RAH and DCB collected data in Figures 2.1 and 2.2, RAH and WMC collected data in Figure 2.3, CMB and RAH collected data in Figures 2.4 and 2.5, and FA collected data in Figure 2.6. We thank Stanley Kim, Jeanot Muster, and Ashlee Evans for assistance in zebrafish husbandry and maintenance at the University of Washington South Lake Union aquatics facility (ISCRM Aquatics Facility). We would also like to acknowledge the Centralized Zebrafish Animal Resource (CZAR) at the University of Utah for providing zebrafish husbandry, laboratory space, and equipment to carry out portions of this research. Expansion of the CZAR is supported in part by NIH grant # 1G20OD018369-01. This work was supported by PHS NRSA T32GM007270 from NIGMS (RAH); NIH grants NEI EY026020 (JBH and SEB), NEI EY028645 (SEB) and P30EY001730 (UW Vision Core). This work was additionally supported by NIH EY014800 (John A. Moran Eye Center), and an Unrestricted Grant from Research to Prevent Blindness, New York, NY, to the Department of Ophthalmology & Visual Sciences, University of Utah.

Methods

Zebrafish Maintenance: Experiments with zebrafish were authorized by the University of Washington and University of Utah Institutional Animal Care and Use Committees. All fish used in this analysis were maintained in the University of Washington South Lake Union aquatics facility or the Centralized Zebrafish Animal Resource (CZAR) at the University of Utah at 27.5C on a 14 h/10 h light/dark cycle, and were maintained in the Roy$^{-/-}$ genetic background. All wild-type fish (WT) used in analysis were age-matched siblings to Tg(gnat2:MCU-T2A-RFP) fish (MCU OE) or age-matched siblings to pde6c^{w59} (pde6c$^{-/-}$).(Stearns et al., 2007) Fish used for slice preparation, protein quantification, and metabolomics analysis were male and female siblings between 3 and 6 months of age. Fish used in ERG analysis were male and female siblings collected at 7 months of age. For histological analysis, ages of sibling fish are included in the figure and legend.

Zebrafish MCU antibody: The cDNA encoding amino acids 21 – 202 of *Danio rerio* MCU (NM_001077325) was cloned downstream of GST using the pGEX-2T (GE) expression vector. Overexpression was induced in *E.coli* (BL21) by addition of 1mM IPTG at 0.2 OD followed by incubation with vigorous shaking for 5h at 37° C. The tiny fraction of soluble fusion was purified using glutathione sepharose following the manufacturer's instructions (GE Healthcare). Polyclonal antibodies were generated using injections of 0.5 – 1mg protein (R and R Research Co.). Two columns were used to clean the serum. One column contained total *E.coli* proteins covalently coupled to cyanogen bromide beads and the second column contained purified GST protein coupled to cyanogen bromide beads (GE Healthcare). Serum was cleaned by sequential incubations of 3 – 5 hours at room temperature with each column after which it was analyzed on an SDS page gel for lack of cross reactivity with GST and *E.coli* proteins from a total cell extract. Identification of MCU was validated by the absence of a protein of the correct molecular weight in extracts obtained from a CRISPR generated KO strain. The zebrafish MCU antibody was used at a dilution of 1:750 for western blotting and 1:50 for immunohistochemistry.

Zebrafish models: The transgenic zebrafish lines Tg(gnat2:GCaMP3), Tg(gnat2:EGFP), and Tg(mito-GCaMP3) have been described previously.(Giarmarco et al., 2017b; Kennedy et al., 2007; Ma et al., 2013) Generation of the global MCU KO line was performed using gRNA with the following sequence 5'-CCTCATACCTGGTGCAGCCCCCC-3' using methods as previously described.(Brockerhoff, 2017) For generation of the Tg(*gnat2*:MCU-T2A-RFP) line, zebrafish MCU cDNA was isolated from WT zebrafish larvae (5 dpf) using the forward primer 5'- AGAGATGGCTGCGAAAAGTGT-3' and reverse primer 5'-TTCTCATCAGTCCTTGCTGGT-3'. Overhang qPCR methods in conjunction with Fast-Cloning were used to add the T2A ribosomal stalling sequence and the RFP protein coding sequence; this was cloned into a pCR8/GW vector (Invitrogen). Plasmids were assembled using the Gateway-Tol2 system.(Villefranc et al., 2007) Expression of MCU-T2A-RFP was driven by the cone transducin alpha promoter (TαCP, gnat2), and the RFP coding sequence was flanked by a polyA tail sequence to increase transcript stability.(Kennedy et al., 2007) A destination vector with a sBFP2 heart marker for aid in transgenic identification was obtained from Cecilia Moens.(Kremers et al., 2007) The fully assembled construct was injected into embryos at the 1-cell stage with Tol2 transposase mRNA. Larvae mosaic for the transgene were raised to adulthood to identify founder carriers. A single F_0 founder was used to generate F_1 fish that were screened for a single insertion of the transgene; F_2 fish from two F_1 substrains with a single insertion were used for analysis in this study.

Primers for qRT-PCR: All designed primers were empirically tested to confirm primer efficiency was between 90-110%. Only primers passing this benchmark were used for analysis. Primer sequences for the reference genes *EF1a*, *b2m*, *Rpl13a*, and *TBF* were identical to previous reports testing zebrafish reference gene stability (*EF1a*, *Rpl13a*: ref (Tang et al., 2007), *b2m*, *TBP*: ref (McCurley et al., 2008)).

MICU1:
Forward: 5’-ACGTTAAAGCAGAATCGTAGAGG-3’
Reverse: 5’-CGCAAGCGGTACATATCAGAC-3’

MICU2:
Forward: 5’-ACTGAGTACCTGTTTCTCCTCAC-3’
Reverse: 5’-GGTCCATTTACTTTCTTCAGCTTCT-3’

MICU3a:
Forward: 5’-CGTCCCATGAGCATCGTTTC-3’
Reverse: 5’-TCCAACTCCTGTTTGGTGAGG-3’

MICU3b:
Forward: 5’-GCTTGGTGCAAGAATAGTTCTCTTT-3’
Reverse: 5’-TGCAGGTTGTCCATGAATCTGT-3’

qRT-PCR: An Applied Biosystems 7500 Fast Real-Time PCR System in conjunction with iTaq™ Universal SYBR® Green Supermix (Bio-Rad, 1725120) was used for qPCR measurements according to the manufacturer's instructions. The reference genes *EF1a*, *b2m*, *TBF*, and *rpl13a* were screened across the tissue panel using NormFinder to identify reference genes with the highest stability.(Andersen et al., 2004) NormFinder identified the combination of *EF1a* and *b2m* as most stable for retina-brain comparisons and *EF1a* as most stable for retina-heart comparisons. *EF1a* was identified as the most stable for WT vs MCU OE retina comparisons. Quantification of relative mRNA quantity used 3 biological replicates of each tissue, each performed in technical triplicate. From each technical triplicate, the average C_t value for the gene of interest and reference gene(s) were used to generate a ΔC_t value for each biological replicate. Comparing each tissue of interest to the retina generated a $\Delta\Delta C_t$ value; these were converted to a normalized expression level using the $2^{-\Delta\Delta Ct}$ method (Livak assumptions). Standard error of the ΔC_t value for each tissue was propagated to the final comparison using standard error propagation rules. Calculations were based off the geNorm method of qPCR normalization.(Vandesompele et al., 2002)

Commercial antibodies and stains:

Mitochondrial cytochrome oxidase, MTCO1 (Abcam, ab14705, RRID:AB_2084810); used in IHC and immunoblotting at 1:1000 dilution.

Succinate dehydrogenase B, SDHB (Abcam, ab14714, RRID:AB_301432); used in IHC and immunoblotting at 1:1000 dilution.

Pyruvate Dehydrogenase E1 subunit, PDH (Abcam, ab110334, RRID:AB_10866116)**;** **u**sed in immunoblotting at 1:1000 dilution.

Phosphorylated Pyruvate Dehydrogenase E1 subunit Ser293, P-PDH (EMD Millipore, ABS204, RRID:AB_11205754); used in immunoblotting at 1:2000 dilution.

Pyruvate Kinase, PK (Abcam, ab137791); used in immunoblotting at 1:1000 dilution.

Hoechst 33342, Trihydrochloride, Trihydrate stain (ThermoFischer, H3570); used in IHC at 5 µM concentration.

Lectin PNA Alexa Fluor 647 conjugate (ThermoFischer, L32460); used in IHC at 1:200 dilution after suspending at a concentration of 1 mg/mL in H2O.

Goat Anti-Mouse IgG H&L, Alexa Fluor 488 (Abcam, ab150113, RRID:AB_2576208);

used in IHC at 1:1000 dilution.
Goat Anti-Rabbit IgG H&L, Alexa Fluor 647 (Abcam, ab150083, RRID:AB_2714032); used in IHC at 1:1000 dilution.
IRDye 800CW donkey anti-rabbit IgG (H+L) (LI-COR Biosciences, 925-32213, RRID: AB_2715510); used at 1:5000 dilution for immunoblotting.
IRDye 680RD donkey anti-mouse IgG (H+L) (LI-COR Biosciences, 925-32212, RRID: AB_2716622); used at 1:5000 dilution for immunoblotting.
IRDye 680RD donkey anti-rabbit IgG (H+L) (LI-COR Biosciences, 925-68073, RRID: AB_2716687); used at 1:5000 dilution for immunoblotting.
IRDye 800CW goat anti-mouse IgG (H+L) (LI-COR Biosciences, 925-32210, RRID: AB_2687825); used at 1:5000 dilution for immunoblotting.

Mitochondrial enrichment and sample preparation for immunoblotting: Organs were snap-frozen in liquid nitrogen after collection, then homogenized with a dounce homogenizer in 50 mM Tris buffer containing sucrose (200 mM), NaCl (150 mM), and EGTA (1 mM) with a protease inhibitor mini tablet (ThermoFischer, 88666). Homogenized samples were centrifuged at a low speed of 1,000 x g for 10 minutes at 4°C, then the supernatant (containing mitochondria) was collected and centrifuged at a high speed of 17,000 x g for 45 minutes. The supernatant was discarded and the pellet (containing mitochondria) was homogenized for 1 minute in RIPA buffer. Homogenized mitochondria were sonicated on ice for three 5 second pulses. A standard BSA assay using Pierce™ BCA Protein Assay Kit (ThermoFischer, 23225) was performed according to the manufacturer's instructions for protein concentration determination. Samples were diluted with RIPA buffer to ensure an equal volume and equal protein concentration of each sample could be loaded into wells for immunoblotting.

Immunoblotting: Samples were loaded into wells on 12-14% acrylamide gels made in-house. Each sample contained 20% 5X SDS buffer containing β-mercaptoethanol. After running the gel at 150V for 1 hr, gels were transferred onto PVDF membranes (Millipore, IPFL00010) and blocked for 1 hr at room temperature in LI-COR Odyssey Blocking Buffer (LI-COR, 927-40000). Primary antibodies were diluted in blocking buffer at specified concentrations and incubated overnight at 4°C. Membranes were washed with PBST and PBS, then incubated with secondary antibody for 1 hr at 25°C and washed again before imaging. Membranes were imaged and bands were quantified using the LI-COR Odyssey CLx Imaging System (RRID:SCR_014579).

Immunohistochemistry (IHC) and degeneration quantification: All adult eyes were isolated from light-adapted zebrafish, and a small incision in the cornea was made to allow 4% paraformaldehyde fixative to enter the eye. Whole larvae were euthanized then incubated in 4% paraformaldehyde. After fixation overnight at 4°C, eyes were rinsed in PBS then subject to a sucrose gradient (20% and 30%), embedding in OCT, and cryosectioned at 12 µm. For sections stained with MCU antibody, antigen retrieval was performed by steaming sections in 10 mM sodium citrate (0.05% Tween-20, pH 6.0). Sections were washed in PBS, then blocked in PBS containing 5% donkey serum, 2 mg/mL bovine serum albumin, and 0.3% Triton X-100 for 1 hr. Primary antibodies were diluted in this buffer as specified, then applied to cryosection overnight at 4°C. Secondary antibodies were diluted as specified and applied to section for 1 hr in darkness at 25C. For PNA-labelled samples, sections were incubated in diluted PNA-647 for 30 minutes at 25°C. Tissues were washed, incubated in Hoescht stain for 10 minutes, then mounted in Fluoromount-G® (SouthernBiotech, 0100-01) under glass coverslips. Slides were imaged using a Leica LSP8 confocal microscope with a 63X oil objective. Leica LAS-X software (RRID:SCR_013673) was used to acquire images.

For quantification of cone nuclei in *gnat2*:GFP fish, high-resolution images of whole zebrafish retina slices were stitched together using ImageJ Grid/Collection stitching.(Preibisch et al., 2009) Both the dorsal and ventral regions of the retina were straightened along the cone nuclei axis using ImageJ from the optic nerve to the cilliary margin. This axis was divided into 5 equal parts, then double-cone nuclei were counted in each region, normalizing to the length in µm (height of the region was equal across samples, double cone nuclei are along a single axis). Double-cone nuclei were used for quantification as they are most easily distinguished from rod nuclei. GFP expression was used to confirm that the double-cone nuclei counted were indeed cone nuclei. All counting was performed blinded (masked) to sample identity.

Live larval imaging of mtGCaMP3: Larvae used for imaging were maintained in embryo media containing 0.003% 1-phenyl 2-thiourea (PTU, Sigma-Aldrich P7629) starting at 20 hours post-fertilization. Live zebrafish larvae were analyzed at 6 days postfertilization (dpf) by transferring to 0.5% low melting point agarose containing embryo media with 0.003% PTU and 0.02% (w/v) Tricaine (Sigma-Aldrich, E10521). Larvae were positioned in agarose in a petri dish containing embryo media and 0.02% (w/v) tricaine to prevent drying out. Imaging of slices was performed using an Olympus FV1000 in conjunction with Olympus FluoView FV10-ASW software (RRID:SCR_014215). A 40X water objective was used for imaging. The excitation/emission wavelengths used for mito-GCaMP3 were 488/510 nm. Timelapse images of live larvae were collected with a z-depth of 2 µm and were collected every 20 minutes. Images of total eye mitochondrial clusters were also collected at a z-depth of 2 µm. For quantification of total mito-GCaMP3 fluorescence, images of whole larval eyes were collected, and a fixed ROI centered on the nasal region of the retina was used for quantification. This region near the ventronasal patch is comprised of the most mature cone photoreceptors.(Schmitt and Dowling, 1999) For quantification of mislocalized mitochondria, laser power was increased to saturate signals and allow visualization of all mitochondria. Stacks of 50 µm in depth were collected across the entire eye for quantification and mitochondrial clusters were counted blinded to sample identity.

Retinal slice imaging of GCaMP3 and mito-GCaMP3: Slices were prepared as described previously.(Giarmarco et al., 2017b, 2018) For GCaMP3 cytosolic clearance experiments, slides were preincubated in KRB containing 0 mM Ca^{2+} and 0.4 mM EGTA for 10 minutes. Images of single optical slices were collected every 2 seconds. A 5 mM $CaCl_2$ bolus (accounting for EGTA) was injected into the slice imaging chamber 30s after the initial timelapse collection to establish baseline fluorescence. Injection volume was 1 mL into the 4mL imaging chamber, mixed thoroughly. These experiments in the MCU-overexpressing fish were additionally performed in the presence of Ru360 (Millipore, 557440) at 100 µM, in which slices were incubated for 1 hr prior to incubation in 0 mM Ca^{2+} media. Retinas treated with Ru360 were maintained in Ru360 throughout timelapse experiments. Dying cells near the cut edge that were constitutively loaded with Ca^{2+} and cells that did not respond to Ca^{2+} were not included in analysis.

For mito-GCaMP3 timelapse experiments, z-stacks of 15, 2 μm slices were collected every 30 seconds. Retinal slices in modified KRB containing 2 mM $CaCl_2$ were first imaged for 5 minutes to establish baseline mito-GCaMP3 fluorescence. Next, the chamber was injected with ionomycin (Sigma, 407950) to a final concentration of 5 μM (prepared in DMSO, at a final concentration of 0.1%) for another 5 minutes of image collection. Finally, an excess of EGTA (5 mM) was injected to chelate the 2 mM Ca^{2+} present in solution and images were collected for another 5 minutes. Injection volume was 1 mL into the 4mL imaging chamber, mixed thoroughly. Dying cells containing fragmented mitochondrial clusters constitutively loaded with Ca^{2+} and clusters that did not respond to ionomycin were not included in analysis. Additionally, any clusters where the maximum fluorescence signal in the presence of ionomycin was completely saturated were excluded from analysis.

The excitation/emission wavelengths used for both GCaMP3 and mito-GCaMP3 were 488/510 nm. Timelapses were analyzed using ImageJ + Fiji software (SCR_002285). Images were corrected for X-Y drift using the MultiStackReg plugin of ImageJ. For both cell body GCaMP3 and mito-GCaMP3 fluorescence ex vivo timelapses, fixed ROIs were used to quantify average fluorescence signal across the cluster/cell at every time point. Fluorescence of cytosolic GCaMP3 for timelapse analysis are reported as F/F_0, where F_0 is the baseline fluorescence. For mito-GCaMP3 fluorescence, the relative fluorescence at maximum was set to 100% for normalization. We used the equation $[Ca^{2+}] = K_D \times \frac{\theta}{1-\theta}$, where $\theta = \frac{F_0 - F_{min}}{F_{max} - F_{min}}$ to approximate $[Ca^{2+}]_{mito}$, where F_0 is the average “baseline” fluorescence, F_{max} is maximum fluorescence upon ionomycin addition, and F_{min} is the baseline fluorescence upon EGTA addition. We approximated the K_D of GCaMP3 at 345 nM for the calculation.(Chen et al., 2013)

Electroretinograms (ERG): Zebrafish were briefly dark-adapted (~30min), before euthanasia by ice water immersion. Eyes were enucleated into Modified Salamander Ringer’s solution(mM): NaCl 110, KCl 2.5, $CaCl_2$ 1.0, $MgCl_2$ 1.6, HEPES 10.0, Glucose 10.0, with pH adjusted to 7.8 with NaOH. The eyes were hemisected and retinas isolated from the eyecup. All procedures after the dark adaptation were performed under dim red light. To ensure *ex vivo* ERG signal was predominantly cone responses, dark adaption was limited to ~30 min to allow cone photopigment regeneration but not provide enough time for full rod photopigment regeneration. Furthermore, experiments were carried out during the day (between 11am-4pm) when rod contributions to retinal responses are at their lowest due to the circadian regulation of photoreceptor biology in the zebrafish retina. *Ex vivo* electroretinogram (ERG) recordings were performed as described previously.(Vinberg and Kefalov, 2015) Isolated retinas were mounted photoreceptor side up onto the specimen holder (ref (Vinberg et al., 2014)), and perfused with Modified Salamander Ringer's solution, supplemented with 40μM DL-AP4 (Tocris Bioscience) and 40μM CNQX (Tocris Bioscience) to isolate the photoreceptor component of the ERG signal (A-wave). The rate of perfusion was ~5 ml/min. and the experiments were conducted at room temperature (~23 ^{o}C).

ERG signal was first amplified (100X) and low-pass filtered at 300 Hz by a differential amplifier (DP-311, Warner Instruments), and data was further amplified (10X) and acquired at 10KHz using an integrated amplifier/digitizer (IPA, Sutter Instrument, CA). A High-Power LED light source (Solis-3C, Thorlabs, Newton, NJ), with filter for red light (630 nm, FWHM bandwidth 69 nm, FF01-630/69-25, Semrock, Rochester, NY) and LED driver (DC2200, Thorlabs) were used to provide the flashes of light stimuli, durations ranged from 5-100ms. The SutterPatch software (SutterPatch v1.1.2, Sutter Instrument, CA) drove both stimulus generation and data acquisition via the IPA amplifier's analogue output and input, respectively. Light stimuli were calibrated before experiments using a calibrated photodiode (FDS100-CAL, Thorlabs, Newton, NJ) and flash intensities converted to photons/μm^2.

Data analysis, including statistical analysis and figure preparation, was performed with GraphPad v 8.00 (for Windows, GraphPad Software, CA, USA). Normalized responses were calculated for each retina by dividing the response amplitude data by the maximal amplitude measured at the peak/plateau of the response to the brightest flash. To quantify the gain of phototransduction activation, we fitted the Lamb-Pugh model to the initial leading edge of the dim flash response for each retina, and compared the average amplification constant (A) between WT and OE siblings.(Lamb and Pugh Jr, 1992)

Metabolic flux analysis: Krebs-Ringer bicarbonate (KRB) buffer optimized for flux analysis (ref (Du et al., 2013a)) was used in these experiments. Zebrafish retinas were first dissected in KRB buffer containing U-^{12}C-glucose or U-^{12}C-glutamine at the same concentration they would be incubated in. After dissection, retinas were placed in dishes of pre-warmed KRB containing either U-^{13}C glucose (5 mM, Cambridge Isotopes, CLM-1396) or U-^{13}C glutamine (0.1 - 2 mM, Cambridge Isotopes, CLM-1822). Retinas were incubated in this solution for the specified time points at 28°C in a NAPCO Series 8000 WT CO_2 incubator (5% CO_2), then washed in ice-cold PBS and flash frozen in liquid nitrogen. Metabolites from each time point were extracted using ice-cold 80% MeOH and lyophilized. Two-step derivatization was performed by the addition of 20 mg/mL Methoxyamine HCl dissolved in pyridine, followed by *tert*-butyldimethylsilyl. Metabolites were analyzed on an Agilent 7890/5975C GC-MS as described extensively in previous work.(Du et al., 2013b, 2013a, 2015, 2016b) Metabolic flux experiments were repeated a minimum of twice, using three retinas from three different zebrafish for each condition in each experiment. Data shown are results from one representative experiment.

Electron microscopy and Richardson's staining: Adult zebrafish eyes were enucleated and a small incision was made in the cornea to allow fixative (4% glutaraldehyde in 0.1 M sodium cacodylate buffer, pH 7.2) to enter the eye. Tissues were stored at 4°C before postfixation in osmium ferrocyanide (2% osmium tetroxide/3% potassium ferrocyanide in buffer) for 1 hr, followed by incubation in 1% thiocarbohydrazide for 20 min. Samples were then incubated in 2% osmium tetroxide for 30 min at RT, and stained with 1% aqueous uranyl acetate overnight at 4°C. Samples were next stained en bloc with Walton's lead aspartate for 30 min at 60°C, dehydrated in a graded ethanol series, and embedded in Durcupan resin. Sections of tissue were cut at 60 nm thickness and imaged using a JEOL JEM-1230 transmission electron microscope or Zeiss Sigma VP scanning electron microscope. Samples of larval zebrafish eyes were imaged in conjunction with a Gatan 3View2XP ultamicrotome apparatus to generate stacks of EM images, which were aligned using TrakEM2 software (RRID:SCR_008954). Position in the eye for EM imaging was confirmed by cutting slices of tissue and staining with Richardson's stain.(Richardson et al., 1960)

These slices were imaged for histological analysis using a Nikon Eclipse E1000 with a Nikon Plan Apo 100X/1.40 DIC lens. Nikon ACT-1 software was used for image capture.

Statistics: Numerical results in text are reported as mean ± standard error of the mean unless otherwise stated. Statistical tests were performed using Graphpad Prism v 8.00 software. For statistical analysis, replicates (n) were always defined as biological replicates. Information on what constitutes n (e.g. larvae, retinas, cells) is listed in the figure legend of each experiment. Samples sizes were estimated based on previous experiments (Du et al., 2016b; Giarmarco et al., 2017b; Sakurai et al., 2015). For data sets with sufficient n to analyze population distribution, tests for normality were administered (Anderson-Darling, D'Agostino & Pearson, Shapiro-Wilk, Kolmogorov-Smirnov). For data sets that did not pass a majority of normality tests, the median is instead reported along with the interquartile range (Q1 and Q3).

Chapter 3: Mitochondrial Calcium Uniporter (MCU) deficiency reveals an alternate path for Ca^{2+} uptake in photoreceptor mitochondria

Introduction

Maintaining proper intracellular Ca^{2+} homeostasis is essential for cellular function. Mitochondria have the ability to sequester Ca^{2+} via the Mitochondrial Calcium Uniporter complex (MCU) (Baughman et al., 2011; De Stefani et al., 2011). Mitochondrial Ca^{2+} uptake via MCU can modulate both cytosolic and mitochondrial Ca^{2+} levels, meaning that Ca^{2+}-sensitive reactions that occur in both compartments can be affected by MCU activity. In the mitochondrial matrix, increasing Ca^{2+} can stimulate tricarboxylic (TCA) cycle dehydrogenases and enhance ATP production, although Ca^{2+} overload in the matrix can trigger cell death (Baumgartner et al., 2009; Denton, 2009). Mitochondrial Ca^{2+} uptake can also regulate cytosolic Ca^{2+} levels and thus influence Ca^{2+}-sensitive cytosolic reactions. Since these Ca^{2+}-sensitive cytosolic reactions vary widely among cell-types depending on each cell's specific function, disruptions in mitochondrial Ca^{2+}-uptake can have tissue-specific consequences (Mammucari et al., 2016, 2018).

Photoreceptors, the light-sensitive neurons in the retina, rely on spatially distinct changes in cytosolic Ca^{2+} to regulate both phototransduction and neurotransmission. At the outer segment, intracellular Ca^{2+} changes in response to light stimulation and this is critical for timely shut-down of the phototransduction cascade and light adaptation (Korenbrot and Rebrik, 2002). At the synapse, changes in intracellular Ca^{2+} modulate vesicle release and neurotransmission (Krizaj and Copenhagen, 1998, 2002; Szikra and Krizaj, 2007). The outer segment and synaptic Ca^{2+} pools that control these functions are separated by a cell body filled with a dense cluster of mitochondria, and evidence suggests that these mitochondria may help isolate these pools from each other. Mitochondria from zebrafish cones can prevent Ca^{2+} in the outer segment from reaching the rest of the cell and conversely, they can prevent Ca^{2+} in the synapse from reaching the outer segment (Giarmarco et al., 2017a). Increasing mitochondrial Ca^{2+} uptake in zebrafish cones by overexpressing MCU also accelerates cytosolic Ca^{2+} clearance, which causes cones to recover from light exposure faster (Hutto et al., 2020).

Efficient uptake of Ca^{2+} into mitochondria could also enhance the ability of photoreceptors to meet their high energy demands. Darkness is the most energetically demanding state of the photoreceptor, and intracellular Ca^{2+} is at its highest levels in darkness (Ames et al., 1992; Okawa et al., 2008). If this Ca^{2+} were to enter mitochondria, it could enhance ATP production by stimulating TCA cycle dehydrogenases (Denton, 2009). In line with this hypothesis, overexpressing MCU in zebrafish cones alters the distribution of TCA cycle metabolites in a way which is consistent with enhanced activity of Ca^{2+}-sensitive dehydrogenases (Hutto et al., 2020).

These observations suggest that mitochondrial Ca^{2+} uptake could play an important role in modulating photoreceptor function. Given this, it is surprising that zebrafish cone photoreceptors express extremely low levels of MCU (Hutto et al., 2020). MCU has been widely thought to be the sole route of Ca^{2+} entry into mitochondria in eukaryotes, as loss of MCU completely inhibits mitochondrial Ca^{2+} uptake in skeletal muscle, liver, heart, brown adipose tissue, and a wide variety of cell lines (Flicker et al., 2019; Gherardi et al., 2018; Kwong et al., 2015; Nichols et al., 2016; Pan et al., 2013). Despite this, it is possible that certain specialized cell types might not rely solely on MCU for mitochondrial Ca^{2+} uptake, since it also has been observed that brain mitochondria lacking MCU expression do not have a complete loss of mitochondrial Ca^{2+} uptake (Hamilton et al., 2018).

To resolve the role MCU-mediated mitochondrial Ca^{2+} uptake plays in modulating photoreceptor function, we evaluated the morphological, biochemical and physiological consequences of loss of MCU expression using both a global *mcu*$^{-/-}$ zebrafish model and a rod photoreceptor-specific *Mcu*$^{-/-}$ mouse model. Our study demonstrates that MCU is remarkably dispensable for photoreceptor function, which is consistent with our discoveries of very low levels of MCU expression and evidence for an additional mechanism for Ca^{2+} uptake into photoreceptor mitochondria.

Results

Mcu contributes to clearance of cytosolic Ca^{2+} in zebrafish cones

We first generated global *mcu*$^{-/-}$ zebrafish so that we could take advantage of well-established *ex vivo* retinal Ca^{2+}-imaging tools and techniques to determine the role Mcu plays in modulating cytosolic and mitochondrial Ca^{2+} dynamics in cone photoreceptors (Giarmarco et al., 2018). Global *mcu*$^{-/-}$ zebrafish were generated using a CRISPR-Cas9 strategy outlined previously (Brockerhoff, 2017). A founder carrying a 12-nucleotide deletion in exon 5, which introduces a premature stop codon in exon 6 of *mcu* was used in this study (*mcu*^{w249}; notated as *mcu*$^{-/-}$, **Figure 3.1A**). We used a custom zebrafish-specific Mcu antibody to probe immunoblots of mitochondria isolated from retinas and brains of WT and global *mcu*$^{-/-}$ zebrafish. Mcu expression is entirely ablated in global *mcu*$^{-/-}$ tissues (**Figure 3.1B**). Similar to the global *Mcu*$^{-/-}$ mouse model, a smaller than expected ratio of homozygous *mcu*$^{-/-}$ zebrafish survive to adulthood from crosses of *mcu*$^{+/-}$ parents (**Figure 3.1C**) (Murphy et al., 2014; Pan et al., 2013). There are no obvious effects of Mcu-deficiency on retinal or photoreceptor morphology (**Figure 3.1D**).

To determine what role Mcu plays in clearing cytosolic Ca^{2+}, we crossed *mcu*$^{-/-}$ zebrafish with zebrafish expressing the cytosolic Ca^{2+} sensor GCaMP3 (*gnat2:*GCaMP3) (Giarmarco et al., 2017a). Retinal slices from *mcu*$^{-/-}$ *gnat2:*GCaMP3 and WT *gnat2:*GCaMP3 siblings were incubated in Krebs-Ringer Bicarbonate (KRB) buffer containing 0 mM $CaCl_2$ and 0.4 mM EGTA for 10 minutes. Cones were then imaged to establish a baseline fluorescence reading prior to delivery of a 5 mM bolus of $CaCl_2$ (**Figure 3.1E**). Cones from global *mcu*$^{-/-}$ zebrafish exhibit a higher maximum fold change in cytosolic GCaMP3 fluorescence compared to WT cones (**Figure 3.1F,** 1.192 (±0.024)-fold greater than WT, mean ±SEM reported). A single exponential decay was fit to each curve and the decay constant was calculated to determine if WT and *mcu*$^{-/-}$ cones clear cytosolic Ca^{2+} at different rates (**Figure 3.1G**). The rate of decay calculated for *mcu*$^{-/-}$ (0.01781 s^{-1}) was significantly smaller compared to WT (0.02433 s^{-1}), indicating that *mcu*$^{-/-}$ cones clear cytosolic Ca^{2+} at a slower rate compared to WT cones. This indicates that Mcu plays a role in mediating mitochondrial uptake of cytosolic Ca^{2+} in zebrafish cones.

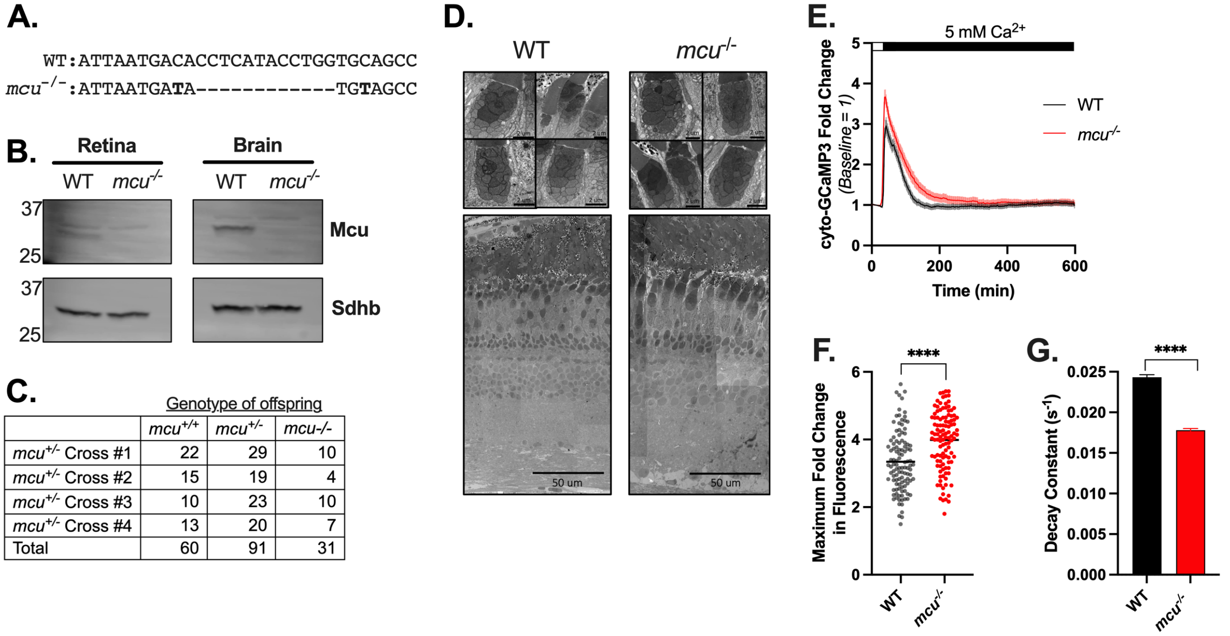

Genotype of offspring

	mcu$^{+/+}$	*mcu*$^{+/-}$	*mcu-/-*
mcu$^{+/-}$ Cross #1	22	29	10
mcu$^{+/-}$ Cross #2	15	19	4
mcu$^{+/-}$ Cross #3	10	23	10
mcu$^{+/-}$ Cross #4	13	20	7
Total	60	91	31

Figure 3.1: Mcu contributes to clearance of cytosolic Ca^{2+} in zebrafish cones

(A) Alignment of a portion of exon 5 of zebrafish *mcu* showing WT (top) and CRISPR-generated *mcu*$^{-/-}$ (*mcu*^{w249}*;* bottom). **(B)** Western blot showing Mcu expression in retina and brain from global *mcu*$^{-/-}$ zebrafish. 20 µg of protein from mitochondrial lysate from 6 pooled retinas and 1 brain was analyzed. The custom Mcu antibody detects a faint non-specific band at a slightly higher molecular weight than Mcu. **(C)** Genotyping results from four separate group crosses of *mcu*$^{+/-}$ zebrafish. Fish were genotyped between 3-4 months of age. A chi-square test determined that the observed *mcu*$^{+/+}$:*mcu*$^{+/-}$:*mcu*$^{-/-}$ ratio of 60:91:31 differed significantly from the expected 1:2:1 ratio (p=0.0098). **(D)** Scanning electron microscopy (SEM) images of WT and *mcu*$^{-/-}$ zebrafish cone mitochondria (top panel) and retinas (bottom panel) from 11-month old sibling fish. Retinal and mitochondrial morphology appear unchanged by loss of Mcu (n=8 retinas from WT and *mcu*$^{/-}$ zebrafish were examined, representative images from 1 WT and 1 *mcu*$^{-/-}$ retina are shown). **(E)** Traces of relative cyto-GCaMP3 fluorescence of cone cell bodies in adult retinal slices of WT or *mcu*$^{-/-}$ fish expressing *gnat2*:cyto-GCaMP3. Baseline mitochondrial fluorescence was determined in KRB buffer containing 0 mM $CaCl_2$ and 0.4 mM EGTA, then a bolus of $CaCl_2$ was delivered in order to bring the $[Ca^{2+}]_{free}$ to 5 mM. The mean is reported and shaded region = 95% CI. (n=110 cells (four fish) for WT and n=112 cells (four fish) for *mcu*$^{-/-}$). **(F)** Maximum fold change in cyto-GCaMP3 fluorescence for each cell body after exposure to 5 mM $[Ca^{2+}]_{free}$. WT: 3.345 ± 0.085, *mcu*$^{-/-}$: 3.985 ± 0.082, mean ± SEM reported, $p<0.0001$ using Welch's t-test. (n=110 cells (from four fish) for WT and n=112 cells (from four fish) for *mcu*$^{-/-}$). **(G)** Decay constants calculated using a single exponential decay fit. WT: 0.02433 s^{-1} (0.02384 to 0.02483), *mcu*$^{-/-}$: 0.01781 s^{-1} (0.01743 to 0.01821), decay constant with 95% CI reported, $p<0.0001$ using Welch's t-test.

Mitochondrial Ca^{2+} uptake in cones from global $mcu^{-/-}$ zebrafish is diminished, but not ablated

To directly observe mitochondrial Ca^{2+} levels in *mcu*$^{-/-}$ photoreceptors, we next crossed *mcu*$^{-/-}$ zebrafish with zebrafish expressing the mitochondrially-targeted Ca^{2+} sensor GCaMP3 in cones (*gnat2*:mito-GCaMP3) (Giarmarco et al., 2017a). Eyes from live larvae were imaged and we found that there is no difference in basal mito-GCaMP3 fluorescence between WT and *mcu*$^{-/-}$ cones (**Figure 3.2A**). Although we analyzed mito-GCaMP3 fluorescence in sibling larvae which had only a single insertion of the mito-GCaMP3 transgene, it is possible that differences in transgene expression between fish could obscure differences in WT and *mcu*$^{-/-}$ basal mitochondrial Ca^{2+}. So, we next determined basal mitochondrial Ca^{2+} levels in mature cones from WT and *mcu*$^{-/-}$ fish and using an *ex vivo* imaging method that reports mito-GCaMP3 fluorescence independent of mito-GCaMP3 probe concentration. We compared baseline mito-GCaMP3 fluorescence (F_0) to the maximum fluorescence (F_{max}, obtained by addition of ionomycin to media containing 2 mM Ca^{2+}) and minimum fluorescence (F_{min}, obtained by the addition of 5 mM EGTA to chelate Ca^{2+}). Similar to larvae, we found that baseline mito-GCaMP3 fluorescence was not significantly different in adult WT and *mcu*$^{-/-}$ zebrafish cones (**Figure 3.2B**, **Figure 3.2C**).

We next tested whether mitochondrial Ca^{2+} uptake is altered in cones from global *mcu*$^{-/-}$ fish. It has been previously established that the treatment of photoreceptors with the PDE inhibitor sildenafil in the presence of the Na^+/Ca^{2+} exchanger inhibitor KB-R7943 causes significant increases in cytoplasmic Ca^{2+} levels and a coincident increase in mitochondrial Ca^{2+} levels.(Giarmarco et al., 2017a) We used the same strategy here to assess changes in mitochondrial Ca^{2+} uptake in *mcu*$^{-/-}$ cones. We imaged WT and global *mcu*$^{-/-}$ *gnat2:*mito-GCaMP3 cones after a 10 minute KB-R7943 preincubation to obtain baseline measurements of mito-GCaMP3 fluorescence, and continued to image after exposing the retinal slices to sildenafil. In WT cones, mito-GCaMP3 fluorescence increases after sildenafil treatment (**Figure 3.2D,** top left panel). The average response of all WT mitochondrial clusters is shown in the dark trace, and the individual responses of each individual mitochondrial cluster is shown in semi-transparent traces. We determined the number of WT mitochondrial clusters which increase mitochondrial Ca^{2+} levels in response to sildenafil and found that 82% of mitochondrial clusters respond (**Figure 3.2E**; in order for a mitochondrial cluster to have considered to have responded, it must have exhibited a 1.2-fold or greater increase in mito-GCaMP3 fluorescence at any time during imaging). The population of mitochondrial clusters which did not respond to sildenafil can be visualized by identifying the traces that do not cross the dotted line on the graph indicating 1.2-fold above baseline.

In *mcu*$^{-/-}$ retinal slices, we found that mito-GCaMP3 fluorescence increases after sildenafil treatment in many cones (**Figure 3.2D,** top right panel). However, we observed that there was a greater proportion of *mcu*$^{-/-}$ cone mitochondrial clusters which never respond to sildenafil (**Figure 3.2E**, 41% of *mcu*$^{-/-}$ mitochondrial clusters never increase 1.2-fold above baseline compared to 18% of WT mitochondrial clusters). The *mcu*$^{-/-}$ cone mitochondrial clusters which do respond to sildenafil treatment exhibited a smaller maximum fold change in mito-GCaMP3 fluorescence compared to WT mitochondrial clusters which respond to sildenafil (**Figure 3.2F**). We also observed that *mcu*$^{-/-}$ cone mitochondrial clusters take longer to respond to sildenafil treatment compared to WT mitochondrial clusters (**Figure 3.2G**, T_{Response} is defined as the time mito-GCaMP3 fluorescence first increased 1.2-fold above baseline). There is heterogeneity in the timing of the mito-GCaMP3 fluorescence increase from within seconds to many minutes after sildenafil addition in both WT and *mcu*$^{-/-}$ cone mitochondrial clusters. However, since *mcu*$^{-/-}$ mitochondrial clusters respond later on average, this suggests that a different biological threshold (such as the size of the cytosolic Ca^{2+} load or the amount of time it is sustained) must be met in order for an *mcu*$^{-/-}$ mitochondria to begin taking up Ca^{2+}.

To assess whether the residual Ca^{2+} uptake exhibited by *mcu*$^{-/-}$ cone mitochondrial clusters in this assay could be attributed to an Mcu-independent mechanism, we repeated this experiment in the presence of the Mcu inhibitor Ru360 (**Figure 3.2D,** bottom two panels). Ru360 treatment increases the proportion of WT mitochondrial clusters which never respond (**Figure 3.2E**, 64% of WT + Ru360 mitochondrial clusters do not respond vs 18% of WT mitochondrial clusters without Ru360). WT + Ru360 cone mitochondrial clusters also exhibit a significantly smaller maximum fold change in fluorescence compared to WT mitochondrial clusters without Ru360 (**Figure 3.2F**). Ru360 treatment also slightly increases the proportion of *mcu*$^{-/-}$ mitochondrial clusters which never respond (**Figure 3.2E**, 53% of *mcu*$^{-/-}$ + Ru360 mitochondrial clusters fail to respond vs 41% of *mcu*$^{-/-}$ mitochondrial clusters without Ru360). Compared to untreated *mcu*$^{-/-}$ mitochondrial clusters, *mcu*$^{-/-}$ + Ru360 mitochondrial clusters do not have a significantly different maximum fold change in fluorescence or $T_{Response}$ (**Figure 3.2F, Figure 3.2G**). Notably, a large number of both WT + Ru360 and *mcu*$^{-/-}$ + Ru360 mitochondrial clusters still exhibit an apparent increase in mitochondrial Ca^{2+} in this assay.

Since GCaMP3 is a GFP derivative, its fluorescence can be sensitive to changes in pH. The fluorescence of cpYFP (another GFP derivative) is not sensitive to Ca^{2+} but has been shown to be extremely sensitive to changes in pH (Schwarzländer et al., 2011). To test if the increases in mito-GCaMP3 fluorescence observed in *mcu*$^{-/-}$ cone mitochondria and cone mitochondria treated with Ru360 could be due to changes in pH and not mitochondrial Ca^{2+} uptake, we treated retinal slices from *gnat2*:mito-cpYFP zebrafish with KB-R7943 and sildenafil **(Figure 3.2H**). We observed no increases in cp-YFP fluorescence over the time course, indicating that the increases in fluorescence we observe with mito-GCaMP3 are due to changes in mitochondrial Ca^{2+} and not pH.

Taken together, these results show that Mcu contributes to some mitochondrial Ca^{2+} uptake in cones, but that Ca^{2+} can also enter cone mitochondria through an alternative pathway.

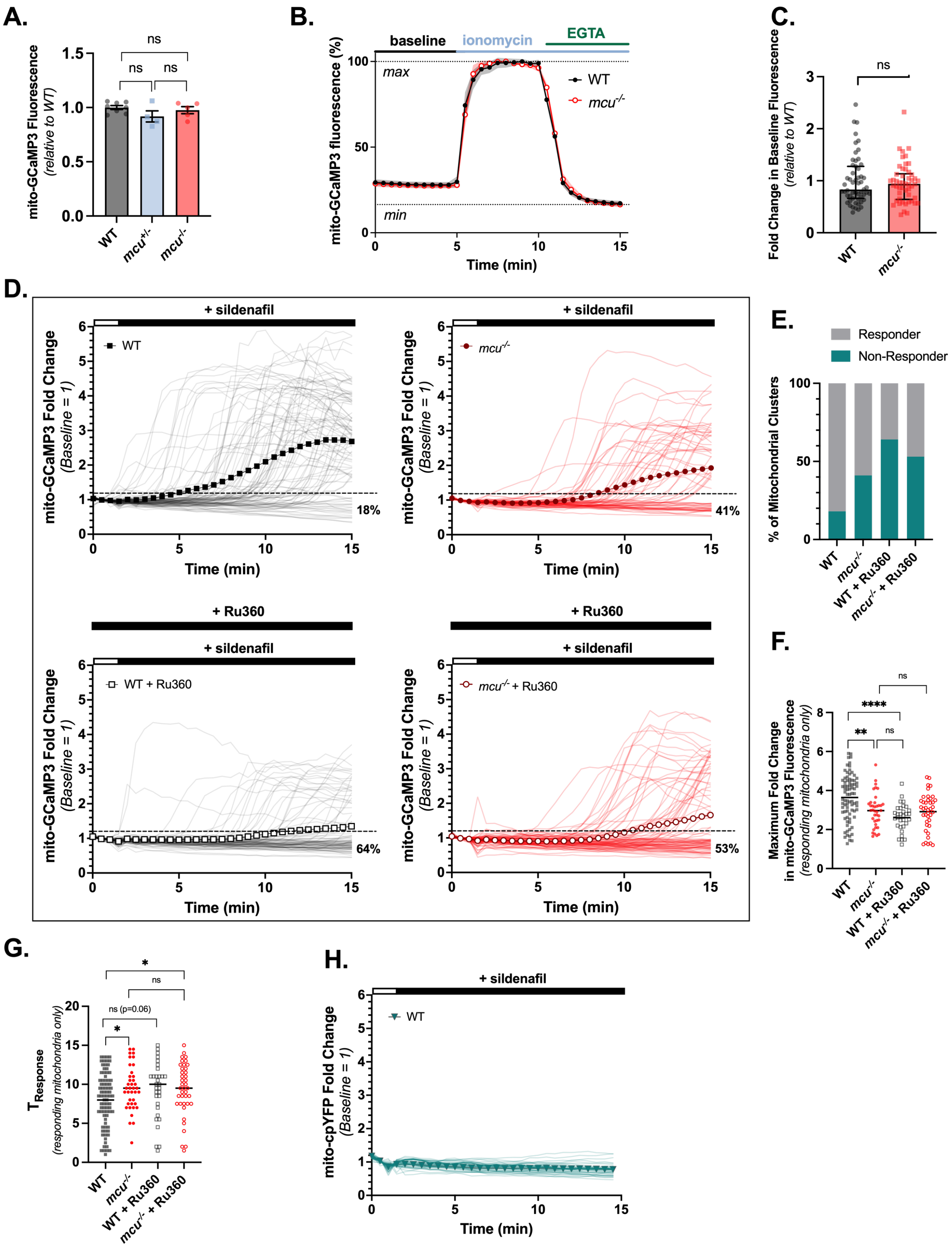

Figure 3.2: Mitochondrial Ca^{2+} uptake in cones from global *mcu*$^{-/-}$ zebrafish is diminished, but not ablated

(Figure 3.2 continued)
(A) Total cone mitochondrial fluorescence in *gnat2*:mito-GCaMP3 larval zebrafish eyes. The mean is reported with bars indicating standard error. (n=8 WT fish, 4 $mcu^{+/-}$ fish, and 5 $mcu^{-/-}$ fish. ns = not significant using one-way ANOVA with Tukey's multiple comparisons test). **(B)** Relative mito-GCaMP3 fluorescence of cone mitochondrial clusters in adult retinal slices of WT or $mcu^{-/-}$ fish expressing *gnat2*:mito-GCaMP3. Baseline mitochondrial fluorescence was determined in KRB buffer containing 2 mM $CaCl_2$, then ionomycin (5 µM) was added to allow 2 mM Ca^{2+} entry into the mitochondria to saturate the probe. Next, EGTA (5 mM) was added to the solution (holding 5 µM ionomycin constant) to chelate Ca^{2+} and determine minimum mito-GCaMP3 fluorescence. The mean is reported and shaded region = 95% CI. (n=55 mitochondrial clusters (three fish) for WT and n=51 mitochondrial clusters (three fish) for $mcu^{-/-}$). **(C)** Fold change in baseline mito-GCaMP3 fluorescence relative to WT average. The median is reported with bars indicating interquartile range. (ns = not significant using Mann-Whitney test). **(D)** *gnat2*:mito-GCaMP3 retina slices preincubated with 100 µM KB-R7943 (10 minutes prior to imaging and white bar) then subjected to 25 µM sildenafil (black bar). For Ru360 treatment, retinal slices were preincubated for 1 hour in 10 µM Ru360 and then the same experiment was performed in the presence of 10 µM Ru360. The mean response of all mitochondrial clusters is reported with the dark trace, while the semi-transparent traces show the responses of each individual mitochondrial cluster. The dotted line indicates 1.2-fold above baseline. (Mitochondrial clusters from n=86 WT, n=64 $mcu^{-/-}$, n=86 WT + Ru360, and n=85 $mcu^{-/-}$ + Ru360 cells are reported. All conditions were tested in multiple slices from n=3 fish each). **(E)** The percent of mitochondrial clusters from each condition which responded or did not respond to sildenafil. Mitochondrial clusters which exhibited an increase in mito-GCaMP3 fluorescence of 1.2-fold or greater above baseline at any time after sildenafil treatment are considered to have responded. (n=86 WT, n=64 $mcu^{-/-}$, n=86 WT + Ru360, and n=85 $mcu^{-/-}$ + Ru360). **(F)** The maximum fold change in mito-GCaMP3 fluorescence at any time during imaging. Mitochondrial clusters which did not respond to sildenafil are excluded. (n=80 WT, n=38 $mcu^{-/-}$, n=31 WT + Ru360, n=40 $mcu^{-/-}$ + Ru360). **(G)** The time at which each mitochondrial cluster first increased mito-GCaMP3 fluorescence 1.2-fold above baseline. (n=80 WT, n=38 $mcu^{-/-}$, n=31 WT + Ru360, n=40 $mcu^{-/-}$ + Ru360). **(H)** *gnat2*:mito-cpYFP (WT for Mcu expression) retina slices preincubated with 100 µM KB-R7943 (10 minutes prior to imaging and white bar) then subjected to 25 µM sildenafil (black bar). The mean response of all mitochondrial clusters is reported with the dark trace, while the semi-transparent traces show the responses of each individual mitochondrial cluster. (Mitochondrial clusters from n=48 WT mitochondrial clusters from multiple slices from 2 fish shown).

Retinas from $mcu^{-/-}$ zebrafish have normal morphology, metabolism, and photoresponses.

We next determined if the diminished ability of $mcu^{-/-}$ mitochondria to take up Ca^{2+} in cones might lead to metabolic or electrophysiological defects. To assess potential changes in metabolism, we measured total metabolite levels from freshly dissected dark-adapted retinas from $mcu^{-/-}$ zebrafish. We detected no changes in total metabolite levels in $mcu^{-/-}$ retinas, although α-ketoglutarate levels trend slightly but not significantly higher after loss of Mcu (**Figure 3.3A**). Previous studies of $MCU^{-/-}$ tissues describe an increase in the amount of phosphorylated pyruvate dehydrogenase (PDH), which is attributed to diminished activity of the Ca^{2+}-sensitive phosphatase PDP1c (Huang et al., 1998; Kwong et al., 2018; Nichols et al., 2016; Pan et al., 2013; Rasmussen et al., 2015). We assessed the P-PDH/PDH ratio found that it is not different between WT and *mcu*$^{-/-}$ retinas (**Figure 3.3B**). This result is consistent with the unaltered resting Ca^{2+} levels we observed in *mcu*$^{-/-}$ cones.

Photoreceptors rely on efficient clearance of cytosolic Ca^{2+} from the outer segment to stimulate recovery of the photoresponse (Vinberg et al., 2018). Photoresponses of zebrafish cones that overexpress Mcu recover faster following a flash of light, suggesting that uptake of Ca^{2+} through Mcu could contribute to clearing outer segment Ca^{2+} in the time course of flash responses (Hutto et al., 2020; Vinberg et al., 2015). Our cyto-GCaMP3 measurements indicate that *mcu*$^{-/-}$ cones clear cytoplasmic Ca^{2+} slower compared to WT cones. Thus, loss of this fraction of Mcu-mediated Ca^{2+} sequestration could slow the recovery kinetics of the cone light responses. To test this, we measured both bright and dim flash responses from WT and *mcu*$^{-/-}$ cones using *ex vivo* electroretinography (ERG). Recovery kinetics are unaltered by Mcu deficiency (**Figures 3.3C** and **3.3D**). Both the maximum amplitude and sensitivity of the response are unchanged by loss of Mcu expression (**Figures 3.3E** and **3.3F**, respectively).

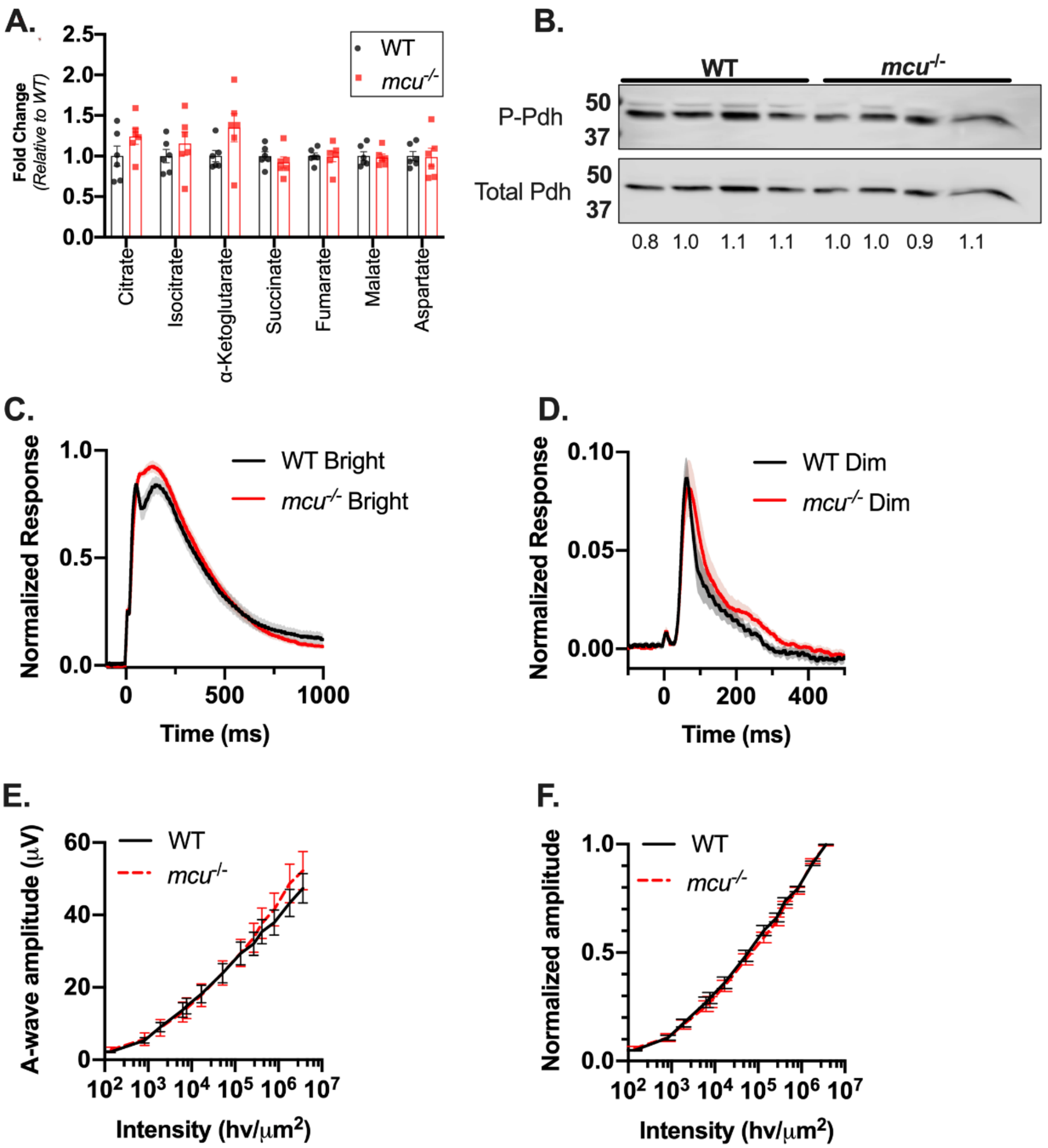

Figure 3.3: Retinas from global *mcu*$^{-/-}$ zebrafish have normal morphology, metabolism, and photoresponse
(A) Total TCA cycle metabolite levels in *mcu*$^{-/-}$ zebrafish retinas relative to WT. Zebrafish were dark-adapted for 18h and retinas were dissected under red light. α-ketoglutarate levels trend higher in *mcu*$^{-/-}$ zebrafish retinas, although they are not significantly different than WT (1.4 ± 0.5-fold higher in *mcu*$^{-/-}$ retinas, p=0.09 using Welch's t-test, mean ± standard deviation is reported, n=6 WT and 6 *mcu*$^{-/-}$ retinas from 3 different fish each). **(B)** P-Pdh and total Pdh immunoblot from dark-adapted WT and global *mcu*$^{-/-}$ zebrafish retinas. 15 µg of protein was loaded in each lane. Quantification of the P-Pdh/Pdh ratio of each sample relative to the average WT P-Pdh/Pdh ratio is shown below each lane (n=4 WT and 4 *mcu*$^{-/-}$ retinas from 4 different fish each). **(C,D)** *Ex vivo* ERG a-wave responses and normalized responses from WT and *mcu*$^{-/-}$ zebrafish retinas. Cone responses were isolated using DL-AP4 (40 µM) and CNQX (40 µM) and normalized to R_{max} (the maximum response at the brightest light intensity). Bright flash stimulus intensity is 3,650,000 photons μm^{-2} and 2-23 ms in duration. The mean is reported and the shaded region indicates standard error (n=21 retinas from 12 WT fish and 21 retinas from 13 global *mcu*$^{-/-}$ fish). **(E,F)** a-wave response amplitude data plotted as a function of stimulus intensity (photons μm^{-2}) of WT and global *mcu*$^{-/-}$ retinas from experiments shown in (C) and (D) (Bars indicate standard error)

Rod photoreceptors express low levels of MCU

We did not detect any metabolic or physiological consequences caused by Mcu deficiency in zebrafish retinas. However, phenotypes can vary significantly between chronic, induced, and tissue-specific *Mcu*$^{-/-}$ animal models (Mammucari et al., 2018). For example, the cardiac phenotype from the global *Mcu* $^{-/-}$ mouse is surprisingly mild, while constitutive and inducible heart-specific *Mcu* knockdown models have both different and more severe phenotypes (Holmström et al., 2015; Kwong et al., 2015; Luongo et al., 2015; Pan et al., 2013; Rasmussen et al., 2015). This indicates that some tissues have both the capacity and the necessity to adapt to chronic loss of MCU. Since we observed that a smaller than expected number of *mcu*$^{-/-}$ fish reach adulthood from *mcu*$^{+/-}$ crosses, it is likely that the *mcu*$^{-/-}$ fish that survived to adulthood adapted to loss of Mcu in some way. In order to ensure that the mild phenotypes we observed in global *mcu*$^{-/-}$ zebrafish retinas were truly due to the dispensable nature of MCU in photoreceptors and not due to adaptations made in response to chronic loss of MCU, we also generated a rod photoreceptor specific *Mcu*$^{-/-}$ mouse model in which MCU expression is lost only upon photoreceptor differentiation.

We blocked expression of MCU specifically in rod photoreceptors by crossing mice with loxP sites flanking exons 5 and 6 of *Mcu* (*Mcu*^{fl}) with mice expressing Cre-recombinase under control of a rod-specific opsin promoter (iCre-75) which is active once rods have differentiated (Kwong et al., 2015; Li et al., 2005). Immunohistochemistry of adult *Mcu*^{fl} iCre-75 (annotated as Rod *Mcu*$^{-/-}$) retinas reveal that MCU expression is ablated in the rod photoreceptors (**Figure 3.4A,** arrow indicates the photoreceptor mitochondria layer). The photoreceptor layer in the mouse retina is composed mainly of rods, with a ~35:1 rod:cone ratio (Jeon et al., 1998). To determine if cones still express MCU in Rod *Mcu*$^{-/-}$ retinas, we co-stained WT and Rod *Mcu*$^{-/-}$ retinal slices with an MCU antibody and the cone marker peanut agglutinin (PNA) (**Figure 3.4B**). We observed MCU staining beneath each PNA-stained outer segment, indicating that cones retain MCU expression.

Cone photoreceptors from zebrafish retinas express very low levels of Mcu (Hutto et al., 2020). To determine if MCU expression in mouse rods is similarly low, we analyzed MCU expression in WT and Rod *Mcu*$^{-/-}$ retinas using immunoblot (**Figure 3.4C**). MCU expression is not significantly altered in Rod *Mcu*$^{-/-}$ retinas relative to WT, despite rods being by far the most abundant cell type in the mouse retina (Jeon et al., 1998). This indicates that MCU expression is extremely low in rods relative to other cell types in the retina. Overall retinal and photoreceptor morphology appears to be unaltered by loss of MCU expression in rods: we observed no defects in our immunohistochemistry images and scanning electron microscopy (SEM) analysis of Rod *Mcu*$^{-/-}$ retinas at 6-months old revealed no changes in retinal morphology (**Figure 3.4D**).

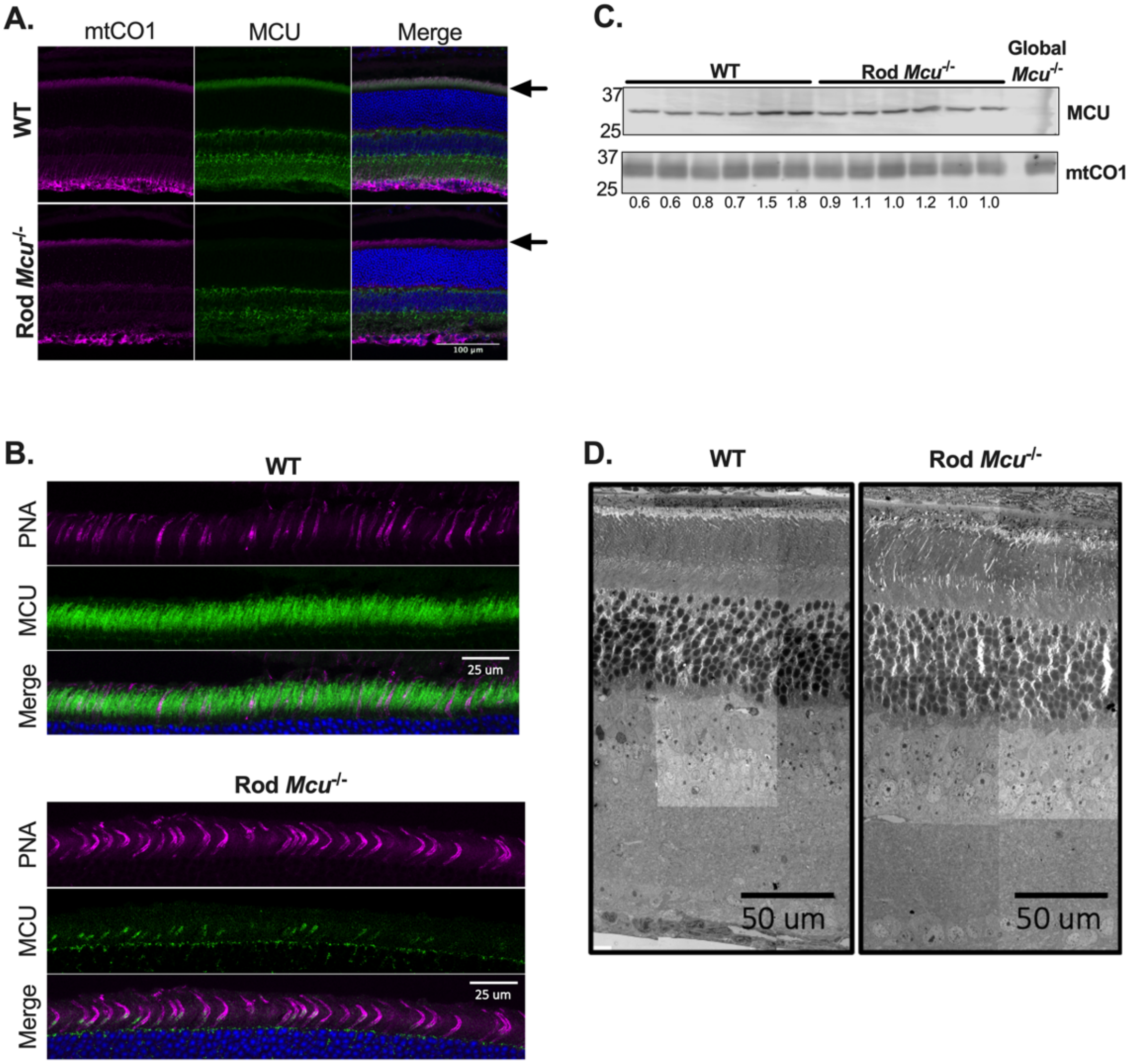

Figure 3.4: Rods express low levels of MCU

(Figure 3.4 continued)
(A) Immunohistochemistry showing MCU expression in WT and Rod *Mcu*$^{-/-}$ retinas. mtCO1 (Mitochondrial Cytochrome Oxidase subunit 1) is used to label mitochondria. An arrow indicates the photoreceptor mitochondria layer. **(B)** Immunohistochemistry showing MCU expression and PNA-647 (staining cone outer segments). MCU is still expressed in cones from Rod *Mcu*$^{-/-}$ retinas. **(C)** Western blot showing MCU expression in whole retinas from Rod *Mcu*$^{-/-}$ mouse. 15 µg of retinal protein lysate was loaded in each lane. MCU expression is not significantly altered in Rod *Mcu*$^{-/-}$ retinas (1.02 ± 0.03 fold higher in Rod *Mcu*$^{-/-}$ retinas, mean ± standard deviation is reported, ns using Welch's t-test). Retinal lysate from a global *Mcu*$^{-/-}$ mouse is used as a control to show specificity of MCU antibody (far right lane). The MCU/mtCO1 ratio for each sample relative to WT average is shown under each lane (n=6 WT and 6 Rod *Mcu*$^{-/-}$ retinas from 3 animals each). **(D)** SEM images from 6-month old WT and Rod *Mcu*$^{-/-}$ retinas. (retinas from n=3 mice were imaged, representative images from 1 WT and 1 Rod *Mcu*$^{-/-}$ retina shown).

Rod Mcu$^{-/-}$ retinas accumulate α-ketoglutarate

Overexpressing MCU in zebrafish cone photoreceptors leads to changes in the steady-state concentrations of TCA cycle metabolites, likely due to increased Ca^{2+} binding lowering the K_m of α-ketoglutarate dehydrogenase (α-KGDH) and isocitrate dehydrogenase (Hutto et al., 2020). To test if the reduced mitochondrial Ca^{2+} uptake ability of *Mcu*$^{-/-}$ photoreceptors causes a subsequent increase in enzyme K_m, we used gas chromatography-mass spectrometry to evaluate the influence of MCU on metabolic flux in retinas. We incubated retinas from WT and Rod *Mcu*$^{-/-}$ light-adapted mice in 5 mM U-^{13}C-glucose for 0, 5, and 30 minutes and quantified accumulation of unlabeled and labeled metabolites using GC-MS (an isotopologue diagram is included in **Supplemental Figure 3.6B**). When we measured total metabolite levels at each time point, we observed that the TCA cycle metabolite α-ketoglutarate was the only metabolite which was consistently elevated in Rod *Mcu*$^{-/-}$ retinas across all time points (α-ketoglutarate levels are elevated 1.99 ± 1.09-fold at 0 minutes; 1.46 ± 0.36-fold 5 minutes, and 1.90 ± 0.77-fold at 15 minutes; mean ± standard deviation propagated to include variation of WT samples reported) (**Figure 3.5A**). Labeled α-ketoglutarate (m2 α-ketoglutarate made in the first round and m3 α-ketoglutarate made in the second round) also accumulate to slightly higher steady state levels in Rod *Mcu*$^{-/-}$ retinas (**Figure 3.5B, Figure 3.6A**). Other metabolites do not accumulate consistently differently in Rod *Mcu*$^{-/-}$ retinas compared to WT. We also measured the lactate/pyruvate ratio at the 0 minute timepoint as a proxy for the cytosolic NADH/NAD$^+$ ratio in freshly dissected retinas and found it to be unaltered in Rod *Mcu*$^{-/-}$ retinas (**Figure 3.6C**).

Photoreceptor energy demands are significantly higher in darkness, and intracellular Ca^{2+} levels in photoreceptors can increase 10- to 60-fold in darkness relative to light (Matthews and Fain, 2003; Okawa et al., 2008; Woodruff et al., 2002). So, it is possible that MCU plays a larger role in modulating photoreceptor metabolism in darkness. We first determined how darkness normally alters steady-state metabolite levels by comparing metabolite abundance between light- and dark-adapted WT retinas (for dark-adapted retinas, mice were dark-adapted for 18h and retinas were dissected and snap-frozen under infrared light). In WT retinas, steady-state levels of many metabolites are slightly but significantly lower in darkness relative to light, with α-ketoglutarate and pyruvate levels being the most reduced (α-ketoglutarate: 0.61 ± 0.12-fold lower; pyruvate: 0.62 ± 0.23-fold lower; mean ± standard deviation propagated to include variation of “light” samples reported) (**Figure 3.5C)**. We repeated this comparison using light- and dark-adapted Rod *Mcu*$^{-/-}$ retinas. We observed the same trend in that the steady-state levels of many metabolites are slightly but significantly lower in dark-adapted Rod *Mcu*$^{-/-}$ retinas compared to light-adapted Rod *Mcu*$^{-/-}$ retinas (**Figure 3.5D**). Similar to what was observed in WT retinas, both pyruvate and α-ketoglutarate levels are the most reduced in Rod *Mcu*$^{-/-}$ retinas (α-ketoglutarate: 0.71 ± 0.20-fold lower; pyruvate: 0.82 ± 0.15-fold lower; mean ± standard deviation propagated to include variation of “light” samples reported). When comparing the fold change in metabolite abundance in darkness relative to light, it appeared as though the influence of darkness in Rod *Mcu*$^{-/-}$ retinas tended to be smaller than that of WT retinas. This would be expected if Ca^{2+} uptake via MCU mediated the change in metabolite pool size we observe in darkness relative to light. To test if this were true, we directly compared the fold change in steady-state metabolite levels in darkness and light between WT and Rod *Mcu*$^{-/-}$ retinas (**Figure 3.5E**). While the influence of darkness on pyruvate and α-ketoglutarate is slightly different between WT and Rod *Mcu*$^{-/-}$ retinas, we found that this difference is not statistically significant. This indicates that while MCU might play a small role in modulating steady-state metabolite levels in darkness, it is likely not the primary effector of change.

We next assessed if loss of MCU expression altered metabolic flux in dark-adapted retinas differently than in light-adapted retinas. WT and Rod *Mcu*$^{-/-}$ mice were dark-adapted for 18h and retinas were dissected, incubated in U-^{13}C-glucose, and snap-frozen all under infrared light. Once again, we found that steady-state α-ketoglutarate levels from freshly-dissected dark-adapted retinas are consistently higher in Rod *Mcu*$^{-/-}$ retinas compared to WT (α-ketoglutarate levels are elevated 1.56 ± 0.20-fold at 0 minutes, 1.93 ± 0.45-fold at 5 minutes, and 1.41 ± 0.17-fold at 30 minutes; mean ± standard deviation propagated to include variation of WT samples reported) (**Figure 3.5F**). We also observed a similar increase in Rod *Mcu*$^{-/-}$ m2 and m3 α-ketoglutarate levels throughout the time course of U-^{13}C-glucose incubation (**Figure 3.5G, Figure 3.6D**). We also assessed the levels of lactate, pyruvate, and the lactate/pyruvate ratio (as a proxy for cytosolic NADH/NAD^{+}) in freshly dissected and snap-frozen dark-adapted retinas and found it was unchanged in Rod *Mcu*$^{-/-}$ retinas (**Figure 3.6E**). Overall, we found that metabolic flux in dark-adapted Rod *Mcu*$^{-/-}$ retinas matches flux in dark-adapted WT retinas with the exception of a consistent accumulation of α-ketoglutarate.

Finally, we determined if loss of MCU expression in rods might alter the P-PDH/PDH ratio. Our immunoblot analysis showed that the P-PDH/PDH ratio in light-adapted Rod *Mcu*$^{-/-}$ retinas was not different than in WT (**Figure 3.6F**). Accordingly, we did not observe a decrease in citrate production in our isotopic labeling experiments in either light- or dark-adapted Rod *Mcu*$^{-/-}$ retinas.

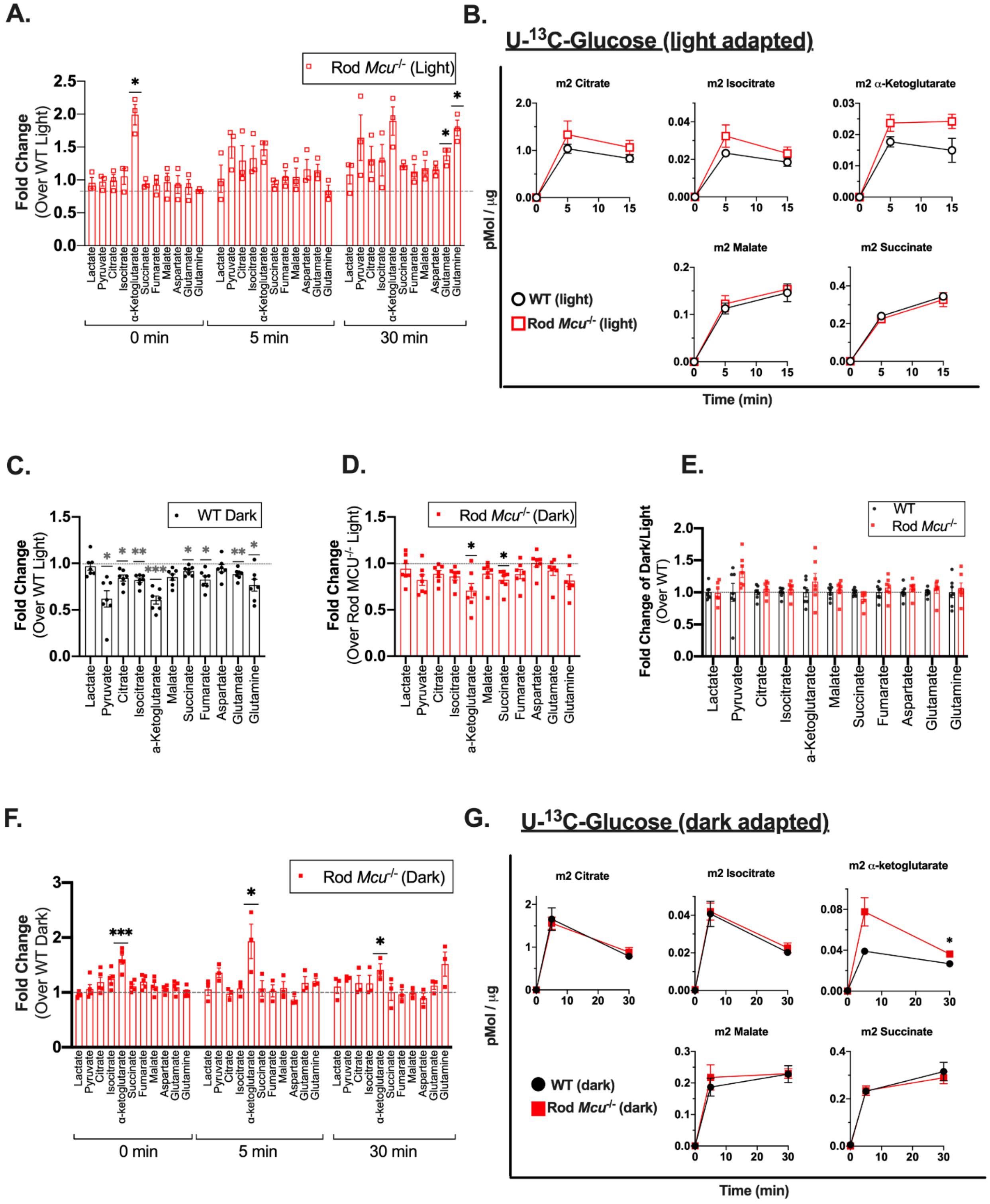

Figure 3.5: Loss of MCU leads to a buildup of α-Ketoglutarate in Rod *Mcu*$^{-/-}$ retinas
(A) Total metabolite levels in light-adapted Rod *Mcu*$^{-/-}$ retinas relative to WT (n=3 WT and 3 Rod *Mcu*$^{-/-}$ retinas per time point. Each time point used retinas from 3 different animals. (* indicates $p<0.05$ using Welch's t-test). **(B)** Time course of labeled metabolite accumulation in light-adapted WT and Rod

Mcu$^{-/-}$ retinas incubated in U-^{13}C-glucose for 0, 5, and 15 minutes (n=3 WT and 3 Rod *Mcu*$^{-/-}$ retinas per time point. Each time point used retinas from 3 different mice. **(C)** Total metabolite levels in dark-adapted WT retinas relative to light-adapted WT retinas (n=4 light adapted retinas and 7 dark adapted retinas, each from four different mice. * indicates $p<0.05$, ** indicates $p<0.01$, *** indicates $p<0.001$ using Welch's t-test). **(D)** Total metabolite levels in dark-adapted Rod *Mcu*$^{-/-}$ retinas relative to light-adapted Rod *Mcu*$^{-/-}$ retinas (n=6 light adapted retinas and 7 dark adapted retinas, each from four different mice. * indicates $p<0.05$ using Welch's t-test). **(E)** Change in metabolite abundance between darkness and light in Rod *Mcu*$^{-/-}$ retinas relative to WT retinas from Figures 4C and 4D. (n=4 light adapted WT retinas, 7 dark adapted WT retinas, 6 light-adapted Rod *Mcu*$^{-/-}$ retinas, and 7 light-adapted Rod *Mcu*$^{-/-}$ retinas, all ns using Welch's t-test). **(F)** Total metabolite levels in dark-adapted Rod *Mcu*$^{-/-}$ retinas relative to WT (n= 4 WT and 5 Rod *Mcu*$^{-/-}$retinas for t=0, n=3 WT and 3 Rod *Mcu*$^{-/-}$ retinas for t=5 and t=30. Each time point used retinas from at least 3 different animals. * indicates $p<0.05$, *** indicates $p<0.001$ using Welch's t-test). **(G)** Time course of dark-adapted WT and Rod *Mcu*$^{-/-}$ retinas incubated in U-^{13}C-glucose for 0, 5, and 30 minutes (n=3 WT and 3 Rod *Mcu*$^{-/-}$ retinas per time point. Each time point used retinas from 3 different animals. * indicates $p<0.05$ using Welch's t-test).

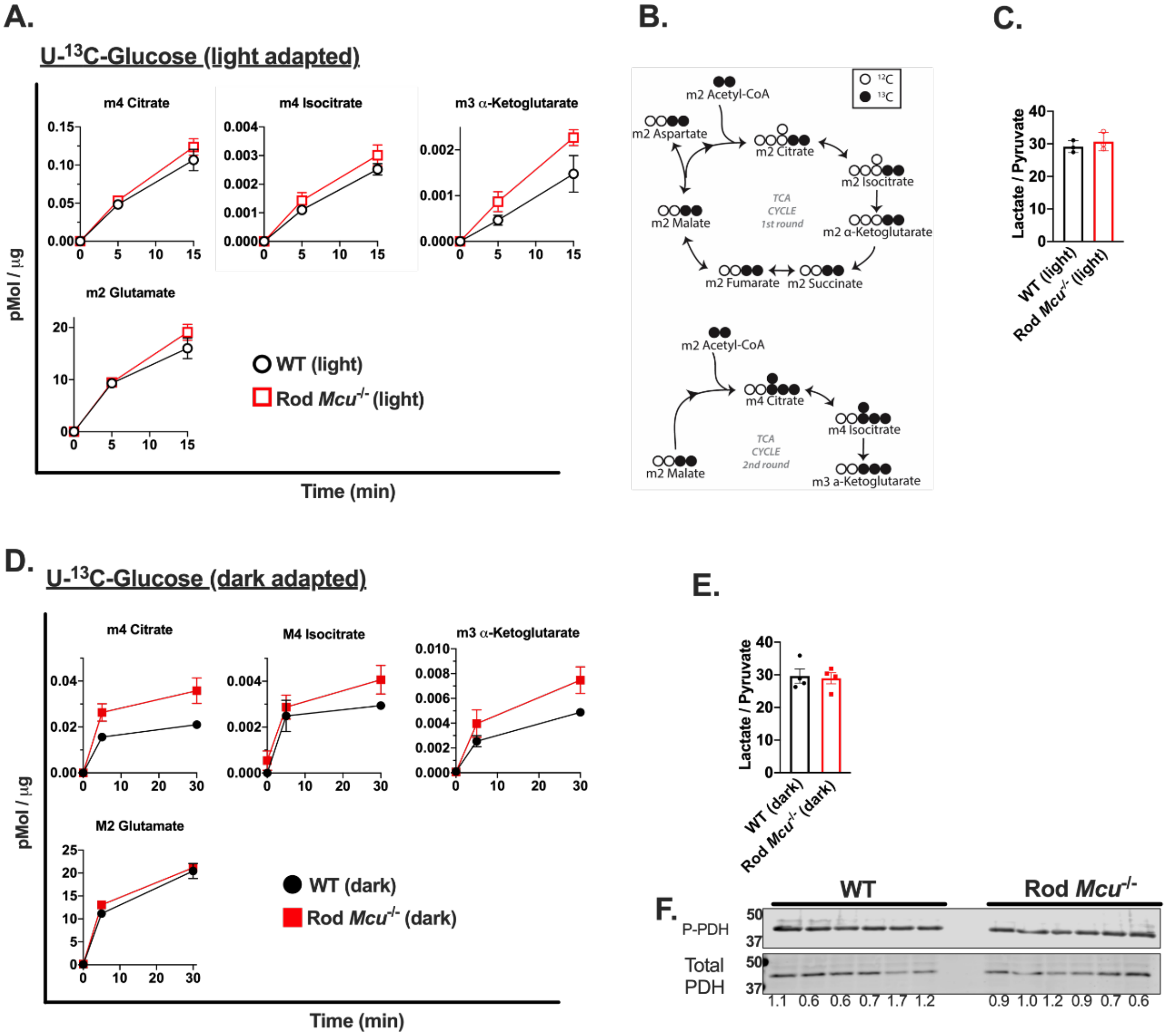

Figure 3.6: Additional metabolic characterization of Rod *Mcu*$^{-/-}$retinas
(A) Additional metabolites from the time course of light-adapted WT and Rod *Mcu*$^{-/-}$ retinas incubated in U-^{13}C-glucose for 0, 5, and 15 minutes (n=3 WT and 3 Rod *Mcu*$^{-/-}$ retinas per time point).

(Figure 3.6 continued)
(B) Isotopomer diagram showing labeling pattern of TCA cycle metabolites made by retinas supplied with U-13C-glucose. **(C)** Lactate/Pyruvate ratio in freshly dissected light-adapted WT and Rod *Mcu*$^{-/-}$ retinas (n=3 WT and 3 Rod MCU$^{-/-}$ retinas). **(D)** Additional metabolites from the time course of dark-adapted WT and Rod *Mcu*$^{-/-}$ retinas incubated in U-^{13}C-glucose for 0, 5, and 15 minutes (n=3 WT and 3 Rod *Mcu*$^{-/-}$ retinas per time point). **(E)** Lactate/Pyruvate ratio in freshly dissected dark-adapted WT and Rod *Mcu*$^{-/-}$ retinas (n=3 WT and 3 Rod MCU$^{-/-}$ retinas). **(F)** Western blot of WT and Rod *Mcu*$^{-/-}$ retinas probed with PDH E1a antibody and a phospho-PDH antibody. The P-PDH/PDH ratio is 0.89 ± 0.42 -fold lower in Rod *Mcu*$^{-/-}$ retinas (ns, mean ± standard deviation propagated to include WT error shown). Quantification of the P-PDH/PDH ratio of each sample relative to the average WT P-PDH/PDH ratio is shown below each lane (n=6 WT and 6 Rod *Mcu*$^{-/-}$ retinas from 3 animals each).

MCU-deficiency does not influence mouse rod photoresponses

We determined how much MCU normally contributes to the rod photoresponse recovery by recording *ex vivo* transretinal ERG responses from Rod *Mcu*$^{-/-}$ mice and WT controls in scotopic conditions. Dark-adapted flash responses of *Mcu*$^{-/-}$ rods are slightly but not significantly larger than controls (**Figure 3.7A, B, and C**). The normalized flash response family plots superimposed over each other, indicating that the intensity to produce half-maximum response (a measure of sensitivity) of *Mcu*$^{-/-}$ rods is not significantly different from controls (**Figure 3.7C, *inset***). A summary of the response parameters in the control and *Mcu*$^{-/-}$ rods is given in **Table 3.1**. There are no notable differences in the time to peak (T_p), integration time (T_{int}), and recovery time constant τ_{rec} of the flash response.

We next tested if Ca^{2+} sequestering through MCU affects light adaptation of rods. When illuminated, photoreceptors must adapt to the light exposure in order to retain the ability to respond. Ca^{2+} levels in the outer segment of photoreceptors modulate the activity of several proteins to mediate this light adaptation (Fain et al., 2001; Nakatani et al., 2002; Pugh et al., 1999). To test if Ca^{2+} sequestering through MCU has an effect on light adaptation of rods, we exposed retinas to a series of background light steps of increasing intensity. The peak response to background light of *Mcu*$^{-/-}$ rods was comparable to controls (**Figure 3.7D and 3.7E**). Notably, the background response plateau of *Mcu*$^{-/-}$ rods was lower than the controls and was significant for the two highest background light steps tested (**Figure 3.7F**). However, the light adapted sensitivity (S_f)

remained largely unaffected in Rod *Mcu*$^{-/-}$ compared to the controls across all background light levels tested (**Figure 3.7G**).

MCU activity is controlled by multiple regulatory proteins that confer cooperativity to the channel so that it can robustly respond to changes in cytoplasmic Ca^{2+} (Csordás et al., 2013; Hoffman et al., 2013; Mallilankaraman et al., 2013; Patron et al., 2014, 2018; Perocchi et al., 2010b; Plovanich et al., 2013b; Sancak et al., 2013b). In the previous experiments, all responses were in either the completely dark-adapted state or in steady-state light adaptation, with cytoplasmic Ca^{2+} being stable at high or low concentrations, respectively. We next examined if MCU modulates responses when photoreceptor intracellular Ca^{2+} levels are rapidly changing and when Ca^{2+} flux through MCU may be changing more dynamically. To do this, we presented test flashes to the retinas that were in the process of dark adapting. After turning off the background light, two test flashes were presented at 2 and 4 seconds, followed by a saturating light flash (**Figure 3.7H**). This allowed us to assess both flash response kinetics (**Figure 3.7I**) and sensitivity (**Table 3.2**). Both parameters were unaltered by the rod MCU deficiency.

	R_{max} (μV)	$I_{1/2}$ (phot/μm^2)	S_{fD} (μV/phot/μm^2)	t_p (ms)	t_{int} (ms)	τ_{rec} (ms)	I_o^* (phot/μm^2/s)	n^*
Control (N=8)	508 ± 79	101 ± 8	0.014 ± 0.001	136 ± 5	359 ± 16	65 ± 4	116 ± 17	0.61 ± 0.06
Rod *Mcu*$^{-/-}$ (N=8)	605 ± 67	100 ± 18	0.015 ± 0.001	141 ± 6	331 ± 18	65 ± 3	194 ± 37	0.69 ± 0.04
p value	0.36	0.94	0.63	0.50	0.28	0.96	0.08	0.3

Table 3.1: Dim Flash Response Sensitivity and Kinetics Parameters.
R_{max}, saturated response amplitude measured at the plateau; $I_{1/2}$, intensity required to produce half of the saturated response; S_{fD}, dark adapted sensitivity; t_p, time to peak of a dim flash response; t_{int}, integration time of the response; τ_{rec}, recovery time constant during response shut off; I_o, intensity required to decay the sensitivity to one half.

	S_f/S_{fD} *(µV/phot/µm^2),* I_{BD} *(1000 Phot/µm^2),* **2s**	S_f/S_{fD} *(µV/phot/µm^2),* I_{BD} *(1000 Phot/µm^2),* **4s**	S_f/S_{fD} *(µV/phot/µm^2),* I_{BD} *(3450 Phot/µm^2),* **2s**	S_f/S_{fD} *(µV/phot/µm^2),* I_{BD} *(3450 Phot/µm^2),* **4s**
Control (N=8)	1.2 ± 0.1	1.3 ± 0.1	0.96 ± 0.05	1.1 ± 0.04
Rod *Mcu*$^{-/-}$ (N=12)	1.3 ± 0.1	1.4 ± 0.1	0.9 ± 0.05	1.2 ± 0.06
p value	0.46	0.45	0.66	0.73

Table 3.2. Normalized sensitivity at 2s and 4s time points after turning off the background light step.
S_f/S_{fD}, Normalized fractional sensitivity; I_{BD} , Intensity of the background illumination

	R_{max} *(µV)*	$I_{1/2}$ *(phot/µm^2)*	S_{fD} *(µV/phot/µm^2)*	t_p *(ms)*	T_{int} *(ms)*	τ_{rec} *(ms)*
Nckx1$^{-/-}$ Control (N=10)	19 ± 2	22.8 ± 1.4	0.02605 ± 0.001	312.9 ± 19	1564 ± 83	441.3 ± 52
Nckx1$^{-/-}$ Rod *Mcu*$^{-/-}$ (N=9)	9.7 ± 1	23.2 ± 2	0.02555 ± 0.002	367.7 ± 24	1687 ± 81	501 ± 103
p value	0.0005	0.87	0.86	0.09	0.3	0.6

Table 3.3: Dim Flash Response Sensitivity and Kinetics Parameters.
R_{max}, saturated response amplitude measured at the plateau; $I_{1/2}$, intensity required to produce half of the saturated response; S_{fD}, dark adapted sensitivity; t_p, time to peak of a dim flash response; t_{int}, integration time of the response; τ_{rec}, recovery time constant during response shut off

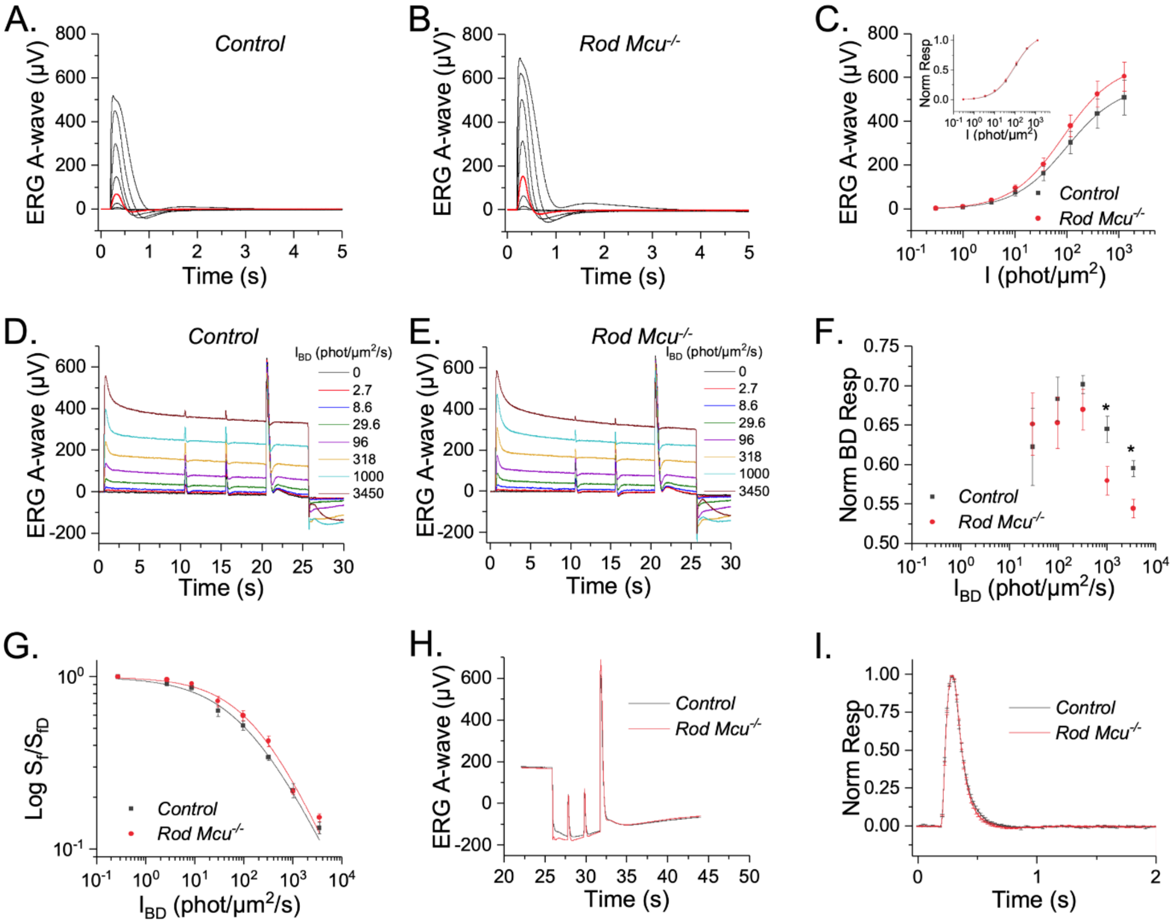

Figure 3.7: Mouse rods lacking Ca^{2+} uptake through MCU exhibit normal photoresponse **(A,B)** Flash response families of dark adapted *iCre*$^+$ (control; A) and *Mcu*$^{f/f}$ *iCre*$^+$ (Rod *Mcu*$^{-/-}$; B) mice from transretinal ERG recordings. Scotopic a-wave responses were recorded by a series of test flashes (1ms in duration) with intensities (in photons/μm^2) 0.3, 1, 3.5, 10.2 (red traces), 35.4, 117, 385, 1270. **(C)** Averaged rod responses (Mean ± SEM) from control (black) and Rod *Mcu*$^{-/-}$ mice (red) plotted as a function of flash intensity show only a marginal ($p>0.05$) difference in the response amplitude between these groups (n=10 for each). The solid lines represent curves fitted to the intensity response using the Naka-Rushton Function, $R/R_{max} = I/(I + I_{1/2})$. (Inset) Normalized intensity response curves showing no difference in sensitivity between control (black) and Rod *Mcu*$^{-/-}$ (red) mice. **(D,E)** ERG responses to steps of incremental background illumination of control (D) and Rod *Mcu*$^{-/-}$ mice (E) with subsequent responses to dim and saturating light flashes (n=8 for each). **(F)** The background light response at plateau, normalized to the peak of the initial background response, as a function of background light intensity. The plateau response for the two brightest backgrounds was significantly lower for the Rod *Mcu*$^{-/-}$ responses compared to these from controls (n=8 for each). **(G)** Light-adapted sensitivity, normalized to the corresponding dark-adapted value, plotted as a function of background light intensity. Solid lines represent curves fitted to the response plots using the Weber Fechner function. (n=8 for each). **(H)** Rod sensitivity during subsequent dark adaptation was estimated from ERG responses to dim flashes recorded at 2 s and 4 s after turning off a step of background light; averaged traces for control (black; n=8) and Rod *Mcu*$^{-/-}$ (red; n=12) retinas are shown. No notable differences in the kinetics of the dim flash response between control and *Mcu*$^{-/-}$ rods at both 2 s and 4 s time points for the two brightest background steps (1000 and 3450 photons/μm^2/s) were evident. **(I)** A representative plot for the flash responses recorded at 4s after turning off the highest background (3450 photons/μm^2/s) shows identical kinetics between control (n=8) and Rod *Mcu*$^{-/-}$ (n=12) responses.

MCU-mediated mitochondrial Ca^{2+} uptake does not contribute to the small photoresponse seen in Nckx1$^{-/-}$ mice

The rod Na^{+}/Ca^{2+}, K^{+} exchanger (NCKX1) is the only known route for Ca^{2+} clearance from the outer segment plasma membrane, and it is thought to be the driver of Ca^{2+} clearance from this compartment. Since MCU expression in mouse rods is extremely low, its contribution to cytosolic Ca^{2+} clearance may be small compared to that of NCKX1. In an effort to unmask any possible modulation of the rod photoresponse by MCU, we investigated the effect of MCU loss on the rod photoresponse in mice lacking NCKX1. NCKX1-deficiency compromises Ca^{2+} extrusion in the rod outer segments and it delays photoresponse recovery following a flash stimulus (Vinberg et al., 2015). If the residual Ca^{2+} extrusion in NCKX1-deficient rods is mediated by MCU, then it would be expected that the subsequent deletion of MCU would further suppress or completely block Ca^{2+} extrusion, causing a further delay in photoresponse recovery and suppressing light adaptation.

We recorded transretinal ERG responses from *Nckx1*$^{-/-}$ control and *Nckx1*$^{-/-}$ Rod *Mcu*$^{-/-}$ mice (**Figure 3.8A and 3.8B**). As previously shown, deletion of NCKX1 results in a significant reduction in the photoresponse generated by mouse rods (compare **Figure 3.8A** with **Figure 3.7A**) (Vinberg et al., 2015). The responses of *Nckx1*$^{-/-}$ *Mcu*$^{-/-}$ double knockout rods are significantly smaller compared to *Nckx1*$^{-/-}$ controls (**Figure 3.8C**). However, the sensitivity and kinetics of the flash response are comparable in *Nckx1*$^{-/-}$ *Mcu*$^{-/-}$ rods and control *Nckx1*$^{-/-}$ rods (**Figure 3.8C inset and 3.8D**, respectively). This indicates that Ca^{2+} sequestration by MCU does not modulate the rod photoresponse recovery even in the absence of the dominant NCKX1 Ca^{2+} extrusion mechanism. We wondered if the smaller responses of the *Nckx1*$^{-/-}$ *Mcu*$^{-/-}$ double knockout rods might be due to accelerated retinal degeneration, since fewer rods would explain the observed reduction in the photoresponse. However, when we measured the thickness of the different retinal layers of H&E stained *Nckx1*$^{-/-}$ control and *Nckx1*$^{-/-}$ *Mcu*$^{-/-}$ eyes we found no differences, indicating that early retinal degeneration is not responsible for the decreased response (**Figure 3.8E, 3.8F**). **Table 3.3** summarizes the rod response properties of *Nckx1*$^{-/-}$ controls and *Nckx1*$^{-/-}$ Rod *Mcu*$^{-/-}$ mice. Overall, these results indicate that Ca^{2+} uptake mediated by MCU does not significantly influence the rod photoresponse.

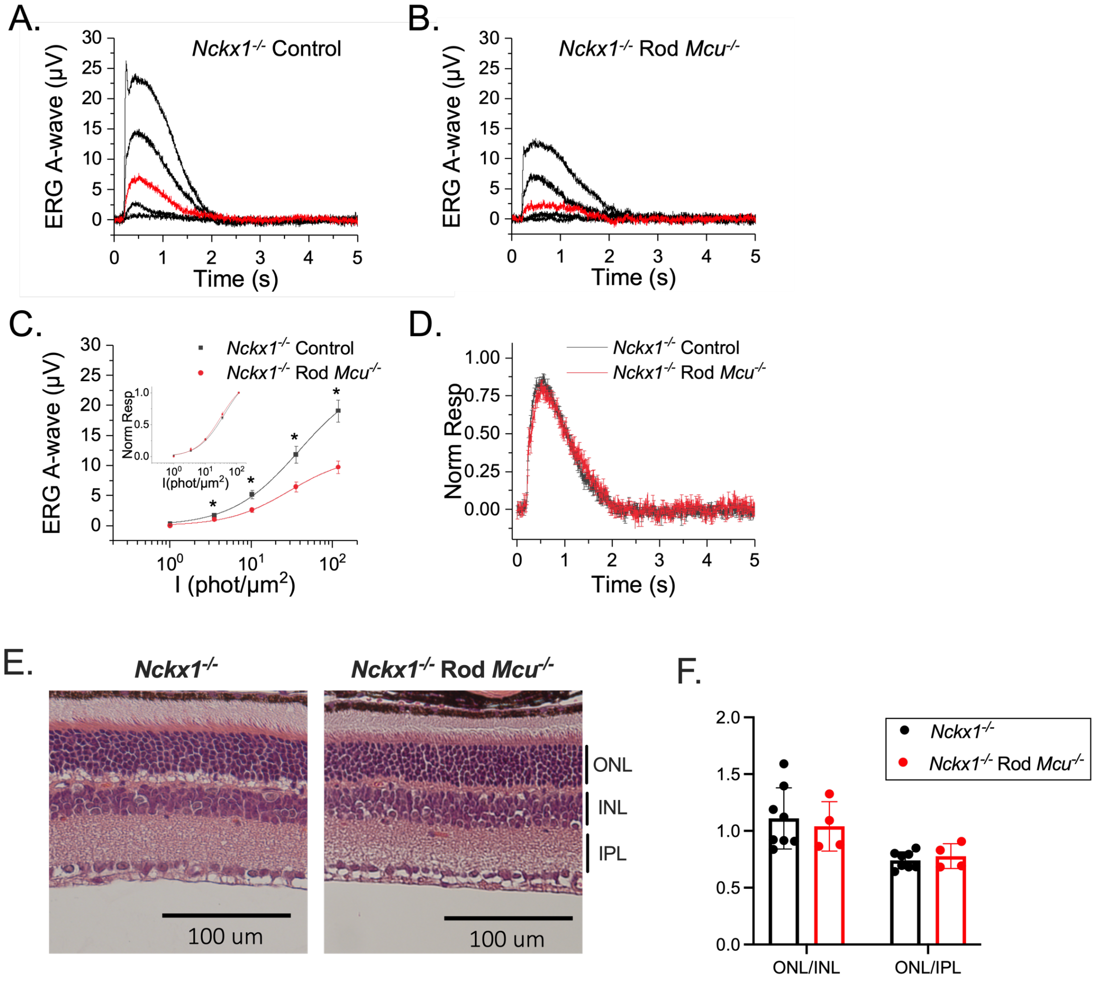

Figure 3.8: MCU-mediated mitochondrial Ca^{2+} uptake does not modulate the photoresponses in Nckx1$^{-/-}$ mice

(A,B) Flash response families of dark adapted *Nckx1*$^{-/-}$ iCre^{+} (*Nckx1*$^{-/-}$ control; A) and *Nckx1*$^{-/-}$ *Mcu*$^{f/f}$ iCre^{+} double knockout (*Nckx1*$^{-/-}$ Rod *Mcu*$^{-/-}$; B) mice from transretinal ERG recordings. Scotopic a-wave responses were recorded by a series of test flashes (1 ms in duration) with intensities (in photons/µm^{2}) 1, 3.5, 10.2 (red traces), 35.4, 117. **(C)** Averaged rod responses (Mean ± SEM) from *Nckx1*$^{-/-}$ control (black; n=10) and *Nckx1*$^{-/-}$ Rod *Mcu*$^{-/-}$ mice (red; n=9) plotted as a function of flash intensity show a substantial reduction of the response amplitude in the double knockouts as compared to the controls. However, the sensitivity of the rods (estimated their normalized intensity response functions; Inset) remained unchanged between *Nckx1*$^{-/-}$ control (black) and *Nckx1*$^{-/-}$ Rod *Mcu*$^{-/-}$ (red) mice. **(D)** The kinetics of the dim flash response were not affected in the *Nckx1*$^{-/-}$ Rod *Mcu*$^{-/-}$ mice (n=9); red trace) as compared to *Nckx1*$^{-/-}$ controls (n=10; black trace). **(E)** Representative images of *Nckx1*$^{-/-}$ and *Nckx1*$^{-/-}$ Rod *Mcu*$^{-/-}$ hemotoxylin and eosin (H&E) stained retinal sections. Mice were between 6-8 weeks of age. Lines to the right of the *Nckx1*$^{-/-}$ Rod *Mcu*$^{-/-}$ image retinal indicate the various layers (ONL = outer nuclear layer; INL = inner nuclear layer; IPL = inner plexiform layer. **(F)** Quantification of H&E stained images. (n=8 eyes from four *Nckx1*$^{-/-}$ mice and 4 eyes from two *Nckx1*$^{-/-}$ Rod *Mcu*$^{-/-}$ mice).

Discussion

Photoreceptors have abundant mitochondria in the compartment of the cell between the nucleus and the outer segment that can influence cytosolic Ca^{2+} pools (Giarmarco et al., 2017a). Photoreceptors also depend on Ca^{2+} homeostasis for proper function and viability (Krizaj and Copenhagen, 2002; Szikra and Krizaj, 2007). Despite this, we find that loss of the presumptive primary Ca^{2+} channel for mitochondrial Ca^{2+} uptake (MCU) is tolerated surprisingly well by photoreceptors. MCU-deficient photoreceptors appear healthy, their TCA cycle activity is largely unaltered, and the photoresponse is preserved. In cones from global *mcu*$^{-/-}$ zebrafish, cytosolic Ca^{2+} is cleared more slowly and mitochondrial Ca^{2+} uptake is reduced in a significant population of mitochondria. However, some mitochondria still display robust increases in mito-GCaMP3 fluorescence in the absence of MCU. Ca^{2+} uptake in these mitochondria appears to occur more slowly and with a lower magnitude than in WT mitochondria. Consistent with this result, we found that both WT and *mcu*$^{-/-}$ cones have a population of mitochondrial clusters which still appear to take up Ca^{2+} even in the presence of the MCU inhibitor Ru360, and the characteristics of this population match those of the responding mitochondria in *mcu*$^{-/-}$ cones. This is similar to what has been observed in non-synaptic brain mitochondria isolated from *Mcu*$^{-/-}$ mice, in which uptake of Ca^{2+} into mitochondria was not blocked but instead occurred at a slower rate compared to controls (Hamilton et al., 2018). Taken together, these results suggest that that neuronal tissue like retina and brain may have an alternative mitochondrial Ca^{2+} uptake pathway with different response kinetics and Ca^{2+} uptake capacity. Future experiments which use other strategies for measuring mitochondrial Ca^{2+} uptake will be critical for confirming, identifying, and assessing the role of MCU-independent mechanisms for mitochondrial Ca^{2+} uptake in photoreceptors.

Other candidates for Ca^{2+} entry have been described but are not as well-characterized as MCU, as MCU is thought to be primarily responsible for mitochondrial Ca^{2+} influx. However, the viability *of Mcu*$^{-/-}$ mice and zebrafish, and the extremely mild consequences of MCU loss in photoreceptors we describe here, suggest that there is an alternative uptake mechanism in at least some cell types.(Pan et al., 2013; Tomar et al., 2019) Letm1 is a Ca^{2+}/H^{+} exchanger on the inner mitochondrial membrane that links Ca^{2+} influx and efflux to electron transport chain activity and mitochondrial pH.(Tsai et al., 2014). Letm1 appears to act primarily as a Ca^{2+} extrusion mechanism, but it is also capable of Ca^{2+} influx. Knockdown of Letm1 impairs Ca^{2+} transport into the mitochondria of Flp-In-293 cells and patient-derived fibroblasts, and Letm1$^{+/-}$ mice have impaired ATP production and PDH activity specifically in neuronal tissue. (Doonan et al., 2014; Jiang et al., 2013) There is also some evidence that mitochondrial ryanodine receptors may exist in neurons and cardiac cells, but they have yet to be unambiguously identified.(Beutner et al., 2001; Jakob et al., 2014) Another candidate is the mitochondrial Na^{+}/Ca^{2+} exchanger, which is associated with Ca^{2+} efflux but can run in reverse to promote Ca^{2+} entry into mitochondria.(Smets et al., 2004)

A possible advantage of relying on these other mechanisms for Ca^{2+} transport is that it would link mitochondrial Ca^{2+} influx to factors other than cytosolic Ca^{2+} levels. The mitochondrial Na^{+}/Ca^{2+} exchanger would couple Ca^{2+} entry to cytosolic Na^{+}, which fluctuates in photoreceptors in response to light. Letm1 would tie Ca^{2+} entry to mitochondrial pH and ATP production; Letm1 has even been shown to be upregulated in cancer tissue, which is highly glycolytic like photoreceptors.(Piao et al., 2009) Whatever the alternative pathway of mitochondrial Ca^{2+} uptake might be photoreceptors, the low expression of MCU in photoreceptors raises the possibility that this alternative pathway could play a significant role in controlling photoreceptor mitochondrial Ca^{2+} uptake.

Loss of MCU has very mild metabolic consequences for photoreceptors. Evidence continues to suggest that tissue-specific metabolic specialization causes the metabolic consequences of MCU loss to vary from to tissue. For example, the liver has the important role of synthesizing fatty acids for the body and can also store lipids. In mouse and zebrafish hepatocytes, loss of MCU disrupts lipid metabolism and leads to hepatic lipid accumulation due to delayed cytosolic Ca^{2+} clearance and subsequent disrupted AMP-activated protein kinase (AMPK) dephosphorylation (Tomar et al., 2019).

Conversely, in skeletal muscle, loss of MCU causes a metabolic shift towards increased lipid oxidation due to PDH inhibition restricting the availability of pyruvate-derived acetyl-CoA (Gherardi et al., 2018; Kwong et al., 2018). These examples suggest that the basal metabolic specialization of a tissue will determine in large part the metabolic consequences of MCU loss. Since photoreceptors rely heavily on aerobic glycolysis to generate ATP, it is not entirely surprising that Rod *Mcu*$^{-/-}$ mouse retinas are metabolically quite normal and exhibit only a mild accumulation of α-ketoglutarate that does not appear to affect photoreceptor function.

α-ketoglutarate participates in multiple mitochondrial and cytosolic reactions, making it difficult to pinpoint the exact reaction that is altered by loss of MCU in rods which leads to this accumulation. This is not the first time an accumulation of α-ketoglutarate has been observed to accompany MCU loss, as a similar accumulation of α-ketoglutarate occurs in *Mcu*$^{-/-}$ fibroblasts. These fibroblasts have defects in glucose metabolism upstream of α-ketoglutarate, and the accumulated α-ketoglutarate was attributed to upregulated glutaminolysis (Lombardi et al., 2019). However, *Mcu*$^{-/-}$ photoreceptors exhibit no defects in glucose metabolism upstream of α-ketoglutarate and we see no evidence for altered synthesis of glutamate or glutamine in retinas supplied with U-^{13}C-glucose, which suggests a different mechanism is responsible.

An alternative possibility is that α-ketoglutarate levels increase after loss of MCU due to decreased Ca^{2+} stimulation of α-KGDH. When α-KGDH is bound to Ca^{2+}, its K_m for α-ketoglutarate is lowered (Denton, 2009; McCormack and Denton, 1979). We previously observed that increased matrix Ca^{2+} in zebrafish cone photoreceptors lowers the steady-state concentration of α-ketoglutarate, presumably because less substrate is needed to activate α-KGDH due to its lowered K_m (Hutto et al., 2020). Since steady-state α-ketoglutarate levels increase in MCU-deficient retinas, it is reasonable to hypothesize that the opposite occurs: more substrate is needed to activate α-KGDH due to its increased K_m when one route of Ca^{2+} entry into the matrix (MCU) is shut down. However, our measurements of matrix Ca^{2+} show that the overall basal matrix Ca^{2+}

levels are unaltered in cone mitochondria lacking MCU. We suggest the following possible explanations for elevated α-ketoglutarate levels in the absence of a detectable change in matrix Ca^{2+}:

1) matrix Ca^{2+} levels are decreased in rods lacking MCU but not in cones from global *mcu*$^{-/-}$ zebrafish. Genetically encoded, mitochondrially-targeted Ca^{2+}-sensors with rod-specific expression do not exist in mice, and we are unable to selectively purify rod mitochondria from the rest of the inner retinal mitochondria, so we were unable to directly measure matrix Ca^{2+} levels in rod photoreceptors.
2) loss of MCU results in subtle changes in matrix Ca^{2+} microdomains which influence α-KGDH activity but that we are unable to detect using our imaging methods
3) α-ketoglutarate levels are affected by an unknown, matrix Ca^{2+}-independent process (such as altered malate-aspartate shuttle activity or changes in another metabolic reaction involving α-ketoglutarate)

Mcu$^{-/-}$ rods exhibit a normal photoresponse with no change in the sensitivity and kinetics of the flash response and light adaptation. However, mitochondrial Ca^{2+} uptake via MCU is regulated cooperatively by several regulatory proteins (Mallilankaraman et al., 2013; Perocchi et al., 2010b; Plovanich et al., 2013b; Sancak et al., 2013b). So, we also investigated if MCU might play a role in modulating the photoresponse only when intracellular Ca^{2+} levels are more rapidly changing, such as when photoreceptors are adapting to background light or during the subsequent recovery back to their dark adapted state. However, *Mcu*$^{-/-}$ rods did not display a change in photoresponse parameters even while dark adapting following exposure to background light. This lack of phenotype may reflect the extremely low expression of MCU in mouse rods relative to the more dominant Ca^{2+} clearance pathways such as NCKX1.

To determine if MCU might play a small role in clearing Ca^{2+} that is difficult to detect in the presence of other Ca^{2+} clearance pathways, we compared photoresponses of single knockout *Nckx1*$^{-/-}$ mice and double knockout *Nckx1*$^{-/-}$ Rod *Mcu*$^{-/-}$ mice. *Nckx1*$^{-/-}$ mice maintain a small photoresponse and are remarkably slow to degenerate, which indicates that they are able to clear a small amount of outer segment Ca^{2+} through a not yet understood pathway (Vinberg et al., 2015). We hypothesized that if the small photoresponse observed in *Nckx1*$^{-/-}$ mice were due to Ca^{2+} sequestering via MCU, that this response would be ablated in the double knockout *Nckx1*$^{-/-}$ Rod *Mcu*$^{-/-}$ mice. However, the sensitivity, flash response kinetics and even light adaptation were unchanged in *Nckx1*$^{-/-}$ Rod *Mcu*$^{-/-}$ mice compared to *Nckx1*$^{-/-}$ controls, which indicates that mitochondrial Ca^{2+} uptake via MCU does not contribute substantially to outer segment Ca^{2+} clearance or photoresponse recovery. It remains a possibility that mitochondrial Ca^{2+} uptake through an alternative pathway contributes to the small photoresponse that is seen in *Nckx1*$^{-/-}$ Rod *Mcu*$^{-/-}$ mice. We did observe a reduction in the flash response amplitude in *Nckx1*$^{-/-}$ Rod *Mcu*$^{-/-}$ as compared to Nckx1$^{-/-}$ rods. The reason for this remains unclear. Although we confirmed that there was no obvious degeneration of rods, it is still possible that there is a subtle shortening of the rod outer segments that we were unable to detect in our sections. Overall, we find that MCU does not play a significant role in Ca^{2+} feedback mechanisms during the photoresponse.

Maintaining intracellular Ca^{2+} homeostasis is vital for many cell types, including photoreceptors. While most cells are thought to facilitate mitochondrial Ca^{2+} uptake primarily through MCU, we find that both rod and cone photoreceptors have limited MCU expression. In the absence of MCU, cone mitochondrial Ca^{2+} uptake is diminished but not entirely ablated. We found that this fraction of MCU-mediated mitochondrial Ca^{2+} uptake has a very limited effect on modulating metabolism and no role in modulating the photoresponse. However, this does not mean that mitochondria do not play a role in modulating photoreceptor function by buffering intracellular Ca^{2+}, as we find evidence for MCU-independent mitochondrial Ca2+ uptake in photoreceptors. Overall, we find that MCU is surprisingly dispensable for photoreceptor function, possibly in favor of an alternative mitochondrial Ca^{2+} uptake pathway.

Acknowledgements

The findings in this chapter are reported in a Scientific Reports publication. The authors on this publication are Celia M. Bisbach (CMB), Rachel A. Hutto (RAH), Whitney M.

Cleghorn (WMC), Deepak Poria (DP), Fatima Abbas (FA), Frans Vinberg (FV), Vladimir Kefalov (VK), James B. Hurley (JBH), and Susan E. Brockerhoff (SEB). CMB, RAH, and WMC performed experiments and prepared the manuscript text related to Figures 3.1-3.3 (excluding the zebrafish electrophysiology experiments). CMB and WMC performed experiments related to Figure 3.4. CMB performed experiments and prepared the manuscript text related to Figures 3.5 and 3.6. DP and VJK designed and performed experiments and prepared the manuscript text related to in Figures 3.7-3.8. FA and FV designed and performed experiments and prepared the manuscript text related to zebrafish electrophysiology experiments in Figure 3.3. All authors reviewed the manuscript. SEB, JBH, VK, and FB helped design and interpret experiments.

Methods

Animal Use: Mice were maintained and used in accordance with the guidelines of experimental protocols approved by the Institutional Animal Care and Use Committees (IACUC) of Washington University in St. Louis (protocol approval number: 20170232) and the University of Washington in Seattle (protocol number: 2050-01). Zebrafish were maintained and used in accordance with the guidelines of experimental protocols approved by the IACUC of both the University of Washington in Seattle (protocol number: 3113-02) and University of Utah (protocol number: 17-11004).

Animal care: At Washington University in St. Louis, mice were kept under a 12h light/dark cycle and given free access to food and water. At the University of Washington, mice were housed in the UW Medicine SLU 3.1 vivarium, where they experienced a 6AM-9PM (fall-winter) and 7AM-9PM (spring-summer) light/dark cycle and had free access to food and water. In figures 3 and 4, “WT” animals are *Mcu*$^{fl/fl}$ iCre- littermates. In figure 5, “Control” animals are iCre+ mice in which *Mcu* is not floxed. In figure 6, “Control” animals are *Nckx1*$^{-/-}$ single knockouts. In figures 5 and 6, the control and experimental mice were obtained from separate lines derived from common parents. iCre-75 mice were a gift from the lab of Ching Kang (Jason) Chen (Li et al., 2005). MCU^{fl} mice (B6;129S-*Mcu*$^{tm1.1Jmol}$/J) were obtained from Jackson Labs. The

Nckx1$^{-/-}$ mice used in this study were generated as described in a previous publication (Vinberg et al., 2015). Mice were maintained on a C57BL/6J background. Rod *Mcu*$^{-/-}$ mice used for histology were 6 and 11 months of age (6 months of age is shown in Figure 1), mice used for metabolic analysis were between 5-9 months of age, mice used for ERG analysis were 6 to 8 weeks of age, and *Nckx1*$^{-/-}$ and Rod *Mcu*$^{-/-}$ mice used for histology were 6 to 8 weeks of age. Mice were genotyped to confirm the absence of the Rd8 mutation. Equal numbers of male and female mice were used in this study.

All fish used in this analysis were maintained in the University of Washington South Lake Union aquatics facility or the Centralized Zebrafish Animal Resource (CZAR) at the University of Utah at 27.5°C on a 14/10 h light/dark cycle and were maintained in the Roy$^{-/-}$ genetic background. All wild-type fish (WT) used in analysis were age-matched siblings to CRISPR-generated *mcu*$^{-/-}$ zebrafish. Fish used for mito-GCaMP3 slice preparation were between 7 and 11 months of age, fish used for cyto-GCaMP3 slice preparation were 18 months of age, fish used for metabolic analysis were 11 months of age, fish used in ERG analysis were 7 months of age, and fish used for retinal morphology analysis were 11 months of age. Equal numbers of male and female fish were used.

Immunoblotting. Protein was extracted by homogenizing in RIPA buffer (150 mM NaCl, 1.0% Triton X-100, 0.5% sodium deoxycholate, 0.1% SDS, 50 mM Tris, pH 8.0) and run on 14% polyacrylamide gels. After running, gels were transferred onto PVDF membranes (Millipore, IPFL00010) and briefly washed with PBS. Primary antibodies were diluted in blocking buffer (LI-COR, 927-40000) and incubated overnight on blots at 4°C. Membranes were washed twice with PBS containing 0.1% Tween-20 and once with PBS, then incubated with secondary antibodies diluted 1:5000 in blocking buffer for 1 hr at RT and washed again before imaging. Membranes were imaged and bands were quantified using the LI-COR Odyssey CLx Imaging System (RRID:SCR_014579). Primary antibodies used: PDH E1 subunit (Abcam Cat# ab110334, RRID:AB_10866116), P-PDH (EMD Millipore Cat# ABS204, RRID:AB_11205754), mtCO1 (Abcam Cat# ab14705, RRID:AB_2084810), SDHB (Abcam Cat# ab14714, RRID:AB_301432), and Cell Signaling MCU (Cell Signaling Technology Cat# 14997, RRID:AB_2721812), custom MCU antibody (Hutto et al., 2020). All primary antibodies were used at 1:1000, with the exception of the custom MCU antibody which was used at 1:100. Secondary antibodies used: IRDye 800CW donkey anti-rabbit IgG (H + L) (LI-COR Biosciences, 925-32213, RRID: AB_2715510); IRDye 680RD donkey anti-mouse IgG (H + L) (LI-COR Biosciences, 925-32212, RRID: AB_2716622); IRDye 680RD donkey anti-rabbit IgG (H + L) (LI-COR Biosciences, 925-68073, RRID: AB_2716687); IRDye 800CW goat anti-mouse IgG (H + L) (LI-COR Biosciences, 925-32210, RRID: AB_2687825).

Immunohistochemistry. For best immunohistochemistry results, mice were perfused with fixative according published methods (Gage et al., 2012). Briefly, PBS was placed in a 37°C water bath and all fixative tubing was flushed repeatedly with PBS to clear any bubbles. Mice were anaesthetized using 270 mg/kg of nebutol. Mice were taped to a dissection board and open-heart surgery was performed in order to insert the perfusion needle into the left ventricle. The right atrium was snipped, and PBS was perfused through the mouse using a peristaltic pump until the outflow was clear. Then, room temperature 4% PFA (prepared from 16% PFA diluted in PBS) was perfused through the mouse. After fixation, eyes were carefully cut out with curved dissection scissors, the sclera was cut off, and eyes were stored in 4% PFA for 2 hours. Eyes were then rinsed with PBS, and moved through a sucrose gradient of 5%, 10%, 20%, and 30% sucrose (eyes were transferred to increasing concentrations of sucrose each time they sank to the bottom of the tube). Eyes were embedded in O.C.T. compound and 20 micron sections were cut using a Leica cryostat. For immunostaining, sections were rehydrated with PBS for 10 minutes and blocked in Normal Goat Serum (NGS) for 1h. Primary antibodies were diluted in NGS and incubated on sections overnight at 4°C in a humidified chamber. Sections were washed three times with PBS, and secondary antibodies were diluted in PBS and incubated on sections for 1h at room temperature. Sections were washed 3x with PBS, with the middle wash containing 5uM Hoechst nuclear stain diluted in PBS (Hoechst 33342, Trihydrochloride, Trihydrate stain (ThermoFischer, H3570). Slides were mounted using Fluoromount (Southern Biotech Cat#:0100-01) and imaged using an Olympus FV1000 Confocal microscope. Antibodies and stains used were: mtCO1 1:500 (Abcam Cat# ab14705, RRID:AB_2084810); MCU

1:2000 (Cell Signaling Technology Cat# 14997, RRID:AB_2721812); PNA 1:200 (after suspending at a concentration of 1 mg/mL in H20) (Lectin PNA Alexa Fluor 647 conjugate, ThermoFischer Cat# L32460); Goat anti-Rabbit IgG (H+L) Alexa Fluor 633 (Thermo Fisher Scientific, Cat# A-21070, RRID AB_2535731; Goat Anti-Mouse IgG H&L Alexa Fluor 488 (Abcam, ab150113, RRID:AB_2576208).

Isotopic Labeling. Krebs-Ringer bicarbonate (KRB) buffer (98.5 mM NaCl, 4.9 mM KCl, 1.2 mM KH_2PO_4 1.2 mM $MGSO_4$-$7H_2O$, 20 mM HEPES, 2.6 mM CaCl-$2H_2O$, 25.9 mM $NaHCO_3$) optimized for isotopic labeling experiments in retinas was used in these experiments. Mice were euthanized by awake cervical dislocation and eyes were rapidly enucleated into a dish of Hank's Buffered Salt Solution (HBSS; Gibco, Cat#: 14025-076). Zebrafish were euthanized using an ice bath and eyes were removed and placed in a dish of KRB + 5mM U-13C Glucose. For flux measurements, retinas were placed in pre-warmed KRB containing D-[U-^{13}C]-glucose (Cambridge Isotope Laboratories, CLM-1396). Retinas were incubated for the specified time points at 37°C mouse at 5% CO_2 and room oxygen, then washed twice in ice-cold PBS and flash frozen in liquid nitrogen. For mouse dark-adapted experiments, mice were dark-adapted for a minimum of 18 hours. Samples were collected exactly as above, but in complete darkness under an infrared light using night vision goggles. For zebrafish dark-adapted experiments, zebrafish were dark adapted for 18 hours and samples were collected under dim red light.

Mass Spectrometry Sample Preparation. Metabolites were extracted from retinas using ice-cold 80% MeOH. 150 µL extraction buffer was added to each sample and tissue was disrupted by sonication. Samples were then spun at maximum speed, the supernatant transferred to a new tube, and the pellet saved for protein quantification. The supernatant was lyophilized at room-temp until dry. Extracted metabolites were derivatized using a two-step process: 1) 10 µL of 20 mg/mL Methoxyamine HCl (Sigma, Cat#: 226904) dissolved in pyridine (Sigma, Cat#: 270970) was added and samples were incubated at 37°C for 90 minutes, then 2) 10 µL of *tert*-butyldimethylsilyl-N-methyltrifluoroacetamide (Sigma, Cat#: 394882) was added and samples were incubated at 70°C for 90 minutes. Metabolites were analyzed on an Agilent 7890/5975C

GC-MS using selected-ion monitoring methods described in previous work.[7–10] Peaks were manually integrated using MSD ChemStation software (Agilent), and correction for natural isotope abundance was performed using Isocor software (Millard et al., 2012). Raw signals for each metabolite were converted to molar amounts using metabolite standard curves which were run alongside each experiment. Molar amounts were normalized to the total amount of protein (determined using a BCA assay) for each sample to determine the molar amount per µg of cellular protein. Statistical analysis and figure preparation was performed with GraphPad v 8.4.3 (for Mac, GraphPad Software, San Diego CA, USA, www.graphpad.com).

Live larval imaging of mito-GCaMP3. Larvae were imaged as described previously (Hutto et al., 2020). Larvae were maintained in embryo media containing 0.0003% 1-phenyl 2-thiourea (PTU, Sigma-Aldrich P7629) starting at 20h postfertilization for confocal imaging. Larvae were analyzed at 6 days postfertilization (dpf) by embedding in 0.5% low melting point agarose containing embryo media with 0.02% (w/v) Tricaine (Sigma-Aldrich, E10521). The agarose was submerged in embryo media containing 0.0003% PTU and 0.02% (w/v) tricaine. Imaging was performed using an Olympus FV1000 with a 40x water objective in conjunction with Olympus FluoView FV10-ASW software (RRID:SCR_014215). The excitation/emission wavelengths used for mito-GCaMP3 were 488/510 nm. Images of total eye mitochondrial clusters were collected at a z-depth of 2 µm, and blinded quantification was performed using ImageJ + Fiji software (SCR_002285).

Retinal slice imaging of cyto-GCaMP3 and mito-GCaMP3. Slices were prepared as described previously (Giarmarco et al., 2017a, 2018). For cyto-GCaMP3 measurements, retinal slices were incubated in KRB buffer (containing 0 mM $CaCl_2$ and 0.4 mM EGTA) for 10 minutes. For basal cyto-GCaMP3 determination, slices were imaged every 2s for 24s to establish baseline cyto-GCaMP3 fluorescence. A bolus of $CaCl_2$ was then injected in the imaging chamber to bring the final $[Ca^{2+}]_{free}$ in the chamber to 5 mM. Retinal slices were imaged for a total of 10 min to monitor Ca^{2+} clearance. For basal mito-GCaMP3 determination, 15 z-slices of 2 µm thickness were collected every 30 s. Retinas were incubated in KRB buffer (containing 2 mM $CaCl_2$) for

5 min, then the chamber was injected with ionomycin to a final concentration of 5 μM (Sigma, 407950, prepared in DMSO) for another 5 min of image collection. An excess of EGTA (5 mM) was then injected and images were collected for another 5 min. For mitochondrial Ca^{2+} uptake experiments, retinas were incubated in KRB buffer containing 100 μM KB-R7943 for 10 minutes. After this preincubation, baseline measurements of mito-GCaMP3 fluorescence were taken for 3 frames (30 seconds each) before treatment with 25 μM sildenafil for a total of 15 minutes of imaging.

For analysis of all GCaMP3 experiments, any cell bodies or mitochondrial clusters where the maximum fluorescence signal was completely saturated were excluded. For basal mito-GCaMP3 fluorescence analysis, mitochondrial clusters that did not respond to ionomycin treatment were not included in the analysis. Analysis was conducted blinded (masked) to sample identity. The excitation/emission wavelengths used for mito- and cyto-GCaMP3 were 488/510 nm. Timelapses were analyzed using ImageJ + Fiji software (SCR_002285) and were corrected for X-Y drift using the MultiStackReg plugin of ImageJ (Schindelin et al., 2012; Schneider et al., 2012). Fixed ROIs were used to quantify average fluorescence signal across the mitochondrial cluster (for mito-GCaMP3) or cell body (for cyto-GCaMP3) at every time point. Statistical analysis and figure preparation for all GCaMP experiments was performed with GraphPad v 8.4.3 (for Mac, GraphPad Software, San Diego CA, USA, www.graphpad.com).

Mouse Electrophysiology. Mice were dark adapted overnight prior to the day of experiment and were euthanized by CO_2 incubation. Eyes were enucleated under dim red light immediately after euthanasia followed by dissection under infrared illumination. The retinas were gently detached from posterior eye cups and were stored in dark in a dish containing oxygenated Ames medium at room temperature until recording. Recordings were conducted using previously described methods (Vinberg and Kefalov, 2015). The retinas were mounted photoreceptors facing up in a closed chamber and were continuously superfused with oxygenated Ames medium (Sigma) at a flow rate of 3-5 ml/minute. For isolating the a-wave of ERG, 50μM DL-AP_4 (Tocris) and 100μM $BaCl_2$ (Sigma) were included in the Ames medium. The recording chamber was maintained at 35-36°C and retinas were allowed to adapt to the chamber temperature for at least 15 minutes before experiments. *Ex-vivo* transretinal ERG recordings were made in scotopic conditions by presenting light flashes produced by LEDs (Thor Labs). The ERG signals were amplified using a differential amplifier (Warner Instruments), low-pass filtered at 300Hz (Krohn Hite Corp.), digitized using digidata 1440 (Molecular Devices), and were recorded at a sampling frequency of 10kHz using pClamp 10 software.

Zebrafish Electrophysiology. Zebrafish were approximately 7 months of age for all electrophysiology experiments. Zebrafish were briefly dark adapted (~30 min), before euthanasia by ice water immersion. Eyes were enucleated into Modified Salamander Ringer's solution (110 mM NaC, 2.5 mM KCl, 1.0 mM CaCl2, 1.6 mM MgCl2, 10.0 mM HEPES, 10.0 mM Glucose) with pH adjusted to 7.8 with NaOH. The eyes were hemisected and retinas isolated from the eyecup. All procedures after the dark adaptation were performed under dim red light. To ensure ex vivo ERG signal was predominantly cone responses, dark adaption was limited to ~30 min to allow cone photopigment regeneration but not provide enough time for full rod photopigment regeneration, and experiments were carried out during the day (between 11AM and 4PM) when rod contributions to retinal responses are at their lowest due to the circadian regulation of photoreceptor biology in the zebrafish retina. Ex vivo ERG recordings were performed as described previously (Vinberg and Kefalov, 2015; Vinberg et al., 2014). Isolated retinas were mounted photoreceptor side up onto the specimen holder and perfused with Modified Salamander Ringer's solution, supplemented with 40 µM DL-AP4 (Tocris Bioscience) and 40 µM CNQX (Tocris Bioscience) to isolate the photoreceptor component of the ERG signal (a-wave). The rate of perfusion was ~5 mL/min and the experiments were conducted at room temperature (~23°C). ERG signal was first amplified (100×) and low-pass filtered at 300 Hz by a differential amplifier (DP-311, Warner Instruments), and data was further amplified (10×) and acquired at 10KHz using an integrated amplifier/digitizer (IPA, Sutter Instrument, CA). A High Power LED light source (Solis-3C, Thorlabs, Newton, NJ), with filter for red light (630 nm, FWHM bandwidth 69 nm, FF01-630/69-25, Semrock, Rochester, NY) and LED driver (DC2200, Thorlabs) were used to provide the flashes of light stimuli, durations ranged from 5 to 100 ms. The SutterPatch soft- ware (SutterPatch v1.1.2, Sutter Instrument, CA) drove both stimulus generation and data acquisition via the IPA amplifier’s analogue output and input, respectively. Light stimuli were calibrated before experiments using a calibrated photodiode (FDS100-CAL, Thorlabs, Newton, NJ) and flash intensities converted to photons/µm^2. Data analysis, including statistical analysis and figure preparation, was performed with GraphPad v 8.0.0 (for Windows, GraphPad Software, San Diego CA, USA, www.graphpad.com). Normalized responses were calculated for each retina by dividing the response amplitude data by the maximal amplitude measured at the peak/plateau of the response to the brightest flash. To quantify the gain of phototransduction activation, we fitted the Lamb–Pugh model to the initial leading edge of the dim flash response for each retina, and compared the average amplification constant (A) between WT and *mcu*$^{-/-}$ siblings (Lamb and Pugh Jr, 1992).

Chapter 4: Succinate can shuttle reducing power from the hypoxic retina to the O_2-rich pigment epithelium

Introduction

The unique architecture of the vertebrate eye places the retina in a chronically hypoxic niche. Choroidal vasculature inside the sclera is the main source of O_2 and nutrients for the outer retina. The retinal pigment epithelium (RPE), form a barrier that selectively regulates the flow of gases and nutrients from the choroid to the outer retina. This results in an O_2-sufficient RPE but a steeply declining O_2 gradient in the outer retina. The extent of hypoxia in the outer retina varies across species, but pO_2 in retinas can reach as low as ~5 mm Hg in mouse and can drop even lower in larger mammals (Linsenmeier and Zhang, 2017; Yu and Cringle, 2006).

O_2 is a key substrate in one of the most important and well-known reactions of energy metabolism. Normally, it is a terminal electron acceptor in the mitochondrial electron transport chain (ETC). The conventional model of the electron transport chain suggests that when O_2 is limiting, electrons from the ETC may be passed onto fumarate. In this "reverse" succinate dehydrogenase (SDH) reaction, SDH removes electrons from the ETC to reduce fumarate to succinate. This bypasses several steps in the ETC that drive ATP synthesis and the need for O_2 (Chouchani et al., 2014; Hochachka et al., 1975). Succinate accumulates in muscle, heart, kidney, liver, brain and blood during hypoxia (Cascarano et al., 1976; Chouchani et al., 2014; Hochachka et al., 1975). However, the degree to which the reverse SDH reaction contributes to succinate produced during hypoxia is debated, and the role of succinate in tissues that are in chronically hypoxic niches is largely unexplored (Chinopoulos, 2019; Chouchani et al., 2014; Zhang et al., 2018).

To better understand the physiological consequences of the disparity in O_2 tension between the retina and RPE, we sought to identify metabolic adaptations used by either tissue to thrive in their respective niches. Retinas already are known to be very glycolytic (Chinchore et al., 2017; Kanow et al., 2017; Krebs, 1927; Winkler, 1981). We discovered that retinas also adapt to hypoxia by reducing fumarate to succinate and exporting the succinate. This form of reverse electron transport at SDH is a major pathway for succinate production in the retina.

These observations about retinal metabolism prompted us to explore the role of succinate in the overall metabolic ecosystem of the eye. The RPE relies on its mitochondria to oxidize diverse fuels including lactate, fatty acids, glutamine and proline, and some of these fuels can be supplied to the RPE by the retina (Adijanto et al., 2014; Du et al., 2016a; Kanow et al., 2017; Reyes-Reveles et al., 2017; Yam et al., 2019). We show that the RPE/choroid complex has an extraordinary capacity to oxidize succinate. When fueled with succinate, the RPE/choroid complex releases malate, which can be converted back into succinate in retinas by reverse SDH activity. Based on these findings, we propose that succinate shuttles unused reducing power from the hypoxic retina to the O_2-rich RPE.

Results

Retinas release succinate which can fuel O_2 consumption in eyecups.

Retinas in an eye are in a chronically hypoxic environment (Linsenmeier and Zhang, 2017; Yu and Cringle, 2006). Exposure to hypoxia can induce tissues to release succinate, so we determined whether freshly isolated mouse retinas export succinate (Cascarano et al., 1976; Chouchani et al., 2014; Hochachka et al., 1975). We incubated freshly dissected retinas from C57BL/6J mice in 5 mM ^{12}C-glucose at atmospheric (21%) O_2 and 5% CO_2 and measured the rate of TCA cycle metabolite export by sampling incubation media at 30, 60, and 90 minutes (**Figure 4.1A**). Succinate was the most abundant TCA cycle metabolite found in the incubation medium, and is exported by retinas at a rate of 0.24 (± 0.04) pmol/µg/min.

The RPE consumes mitochondrial fuels. RPE cells are in direct contact with the retina and metabolites exchange between these tissues within an eye (Adijanto et al., 2014; Du et al., 2016a; Kanow et al., 2017; Nickla and Wallman, 2010; Reyes-Reveles et al., 2017; Swarup et al., 2019; Yam et al., 2019; Young and Bok, 1969). Since we found that the retina secretes succinate, we tested the capacity of RPE cells to consume it. For these experiments we used a custom-built perifusion oximeter, loaded with either intact retina or eyecup tissue (Sweet et al., 2002). Exposure of this tissue to 5 mM succinate causes a 0.7 (± 0.3) nmol/eyecup/min increase in eyecup O_2 consumption rate (OCR), which is a ~130% increase in OCR compared to eyecups supplied with 5 mM glucose alone (n=17). In retinas, 5 mM succinate increases OCR by only 0.2 (± 0.1) nmol/retina/min, which is a ~15% increase in OCR compared to retinas supplied with 5 mM glucose alone (n=7) (**Figure 4.1B**). The K_m for eyecup O_2 consumption when fueled with succinate is 2.1 (± 0.1) mM and the maximal respiration rate is 1.0 (± 0.4) nmol/eyecup/min (**Figure 4.2A**). No other glycolytic or TCA cycle metabolite we tested stimulates O_2 consumption as much as succinate, and the metabolites we tested did not synergistically enhance succinate-induced OCR, though 5 mM lactate impaired the succinate-mediated increase in OCR (**Figure 4.1C)**. Addition of the downstream TCA cycle metabolites fumarate and malate partially suppress O_2 consumption in eyecups stimulated by succinate (consistent with mass action) (**Figure 4.2B**). We confirmed the specificity of this effect to succinate dehydrogenase (SDH), as succinate-stimulated increases in OCR are blocked by the SDH inhibitor malonate (**Figure 4.1D,** composite trace shown in **Figure 4.2C**). Compiled OCR measurements for all conditions tested are shown in **Figure 4.2E**.

We next used isotopic tracers to determine how succinate alters TCA cycle activity compared to when glucose is the only fuel present. We supplied retinas and eyecups with either 5 mM U-^{13}C-glucose or with 5 mM ^{12}C-glucose and 1 mM U-^{13}C-succinate for times ranging from 0 to 5 minutes. We compared the formation of m2 citrate formed from glucose alone (left panel of **Figure 4.1E**) with the rate of m4 citrate formed from exogenous succinate (right panel of **Figure 4.1E**) within each tissue. Eyecups make citrate from succinate carbons (m4) ~5-fold faster than from glucose alone (m2) (**Figure**

4.1F). When supplied with U-^{13}C-succinate, the eyecup fumarate pool is 54% (± 0.8%) m4 labeled at 5 minutes, indicating that eyecups have a high capacity to import and metabolize succinate (**Figure 4.2G**). In striking contrast, retinas make citrate using carbons from glucose (m2) faster than with carbons from exogenous succinate (m4) (**Figure 4.1G**). When supplied with U-^{13}C-succinate, the retinal fumarate pool is only 9% (± 0.8%) m4 labeled at 5 minutes, suggesting that either 1) retinas do not take up succinate well, or 2) succinate is taken up well by retinas but not easily converted to fumarate (**Figure 4.2I**). Other TCA cycle isotopomers and the full isotopic distribution for the 5-minute time point are shown in **Figure 4.2**. Succinate does not significantly alter metabolite pool sizes in retinas, but it is anapleurotic in eyecups, acting to supplement fumarate and malate pools in eyecups ~3-fold relative to when glucose is the only fuel supplied (**Figure 4.1H**). Eyecup preparations were used for these experiments because removing the RPE (mechanically or enzymatically) from the eyecups can damage it and alter its metabolic features. Since eyecups contain multiple cell types (RPE, choroidal endothelial, and sclera) we repeated the flux analysis with cultured human fetal RPE (hfRPE) at 2 minutes to assess if RPE uses succinate. These fully differentiated RPE cells make twice as much citrate from succinate carbons (m4) as citrate from glucose carbons (m2) (**Figure 4.2D**). This suggests that RPE cells are at least one of the types of cells in RPE/choroid preparations that oxidizes succinate.

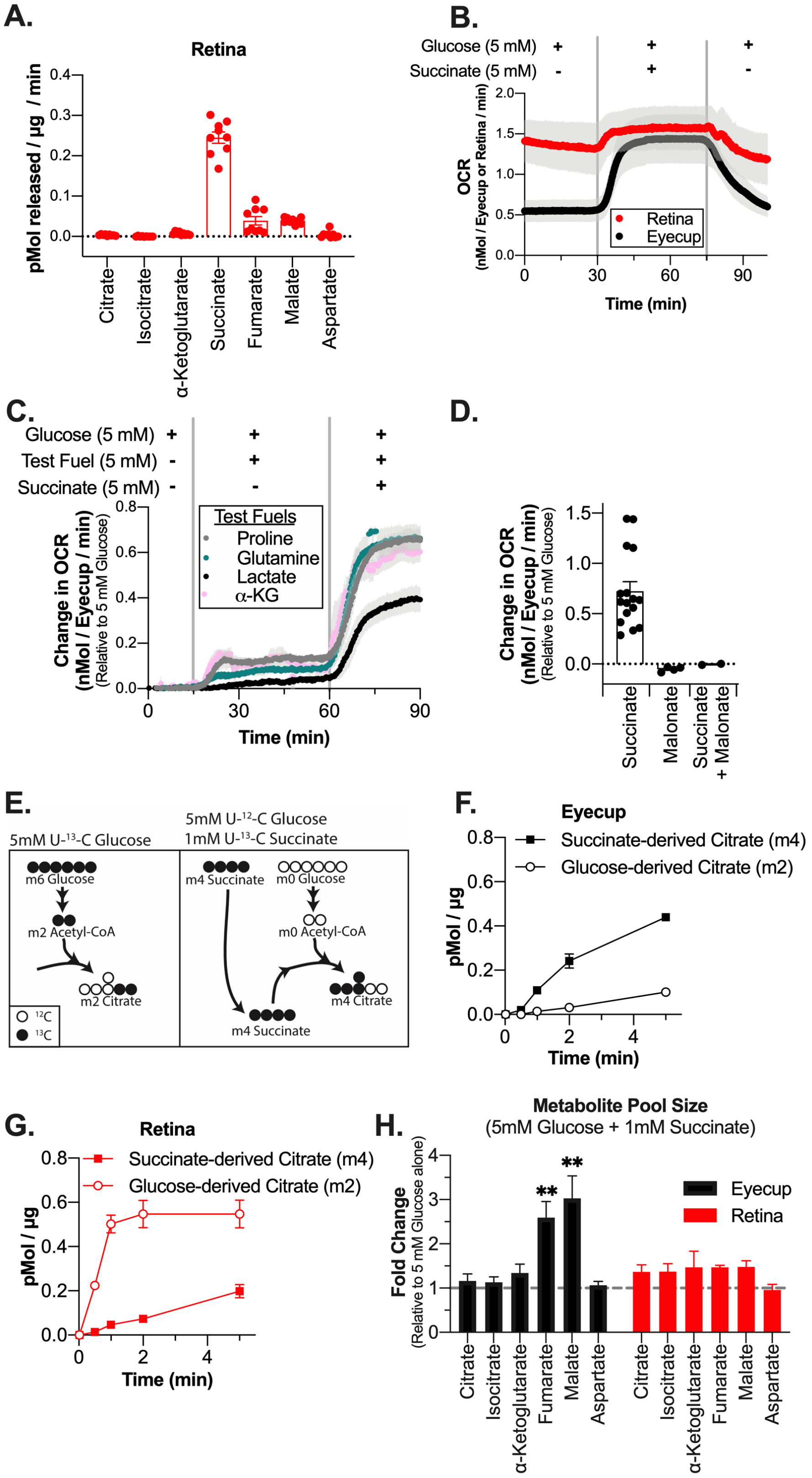

Figure 4.1: Retinas release succinate which can fuel O_2 consumption in eyecups

(Figure 4.1 continued)
(A) Rate of TCA cycle metabolite release by retinas incubated in 5 mM ^{12}C-glucose. Media samples were taken at 30, 60, and 90 minutes (n=9 retinas, 3 per time point). **(B)** O_2 consumption trace from retinas and eyecups perifused with media containing 5 mM glucose, then 5 mM glucose + 5 mM succinate, then 5 mM glucose. Vertical gray bars indicate the approximate time media containing the new metabolite condition reached tissue (n=4 retina and 4 eyecup chambers). **(C)** O_2 consumption trace of eyecups supplied with 5 mM glucose, then 5 mM glucose + 5 mM of a test metabolite, then 5 mM glucose + 5 mM test metabolite + 5 mM succinate. Test metabolites are proline (gray), glutamine (teal), lactate (black), and α-ketoglutarate (pink) (n=3 eyecup chambers per condition). **(D)** Change in OCR (relative to 5 mM glucose alone) for eyecups supplied with 5 mM glucose + 5 mM succinate, 5 mM glucose + 20 mM malonate, or 5 mM glucose + 20 mM malonate + 5 mM succinate (n=4 eyecup chambers for malonate and 2 eyecup chambers for malonate + succinate). **(E)** Labeling schematic showing isotopomers of citrate produced by either U-^{13}C-glucose alone (left panel) or ^{12}C-glucose + U-^{13}C-succinate (right panel). **(F)** Citrate production in eyecups supplied with either 5 mM U-^{13}C-glucose alone or 5 mM ^{12}C-glucose + 1 mM U-^{13}C-succinate (n=2 eyecups per time point). **(G)** Citrate production in retinas supplied with either 5 mM U-^{13}C-glucose alone or 5 mM ^{12}C-glucose + 1 mM U-^{13}C-succinate (n=2 retinas per time point). **(H)** Pool size of TCA cycle metabolites in eyecups and retinas supplied with 5 mM ^{12}C-glucose + 1 mM U-^{13}C-succinate for 10 minutes, relative to tissue supplied with 5 mM ^{12}C-glucose alone (n=2 retinas or eyecups).

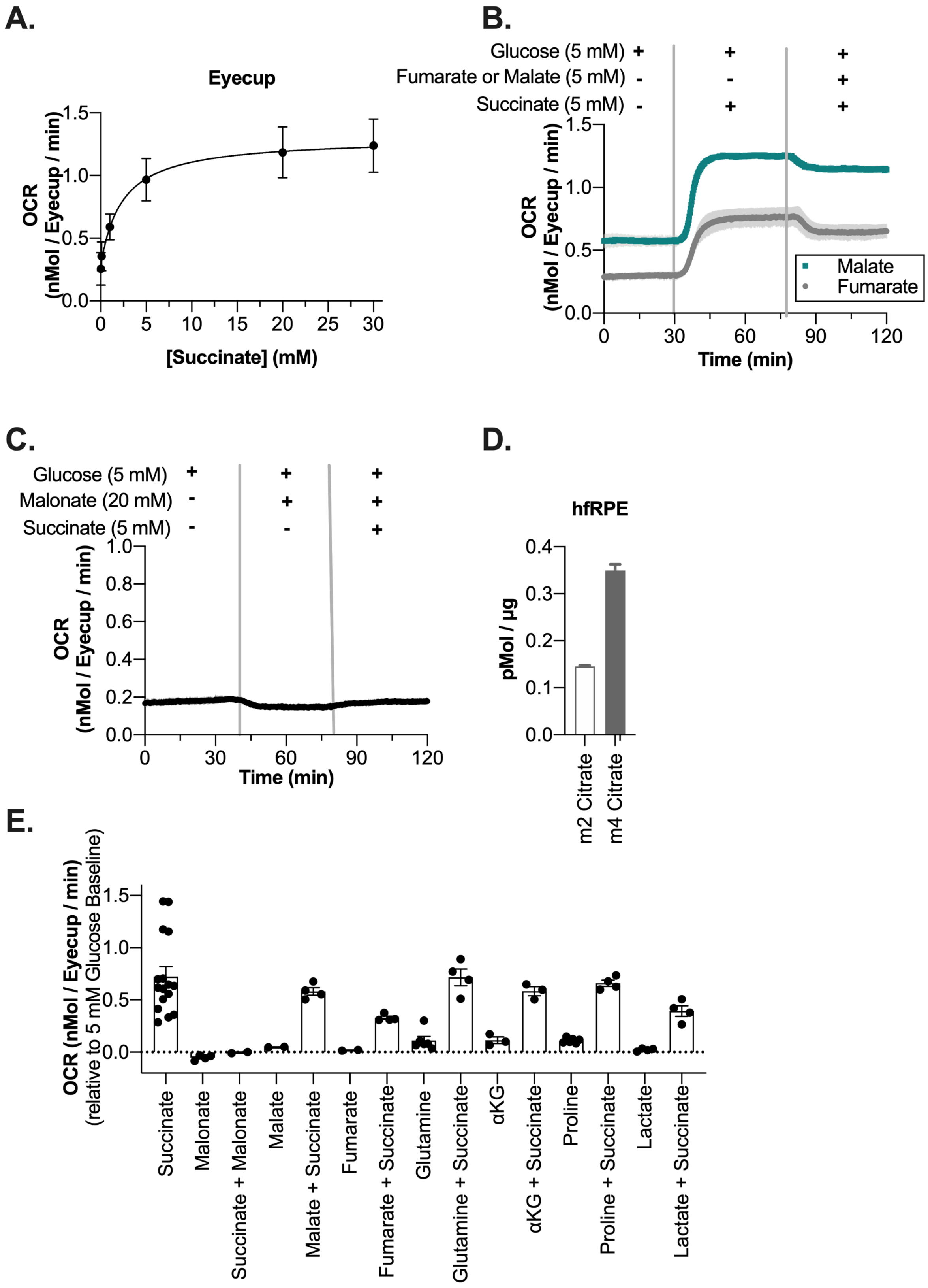

Figure 4.2: Additional metabolic data gathered in experiments conducted in Figure 4.1 *(1/3)*

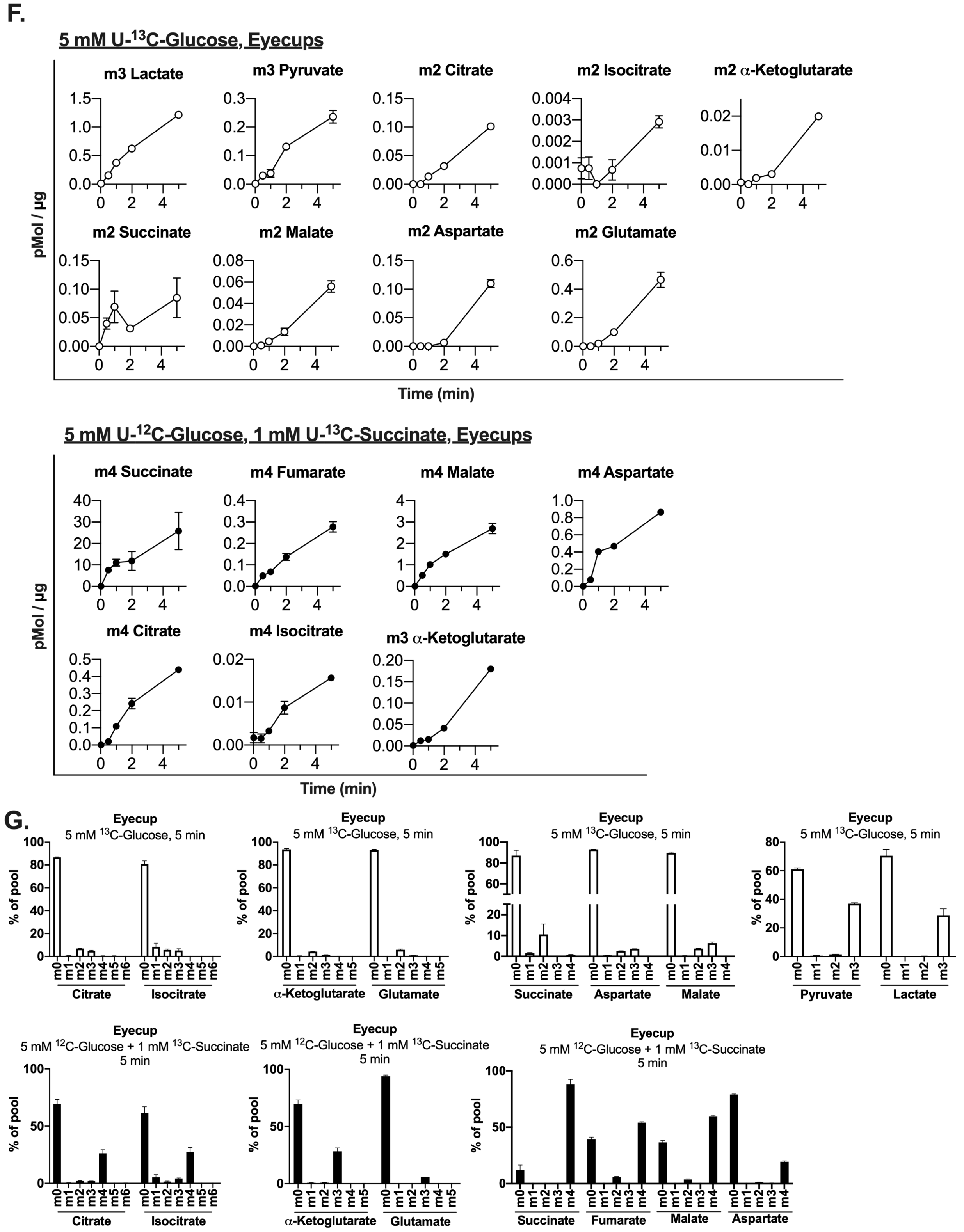

Figure 4.2: Additional metabolic data gathered in experiments conducted in Figure 4.1 ***(2/3)***

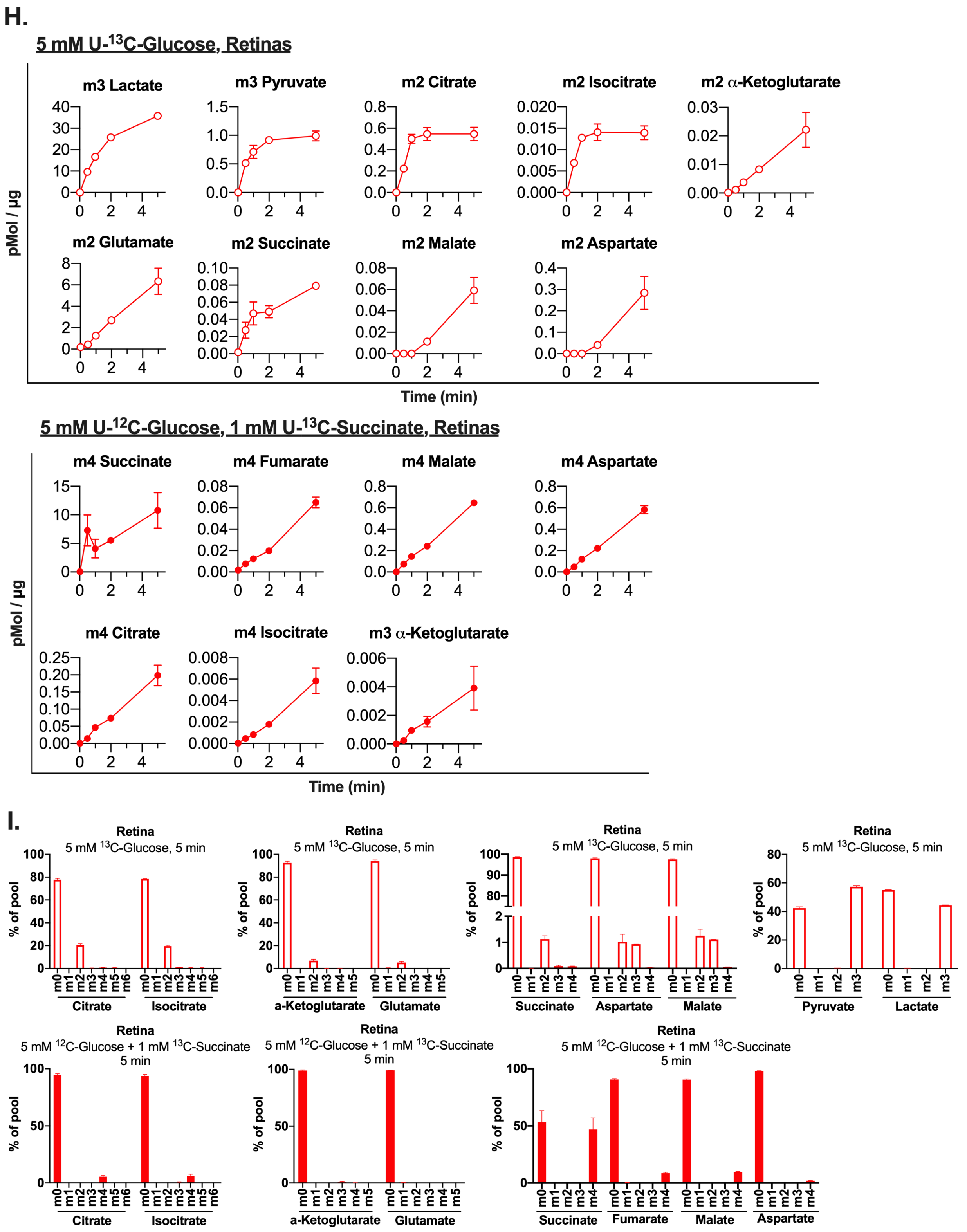

Figure 4.2: Additional metabolic data gathered in experiments conducted in Figure 4.1 *(3/3)*

Figure 4.2: Additional metabolic data gathered in experiments conducted in Figure 4.1
(A) Oxygen consumption of eyecup tissue perifused with 0, 0.1, 1, 5, 20, and 30 mM succinate in the presence of 5 mM glucose (n=3 chambers). **(B)** Oxygen consumption of eyecups perifused with media containing 5 mM glucose, then 5 mM glucose + 5 mM fumarate (gray) or malate (teal), then 5 mM glucose + 5 mM fumarate or malate + 5 mM succinate (n=2 chambers). **(C)** Raw trace of eyecups supplied with 5 mM glucose, then 5 mM glucose + 20 mM malonate, then 5 mM glucose + 20 mM malonate + 5 mM succinate. (n=2 chambers). **(D)** Citrate production in human fetal RPE (hfRPE) supplied with either 5 mM U-^{13}C-glucose alone (m2 Citrate) or 5 mM ^{12}C-glucose + 1 mM U-^{13}C-succinate (m4 Citrate) for 2 minutes (n=2 plates of cells). **(E)** Compiled change in OCR for eyecups supplied with various metabolites (relative to 5 mM glucose condition alone). All metabolites were supplied at 5 mM, with the exception of malonate which was supplied at 20 mM. All metabolites were supplied in the presence of 5 mM glucose. Succinate, malonate, and succinate + malonate conditions are duplicated from figure 1D for ease of comparison (each dot represents measurements taken from a single chamber). **(F)** Accumulation of labeled TCA cycle metabolites in eyecups supplied with 5 mM ^{12}C-glucose alone (top panel) or 5 mM ^{12}C-glucose + 1 mM U-^{13}C-succinate (bottom panel) (n=2 eyecups per time point). **(G)** Full isotopic distribution of metabolites in eyecups at the 5 minute time point from the experiments described in (F). **(H)** Accumulation of labeled TCA cycle metabolites in retinas supplied with 5 mM ^{12}C-glucose alone (top panel) or 5 mM ^{12}C-glucose + 1 mM U-^{13}C-succinate (bottom panel). Of note, equilibration of α-ketoglutarate with the large, unlabeled glutamate pool in retinas makes causes the specific activity of the ^{13}C tracer to drop for metabolites after and including α-ketoglutarate in retinas supplied with U-^{13}C-glucose (Du et al., 2013c) (n=2 retinas per time point). **(I)** Full isotopic distribution of metabolites in retinas at the 5 minute time point from the experiments described in (H).

Succinate enhances export of malate in eyecups

The findings in **Figure 4.1** show that retinas export succinate and that succinate fuels mitochondrial respiration in eyecups. We next tested the hypothesis that there is a reciprocal exchange of metabolites from the RPE/choroid to the retina. To determine if eyecups release a metabolite that retinas can use to enhance succinate production, we supplied eyecups with 5 mM ^{12}C-glucose and quantified the rate that TCA cycle metabolites are released into the medium. Eyecups release citrate, α-ketoglutarate, malate, and aspartate; but not succinate (**Figure 4.3A)**. Malate is the most abundant TCA cycle metabolite exported, released at a rate of 0.07 (± 0.03) pmol/µg/min. We then determined if succinate influences the export of any of these metabolites by supplying eyecups with U-^{13}C-succinate in addition to ^{12}C-glucose (**Figure 4.3B**). When we provide eyecups with 5 mM ^{12}C-glucose and 2 mM U-^{13}C-succinate for 60 and 90 minutes, export of both fumarate and malate is enhanced. Malate is exported at a rate of 3.2 (± 0.94) pmol/µg/min and fumarate is exported at a rate of 4.1 (± 1.1) pmol/µg/min. 93% (± 2%) of the total fumarate exported was m4 and 94% (± 2%) of the total malate exported was m4. (**Figure 4.3C**). Succinate present at 2 mM is consumed at a rate of 16.5 (± 6.6) pmol/µg/min, and of the succinate carbons consumed, approximately 43% (± 19%) are released as fumarate and malate.

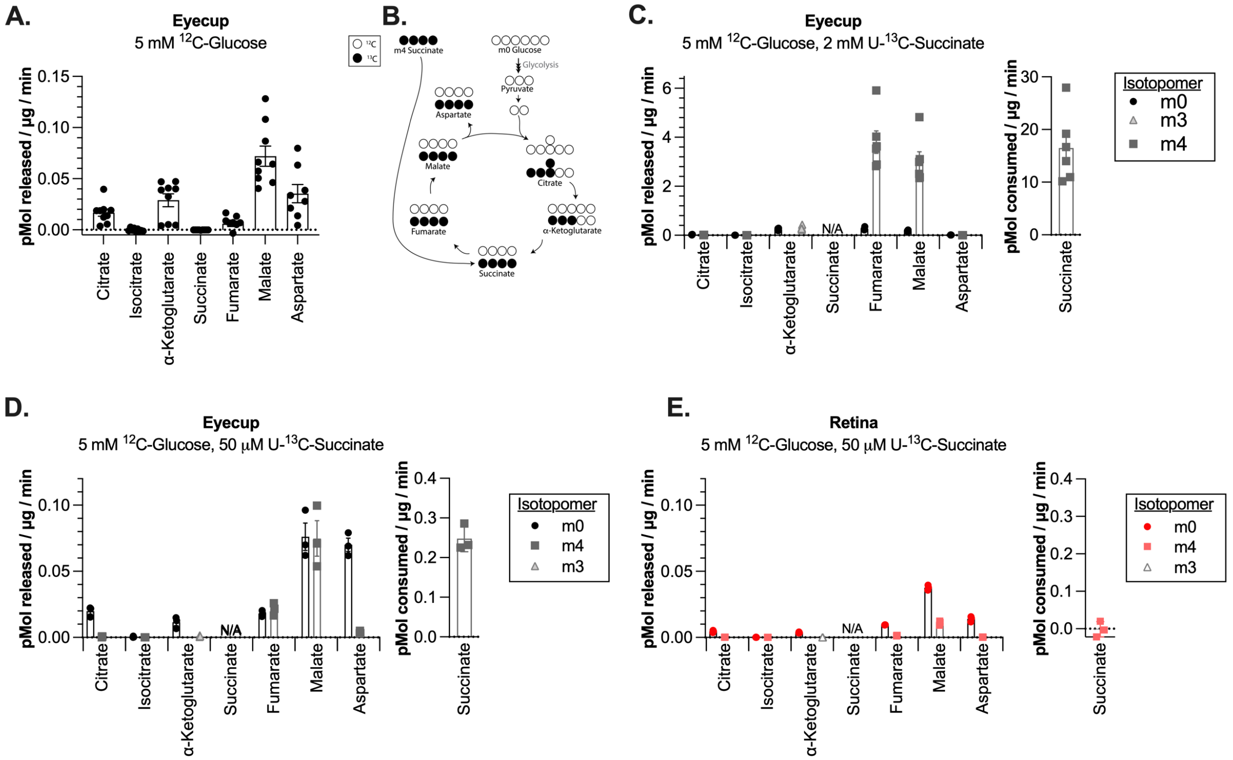

Figure 4.3: Succinate enhances export of malate in eyecups
(A) Rate of TCA cycle metabolite release by eyecups incubated in 5 mM ^{12}C-glucose. Media samples were taken at 30, 60, and 90 minutes (n=9 eyecups, 3 per time point). **(B)** Labeling schematic showing TCA cycle isotopomers produced by eyecups supplied with ^{12}C-glucose and U-^{13}C-succinate. For simplicity, only isotopomers originating from either metabolite produced in a single turn of the TCA cycle are shown. **(C)** Rate of TCA cycle metabolite release by eyecups incubated in 5 mM ^{12}C-glucose + 2 mM U-^{13}C-succinate for 60 and 90 minutes. The rate that succinate is consumed by eyecups during the incubation is shown on the right panel (n=6 eyecups, 3 per time point). **(D)** Rate of TCA cycle metabolite release by eyecups incubated in 5 mM ^{12}C-glucose + 50 µM U-^{13}C-succinate for 30 minutes. The rate that succinate is consumed by eyecups during the incubation is shown on the right panel (n=3 eyecups). **(E)** Rate of TCA cycle metabolite release by retinas incubated in 5 mM ^{12}C-glucose + 50 µM U-^{13}C-succinate for 30 minutes. The rate of succinate consumption by retinas during incubation is shown on the right panel (n=3 retinas).

Since the interface volume between the retina and RPE in a living eye is unknown, we cannot determine the concentration of succinate that RPE cells in an eye might receive from the retina. Plasma succinate in humans has been measured in the low micromolar range, so we also performed this experiment with a much lower concentration of succinate (Kushnir et al., 2001). When eyecups are supplied with 5 mM ^{12}C-glucose and 50 µM U-^{13}C-succinate for 30 minutes, malate is exported at a rate of 0.15 (± 0.04) pmol/µg/min and fumarate is exported at a rate of 0.04 (± 0.01) pmol/µg/min. 54% (± 3%) of the total fumarate exported was m4 and 49% (± 2%) of the total malate exported was m4. (**Figure 4.3D**). The roughly equivalent amounts of m4 (produced from succinate) and m0 (produced from glucose) exported metabolites is remarkable, given that succinate was available at a 100-fold lower concentration than glucose in this experiment. Succinate present at 50 µM is consumed by eyecups at a rate of 0.25 (± 0.03) pmol/µg/min. Similar to high succinate exposure, 39% (± 11%) of the succinate carbons consumed are released as fumarate and malate. Incubating retinas in 5 mM ^{12}C-glucose and 50 µM U-^{13}C-succinate for 30 minutes does not similarly enhance fumarate and malate export, and retinas do not measurably deplete succinate from the incubation media (**Figure 4.3E).**

Retinas can use malate to produce succinate via reverse electron transport at SDH

Succinate enhances the export of malate and fumarate from the RPE/choroid complex (**Figure 4.3**). We next tested whether malate exported by eyecups can influence retinal metabolism. Retinas in an eye are in a hypoxic environment, and hypoxic tissues can produce succinate by both canonical oxidative TCA cycle activity as well as through reverse electron transport at SDH (Chouchani et al., 2014; Linsenmeier and Zhang, 2017; Yu and Cringle, 2006; Zhang et al., 2018). Since retinas export succinate (**Figure 4.1**), they require an anaplerotic source of metabolites, to avoid running out of TCA cycle intermediates. Based on this premise, we tested if retinas might use malate for anaplerosis to sustain succinate synthesis by reverse electron transport at SDH.

We used U-^{13}C-malate to quantify reverse electron transport at SDH in both retinas and eyecups (**Figure 4.4A**). We incubated retinas and eyecups for 5 minutes in U-^{13}C-malate at a range of concentrations (5, 50, and 500 μM), all in the presence of 5 mM ^{12}C-glucose. At all concentrations, retinas form much more m4 succinate than eyecups (**Figure 4.4B**). None of these concentrations of malate increase the size of the fumarate pool in retinas (**Figure 4.4C**). This shows that the formation of m4 succinate we observe in retinas is due to a property that is inherent to retinas and is not driven simply by an increase in concentration of the reactant of the reverse SDH reaction (fumarate). Total levels of other metabolites are reported in **Figure 4.5A.** To test if the m4 succinate we observe is formed by the reverse activity of SDH or by an alternative metabolic pathway, we incubated retinas with 5 mM ^{12}C-glucose, 50 μM U-^{13}C-malate, and 20 mM of the SDH inhibitor malonate. Retinas still produce m4 fumarate but are unable to form m4 succinate when in the presence of malonate, indicating that reversal of SDH is the pathway of m4 succinate formation (**Figure 4.4D,** other m4 metabolites shown in **Figure 4.5B**). To further validate SDH as the site of m4 succinate production, we tested another SDH inhibitor, Atpenin A5 (Miyadera et al., 2003). 2 μM Atpenin A5 also inhibits the formation of m4 succinate in retinas incubated with 5 mM ^{12}C-glucose and 50 μM U-^{13}C-malate (**Figure 5.4C**). However, we observed that incubating retinas in the same concentration of vehicle alone (0.2% DMSO) for 5 minutes causes a dramatic drop in total fumarate levels and a slight drop in total citrate and isocitrate levels compared to retinas without DMSO (**Figure 4.5D**). These unexpected changes in retinal metabolism due to DMSO led us to rely on malonate as an SDH inhibitor for our remaining experiments, as it is water soluble.

Retinas are composed of several types of neurons, so we next investigated if a specific cell type in the retina favors reverse SDH activity. Photoreceptors are the neurons in the lowest pO_2 layer of the mouse retina and their outer segments are in direct contact with the RPE in an intact eye, so they are a candidate site of reverse SDH activity. To determine if photoreceptors favor reverse SDH activity, we used retinas from *Aipl1*$^{-/-}$ mice, a genetic model of Leber's Congenital Amaurosis wherein photoreceptors degenerate before the first month of life is complete (Ramamurthy et al., 2004). We incubated *Aipl1*$^{-/-}$ retinas with 5 mM ^{12}C-glucose and 50 µM U-^{13}C-malate for 5 minutes. *Aipl1*$^{-/-}$ retinas produce equivalent amounts of m4 fumarate but less than half as much m4 succinate as WT retinas per µg of protein (**Figure 4.4E,** other m4 metabolites shown **Figure 4.5E**). This indicates that the contribution of photoreceptors to reverse SDH activity is greater than that of the inner retina.

We next determined if succinate released by retinas might be in some part produced by reverse SDH activity. We incubated retinas in 5 mM ^{12}C-glucose and 500 µM U-^{13}C-malate for 60 and 90 minutes and calculated the rate of metabolites exported in that time (**Figure 4.5F**). We found that retinas export both m4 fumarate and m4 succinate, indicating that succinate produced via reverse SDH activity is exported from retinas. Succinate is exported at a rate of 0.47 (± 0.04) pmol/µg/min, and 29% (±5%) of the succinate exported was found to be m4. Since it is impossible to determine what concentration of malate a retina might receive from the RPE in an intact eye, we also tested if retinas would export succinate when incubated in lower concentration of malate by incubating retinas in 5 mM ^{12}C-glucose and 50 µM U-^{13}C-malate for 30 minutes and measuring metabolites released into the incubation media (**Figure 4.5G**). Retinas also export both m4 fumarate and m4 succinate when incubated in 50 µM U-^{13}C-malate. Succinate is exported at a rate of 0.21 (± 0.02) pmol/µg/min, and 5% (±0.04%) of the succinate exported was found to be m4. The approximately 10-fold decrease in the fractional enrichment of m4 succinate exported from retinas supplied with 50 µM U-^{13}C-malate vs. 500 µM U-^{13}C-malate corresponds with the 10-fold decrease in U-^{13}C-malate we supplied the retinas in this experiment.

We also tested if photoreceptors are a specific cell type in the retina which releases succinate by incubating WT and *Aipl1*$^{-/-}$ retinas in 5 mM ^{12}C-glucose and 50 µM U-^{12}C-malate for 30 minutes and measuring exported TCA cycle metabolites (**Figure 4.5H**). We found that retinas lacking photoreceptors release less succinate and more fumarate per µg of protein. This indicates that while photoreceptors are not the only retinal cell type which releases succinate, they are a major contributor as they release more succinate per µg of cellular protein compared to the inner retina.

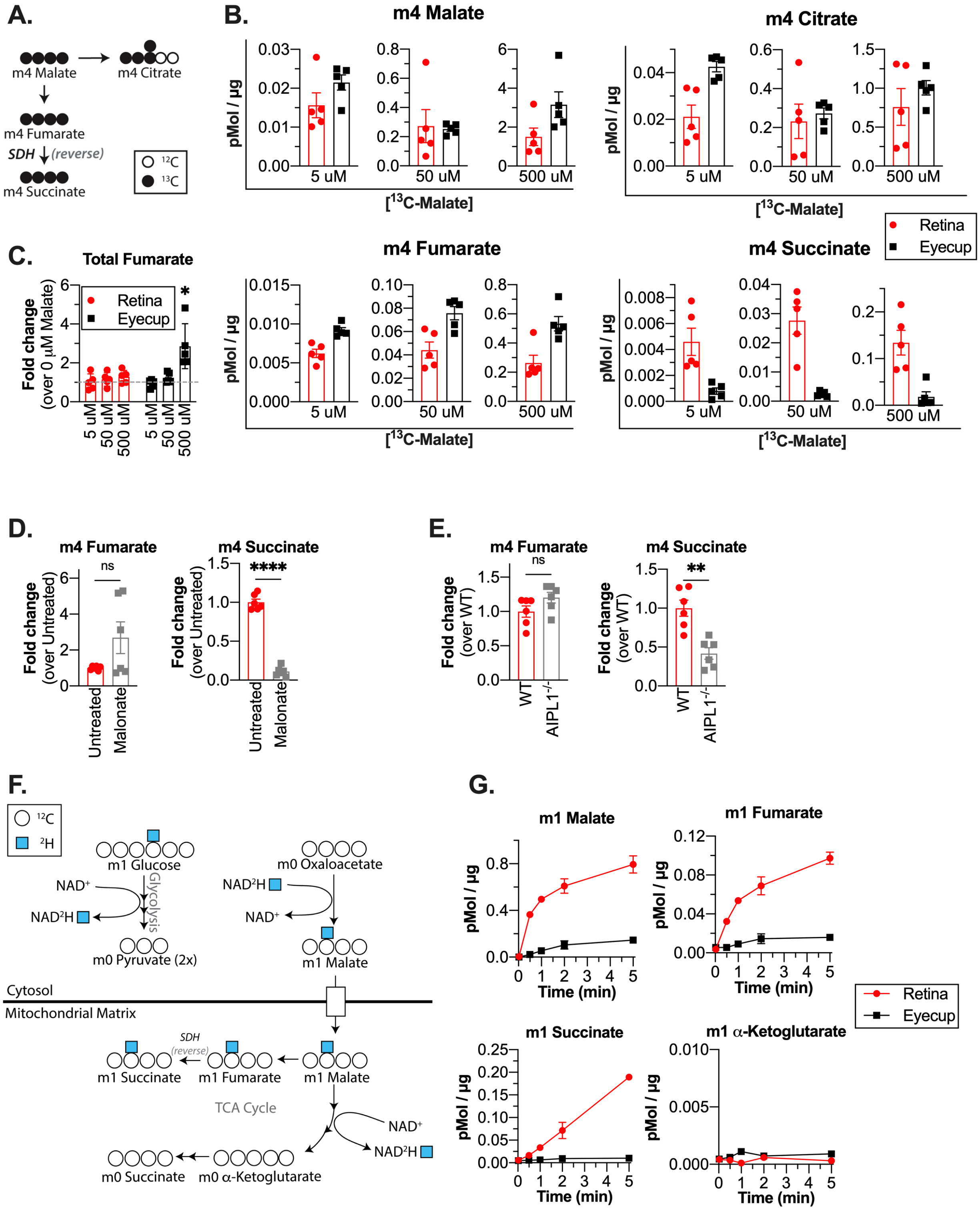

Figure 4.4: Retinas can use malate to produce succinate via reverse electron transport at SDH (A) Labeling schematic showing isotopomers of TCA cycle metabolites produced by tissue incubated in U-^{13}C-malate + ^{12}C-glucose. **(B)** Isotopomers produced by retinas and eyecups incubated in 5 mM

(Figure 4.4 continued)
^{12}C-glucose and 5, 50, or 500 µM U-^{13}C-malate for 5 minutes (n=5 retinas or eyecups per concentration). **(C)** Total fumarate levels in retinas and eyecups incubated in 5 mM ^{12}C-glucose and 5, 50, or 500 µM U-^{13}C-malate for 5 minutes (n=5 retinas or eyecups per concentration). **(D)** m4 fumarate and m4 succinate in retinas supplied with 5 mM ^{12}C-glucose and 50 µM U-^{13}C-malate + 20 mM malonate for 5 minutes (n=6 retinas). **(E)** m4 fumarate and m4 succinate in WT and AIPL1$^{-/-}$ retinas supplied with 5 mM ^{12}C-glucose + 50 µM U-^{13}C-malate for 5 minutes (n=6 retinas). **(F)** Labeling schematic showing isotopomers produced by 4-^{2}H-glucose. **(G)** Accumulation of deuterated (m1) malate, fumarate, succinate α-ketoglutarate in retinas and eyecups incubated in 5 mM 4-^{2}H-glucose for 0.02, 0.5, 1, 2, and 5 minutes (n=2 retinas per time point).

When supplying U-^{13}C-malate to eyecups, we observed that sufficient concentrations (500 µM) of U-^{13}C-malate can increase the total amount of fumarate and drive SDH to operate in reverse, consistent with Le Chatelier’s principle (**Figure 4.4B** and **4.4C**). To confirm that the reverse SDH activity we observe in the retina is due to a characteristic inherent to them and not one we are artificially driving, we sought to also measure reverse SDH activity in a manner that does not perturb the size of the fumarate pool, i.e. in the presence of glucose alone. We used 4-^{2}H-glucose to track reverse electron transport in the absence of added mitochondrial fuels. When cells metabolize 4-^{2}H-glucose, the deuterium is transferred from the carbon skeleton to NAD^{+} during the GAPDH reaction in glycolysis, producing deuterated NADH (NAD^{2}H) (**Figure 4.4F)** (Lewis et al., 2014). This NAD^{2}H then can be used in cytosolic reactions, including reduction of oxaloacetate to malate. Deuterated malate then can enter mitochondria. Since the fumarase reaction is readily reversible, deuterated malate will equilibrate with the fumarate pool. In the case of reverse SDH activity, deuterated fumarate will be converted to deuterated succinate. We incubated retinas and eyecups in 5 mM 4-^{2}H-glucose for times ranging from 0 to 5 min and observed steady accumulation of m1 (deuterated) succinate in retinas but not in eyecups **(Figure 4.4G)**. This further indicates that retinas but not eyecups perform reverse SDH activity. To ensure that the deuterated succinate we observe is produced solely from reverse SDH activity, we confirmed that the deuterium was transferred off of the carbon skeleton during oxidative TCA cycle activity prior to the formation of α-ketoglutarate (**Figure 4.4G**).

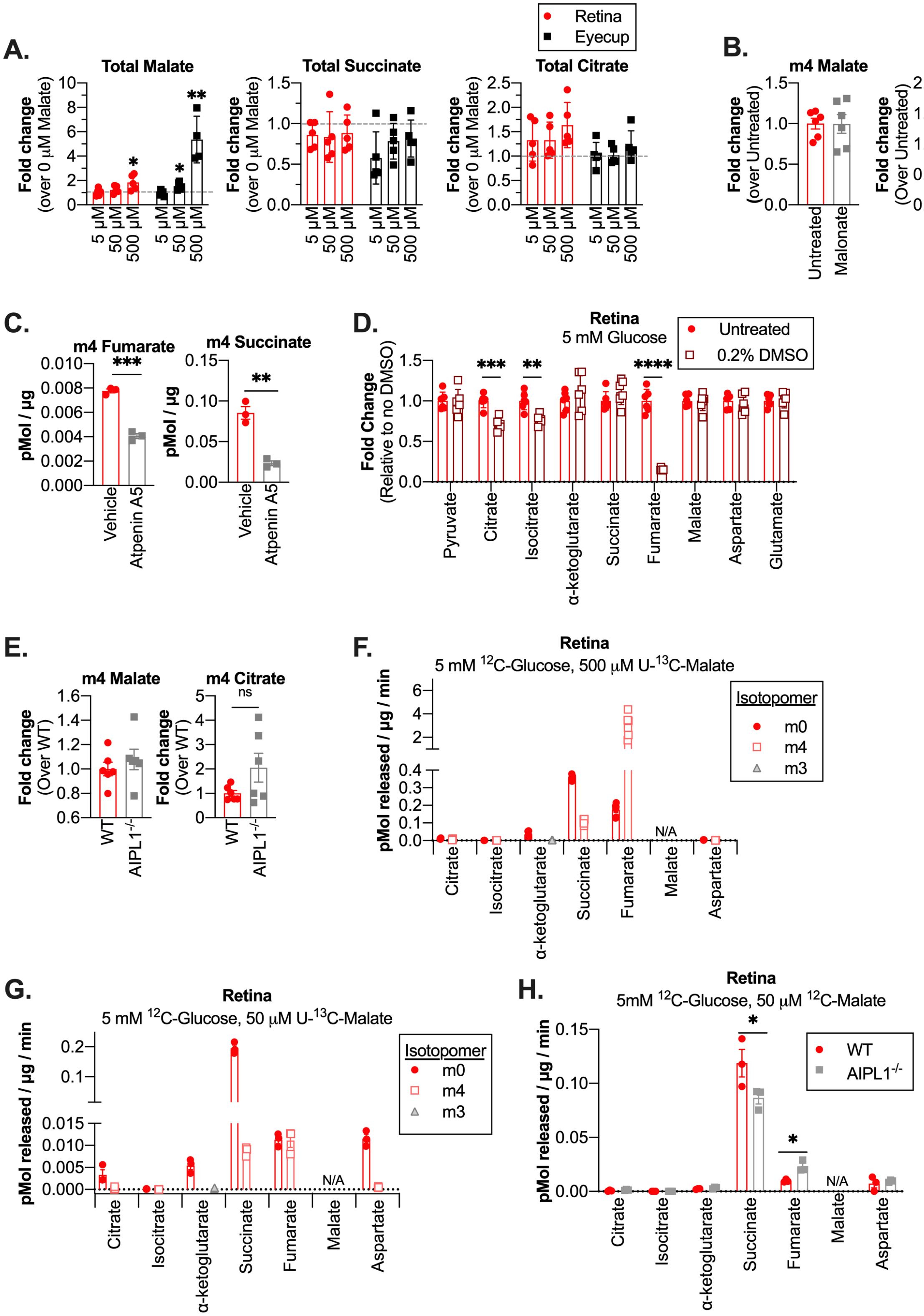

Figure 4.5: Additional experiments characterizing reversal of SDH in retinas
(A) Total malate, succinate, and citrate levels in retinas and eyecups incubated in 5 mM ^{12}C-glucose and 5, 50, or 500 μM U-^{13}C-malate for 5 minutes (n=5 retinas or eyecups per concentration).

(Figure 4.5 continued)
(B) m4 malate and m4 citrate levels in retinas incubated in 5 mM ^{12}C-glucose + 50 µM U-^{13}C-malate in the presence or absence of malonate for 5 minutes (relative to untreated) (n=6 retinas). **(C)** m4 fumarate and m4 succinate levels in retinas incubated in 5 mM ^{12}C-glucose + 50 µM U-^{13}C-malate and either 2 µM Atpenin A5 or vehicle (0.2% DMSO) for 5 minutes (n=3 retinas). **(D)** Total metabolite levels in retinas incubated in 5 mM ^{12}C-glucose in the presence or absence of 0.2% DMSO for 5 minutes (n=6 retinas). **(E)** m4 malate and m4 citrate produced by WT and AIPL1$^{-/-}$ retinas supplied with 5 mM ^{12}C-glucose + 50 µM U-^{13}C-malate for 5 minutes (n=6 retinas). **(F)** Rate of TCA cycle metabolite release by retinas incubated in 5 mM ^{12}C-glucose + 500 µM U-^{13}C-malate for 60 and 90 minutes (n=6 retinas, 3 per time point). **(G)** Rate of TCA cycle metabolite release by retinas incubated in 5 mM ^{12}C-glucose + 50 µM U-^{13}C-malate for 30 minutes (n=3 retinas). **(H)** Rate of TCA cycle metabolite release by WT and AIPL1$^{-/-}$ retinas incubated in 5 mM ^{12}C-glucose + 50 µM ^{12}C-malate for 30 minutes (n=3 retinas).

Reverse SDH activity maintains a significant portion of the succinate pool in retinas

It has been estimated that reverse SDH activity produces only about ~6% of succinate during ischemia in the heart (Zhang et al., 2018). To determine whether reverse SDH activity produces significant amounts of succinate in the retina, we quantified the contributions of reverse SDH activity and oxidative (canonical forward) TCA cycle activity to the retinal succinate pool.

To compare the different modes of succinate production under the same conditions, we used U-^{13}C-glucose to track oxidative TCA cycle activity and 4-^{2}H-glucose to track reverse SDH activity. To assess the contribution of oxidative TCA cycle activity to succinate production, we incubated retinas in 5 mM U-^{13}C-glucose from 0 to 60 minutes and determined the fractional enrichment of m2 succinate at the steady-state by fitting a curve assuming a first order reaction (**Figure 4.6A**). At the steady-state, 6.9% of the succinate pool is m2 in retinas. However, this does not mean that only 6.9% of the succinate pool is maintained by oxidative TCA cycle activity, since its oxidative precursor α-ketoglutarate is only 22.8% m2-labeled at the steady-state. In order to account for incomplete m2 labeling of the α-ketoglutarate pool, we scaled these values to determine what the fractional enrichment of m2 succinate would be if 100% of the α-ketoglutarate pool were m2 ($\frac{6.9\%\ m2\ succinate}{22.8\%\ m2\ \alpha\text{−}ketoglutarate} = \frac{30.4\%\ m2\ succinate}{100\%\ m2\ \alpha\text{−}ketoglutarate}$). This calculation predicts that the fraction of the succinate pool that is formed from α-ketoglutarate (via oxidative TCA cycle activity) is 30.4%.

To directly measure the contribution of reverse SDH activity to succinate production when glucose is the only fuel source available, we repeated this experiment using 4-^{2}H-glucose. At the steady-state, the fractional enrichment of m1 fumarate is 18.2% and m1 succinate is 10.2% (**Figure 4.6B**). Scaling these values for 100% m1 labeling of the fumarate pool predicts that reverse SDH activity maintains 55.8% of the succinate pool. m1 α-ketoglutarate is not detected at any time, indicating that m1 succinate does not form by oxidative TCA cycle activity (**Figure 4.7A**). To further confirm that reversal of SDH is responsible for producing all of the m1 succinate observed at the steady-state, we incubated retinas in 5 mM 4-^{2}H-glucose in the presence of malonate for 5 and 30 minutes (**Figure 4.7B)**. Malonate inhibits the formation of m1 succinate in retinas supplied with 4-^{2}H-glucose at both time points, indicating that reversal of SDH is the pathway of m1 succinate formation. To further validate the use of 4-^{2}H-glucose as a tracer that will lead to production of m1 succinate only through reverse SDH activity and not another pathway even after 60 minutes, we performed an identical time course using eyecups (which do not perform reverse SDH activity). If an alternative metabolic pathway were responsible for producing m1 succinate, we might expect to see some accumulate in eyecups; however, m1 succinate is not observed in eyecups even after 60 minutes in 5 mM 4-^{2}H-glucose (**Figure 4.7C**).

We also determined the fraction of the retinal succinate pool that is maintained by reverse SDH activity from exogenous malate. We incubated retinas in 50 μM U-^{13}C-malate and 5 mM ^{12}C glucose for times ranging from 0 to 60 minutes (**Figure 4.6C**). The steady-state fractional enrichment was calculated as 15.3% for m4 fumarate and 5.7% for m4 succinate. Scaling these values for 100% m4 labeling of the fumarate pool predicts that 37.2% of the succinate pool is maintained from exogenous malate. This value is lower than the fraction of the succinate pool maintained by reverse SDH activity when glucose is the only fuel. Since the retina contains many cell types, a possible explanation for this difference is that there is a population of cells in the retina that consumes malate (producing m4 fumarate) but does not produce m4 succinate.

In summary, our analysis in retinas supplied with glucose alone (i.e. under identical conditions) predicts that 30.4% of retinal succinate is maintained by oxidative TCA cycle activity and 55.8% is maintained by reverse SDH activity (**Figure 4.6D**). All steady-state fractional enrichment values and reaction constants with confidence intervals are reported in **Figure 4.7I**. Fractional enrichment of all isotopomers for relevant metabolites at 60 minutes are reported in **Figures 4.7D, 4.7E**, and **4.7F**. Total levels of relevant metabolites for each time point are reported in **Figures 4.7G** and **4.7H**.

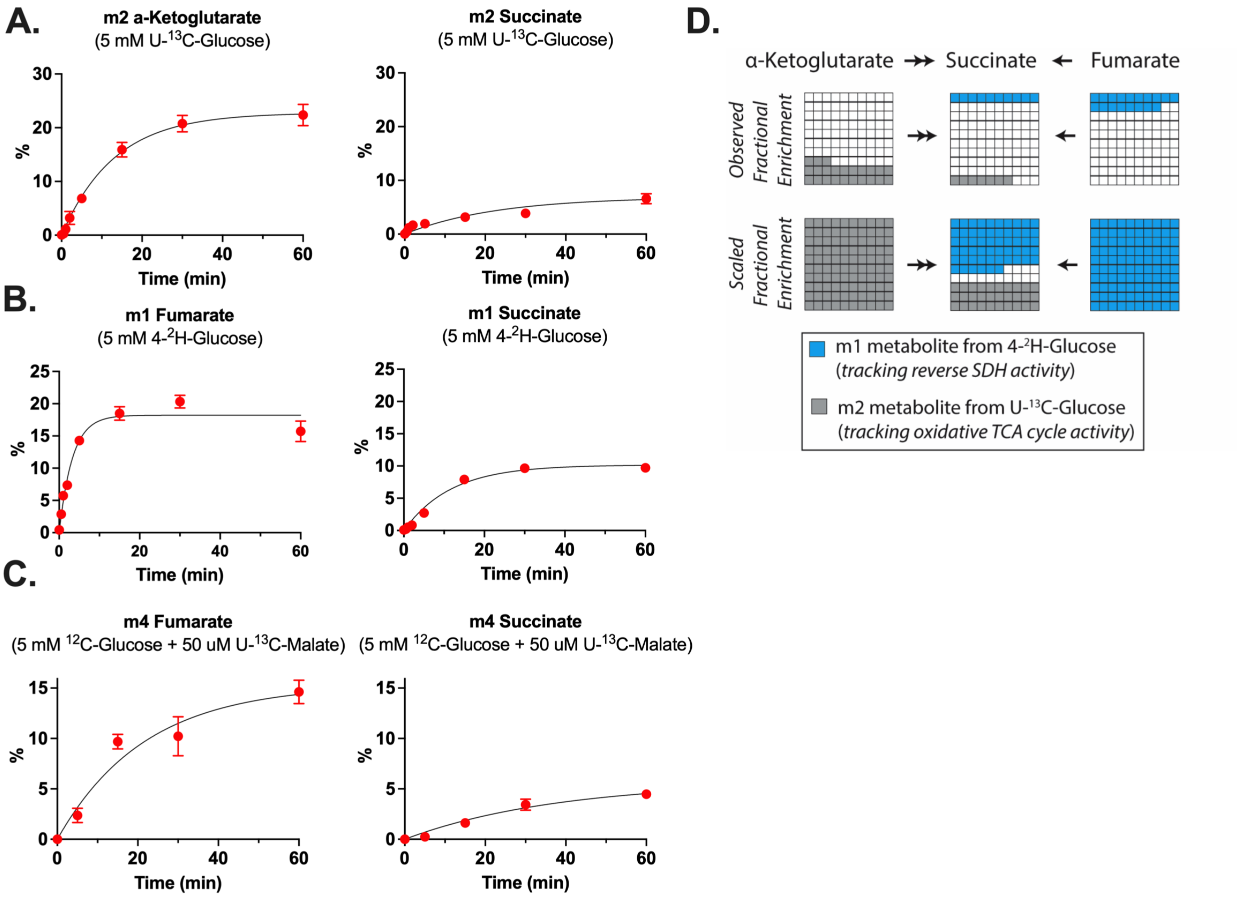

Figure 4.6: Reverse SDH activity maintains a significant portion of the succinate pool in retinas **(A)** Fractional enrichment of m2 α-ketoglutarate and m2 succinate in retinas supplied with 5 mM U-^{13}C-glucose for 0.02, 0.5, 1, 2, 5, 15, 30, and 60 minutes (n=3 to 7 retinas per time point). **(B)** Fractional enrichment of m1 fumarate and m1 succinate in retinas supplied with 5 mM 4-^{2}H-glucose for 0.02, 0.5, 1, 2, 5, 15, 30, and 60 minutes (n=3 retinas per time point). **(C)** Fractional enrichment of m4 fumarate and m4 succinate in retinas supplied with 5 mM ^{12}C-glucose + 50 μM U-^{13}C-malate for 0.02, 5, 15, 30, and 60 minutes (n=3 to 5 retinas per time point). **(D)** Graphical description of observed (top panel) and maximal (bottom panel) contributions of oxidative TCA cycle activity and reverse SDH activity to maintaining the retinal succinate pool.

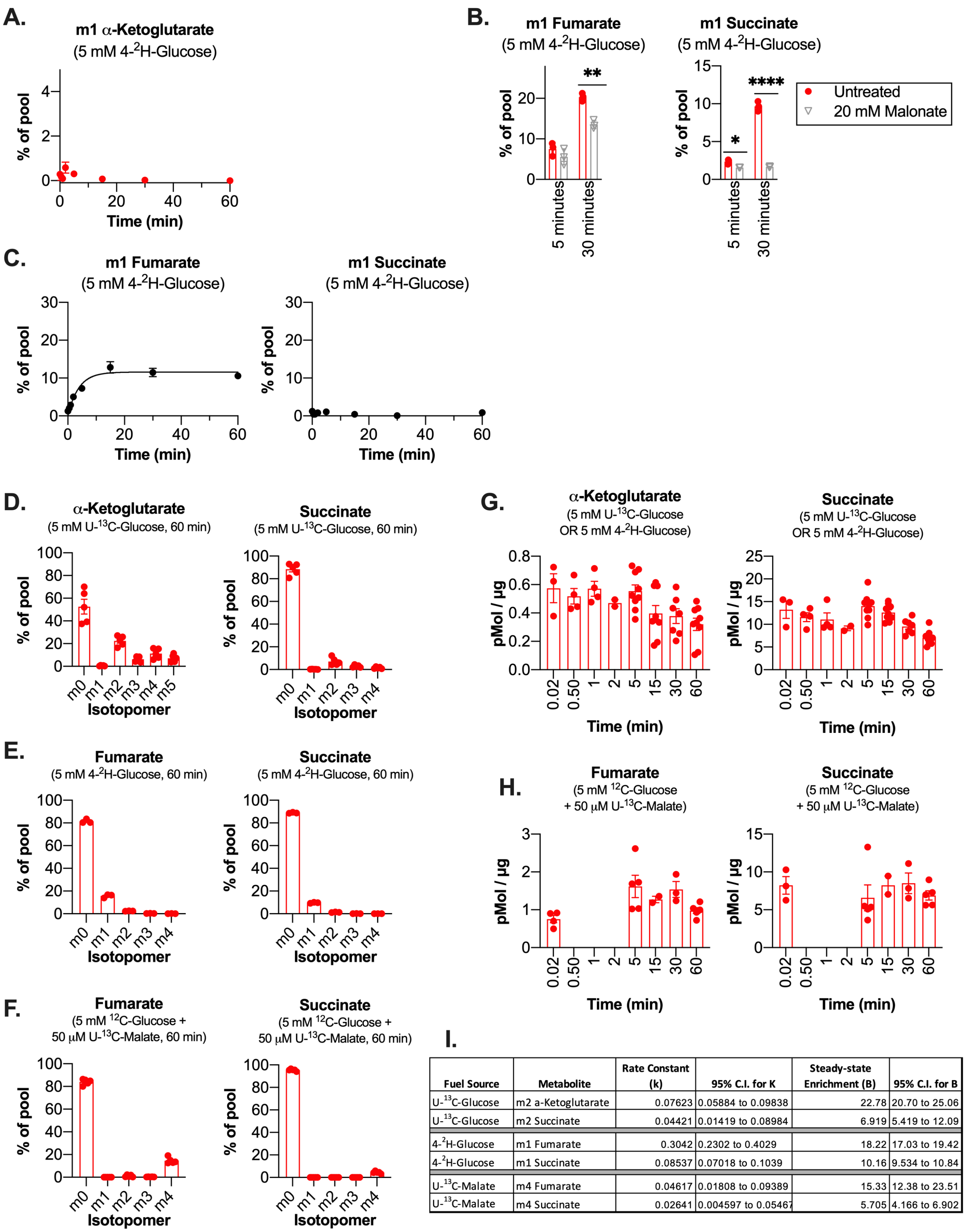

Fuel Source	Metabolite	Rate Constant (k)	95% C.I. for K	Steady-state Enrichment (B)	95% C.I. for B
U-^{13}C-Glucose	m2 a-Ketoglutarate	0.07623	0.05884 to 0.09838	22.78	20.70 to 25.06
U-^{13}C-Glucose	m2 Succinate	0.04421	0.01419 to 0.08984	6.919	5.419 to 12.09
4-^{2}H-Glucose	m1 Fumarate	0.3042	0.2302 to 0.4029	18.22	17.03 to 19.42
4-^{2}H-Glucose	m1 Succinate	0.08537	0.07018 to 0.1039	10.16	9.534 to 10.84
U-^{13}C-Malate	m4 Fumarate	0.04617	0.01808 to 0.09389	15.33	12.38 to 23.51
U-^{13}C-Malate	m4 Succinate	0.02641	0.004597 to 0.05467	5.705	4.166 to 6.902

Figure 4.7: Full metabolite information from quantification of SDH reversal

Figure 4.7: Full metabolite information from quantification of SDH reversal
(A) m1 α-ketoglutarate signal from retinas supplied with 5 mM 4-^{2}H-glucose for 0.02, 0.5, 1, 2, 5, 15, 30, and 60 minutes (n=3 retinas per time point). **(B)** % enrichment of m1 fumarate and m1 succinate in retinas incubated in 5 mM 4-^{2}H-glucose for 5 and 30 minutes, in the presence or absence of 20 mM malonate (n=3 retinas per time point). **(C)** % enrichment of m1 fumarate and m1 succinate in eyecups incubated in 5 mM 4-^{2}H-glucose for 0.02, 0.5, 1, 2, 5, 15, 30, and 60 minutes (n=3 eyecups per time point). **(D)** Fractional enrichment for all isotopomers of α-ketoglutarate and succinate in retinas supplied with 5 mM U-^{13}C-glucose for 60 minutes (n=5 retinas). **(E)** Fractional enrichment for all isotopomers of fumarate and succinate in retinas supplied with 5 mM 4-^{2}H-glucose for 60 minutes (n=3 retinas). **(F)** Fractional enrichment for all isotopomers of fumarate and succinate in retinas supplied with 5 mM ^{12}C-glucose + 50 μM U-^{13}C-malate for 60 minutes (n=5 retinas). **(G)** Total succinate and α-ketoglutarate levels in retinas supplied with 5 mM glucose for 0.02, 0.5, 1, 2, 5, 15, 30, and 60 minutes (n=3 to 9 retinas per time point). **(H)** Total fumarate and succinate levels in retinas supplied with 5 mM glucose + 50 μM malate for 0.02, 0.5, 1, 2, 5, 15, 30, and 60 minutes (n=3 to 5 retinas per timepoint). **(I)** Table of constants and confidence intervals calculated by Graphpad Prism using the equation $\%metabolite = B * (1 - e^{-kt})$ to fit each curve. B is the fractional enrichment at the steady state, k is the rate constant for the reaction, t is time, and %metabolite is the fractional enrichment at a given time.

Low COXIV expression drives reversal of SDH in retinas

Figures 4.4 and **4.6** show that reverse electron transport at SDH is a predominant pathway for succinate generation in retinas and not in eyecups. Initially, we hypothesized that retinas utilize fumarate as an electron acceptor because they exist in a hypoxic niche in the eye and O_2 is limiting. However, we observe in **Figures 4.4** and **4.6** that fumarate may be converted to succinate even in retinal explants assayed at 21% O_2. This suggests that lack of O_2 alone does not directly drive reversal of SDH in the retina. Instead, chronic low O_2 in the retina may drive a molecular adaptation which leads to reversal of SDH and persists at 21% O_2. Since electrons from QH_2 can reduce either O_2 via complex IV or fumarate via SDH, we hypothesized that low O_2 in retinal mitochondria might suppress complex IV expression, thus leading to an accumulation of QH_2 that can drive reversal of SDH even during normoxia.

We evaluated expression of ETC component protein levels in retinal and eyecup homogenates by immunoblotting with antibodies that recognize representative subunits of the ETC complexes (**Figure 4.8A**). We found that freshly dissected retinas have a lower ratio of COXIV (a component of complex IV) to ATP5A (a component of ATP synthase) compared to eyecups (**Figure 4.8A**, lanes labeled “Fresh”). Hypoxia can decrease COXIV protein levels (Fukuda et al., 2007; Vijayasarathy et al., 2003). This motivated us to evaluate the influence of O_2 levels on COXIV expression in retinas and eyecups. We incubated retinas at 0%, 1%, 5%, 21% and 95% O_2 for 2 hours in 5 mM glucose and then analyzed ETC component expression by immunoblotting. The low COXIV/ATP5A ratio in freshly dissected retinas is similar to the ratio in retinas cultured in 0% O_2. Increasing pO_2 leads to a higher COXIV/ATP5A ratio in retinas. **Figure 4.8A** shows a representative immunoblot**,** and quantification of multiple independent experiments is shown in **Figure 4.8B**. Altering pO_2 does not have a substantial effect on the COXIV/ATP5A ratio in eyecups. These results indicate that the hypoxic niche retinas reside in could suppress COXIV expression and thus complex IV activity.

Based on these observations, we hypothesized that raising COXIV expression by pre-incubating retinas with higher O_2 levels would diminish the conversion of fumarate to succinate. To test this, we preconditioned retinas and eyecups for 2 hours in pre-equilibrated media containing 5 mM ^{12}C-glucose at 0%, 1%, 5%, 21% and 95% O_2. After 2 hours, reverse SDH activity was assessed by transferring retinas into fresh media containing 5 mM ^{12}C-glucose and 50 μM U-^{13}C-malate and incubating at the same pO_2 as before for 5 minutes. Retinas incubated at increasing pO_2 exhibit less reverse SDH activity, as measured by both m4 succinate production and by the m4 succinate/m4 fumarate ratio (**Figure 4.8C**) However, we also noted that pre-equilibration for 2h (at any pO_2) drastically alters the total succinate pool size in retinas (**Figure 4.8D**).

Pre-incubating retinas at increasing pO_2 increases COXIV levels and also decreases reverse SDH activity. However, changes in total metabolite levels suggest that pre-incubation also causes other metabolic changes which are independent of COXIV but could also influence reversal of SDH. For this reason, we also used other means to more directly interrogate the influence of complex IV on reverse SDH activity. We hypothesized that treating freshly dissected retinas with the complex IV inhibitor KCN would further increase the reduction state of the retinal Q pool and drive more reverse SDH activity. We incubated retinas in 5 mM ^{12}C-glucose and 50 μM U-^{12}C-malate with 3 mM KCN for 5 minutes to allow QH_2 to accumulate, then transferred the retinas to fresh media containing 5 mM ^{12}C-glucose and 50 µM U-^{13}C-malate with 3 mM KCN for 5 minutes to assay reverse SDH activity. We found that retinas treated with KCN produce more m4 succinate, which is consistent with a buildup of QH_2 further driving reverse SDH activity (**Figure 4.8E**). We also observed that KCN treatment reduced the total fumarate pool in retinas (**Figure 4.8F**).

Next, we tested if an *in vivo* disruption to the mitochondrial QH_2 supply could influence the amount of reverse SDH activity we measure in our *ex vivo* assays. We used retinas from *Ndufs4*$^{-/-}$ mice, which lack a critical component of Complex I (Kruse et al., 2008). We hypothesized that complex I deficiency would lead to retinal mitochondria from these mice accumulating less QH_2, providing less driving force to reduce fumarate to succinate. We incubated retinas from P21 and P30 *Ndufs4*$^{-/-}$ mice and WT littermates in 5 mM 4-^{2}H-glucose for 5 minutes and found that *Ndufs4*$^{-/-}$ retinas still accumulate m1 fumarate but produce less m1 succinate, leading to a smaller m1 succinate / m1 fumarate ratio (**Figure 4.8G**). This indicates that retinas from *Ndufs4*$^{-/-}$ mice perform less reverse SDH activity. We also tested if the decrease in the mitochondrial QH_2 pool in *Ndufs4*$^{-/-}$ retinas would enhance forward SDH activity. We incubated retinas from P21 and P30 *Ndufs4*$^{-/-}$ mice and WT littermates in 5 mM U-^{13}C-glucose for 5 minutes and found that *Ndufs4*$^{-/-}$ retinas accumulate less m2 succinate but equivalent amounts of m2 fumarate, leading to a higher m2 fumarate / m2 succinate ratio (**Figure 4.8H**). This indicates that the forward SDH reaction is enhanced in *Ndufs4*$^{-/-}$ retinas. Total fumarate and α-ketoglutarate levels are not different, but there is substantially less total succinate in *Ndufs4*$^{-/-}$ retinas incubated in 5 mM glucose for 5 minutes (**Figure 4.8I**). Enhanced forward SDH activity and diminished reverse SDH activity both may contribute to the diminished size of the succinate pool in retinas from *Ndufs4*$^{-/-}$ mice.

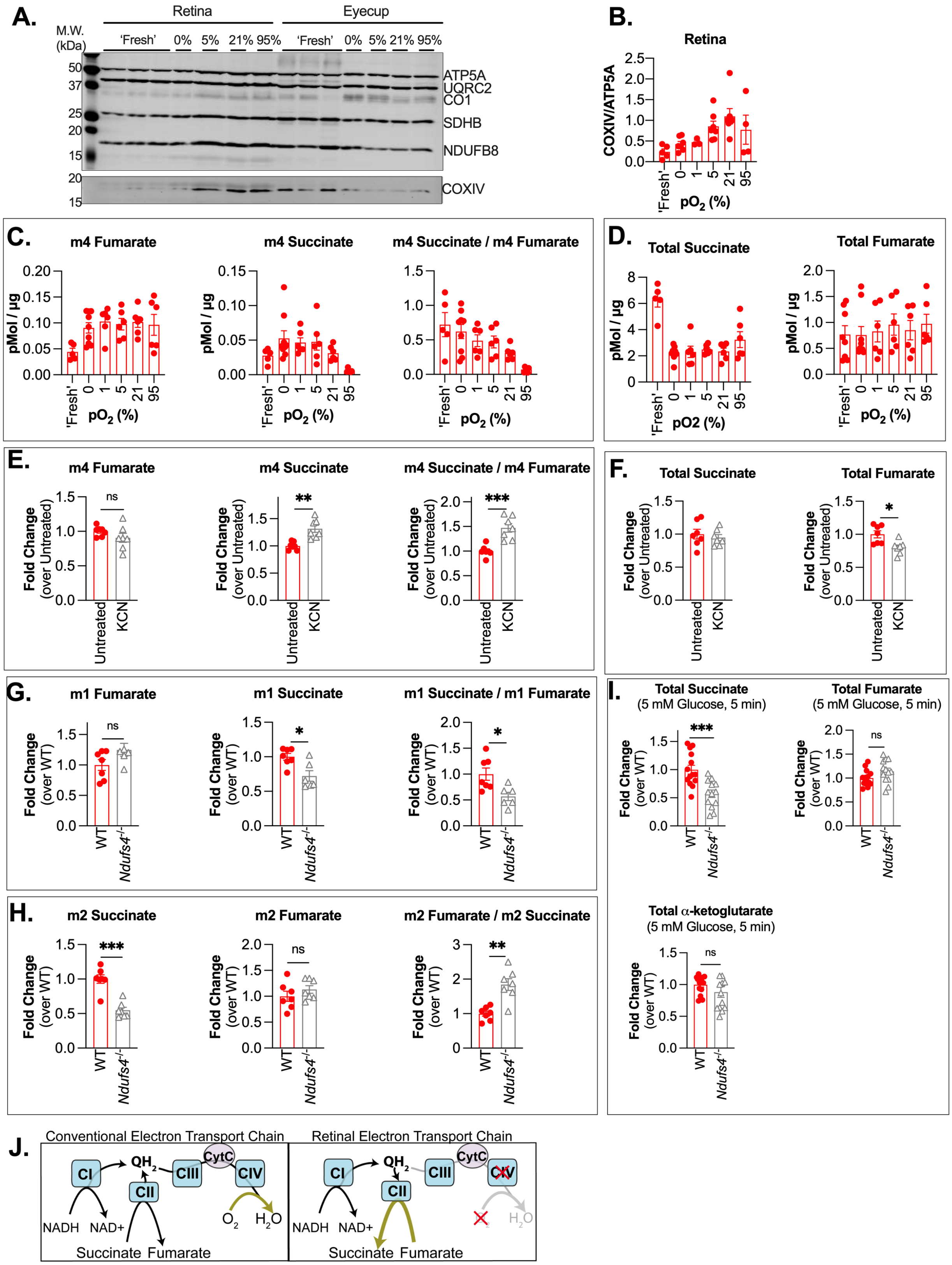

Figure 4.8: Low COXIV expression drives reversal of SDH in retinas

Figure 4.8: Low COXIV expression drives reversal of SDH in retinas
(A) Immunoblot of retinas and eyecups using an ETC component cocktail (top blot) and a single antibody against COX4 (bottom blot). ATP5A: ATP synthase subunit 5A, UQRC2: ubiquinol cytochrome c oxidoreductase subunit core 2, CO1: cytochrome *c* oxidase subunit 1, SDHB: succinate dehydrogenase B, NDUFB8: NADH Ubiquinone Oxidoreductase Subunit B8, COX4: cytochrome *c* oxidase subunit 4. **(B)** Quantification of multiple immunoblots probed with COX4 and ATP5A (each dot represents a biological replicate, n=3 to 7 retinas per pO_2 condition). **(C)** m4 fumarate, m4 succinate, and the m4 succinate/m4 fumarate ratio measured in retinas supplied with 5 mM ^{12}C-glucose + 50 μM U-^{13}C-malate for 5 minutes after pre-equilibration at specified pO_2 for 2h (n=6 to 9 retinas per pO_2 condition). **(D)** Total fumarate and succinate levels in retinas incubated in 5 mM ^{12}C-glucose + 50 μM U-^{13}C-malate for 5 minutes. “Fresh” indicates that retinas were incubated immediately after dissection. “pO_2” indicates that retinas were incubated at the specified level of oxygen for 2 hours (in 5 mM ^{12}C-glucose) prior to incubation in labeled malate (n=6 to 9 retinas per pO2 condition). **(E)** m4 fumarate, m4 succinate, and the m4 succinate/m4 fumarate ratio measured in retinas supplied with 5 mM ^{12}C-glucose + 50 μM U-^{13}C-malate in the presence of 3 mM KCN (n=6 retinas). **(F)** Total fumarate and succinate levels in retinas supplied with 5 mM ^{12}C-glucose + 50 μM U-^{13}C-malate in the presence of 3 mM KCN (n=6 retinas). **(G)** m1 fumarate, m1 succinate, and the m1 succinate/m1 fumarate ratio in WT and Ndufs4$^{-/-}$ retinas supplied with 5 mM 4-^{2}H-glucose for 5 minutes (n=7 WT and 6 Ndufs4$^{-/-}$ retinas). **(H)** m2 fumarate, m2 succinate, and the m2 fumarate / m2 succinate ratio in WT and Ndufs4$^{-/-}$ retinas supplied with 5 mM 4-^{2}H-glucose for 5 minutes (n=7 WT and 7 Ndufs4$^{-/-}$ retinas). **(I)** Total fumarate, succinate, and α-ketoglutarate levels in WT and Ndufs4$^{-/-}$ retinas supplied with 5 mM glucose for 5 min (n=14 WT and 13 Ndufs4$^{-/-}$ retinas). **(J)** Diagram showing canonical electron transport chain function (left) and proposed electron transport chain function in retinas (right).

Discussion

We have identified aspects of metabolic specialization in the retina and RPE which support the existence of a succinate/malate cycle between the two tissues. We have found that the retina releases succinate, the RPE/choroid imports succinate to fuel mitochondrial respiration and in turn exports malate, which is capable of refueling succinate production in the retina via reverse SDH activity. We find that pO_2 influences expression of COXIV in retinal explants, suggesting that it is the hypoxic environment of the retina that keeps complex IV activity low and allows QH_2 to build-up to levels which can drive reversal of SDH.

Previous studies have shown that reverse electron transport can produce succinate in the ischemic heart; however, it was calculated that only 5.7% of the succinate pool was made by reverse SDH activity (Chouchani et al., 2014; Zhang et al., 2018). In contrast, our data show that as much as 55% of the succinate pool in retinas derives from reverse SDH activity. Remarkably, this is greater than the amount of succinate produced from oxidative TCA cycle activity.

We specifically tested malate as a candidate metabolite used by retinas to resupply succinate pools since (1) eyecups release malate in the presence of glucose alone and (2) malate release from eyecups is enhanced by succinate. However, we also observed that while eyecups do not release fumarate at a high rate in the presence of glucose alone, fumarate export is enhanced similarly to malate export in the presence of succinate. Thus, it is possible that retinas also use fumarate released by eyecups to resupply their succinate pools via reverse SDH activity.

The retina relies heavily on glycolysis to produce ATP (Kanow et al., 2017; Krebs, 1927). Since the RPE lies between the retina and the choroidal blood supply, glucose must pass through the RPE mostly unconsumed in order to fuel glycolysis in the retina. Export of succinate from the retina to the RPE could provide the RPE with an alternative fuel source to glucose. This would allow a greater fraction of glucose to pass through the RPE unconsumed so that it can reach the retina. This suggests that the RPE has specifically adapted to consume succinate, since many other tissues (except brown fat) are thought to be impermeable to succinate (Ehinger et al., 2016; Hems et al., 1968; Mills et al., 2018).

Succinate exported from the retina is carrying reducing power which would be otherwise wasted if it were not used as a fuel by another tissue. The RPE is extremely well situated to use this succinate, as it is positioned in an O_2-rich niche where electrons from succinate can be donated to O_2 via the ETC. This is not the first succinate-mediated ‘redox shuttle’ to be proposed. During whole-body hypoxia in rats, succinate released from peripheral tissues has also been hypothesized to carry unused reducing power to the lungs, where O_2 is relatively more accessible during hypoxia (Cascarano et al., 1976).

RPE consumption of succinate could protect the retina in more than one way. For one, RPE consumption of succinate could prevent unwanted succinate accumulation in the retina. In an oxygen-induced retinopathy model, rats were exposed to 24-hour cycles of hypoxia and hyperoxia from P0 to P21, which caused a 3-fold increase in retinal succinate. Accumulated succinate signaled through GPR91 in retinal ganglion cells to induce pathological extraretinal neovascularization (Sapieha et al., 2008). We have shown that retinas constitutively release succinate. If the RPE were not also constitutively consuming this succinate (as in the case of whole-body hypoxia), it could accumulate in the retina and stimulate unwanted angiogenesis.

RPE consumption of succinate might also be protective by reducing oxidative stress in the retina. Mammalian retinas are composed of terminally differentiated neurons that cannot be replaced when damaged. Reactive oxygen species pose a great risk to these neurons since they can damage proteins, membranes, and nucleic acids. However, as long as photoreceptors release succinate, succinate can stimulate the RPE to consume a significant portion of O_2 from the choroidal blood supply, thus preventing O_2 from reaching the retina where it could form reactive oxygen species. This is supported by the observation that although mouse eyecups contain approximately 3-fold less cellular material than retinas, they are able to consume as much O_2 as the entire retina when stimulated by succinate (**Figure 4.1B**).

The metabolic ecosystem formed by succinate-malate exchange between the retina and RPE illustrates another way that photoreceptor degeneration can drastically impact eye health. In the absence of photoreceptors, we found that retinal succinate export decreases. We expect that in an intact eye, this will lead to a decrease in RPE O_2 consumption. If succinate stimulated RPE O_2 consumption normally protects the retina, a loss of photoreceptors would exacerbate oxidative damage to the retina. This may occur in retinitis pigmentosa, where degeneration of rod photoreceptors causes an increase in photoreceptor layer O_2 tension and leads to secondary cone photoreceptor death (Campochiaro and Mir, 2018; Yu et al., 2000). It may be possible to prevent secondary cone degeneration by supplying exogenous succinate to the RPE, which could recapitulate a critical aspect of this metabolic ecosystem for therapeutic benefit.

Overall, our findings suggest that the retina has adapted to its hypoxic niche in the eye by altering the stoichiometry of its respiratory complexes to favor a reversal of the SDH reaction. This adaptation can divert electrons out of the electron transport chain to reduce fumarate to succinate. The succinate released from the retina can shuttle electrons to the RPE/choroid where they reduce O_2 to H_2O. This exchange of metabolites facilitates transport of electrons away from a tissue that is not well poised to transfer them to O_2 (the retina) to one that is better suited to use them to reduce O_2 to H_2O (the RPE/choroid). Succinate stimulates RPE cells to release malate as “empty” electron shuttles, which retinas can then refill with electrons via reverse SDH activity. This succinate/malate exchange is another aspect of the metabolic ecosystem formed by the retina, RPE, and choroid; where tissue specialization of metabolic reactions is coordinated to generate the energy needed for visual function in the face of low O_2 availability.

We have rigorously demonstrated that these activities occur in isolated retinas and RPE/choroid complexes that are alive and functional. The next steps toward establishing the significance of this mechanism *in vivo* will be (1) to document SDH reversal and the transfer of metabolites between these tissues in living animals, (2) to explore how succinate/malate exchange is influenced by genetic perturbations which interfere with the ability of the retina to produce succinate or the ability of the RPE/choroid to consume it, (3) to determine how disrupting this metabolite transfer *in vivo* influences the health of the retina and RPE/choroid, and (4) to identify how the exchange of succinate and malate is disrupted in disease.

Acknowledgements

The work in this chapter is published in Cell Reports (Cell Press). The authors that contributed to this work were Celia M. Bisbach (CMB) Daniel T. Hass (DTH), Brian M. Robbings (BMR), Austin M. Rountree (AMR), Martin Sadilek (MS), Ian R. Sweet (IRS), and James B. Hurley (JBH). Experiments were designed by CMB, JBH, and DTH. CMB led collection and analysis of data in figures 4.1-4.7 with assistance from DTH, and DTH led collection and analysis of data in figure 4.8 with assistance from CMB. BMR and AMR provided technical assistance with running oxygen consumption experiments. MS provided technical assistance with creating and maintaining GC-MS methods. In addition, we thank Whitney Cleghorn for her assistance in maintaining the mouse colony in the lab of J.B.H., Kristine Tsantilas for assisting with mass spectrometry method maintenance, Abbi Engel and Jennifer Chao for supplying us with hfRPE cells, and Rong Tian (University of Washington) and Simon C. Johnson and Rebecca Bornstein (Seattle Children's Hospital) for sharing *Ndufs4*$^{-/-}$ mice. Work in the lab of J.B.H. was funded by NIH grants (EY06641 and EY017863). Work in the lab of I.R.S. was funded by (DK17047). C.M.B. was funded by the NIH grant (F31EY031165). D.T.H. was funded by NIH grant (5T32EY007031-42).

Methods

Mouse Models: Experimental procedures complied with NIH guidelines and were approved by the University of Washington IACUC. C57BL/6J mice (RRID:IMSR_JAX:000664) were purchased from The Jackson Laboratory at 6-8 weeks old and housed at the UW Medicine SLU 3.1 vivarium, where they experienced a 12-h light/dark cycle and free access to food and water. AIPL1$^{-/-}$ mice were generated in house (Ramamurthy et al., 2004) and housed in the SLU 3.1 facility under the same conditions. Retinas from Ndufs4$^{-/-}$ mice were obtained from two sources: the Rong Tian lab at the University of Washington, and the Simon Johnson lab at Seattle Children's Research Hospital (B6.129S4-Ndufs4tm1.1Rpa/J, RRID:IMSR_JAX:027058). C57BL/6J and AIPL1$^{-/-}$ mice were between 8-20 weeks old at the time of experiment. Ndufs4$^{-/-}$ mice were aged P21 (n=4 mice) and P30 (n=3 mice) at the time of experiment. Mice were euthanized by awake cervical dislocation for all experiments. Equal numbers of male and female mice were used.

RPE Cell Culture: RPE cell culture was performed in the lab of Jennifer Chao at the University of Washington. Human fetal RPE tissue with a gestational age of 115 days was obtained from the Thomas Reh lab at the University of Washington. Fetal RPE dissection and culture was performed according to (Sonoda et al., 2009). Fetal RPE sheets were cultured at 37°C with 5% CO_2 in RPE media (MEM alpha (Life Technologies), 5% FBS (Atlanta Biologicals), N1-Supplement (Sigma-Aldrich), Nonessential Amino Acids (Gibco), and Penicillin-Streptomycin (Gibco)). 3-4 weeks after dissection, RPE sheets reached confluency and strained using a 40 μm cell strainer to create a suspension of single cells. After counting, the RPE cells were plated onto a 12-well plate coated with matrigel (Corning) at 500,000 cells per insert.

Immunoblotting: Protein was extracted by homogenizing in RIPA buffer (150 mM NaCl, 1.0% Triton X-100, 0.5% sodium deoxycholate, 0.1% SDS, 50 mM Tris, pH 8.0) and run on 12% polyacrylamide gels. After running, gels were transferred onto PVDF membranes (Millipore, IPFL00010) and blocked for 1 hr at room temperature in LI-COR Odyssey Blocking Buffer (LI-COR, 927-40000). Primary antibodies were diluted in blocking buffer at specified concentrations and incubated overnight at 4°C. Membranes were washed with 1x phosphate buffered saline (PBS) and PBS with 0.1% Tween-20 (PBS-T), then incubated with secondary antibody for 1 hr at 25°C and washed again before imaging. Membranes were imaged and bands were quantified using the LI-COR Odyssey CLx Imaging System (RRID: SCR_014579). Antibodies used are: [anti-Total Oxphos, 1:1000 dilution, RRID: AB_2629281, Lot# P3338], [anti-COXIV, 1:500 dilution, RRID: AB_2085424, Lot# 10], [anti-rabbit secondary, 1:2500, RRID: AB_2715510, Lot# C61012-02], [anti-mouse secondary, 1:2500, RRID: AB_2716622, Lot# C60217-15].

***Ex Vivo* Isotopic Labeling of retinas and eyecups:** Krebs-Ringer bicarbonate (KRB) buffer (98.5 mM NaCl, 4.9 mM KCl, 1.2 mM KH_2PO_4 1.2 mM $MGSO_4$-$7H_2O$, 20 mM HEPES, 2.6 mM CaCl-$2H_2O$, 25.9 mM $NaHCO_3$) optimized for isotopic labeling experiments in retinas was used in these experiments. Mice were euthanized by awake cervical dislocation and eyes were rapidly enucleated into a dish of Hank's Buffered Salt Solution (HBSS; Gibco, Cat#: 14025-076). Excess fat and connective tissue was trimmed from each eye, then retinas were dissected away from eyecups and the lens was removed. After dissection, retinas were placed in pre-warmed KRB containing labeled metabolites at concentrations in each experiment that was equilibrated at 21% O_2 and 5% CO_2 (unless otherwise specified in the text). Retinas were incubated for the specified time points at 37°C (at 5% CO_2 and 21% oxygen, unless otherwise specified in the main text), then washed twice in ice-cold PBS and flash frozen in liquid nitrogen. Metabolites used were: D-[U-^{13}C]-glucose (Cambridge Isotope Laboratories, CLM-1396), D-[U-^{13}C]-malate (Cambridge Isotope Laboratories, CLM-8065), (D-[4-^{2}H]-glucose, Omicron Biochemicals, GLC-035), ([U-^{13}C]-succinic acid, Sigma #491985)

Metabolite Analysis by Gas-Chromatography Mass Spectrometry: Metabolites were extracted from both retinas and eyecups using ice-cold 80% MeOH. 150 µL extraction buffer was added to each sample and tissue was disrupted by sonication. Samples were incubated on dry ice for 45 minutes and centrifuged at maximum speed for 30 minutes. The resulting pellet was resuspended in RIPA buffer and the amount of protein in each retina or eyecup was determined by a BCA assay. The resulting supernatant was lyophilized at room-temperature until dry, then derivatized in 10 µL of 20 mg/mL Methoxyamine HCl (Sigma, Cat#: 226904) dissolved in pyridine (Sigma, Cat#: 270970) at 37°C for 90 minutes, and subsequently with 10 µL *tert*-butyldimethylsilyl-N-methyltrifluoroacetamide (Sigma, Cat#: 394882) at 70°C for 90 minutes. Metabolites were analyzed on an Agilent 7890/5975C GC-MS using selected-ion monitoring methods described extensively in previous work.[7–10] Peaks were manually integrated using MSD ChemStation software (Agilent), and correction for natural isotope abundance was performed using the software Isocor (Millard et al., 2012). Raw signals for each metabolite were converted to molar amounts using metabolite standard curves which were run alongside each experiment. Molar amounts were normalized to the total amount of protein (determined in a BCA assay) for each sample to determine the molar amount per µg of cellular protein. To determine steady-state fractional enrichment values in Figure 4, a curve was fit to each time course using Graphpad Prism software (Version 8) assuming a first order reaction by using the equation $\%metabolite = B * (1 - e^{-kt})$. B is the fractional enrichment at the steady state, k is the rate constant for the reaction, t is time, and %metabolite is the fractional enrichment at a given time.

Oxygen Consumption Measurement: Oxygen consumption measurements were performed using a perifusion flow-culture system described in (Sweet et al., 2002, 2004). KRB buffer modified for perifusion was prepared as follows: 98.5 mM NaCl, 4.9 mM KCl, 1.2 mM KH_2PO_4, 1.2 mM $MgSO_4$-$7H_2O$, 20 mM HEPES, and 2.6 mM $CaCl_2$-$2H_2O$, 25.9 mM $NaHCO_3$, 1x Gibco Antibiotic-Antimycotic, and 0.1 g/100 mL Fatty Acid Free Bovine Serum Albumin. Retinas and eyecups were dissected in KRB buffer supplemented with 5 mM glucose, then cut into quarters and loaded into chambers. Each chamber contained either tissue from 2 retinas or 4 eyecups. Retina and eyecup tissue was layered into chambers between Cytopore beads (Amersham Biosciences, Piscataway, NJ) and kept in place by two porous frits. KRB buffer modified for perifusion was pumped through the system using a peristaltic pump. Media passed first through an artificial lung where it was oxygenated with a 21% O_2, 5% CO_2, 74% N_2 mixture. Media then passed through a bubble trap before moving through the chambers containing retina or eyecup tissue. The glass of each chamber is coated with a thin layer of oxygen sensitive polymerized Pt(II) Meso-tetra(pentafluorophenyl)porphine dye (Frontier Scientific, Logan, UT). A fiber optic cable positioned to measure the oxygen-tension of the media after it has passed over the tissue detects emitted phosphorescent light from the oxygen-sensitive dye when pulsed with 405 nm ultraviolet LED. The lifetime of the phosphorescence signal decay is then correlated with oxygen tension.

Quantification and Statistical Analysis: Graphpad Prism software (Version 8) was used to perform statistical analysis. In all cases, comparisons between two conditions were made using Welch's t-test. In all figures, significance is defined as: * indicates $p<0.05$; ** indicates $p<0.005$, *** indicates $p<0.001$, **** indicates $p<0.0001$. The "n" used for each experiment is indicated in each figure legend. For oxygen consumption measurements, "n" indicates measurements made from a single chamber. Each retina chamber contained tissue from 2 retinas, and each eyecup chamber contained tissue from 4 eyecups. For isotopic labeling experiments, “n” indicates 1 retina or 1 eyecup. All values reported in the text are mean ± S.D., while error bars on graphs show S.E.M.

Chapter 5: Monocarboxylate Transporter 1 (MCT1) mediates succinate export but not import in the retinal ecosystem

Introduction

The dicarboxylate succinate is metabolized by Succinate Dehydrogenase (SDH, also known as Complex II) in the TCA cycle. In the conventional form of this reaction, electrons are taken from succinate and deposited onto Coenzyme Q (CoQ) by SDH, forming fumarate and reduced CoQ ($CoQH_2$). SDH sits at a metabolic crossroads where the TCA cycle and electron transport chain (ETC) directly interact, meaning information about the state of both metabolic pathways can be integrated at succinate.

The diverse roles that succinate can play both inside and outside of the mitochondria are under new scrutiny. Succinate levels rise in a variety of tissues during hypoxia, and oxidation of succinate upon reperfusion is implicated as a primary driver of ROS production (Andrienko et al., 2017; Chouchani et al., 2014, 2016; Cordes et al., 2020). Succinate accumulates in macrophages during inflammation and has been shown to drive changes in gene expression (Tannahill 2013, Lampropoulou 2016). Succinate signaling through its G-protein coupled receptor SUCNR1 is implicated in regulating varied processes, including retinal angiogenesis (Sapieha et al., 2008), muscle remodeling in response to exercise (Reddy et al., 2020), and inflammatory signaling in the liver (Mills et al., 2021). Succinate has also been reported to be imported by eyecup explants and exported by retinal explants under basal conditions, although the role this exchange plays in the eye is not yet understood (Bisbach et al., 2020).

Despite the rise of succinate as a regulator of such varied processes, questions remain regarding how widespread its transport into and out of tissues is. It has been reported that exogenous succinate is not able to be imported and oxidized by most tissues. The main observations that support this are 1) the finding that some cultured cells and tissues exhibit a greater degree of succinate oxidation upon plasma membrane permeabilization, and 2) some cultured cells and tissues oxidize succinate analogs which have been modified to pass the plasma membrane to a greater degree than unmodified succinate (Ehinger et al., 2016; Jolly et al., 1979; MacDonald et al., 1989).

Contrary to the above reports, three members of the Slc13 family of dicarboxylate carriers have micromolar-affinities for succinate and are reported to be expressed in some of the same tissues that have been previously described as succinate-impermeant, such as liver (Pajor, 2006, 2014). Monocarboxylate Transporter 1 (MCT1), the most ubiquitously expressed monocarboxylate transporter, has also been shown to transport succinate under acidic conditions (Prag et al., 2020; Reddy et al., 2020).

The widespread expression of these transporters indicates that the permeability of succinate in many tissues needs to be more thoroughly investigated. We began by testing the capability of several tissues to oxidize succinate using an *ex vivo* flow perifusion system and specifically investigated the mechanism of eyecup succinate import and retinal succinate export in the retinal ecosystem. We found that eyecup succinate import occurs via a bona fide transporter, not due to loss of plasma membrane integrity. We determined that retinal succinate export occurs via MCT1, and that intracellular succinate concentrations are one factor that determines whether an MCT1-expressing tissue might export succinate.

Results

ex vivo succinate oxidation occurs in a range of tissues

In the conventional Krebs cycle, succinate dehydrogenase oxidizes succinate to fumarate. The electrons from that reaction reduce coenzyme Q_{10}, cytochrome C, then O_2 (**Figure 5.1A**). Oxidation of succinate therefore stimulates O_2 consumption (OCR) by complex IV. We used a perifusion respirometer to quantify OCR that is inhibited by the complex IV inhibitor KCN. **Figure 5.1B** shows how OCR depends on succinate concentration. Increasing succinate concentrations (30 μM, 100 μM, 300 μM, 1 mM, 3 mM, 10 mM, 30 mM, and 100 mM all with 5 mM glucose present) stimulate OCR in liver, cerebellum, interscapular brown adipose tissue (BAT), kidney, eyecup (containing retinal pigment epithelium, choroid, and sclera), and retina tissue. The data are fit with an allosteric sigmoidal function (**Figure 5.1C-H, Table 5.1**). In most tissues, succinate enhances OCR with a best-fit V_{max} of 0.34-0.89 nmol O_2 / mg tissue / minute, and best-fit $K_{1/2}$ values ranged from 0.9-2.72 mM (**Table 5.1**), The retina lay far outside this range (V_{max} of 0.12 nmol O_2 / mg tissue / minute and $K_{1/2}$ of 8.9 mM). This dependence of OCR on succinate is an estimate because it did not reach saturation. This suggests either that in retinas there is unusually limited plasma membrane succinate import and/or that the ETC of the retina has an unusually poor ability to oxidize succinate.

Tissue	Basal OCR (nmol O_2 / mg / min)$^{\&}$	V_{max} (nmol O_2 / mg / min)	$K_{1/2}$ ([succinate])	H*	R^2	n
Retina	0.31 (0.12-0.50)	0.12 (?**)	8.89 (1.06-?**)	0.42 (0.19-0.77)	0.81	4
Cerebellum	0.22 (0.07-0.37)	0.36 (0.31-0.42)	2.72 (1.67-4.94)	1.38 (0.81-0.73)	0.90	3
Eyecup	0.15 (0.06-0.24)	0.34 (0.28-0.46)	2.49 (1.33-8.31)	1.05 (0.55-2.24)	0.81	5
Liver	0.07 (-0.32-0.46)	0.89 (0.77-1.04)	0.90 (0.49-1.75)	1.40 (0.72-?**)	0.85	3
BAT	0.21 (0.12-0.30)	0.57 (0.51-0.66)	1.45 (0.9-2.58)	1.15 (0.72-2.04)	0.91	3
Kidney	0.48 (0.38-0.58)	0.66 (0.52-1.20)	1.50 (0.84-8.53)	1.21 (0.64-2.35)	0.88	4

Table 5.1. Best-Fit Kinetic Parameters for *ex vivo* Succinate oxidation
Least squares fit, Parameters are represented as [mean (95% Confidence Interval)

** Hill's Slope*

*** "?" indicates that the curve fit is unable to estimate this parameter*

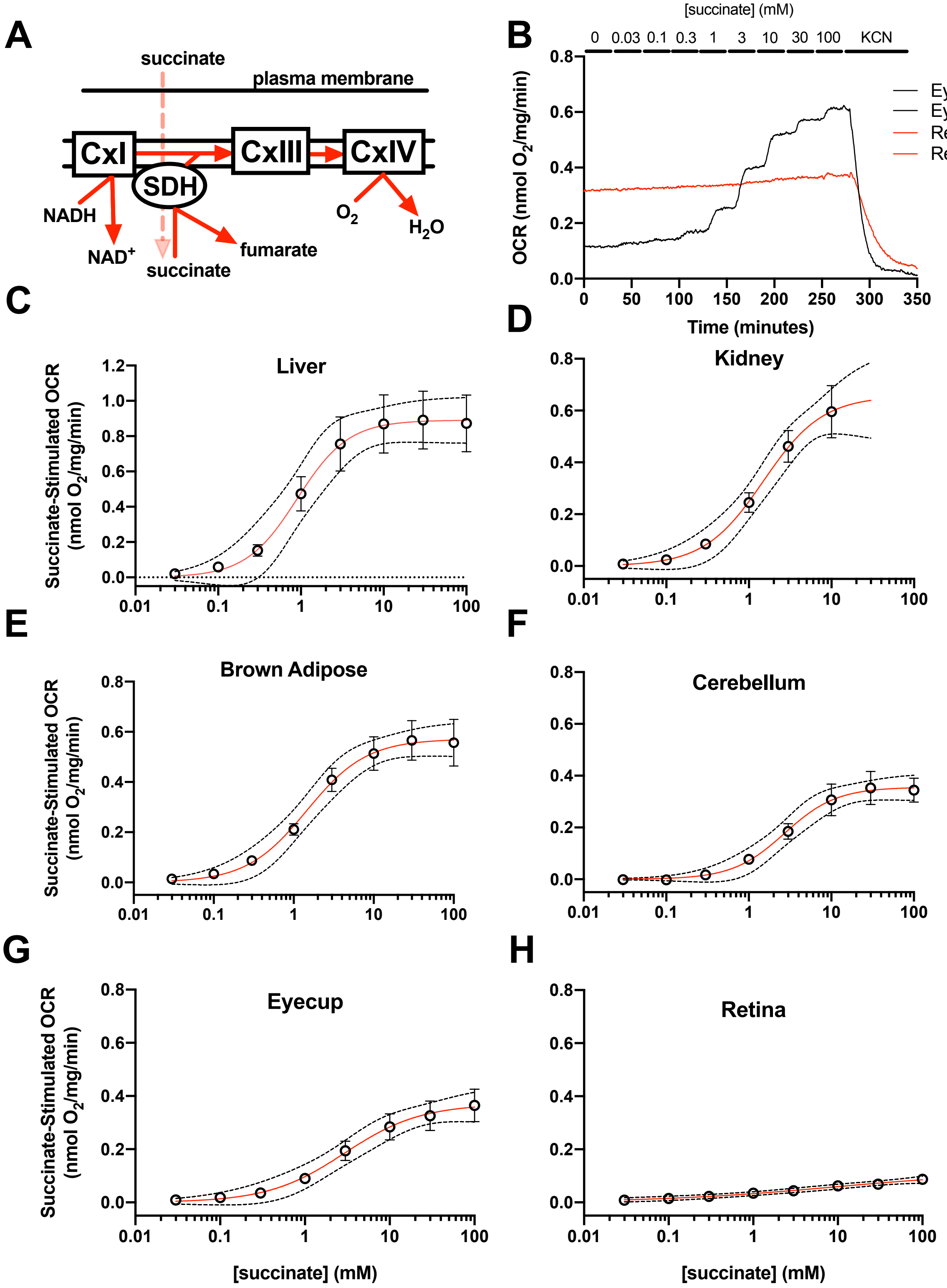

Figure 5.1: Extracellular Succinate Increases Oxygen Consumption in Diverse Tissues Ex Vivo
(**A**) Schematic of the mitochondrial electron transport chain. We measured O_2 consumption rate (OCR) in freshly dissected (**C**) liver (n=3), (**D**) kidney (n=4), (**E**) brown adipose (n=3))

(Figure 5.1 continued)
(**F**) cerebellum (n=3), (**B,G**) eyecup (n=3), and (**B,H**) retina (n=4) tissue from C57BL6/J mice, respiring in KRB buffer with 5 mM glucose. We supplied this media with increasing concentrations of disodium succinate (30 μM, 100 μM, 300 μM, 1 mM, 3 mM, 10 mM, 30 mM, or 100 mM) and determined the OCR above the 5 mM glucose “baseline” respiration. Example experiments are shown in (**B**). Mean ± SEM steady state OCR as a function of [succinate] are summarized for different tissues in C-H -state. We fit the data with an allosteric sigmoidal curve (red lines). Best-fit parameters are available in **Table 5.1**. Dotted lines surrounding the curves represent 95% confidence intervals from the curve fit.

Intact cells in RPE/choroid preparations consume succinate

We observe robust succinate-stimulated O_2 consumption in many different *ex vivo* tissue preparations, except for retina. One possibility is that cells in these tissues do not normally consume succinate, but they have become damaged in the tissue dissection process, making them permeable to succinate. To determine if this is a valid interpretation of our results specifically in the eye, we assessed the quality of our RPE/choroid and retina preparations to determine if they contain mostly intact or mostly lysed cells. Freshly dissected eyecups and retinas were incubated with increasing concentrations of digitonin, and the release of lactate dehydrogenase (LDH) was used to assess membrane integrity (**Figure 5.2A** eyecups and **5.2B** retinas). In the absence of digitonin, ~90% of LDH was retained in RPE/choroid preparations and ~99% of LDH was retained in retina preparations, indicating that most cells remain intact after tissue dissection.

Although ~90% of the cells in eyecups remain intact after dissection, it is possible that succinate is impermeable to intact cells in eyecups and that the ~10% of broken cells in eyecups are responsible for 100% of the succinate-stimulated oxygen consumption observed in **Figure 5.1**. In some cells which do not normally consume succinate, permeabilizing with digitonin increases succinate oxidation by removing the barrier to entry (Ehinger et al., 2016; Jolly et al., 1979). Because we found digitonin to be incompatible with our perifusion system, we used GC-MS to determine if permeabilization by digitonin altered the rate of U-^{13}C succinate uptake by eyecups (**Figure 5.2C**). If succinate were only oxidized by the few broken cells in eyecups, we would expect to see an increase in the rate of succinate depletion from the media as more cells became permeabilized by digitonin. Instead, succinate depletion occurs at the same rate independent of digitonin concentration (**Figure 5.2D**). This indicates that intact cells import and oxidize succinate, and that transport of succinate across the plasma membrane is not rate-limiting for its consumption in eyecups. The altered rates of pyruvate and lactate export in digitonin-permeabilized eyecups further support the likelihood that most cells in eyecup preparations are intact. There is a steep drop-off in the amount of exported pyruvate and lactate as cells become fully permeabilized, likely due to cytosolic enzymes required for glycolysis exiting the cell along with LDH.

To validate that this strategy can confer a normally succinate-impermeable tissue with the ability to use succinate in our hands, we repeated this experiment with retinas (**Figure 5.2E**). Succinate does not stimulate robust oxygen consumption in retinas, and we are unable to detect measurable depletion of ^{13}C-succinate from the media by retinas in the absence of digitonin. However, as retinas become increasingly permeabilized, they begin to deplete succinate from the incubation media. This indicates that if eyecups contained a large population of intact and succinate impermeant cells, we would be able to detect their presence using this method.

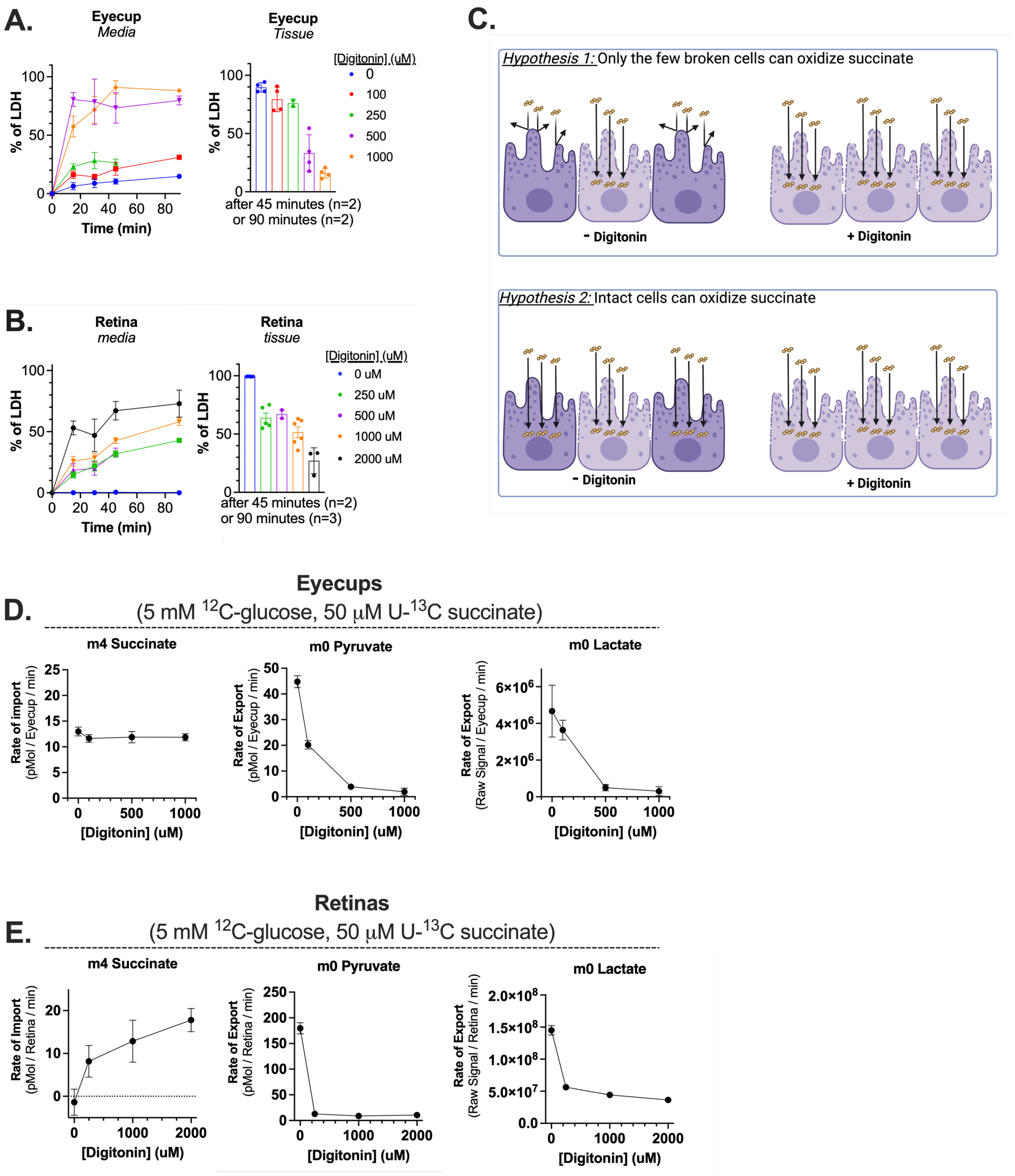

Figure 5.2: Intact cells in eyecup preparations oxidize succinate
(A) Permeability assessment of eyecups. Left panel: quantification of LDH released into the media by eyecups incubated in increasing [digitonin] over time. Right panel: quantification of LDH remaining in eyecups at the end of the experiment (n=4 eyecups per concentration of digitonin). **(B)** Permeability assessment of retinas. Left panel: quantification of LDH released into the media by retinas incubated in increasing [digitonin] over time. Right panel: quantification of LDH remaining in retinas at the end of the experiment (n= (6 retinas; 0 and 1000 μM digitonin) (5 retinas; 250 μM digitonin) (3 retinas; 2000 μM digitonin). **(C)** Graphical representation of possible outcomes given different permeability of succinate into intact cells. **(D, E)** Quantification of succinate import and metabolite release by eyecups (D) and retinas (E) incubated in varying concentrations of digitonin (n= (4 eyecups at each concentration of digitonin) (6 retinas; 0 and 1000 μM digitonin) (5 retinas; 250 μM digitonin) (3 retinas; 2000 μM digitonin)

Succinate uptake by RPE/choroid preparations is sodium-independent

We next sought to identify the transporter responsible for succinate uptake in eyecups. We began by testing if the Slc13a family of Na^+-coupled dicarboxylate carriers might be responsible. NaDC1 (Slc13a2), NaDC3 (Slc13A3), and NaCT (Slc13a5) couple transport of succinate and other dicarboxylates to transport of sodium cations. Each protein has varying affinity for succinate, with reported K_M values for succinate ranging from 2-25 μM (NaDC3), 590-800 μM (NaDC1), and 1900 μM (NaCT) (Pajor, 2006, 2014). Protein expression for all three transporters has been reported in kidney, intestine, liver, and brain (Pajor, 2006, 2014). Notably, NaDC3 mRNA expression has been reported in the RPE, and NaDC1 mRNA expression has been reported in both the retina and RPE (George et al., 2004; Lee et al., 2015).

We probed a panel of mouse tissues with commercially available NaDC3, NaDC1, and NaCT antibodies; however, we were only able to obtain reproducible results with NaDC3 antibodies (**Figure 5.3A, B**). As reported by others, we saw NaDC3 expression in liver and kidney, as well as BAT, retina, and eyecup. We determined that succinate uptake by eyecups occurs with a K_M of 1070 μM (95% CI 646-1943 μM) (**Figure 5.3C**). This K_M value is determined by both the K_M of any succinate transporter(s), as well as the K_M of any downstream step of succinate oxidation which may be rate limiting, meaning it cannot be used to conclusively exclude any transporter with a lower K_M (Brown et al., 2014).

Since both NaDC1 and NaDC3 mRNAs have been reported to be expressed in the RPE and because we observed evidence of NaDC3 protein in the RPE, we sought to further test if either protein might facilitate succinate uptake in eyecups. Potent and specific pharmacological inhibitors for NaDC1 and NaDC3 are not available. However, the degree of inhibition of succinate uptake by NaDC1 and NaDC3 when other dicarboxylates are present has been well characterized (Kekuda et al., 1999; Pajor, 1995, 1996; Pajor and Sun, 1996; Pajor et al., 2001). To determine if succinate uptake might be mediated by either of these dicarboxylate carriers in eyecups, we next tested if a variety of known NaDC1 and NaDC3 substrates might compete with succinate for import. The substrate specificity of NaDC1 and NaDC3 are extremely similar, and it has been shown in a number of experiments that transport of 10 μM succinate by either transporter is significantly reduced by the presence of 1mM fumarate or α-ketoglutarate (Pajor, 1995, 1996; Pajor et al., 2001). We tested the same concentrations of succinate and inhibiting metabolite and observed the same pattern of inhibition (**Figure 5.3D**). We also tested n-acetylaspartate, a known substrate of NaDC3 in ocular tissues, and found that n-acetylaspartate outcompeted the predicted fraction of succinate uptake (Huang et al., 2000; Pajor et al., 2001).

Not all results from the competition assessment aligned with the hypothesis that NaDC1 and/or NaDC3 mediate succinate transport. Citrate effectively reduces NaDC1 mediated succinate uptake while having no effect on NaDC3 mediated succinate uptake at pH 7.5 (Kekuda et al., 1999; Pajor, 1995; Pajor and Sun, 1996). We observed no influence of citrate on succinate uptake at pH 7.5, which could be consistent with the hypothesis that NaDC3 is the primary route of succinate import (**Figure 5.3D**). Citrate becomes an effective competitor for NaDC3-mediated succinate transport at acidic pH, since NaDC3 more effectively transports citrate in its divalent anion form (Kekuda et al., 1999; Pajor, 1995; Pajor and Sun, 1996). However, we observed no additional competitive influence of citrate on succinate import at pH 6.5 (**Figure 5.3D**).

To more conclusively test if any sodium-coupled dicarboxylate carrier might be responsible for succinate import, we determined the dependence of succinate uptake on sodium (using n-methyl D-glucamine replacement). NaDC1 and NaDC3 both couple transport of succinate to sodium with a half-maximal saturation value of between 10-50 mM (Pajor, 1995; Pajor and Sun, 2000; Pajor et al., 2001). Unexpectedly, decreasing sodium levels had no influence on the rate of succinate uptake up until 0 mM sodium was reached, at which point succinate uptake diminished by ~50%. There are two non-exclusive explanations for this observation: 1) part of the succinate uptake we observe is mediated by NaDC1 and/or NaDC3, and part by a sodium-independent transport mechanism, or 2) eyecup succinate uptake is not directly sodium-linked, and other sodium-dependent changes in cell function result in a decrease in ATP consumption when eyecups are incubated in 0 mM sodium media which lowers the demand for succinate uptake. We investigated if we could restore full succinate uptake capabilities to RPE/choroid preparations in the absence of sodium by permeabilizing them with digitonin. However, digitonin-permeabilized eyecup preparations incubated in 0 mM sodium medium exhibited the same degree of succinate depletion as fully intact RPE/choroid in 0mM sodium medium. This indicates that the decrease in succinate depletion observed in 0 mM sodium might instead be due to other sodium-dependent changes in cell metabolism which lower the demand for succinate oxidation.

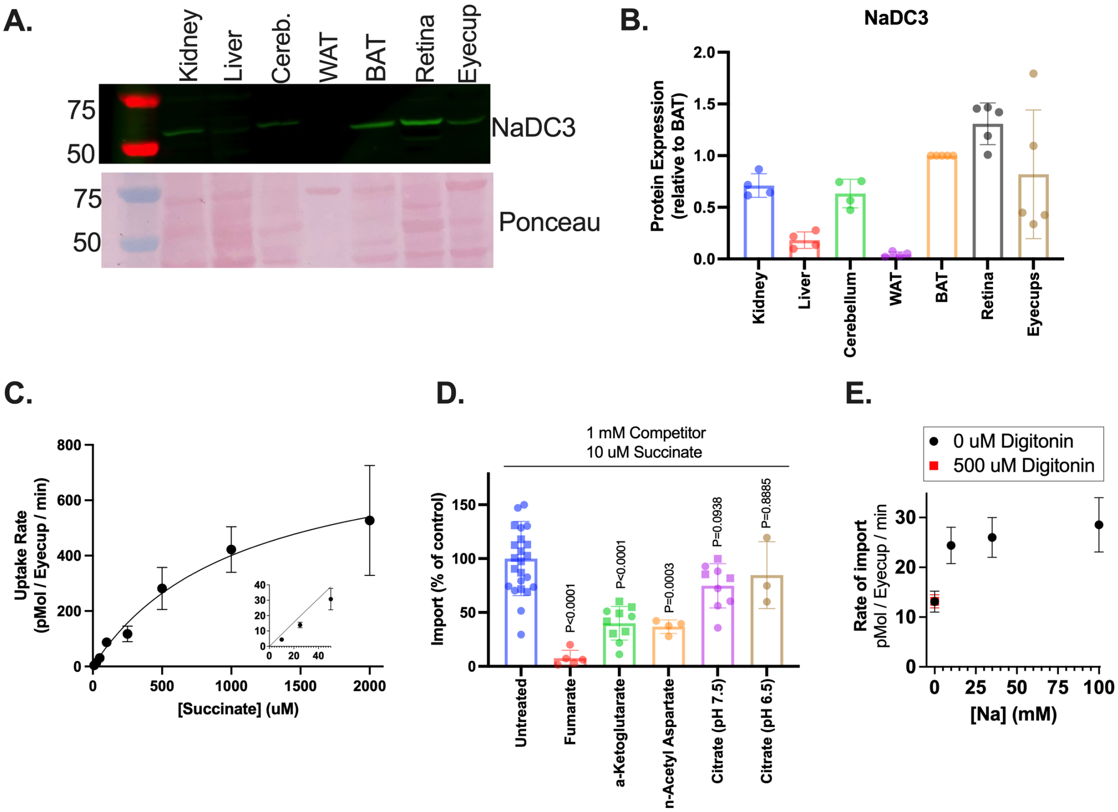

Figure 5.3: Succinate transport is not sodium linked in eyecups
(A) Representative western blot showing NaDC3 expression in a panel of tissues. **(B)** Quantitation of three NaDC3 blots. (n=3 biological replicates per sample, any additional datapoints represent technical replicates). **(C)** Rate of uptake of U-^{13}C-Succinate assessed over 10, 25, 50, 250, 500, 1000, and 2000 µM succinate using GC-MS. (n= (6, 10uM) (3, 25uM) (15, 50uM) (3, 100uM) (3, 250uM) (9, 500uM) (6, 1000uM) (3, 2000uM). **(D)** Competition assay showing the fraction of succinate imported in the presence of various inhibitors. Square data points were obtained using U-^{13}C-succinate and GC-MS, circular data points were obtained using 2,3-^{3}H-succinate and liquid scintillation counting (p values reported were calculated using a one-way ANOVA, data points represent biological replicates). **(E)** Rate of succinate uptake at varying concentrations of Na^{+}. (n= (6, 0 mM) (3, 10 mM) (3, 35 mM) (6, 100mM) (6, 0mM + digitonin)).

MCTs do not facilitate succinate import in eyecups

Despite the apparent expression of NaDC3 in eyecups and the similar inhibition pattern observed when succinate is incubated with a panel of dicarboxylates, the sustained import of succinate in the absence of sodium implicates the involvement of a sodium-independent transporter. Since monocarboxylate transporter 1 (MCT1) has recently been shown to transport succinate at low pH, we next investigated if MCTs might contribute to succinate uptake in eyecups (Prag et al., 2020; Reddy et al., 2020).

RPE cells have polarized expression of MCT isoforms, with MCT3 localized to the basal cell surface (adjacent to the choroid) and MCT1 found on the apical processes (adjacent to the photoreceptors) (Adijanto and Philp, 2012; Philp et al., 2001, 2003). We first tested if MCT1 might be responsible for succinate uptake in eyecups by measuring uptake of 50 μM U-^{13}C-succinate at pH 7.4 in the presence of the MCT1 inhibitor AZD3965 (**Figure 5.4A**). We saw no effect of MCT1 inhibition on the rate of succinate import; however, it is possible that MCT3 compensates and maintains transport of MCT substrates when MCT1 is inhibited. To determine if both MCTs might facilitate succinate transport in eyecups at pH 7.4, we tested if we could outcompete import of 50 μM U-^{13}C-succinate with an excess of lactate and pyruvate (**Figure 5.4B**). We found no change in the rate of succinate import when other MCT substrates were present.

We next considered that MCTs might only become engaged in succinate transport under specific conditions, such as when pH is low and/or when extracellular succinate concentrations are high. Low pH has been shown to facilitate MCT-mediated succinate transport in two ways: 1) a greater fraction of succinate exists in a MCT-transportable monocarboxylate form as pH acidifies (**Figure 5.4C,** left panel) and 2) since MCTs couple transport of monocarboxylates to protons, a high proton gradient can drive transport (**Figure 5.4C**, right panel) (Prag et al., 2020; Reddy et al., 2020). If MCTs contribute to only a small portion of succinate uptake under the pH 7.4 conditions we normally incubate eyecups in, we reasoned that the rate of succinate import would increase as extracellular pH was acidified. To test this hypothesis, we measured the rate of succinate import by eyecups in increasingly acidified incubation media (**Figure 5.4D**). As expected, the rate of lactate and pyruvate export decreased as pH was acidified and MCTs began to export these substrates against an increasingly steep proton gradient. However, the rate of succinate import decreased as pH acidified, indicating that the steeper proton gradient was ineffective at enhancing succinate import. Since lowering pH may lead to downstream metabolic changes independent of transport that alter the rate of succinate oxidation and obscure any MCT-dependent changes in succinate uptake, we also tested if MCT substrates lactate and pyruvate might outcompete a greater fraction of succinate for uptake at acidic pH; however, we observed no significant inhibition by lactate and pyruvate at any pH (**Figure 5.4D**).

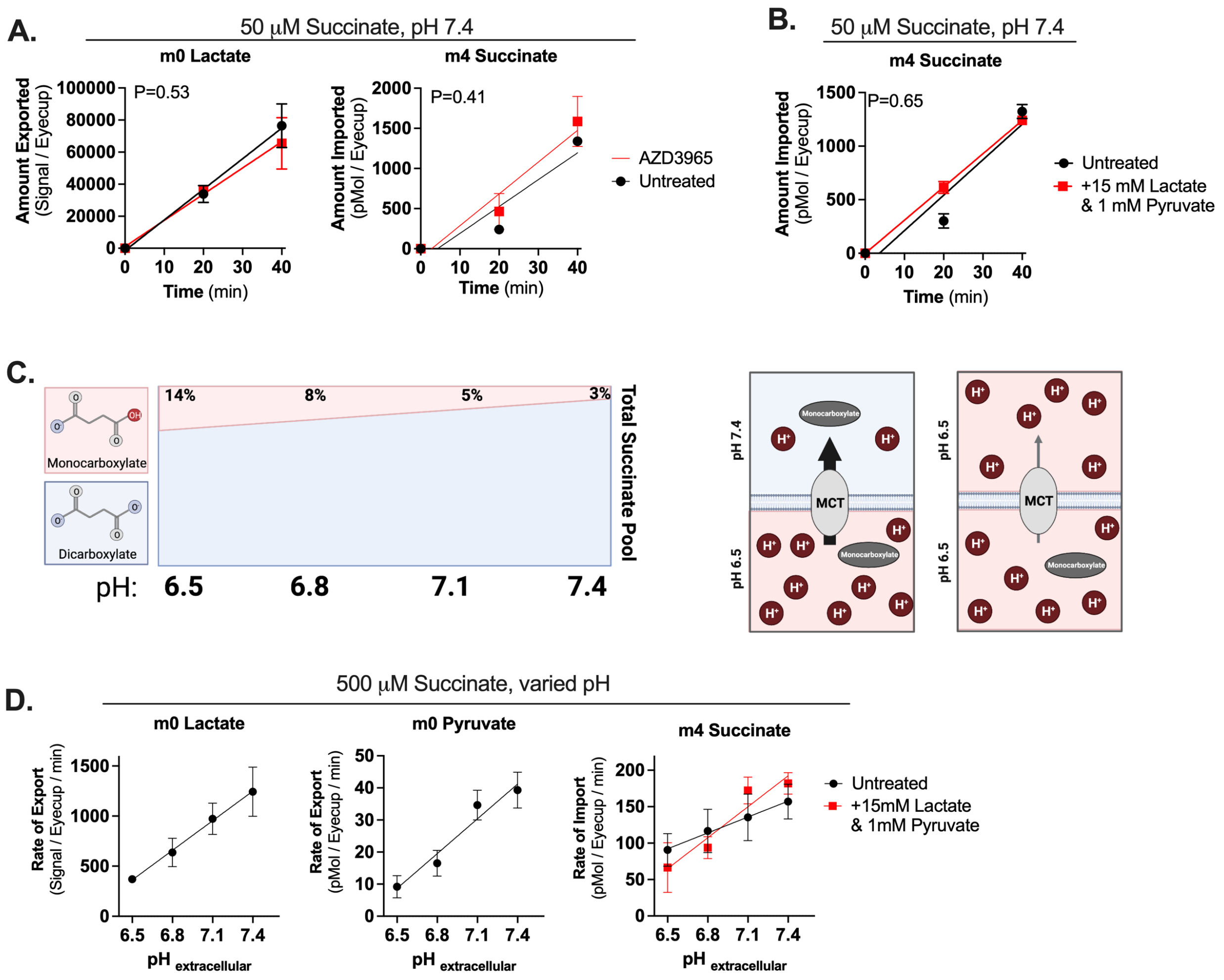

Figure 5.4. MCTs are not the primary succinate importer in eyecups
(A) Lactate export or succinate import over time in the presence of 100 μM AZD3965. (n=3 eyecups for each condition. Each condition was fit with a linear regression, and two-tailed ANCOVA was used to test if slopes were significantly different with p-values reported on each graph). **(B)** Dependence

(Figure 5.4 continued)
of succinate transport on MCT substrates lactate and pyruvate. (n=3 eyecups for each condition. Each condition was fit with a linear regression, and two-tailed ANCOVA was used to test if slopes were significantly different with p-values reported on each graph). **(C)** Graphical representation of the ways in which pH can modulate MCT-mediated succinate transport. Left panel shows the fraction of succinate which exists as a MCT-transportable monocarboxylate at various pH (determined using the Henderson-Hasselbalch equation and a pKa of 5.69). Right panel shows how a pH-gradient across a membrane can influence MCT activity. **(D)** pH-dependence of succinate import by eyecups incubated in 5 mM ^{12}C-glucose and 500 μM ^{13}C-succinate. Rates of metabolite import/export determined by sampling incubation media at 0, 20, and 40 minutes at pH 6.5, 6.8, 7.1, and 7.4. (n= (6, all untreated samples) (3, all +lactate/pyruvate samples))

MCTs contribute to succinate export in retinas

Succinate is a very abundant TCA cycle metabolite in retinas, and retinas export a molar amount of succinate equivalent to their entire intracellular succinate pool approximately every 40 minutes (**Figure 5.5A**, also **Figure 4.1A**). Since we observed that 99% of the cells in retinas are intact (**Figure 5.2B)**, this succinate must exit retinas through a transporter.

Even though we found that MCTs do not contribute to succinate import in eyecups, we did not discount them from being the succinate exporter in retinas for several reasons. Retinas express high levels of MCT1 and some MCT4 (Adijanto and Philp, 2012; Han et al., 2020). There are conflicting reports regarding MCT2 expression in the retina, but it appears to not be expressed or expressed only at very low levels (Philp et al., 2003; Voigt et al., 2020; Zhao et al., 2001). MCT1 has not yet been shown to import succinate in other tissues, only to export it, meaning that an MCT may be the retinal succinate exporter even if it is not the eyecup succinate importer (Prag et al., 2020; Reddy et al., 2020). Finally, the pH of the retina is reported to be lower than that of the RPE, with a pH minimum at the photoreceptor layer (where most of the retinal succinate is exported) (Bisbach et al., 2020; Padnick-Silver and Linsenmeier, 2002). This pH gradient could enhance MCT-mediated succinate export from retinas (**Figure 5.4C**).

Retinas are exceptionally glycolytic and modulating or inhibiting MCT activity could substantially decrease flux through glycolysis. This would reduce mitochondrial acetyl-CoA availability and thus reduce oxidative TCA cycle activity and canonical succinate production. This sequence of metabolic events following MCT inhibition could provide a “false positive” result, making it appear as though inhibition of MCT-mediated succinate transport has been inhibited when production of succinate is what has been reduced.

To control for this, we supplied retinas with 5 mM ^{12}C-glucose and 50 μM ^{13}C-malate in all experiments testing the role of MCTs in succinate export in this section (**Figure 5.5B**). This allows for succinate produced by both oxidative (m0 succinate) and reductive (m4 succinate) TCA cycle activity to be traced (Bisbach et al., 2020). m4 succinate production does not depend on acetyl-CoA availability, so by monitoring rates of both m0 and m4 succinate export we can attribute a decrease in succinate export to specific inhibition of MCT-mediated succinate transport and rule out decreased glycolytic flux as the cause.

We first tested if retinal succinate export shared characteristics of MCT-mediated transport by testing its pH-dependence. Lowering pH on the *trans* (in this case extracellular) side of a MCT decreases its activity, as it must now transport protons against a concentration gradient (**Figure 5.4C**). We measured succinate export in retinas incubated in medium adjusted to pH 7.4 and 6.5 and observed that decreasing extracellular pH reduced m0 and m4 succinate export, as well as export of the canonical MCT substrates lactate and pyruvate (**Figure 5.5C)**. We also treated retinas incubated in pH 7.4 medium with the H^+/Na^+ ionophore monensin or the H^+/K^+ ionophore nigericin to reduce any proton gradient that may normally drive MCT-mediated export in retinas. Rates of m0 lactate, m0 succinate, and m4 succinate export were all diminished by both ionophore, while m0 pyruvate export was diminished by monensin but not by nigericin (**Figure 5.5D**). The high concentration of Na^+ in KRB buffer may contribute to the more dramatic influence of monensin relative to nigericin.

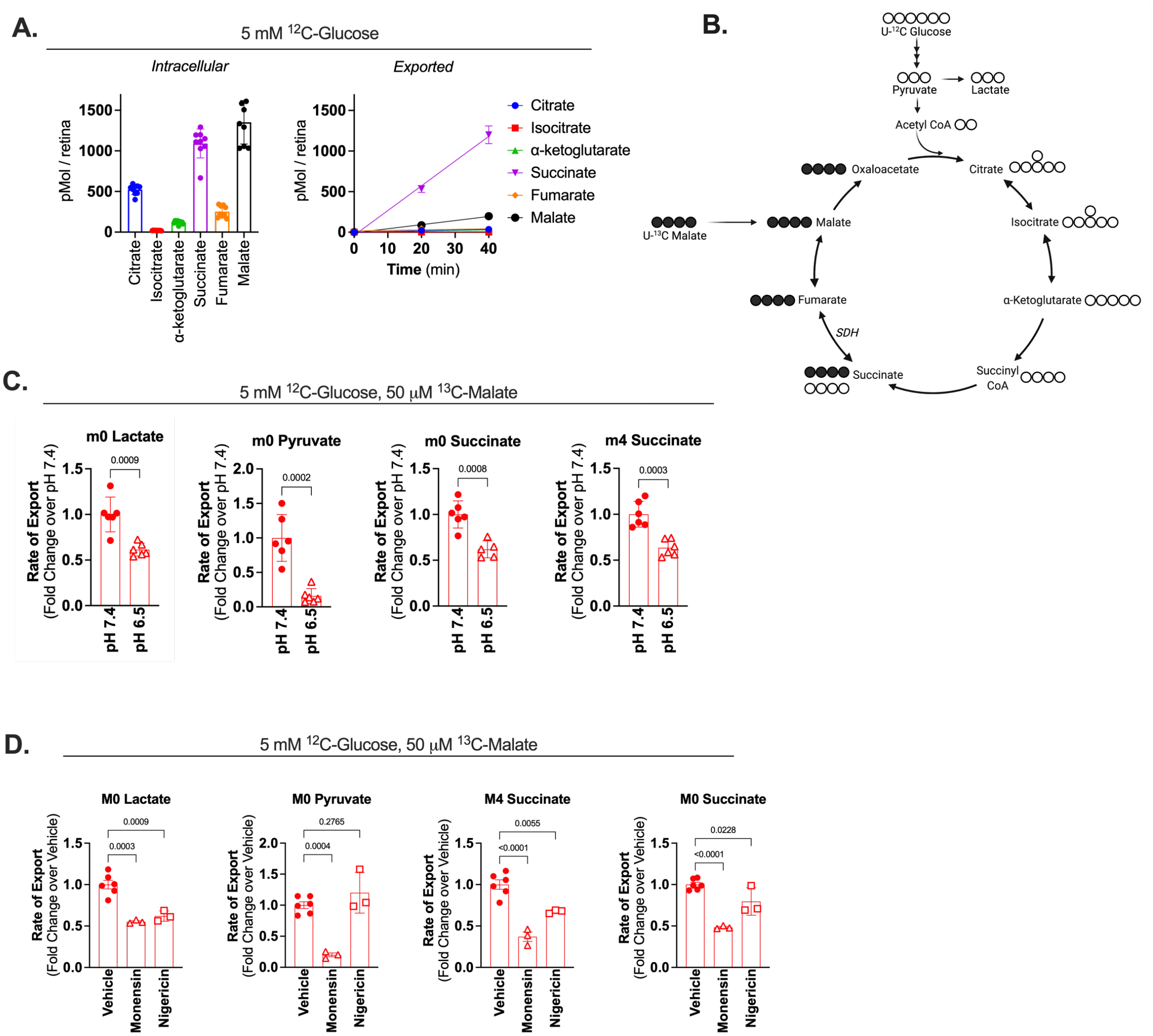

Figure 5.5. pH dependence of succinate export in retinas
(A) intracellular levels of TCA cycle metabolites in freshly dissected and snap frozen retinas (left) and rate at which they are exported (right) by retinas (n=8). **(B)** Diagram showing the isotopologues of succinate which are made by oxidative metabolism of U-^{12}C-glucose and U-^{13}C-succinate. Open circles represent ^{12}C, filled circles represent ^{13}C. **(C)** Rate of export of the canonical MCT substrate m0 lactate and m0 pyruvate, as well as m0 succinate and m4 succinate. p-values determined using Welch's t test. (n=6 retinas). **(D)** Rate of export of m0 lactate, m0 pyruvate, m0 succinate, and m4 succinate from retinas in the presence of 100 μM monensin or 100 μM nigericin (n= (6, vehicle) (3, monensin) (3, nigericin)).

We next tested a variety of MCT inhibitors to determine if we could identify which specific MCT(s) might facilitate succinate export in retinas (**Table 5.1**). We observed that incubation with the dual MCT1/MCT2 inhibitors AR-C155858 or AZD3965 (**Figure 5.6A** and **Figure 5.6B**) resulted in a dose-dependent decrease in both m0 and m4 succinate export. Since retinas express such low levels of MCT2, we think it likely that these effects are mainly mediated by inhibition of MCT1. We also tested the dual MCT1/MCT4 inhibitor Diclofenac (**Figure 5.6C**) and observed a similar dose-dependent decrease in both m0 and m4 succinate export. It is possible that the increased effectiveness of diclofenac relative to the dual MCT1/MCT2 inhibitors is due to inhibition of MCT4 in addition to MCT1. However, in cultured myotubules expressing MCTs 1, 2, and 4, reducing MCT4 expression did not alter succinate export (Reddy et al., 2020). Since diclofenac is structurally distinct from AZD3965 and AR-C155858, its increased effectiveness could also be due to an altered mechanism of action or increased permeability. As a result, these experiments show that MCT1 is responsible for a portion of succinate export in retinas and MCT4 may transport a portion of succinate in retinas.

Inhibitor	*MCT1*	*MCT2*	*MCT3*	*MCT4*	*references*
AZD3965	3.2 nM (K_i)	20 nM (K_i)	No Inhibition	No inhibition*	(Curtis et al., 2017)
AR-C155858	2.3 nM (K_i)	10 nM (K_i)	n.d.	Minimal inhibition †	(Ovens et al., 2010)
Diclofenac‡	1.45 μM (IC_{50})	n.d.	n.d.	0.14 μM (IC_{50})	(Renner et al., 2019; Sasaki et al., 2016)

Table 5.1: Reported kinetic parameters for various MCT inhibitors
"n.d." indicates no data for the effectiveness of an inhibitor for that MCT has been reported.
*no inhibition observed up to 10 μM
† no inhibition observed up to 1 μM, some inhibition observed at 10 μM
‡ The K_i for diclofenac in a mixed population of MCT1, MCT2, and MCT4 is 20 μM

A. *MCT1 & MCT2 Inhibition*

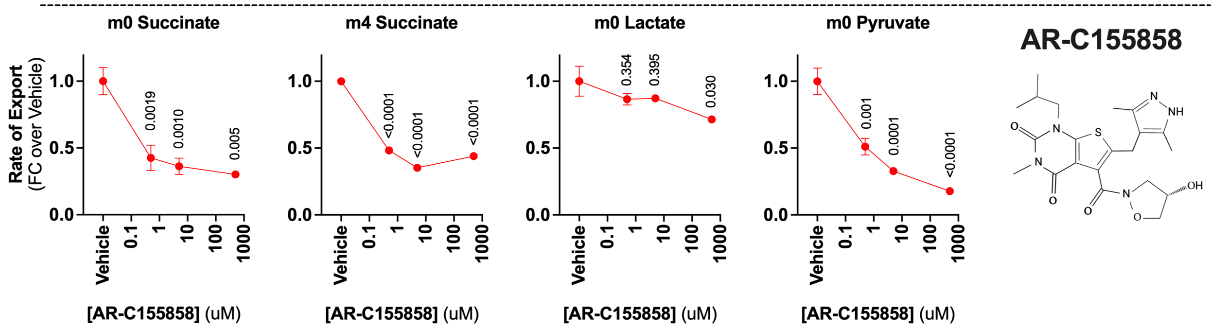

B. *MCT1 & MCT2 Inhibition*

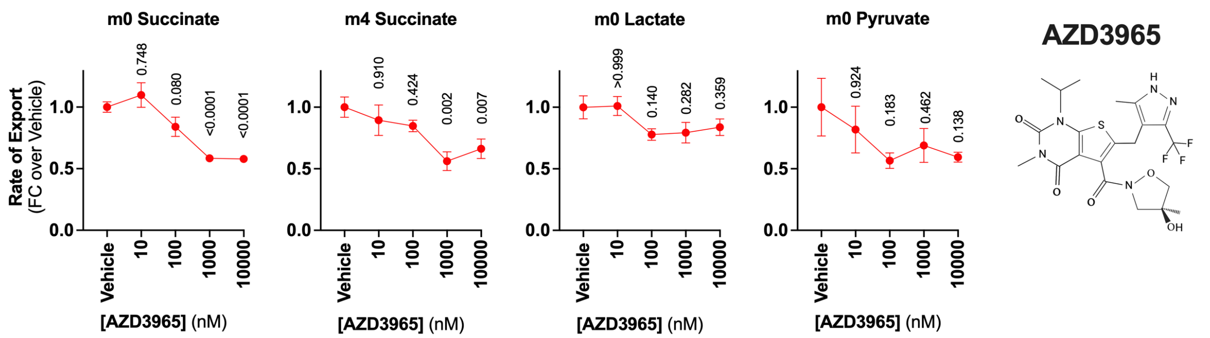

C. *MCT1 & MCT4 Inhibition*

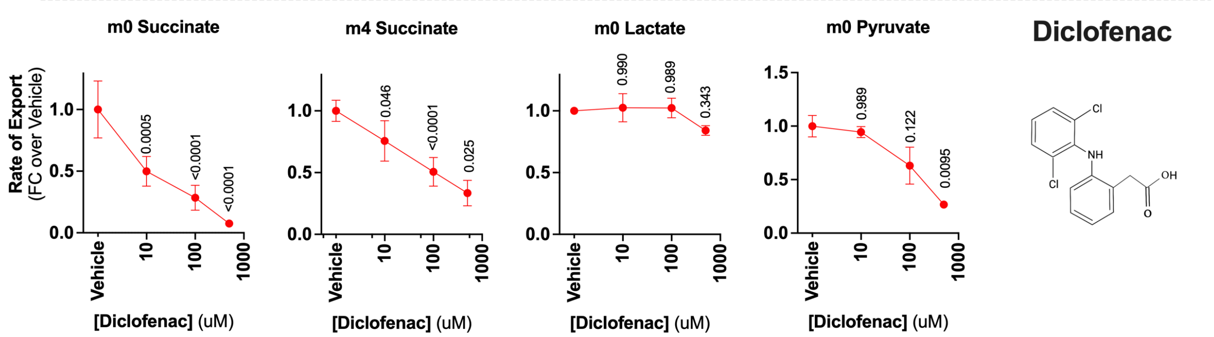

Figure 5.6: Effect of MCT inhibition on succinate export in retinas. (A,B,C) Influences of various MCT inhibitors on retinal export of m0 succinate, m4 succinate, m0 lactate and m0 pyruvate. Rates determined by sampling incubation media from retinas incubated in 5 mM ^{12}C-glucose and 50 μM ^{13}C-malate. P-values shown above each point were calculated using an ordinary one-way ANOVA (all conditions compared to vehicle) followed by Dunnett's correction for multiple comparisons. **(A)** AR-C155858 (n = (3, 0 nM) (3, 500 nM) (3, 5 μM) (3, 500 μM). **(B)** AZD3965 (n = (9, 0 nM) (3, 10 nM) (9, 100 nM) (6, 1 μM) (9, 10 μM)). **(C)** Diclofenac (n = (6, 0 nM) (3, 10 uM) (6, 100 uM) (3, 500 μM).

Eyecups can be induced to export succinate via MCT1

MCT1 is the most ubiquitously expressed MCT. In addition to the retina and RPE, it is found on red skeletal muscle, cardiac muscle, red blood cells, liver, kidney cortex and tubule cells, adipose tissue, cerebral neurons, and glia (Adijanto and Philp, 2012; Halestrap, 2013). Since MCT1 is broadly expressed but retina is the only tissue reported to export succinate under basal conditions to date, we compared retina and eyecup to see if we could identify an intracellular difference that could contribute to determining if an MCT1-expressing tissue will export succinate.

In other tissues which can be induced to export succinate (such as exercising muscle or ischemic heart tissue), succinate export is accompanied by an increase in intracellular succinate levels (Chouchani et al., 2014; Prag et al., 2020; Reddy et al., 2020). We compared intracellular succinate levels between retina and eyecup tissue and saw that freshly-dissected retinas contain approximately 20-fold more succinate per μg protein compared to eyecups (**Figure 5.7A**). To test if increasing eyecup succinate levels might be sufficient to induce succinate export, we treated eyecups with the SDH inhibitor malonate and observed a dose-dependent increase in intracellular succinate levels **(Figure 5.7C**). When we sampled incubation media from eyecups incubated with malonate, we observed that import of exogenous succinate (m4) was significantly reduced, and that eyecups instead began to export endogenous succinate (m0) **(Figure 5.7D**). Export of endogenous m0 succinate was effectively shut down by the MCT1 inhibitors AZD3965 and Diclofenac. The nearly complete inhibition of malonate-induced m0 succinate export by AZD3965 in eyecups indicates that MCT3 is unable to transport succinate, since AZD3965 has been shown to have no inhibitory effect on MCT3 well below the concentration we used (Curtis et al., 2017). Taken together, these results show that a high intracellular succinate concentration is at least one contributing factor which determines if an MCT1-expressing tissue will export succinate **(Figure 5.7B**).

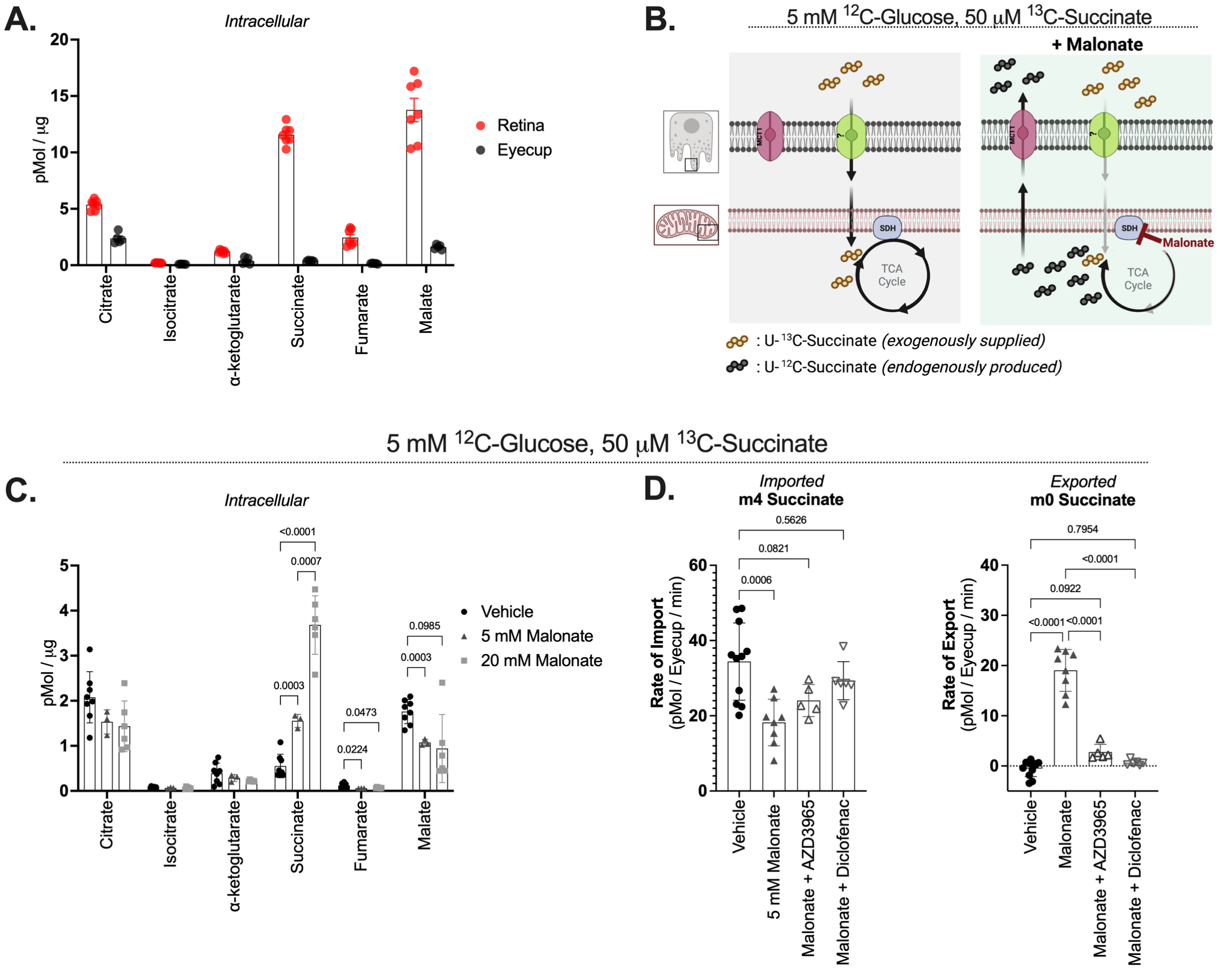

Figure 5.7: Inducible succinate export from eyecups
(A) Total intracellular metabolites per µg dry protein in freshly dissected retinas and eyecups (n = 7 retinas and 5 eyecups). **(B)** Influences of malonate on succinate dynamics in eyecups. **(C)** Intracellular metabolite levels per µg dry tissue in eyecups incubated in 0, 5, or 20 mM malonate for 40 minutes. P values determined using a one-way ANOVA followed by Dunnett's correction for multiple comparisons. (n = (8, Vehicle) (3, 5 mM) (6, 20 mM). **(D)** Rates of m4 succinate import and m0 succinate export from eyecup incubated with 5 mM malonate, 5 mM malonate + 100 nM AZD3965, or 5 mM malonate + 100 µM diclofenac. P values determined using a one-way ANOVA followed by Dunnett's correction for multiple comparisons. (n = (11, vehicle) (8, malonate) (5, Malonate + AZD3965) (6, malonate + diclofenac).

Discussion

This study was motivated by conflicting reports regarding the permeability of succinate and a desire to understand how succinate might move between cells in the eye. We observe that cerebellum, eyecup, liver, BAT, and kidney tissue are capable of oxidizing succinate *ex vivo*, and we conclusively confirm that eyecup succinate oxidation is legitimately transporter-mediated and does not occur due to loss of plasma membrane integrity. We add MCT1 to the model of succinate transit in the retinal ecosystem as the retinal succinate exporter, but not the eyecup succinate importer.

Since retinas can oxidize significant quantities of succinate only when permeabilized, they must be lacking the plasma membrane transporter that is expressed on eyecups. Based off this, published proteomics or RNAseq datasets (such as singlecell-eye.org) could be used to identify plasma membrane transporters which are expressed on the RPE but not the retina which could be screened for succinate transport capabilities.

We initially hypothesized that the inability of retinas to import and oxidize a significant quantity of succinate might be due to a limitation of mitochondrial function (for example, the retinal QH_2 pool might normally be too reduced to accept any electrons from succinate at SDH). However, since digitonin permeabilization confers retinas with the ability to deplete succinate from the incubation media (**Figure 5.2D**), entry into the cell must be the rate limiting step for succinate oxidation. This was unexpected, since retinas express high levels of MCT1 which we show is capable of exporting succinate.

Determining why MCT1 plays no significant role in importing succinate under physiological *ex vivo* conditions in both retinas and eyecups is important to understanding the biological implications of circulating succinate. The current understanding of MCT activity states that at equilibrium, there will be a balance between the $[H^+]_{out,}$ $[\text{monocarboxylate}]_{out}$ and $[H^+]_{in,}$ $[\text{monocarboxylate}]_{in}$ (Halestrap, 2012). Based off this, we reasoned that we might be able to detect MCT1-mediated succinate import in eyecups if we enhanced it by significantly lowering the extracellular pH and supplying a higher concentration of extracellular succinate (**Figure 5.4**); however, we were unable to detect any MCT1-mediated succinate import in this experiment. It is also surprising that even 100 mM succinate is unable to stimulate appreciable MCT1-mediated succinate import in retinas (**Figure 5.1**). One explanation is that retinas have an exceedingly low intracellular pH coupled with high intracellular succinate concentrations. Alternatively, there may be an undiscovered aspect to the mechanism of MCT1-mediated transport which favors succinate export over import.

In addition to being widely expressed in healthy tissues, MCT1 is upregulated in several types of cancer (Payen et al., 2020). Like healthy retina tissue, MCT1 overexpressing cancers rely heavily on aerobic glycolysis and convert a large fraction of the glucose they consume to lactate. Succinate has recently been identified as a metabolite exported by cancer cells and has been shown to promote metastatic activity through SUCNR1 signaling (Wu et al., 2020). Determining if this succinate export is MCT1 mediated will allow it to be targeted for inhibition by existing MCT1-specific chemotherapy drugs.

Acknowledgements

A portion of the results in this chapter can be found in two BioRxiv articles (https://doi.org/10.1101/2021.02.10.430650, https://doi.org/10.1101/2021.11.19.469314). The individuals who contributed to the work in this chapter are Celia M. Bisbach (CMB), Daniel T. Hass (DTH), Brian M. Robbings (BMR), Ian R. Sweet (IRS) and James B. Hurley (JBH). CMB, DTH, and JBH lead the conceptualization of the work and designed experiments. BMR contributed his excellent technical expertise by running perifusion experiments. IRS shared his lab space and training to allow CMB to perform radiation experiments and assisted with experimental design for perifusion experiments. DTH lead the collection and analysis of data shown in figures 5.1, and CMB collected and analyzed data shown in figures 5.2 – 5.7.

Methods

Ethical Approval: This study was carried out in accordance with the National Research Council's Guide for the Care and Use of Laboratory Animals (8th ed). All protocols were approved by the Institutional Animal Care and Use Committees at the University of Washington and the VA Puget Sound Hospital.

Animals: All experiments used 2-5 month-old male and female wild-type C57BL6/J mice. These mice were housed at an ambient temperature of 25°C, with a 12-hour light cycle and ad libitum access to water and normal rodent chow.

***Ex vivo* metabolite uptake/export:** In all *ex vivo* metabolic analysis experiments, mice were euthanized by awake cervical dislocation and retinas and/or eyecups were dissected in Hank's Buffered Salt Solution (HBSS; GIBCO, Cat#: 14025-076). Tissue was incubated them in Krebs-Ringer buffer (formulations used in each figure specified below below) supplemented with 5 mM glucose and [U-^{13}C]-succinic acid (Cambridge isotope CLM-1571-0.1) or [U-^{13}C]-malate (Cambridge isotope CLM-8065) as indicated in each figure. For experiments using KRB buffer, buffer was pre-equilibrated at 37°C, 21% O_2, and 5% CO_2 prior to incubations and incubations were carried out at those conditions. For experiments where pH was modulated KRM buffer was used, buffer was pre-equilibrated at 37°C and room oxygen and incubations were carried out under those conditions. For determination of metabolite uptake or export rates, incubation media was sampled at 3 timepoints (typically 0, 20, and 40 minutes) and export or uptake was confirmed to be in the linear range. Retinas were incubated in 200 μL and eyecups in 100 μL over this range of time. Inhibitors used were AZD3965 (Cayman Chemical no. 19912), AR-C155858 (MedChemExpress HY-13248), diclofenac sodium salt (Cayman Chemical no. 70680). Ethanol was used as a solvent for AZD3965, DMSO was used as a solvent for AR-C155858, and separate experiments were done using both DMSO and ethanol as a solvent for diclofenac.

Buffer formulations used: The experiments in figure 5.3E used conventional KRB (Krebs-Ringer Bicarbonate) buffer and sodium-free KRB, mixed to give the desired concentration of Na^+. The experiment in figure 5.4 used pH-adjustable KRM (Krebs-Ringer MOPS) buffer. All other experiments used conventional KRB.

Component (mM)	**Conventional KRB**	**Sodium-free KRB**	**pH-adjustable KRM**
NaCl	98.5	0	98.5
n-methyl-D-glucamine	0	98.5	0
KCl	5.1	5.1	5.1
KH_2PO_4	1.2	1.2	1.2
$MgSO_4$-$7H_2O$	1.2	1.2	1.2
$CaCl_2$-$2H_2O$	2.7	2.7	2.7
HEPES	20.8	20.8	10
$NaHCO_3$	25.9	0	0
Choline Bicarbonate	0	25.9	0
MOPs	0	0	15
HCl	0	To pH 7.4 at 37°C, 5% CO_2	To desired pH at 37°C, room air

Metabolite Extraction: Metabolites were extracted from tissue using 80% MeOH, 20% H_2O supplemented with 10 µM methylsuccinate (Sigma, M81209) as an internal standard to adjust for any metabolite loss during the extraction and derivatization procedures. The extraction buffer was equilibrated on dry ice, and 150 µL was added to each sample. Tissues were then disrupted by sonication and incubated on dry ice for 45 minutes to precipitate protein. Proteins were pelleted at 17,000 x g for 30 minutes at 4°C. The supernatant containing metabolites was lyophilized at room-temperature until dry and stored at -80°C until derivatization. The pellet containing protein was resuspended by sonication in RIPA buffer (150 mM NaCl, 1.0% Triton X-100, 0.5% sodium deoxycholate, 0.1% SDS, 50 mM Tris, pH 8.0) and the amount of protein was determined by a BCA assay (ThermoFisher, 23225). Media samples were directly added to 100% MeOH supplemented with 10 µM methylsuccinate and immediately lyophilized, then stored at -80 until derivatization.

Metabolite Derivatization: Lyophilized samples were first derivatized in 10 µL of 20 mg/mL methoxyamine HCl (Sigma, Cat#: 226904) dissolved in pyridine (Sigma, Cat#: 270970) at 37°C for 90 minutes, and subsequently with 10 µL tert-butyldimethylsilyl-N-methyltrifluoroacetamide (Sigma, Cat#: 394882) at 70°C for 60 minutes.

Gas Chromatography-Mass Spectrometry: Metabolites were analyzed on an Agilent 7890/5975C GC-MS using selected-ion monitoring methods described extensively in previous work (Du et al., 2015). Peaks were integrated in MSD ChemStation (Agilent), and correction for natural isotope abundance was performed using the software IsoCor (Millard et al., 2012). Corrected metabolite signals were converted to molar amounts by comparing metabolite peak abundances in samples with those in a 'standard mix' containing known quantities of metabolites we routinely measure. Multiple concentrations of this mix were extracted, derivatized, and run alongside samples in each experiment. These known metabolite concentrations were used to generate a standard curve which allowed for metabolite quantification. Metabolite abundance was normalized to tissue protein concentration. Following this, paired tissues such as retinas and eyecups from the same mouse were treated as technical replicates and averaged for in vivo infusion experiments. For ex vivo metabolite import/export analysis, retinas and eyecups from the same mouse were always used in different experimental conditions and thus were considered biological replicates.

Radioactivity: 2,3-^{3}H Succinic acid was obtained from American Radiolabeled Chemicals (ART-1700). KRB was prepared with 2,3-^{3}H Succinic acid and unlabeled succinate at a final concentration of 10 μM succinate (specific activity 60 μCi/mmol), and media was supplemented with 1 mM of competing dicarboxylate when applicable. Eyecups were incubated for 2 minutes (which was experimentally determined to be in the linear range of uptake) at 37°C in a 5% CO_2 incubator, then rinsed 3 times in 3 mL ice-cold KRB, transferred to a new vial, and sonicated in 200uL KRB in a water bath sonicator. The lysate was then transferred to a scintillation vial with 5mL scintillation fluid and ^{3}H counts were measured for 1 minute per sample.

LDH Assay: LDH quantification was performed using the CyQuant™ Cytotoxicity Assay kit (ThermoFisher C20300). Briefly, freshly dissected retinas and eyecups were incubated in 200 uL (retina) or 100 uL (eyecup) KRB buffer, supplemented with 5 mM ^{12}C-glucose and 50 μM ^{13}C-succinate and the indicated concentration of digitonin. 5 μL samples of the incubation media was taken at the indicated times for analysis. At the end of the experiment, tissue was homogenized in 200 uL of kit lysis buffer and 5 μL was used for tissue LDH quantification. Absorbance (490 nm) was measured during what was confirmed to be in the linear range of the reaction using a BioTek Synergy 4 plate reader.

***Ex vivo* oxygen consumption:** Following euthanasia, mouse tissues were dissected and cut into small segments in Hank's buffered salt solution. These tissues were incubated in Krebs-Ringer bicarbonate buffer (KRB) supplemented with 5 mM glucose and pre-equilibrated at 37°C and 5% CO_2. We determined OCR using a custom-built perifusion flow-culture system (Neal et al., 2015; Sweet et al., 2002). Tissues were perifused in chambers between Cytopore beads (Amersham Biosciences, Piscatawy, NJ) and porous frits. With KRB supplemented with 5 mM glucose, 1x Antibiotic-Antimycotic (Gibco), and 1 mg/mL fatty acid-free bovine serum albumin. An artificial lung oxygenated supplemented KRB with a mixture of 21% O_2, 5% CO_2, and 74% N_2.Oxygenated media was passed through a bubble trap before exposure to mouse tissues. Outflow media came into contact with a glass wall coated with a thin layer of oxygen sensitive polymerized Pt(II) Meso-tetra(pentafluorophenyl)porphine dye (Frontier Scientific, Logan, UT) painted on the inner glass wall of the chamber. Following a 405 nm light pulse, the dye-coated glass emits a phosphorescent signal detected at 650 nm. The decay lifetime is dependent on oxygen tension. The flow rate of KRB along with the quantitative relationship between dye phosphorescent decay and oxygen concentration were used to determine tissue OCR. All OCR measurements were obtained under control conditions (baseline, 5 mM glucose), one or more experimental conditions, and a ‘zeroed’ condition wherein 3 mM potassium cyanide (KCN) was used to directly inhibit complex IV and thus subtract the effect of residual non-mitochondrial oxygen consumption from our measurements.

Western Blot: Protein was extracted by sonication in RIPA buffer supplemented with a protease and phosphatase inhibitor cocktails (ThermoFisher, Cat#: 78442). SDS sample buffer was added and samples were run on 13% polyacrylamide gels. After running, gels were transferred onto PVDF membranes (Millipore, IPFL00010) and rinsed with PBS. Primary antibody (anti-NaDC3, 1:200 dilution, Ab56017 for blot shown in figure, similar results obtained with anti-NaDC3, 1:500 dilution, NBP1-69630, anti-Total OXPHOS antibody, Abcam, ab110413, 1:1000 dilution) was diluted in blocking buffer (LI-COR, 927–40,000) and incubated overnight on blots at 4°C. Membranes were washed twice with PBS containing 0.1% Tween-20 and once with PBS, then incubated with secondary antibody (IRDye 680RD goat anti-rabbit IgG (H + L) (LI- COR Biosciences, RRID AB_2721181) at 1:5000 in blocking buffer for 1 h at RT and washed again before imaging. Membranes were imaged and bands were quantified using the LI-COR Odyssey CLx Imaging System (RRID:SCR_014579).

Statistical Analysis: We performed all statistical data analyses using Prism Version 8 (GraphPad Software). The significance threshold was set at $p<0.05$. In all figures, *$p<0.05$, **$p<0.01$, ***$p<0.001$, and ****$p<0.0001$. (Figure 1) To fit curves of oxygen consumption as a function of [succinate], for each sample we averaged steady-state oxygen consumption over >5 minutes at the end of a given treatment. These averaged values were considered to be the OCR at each given [succinate] for each sample. We fit the curve to an allosteric sigmoidal shape in order to obtain approximations of V_{max}, $K_{1/2}$, and Hill's coefficient (h) (Table 1). (Figure 2) We estimated the half-life of infused m+4 succinate in blood by a one-phase decay function to the data. The abundance (Figure 2C), fractional labeling (Figure 2D), and ratios of metabolite isotopologues (Figure 2E) were compared using a one-way ANOVA. (Figure 5) We analyzed differences in respiration following treatments using one-way ANOVAs . The values input into these ANOVAs are averaged steady-state oxygen consumption over >5 minutes at the end of a given treatment.

Chapter 6: Concluding Remarks and Future Directions

Roles of mitochondrial Ca^{2+} uptake in photoreceptors

To address how mitochondrial Ca^{2+} uptake might influence photoreceptor metabolism and function, we used genetic strategies to increase or ablate expression of the Mitochondrial Calcium Uniporter (MCU) protein in photoreceptors and identified consequent changes in metabolism and physiology. The main conclusions from these experiments are:

1. Isocitrate Dehydrogenase (IDH) and α-ketoglutarate dehydrogenase (α-KGDH) are Ca^{2+} sensitive *in vivo*
2. MCU is not important for regulating metabolism or physiology in photoreceptors
3. Photoreceptors possess an MCU-independent mitochondrial Ca^{2+} uptake pathway

Isocitrate Dehydrogenase and α-ketoglutarate Dehydrogenase are stimulated by Ca2+ in vivo

Approximately 40 years ago, α-KGDH, IDH, and an isoform of Pyruvate Dehydrogenase Phosphatase (PDH1c) were identified as being stimulated by physiological levels of Ca^{2+} (Denton, 2009; Denton et al., 1972; McCormack and Denton, 1979; Rutter and Denton, 1988). This observation contributed to the following model describing how Ca^{2+}-stimulates ATP production:

1) cytosolic Ca^{2+} rises during conditions of transient high energy demand,
2) mitochondria take up cytosolic Ca^{2+} (through an as-yet-unidentified transporter),
3) Ca^{2+} stimulates the three mitochondrial dehydrogenases to enhance NADH production, allowing cells to increase oxidative phosphorylation to meet the new ATP demand.

This model was built upon *ex vivo* experiments using isolated enzymes and purified mitochondria. More recently, the identification of the molecular identity of the MCU has allowed this model to be better tested. Of the three dehydrogenases, only the *in vivo* regulation of PDP1c by Ca^{2+} has been convincingly demonstrated in some $MCU^{-/-}$ mouse tissues. However, it is notable that a Ca^{2+}-dependent PDP1c phenotype was only observed under conditions of fasting, when PDH has been phosphorylated via an alternative regulation pathway. The fact that secondary regulation of PDH must first be engaged for the Ca^{2+}-dependent activity of PDP1c to be observed calls into question the hypothesis that Ca^{2+} stimulation of PDP1c can effectively stimulate metabolism in isolation.

Direct *in vivo* proof that α-KGDH and IDH are Ca^{2+} sensitive and that their activities are rate limiting in periods of high energy demand has been much more difficult to obtain, since Ca^{2+} binding to these enzymes does not result in measurable post-translational modifications. Our observation that the distribution of TCA cycle metabolites up- and downstream of these two dehydrogenases shifts upon MCU overexpression appears to be the most direct *in vivo* evidence of their Ca^{2+} sensitivity to date. However, just because the K_M's of these enzymes can be changed by Ca^{2+} *in vivo* does not automatically mean there will be a physiologically significant increase in the amount of ATP produced through oxidative phosphorylation. The fact that we see no metabolic or functional defects upon loss of $MCU^{-/-}$ expression in photoreceptors (even in the high-Ca^{2+}, high energy-demanding state of darkness) suggests that α-KGDH and IDH may not normally be rate limiting for flux through OXHPOS. This further calls the importance of Ca^{2+} stimulation of these enzymes into question.

Recently, an alternative hypothesis has been presented which suggests that instead of Ca^{2+}-sensitive matrix dehydrogenases, the Malate-Aspartate Shuttle (MAS) is the link between Ca^{2+} and stimulation of mitochondrial ATP production (Szibor et al., 2020). This model states that:

1. cytosolic Ca^{2+} rises during conditions of transient high energy demand
2. Ca^{2+} stimulates Aralar via its IMS-facing EF hands, enhancing flux through the MAS and regenerating cytosolic NAD^+
3. cytosolic NAD^+ availability increases flux through glycolysis, increasing pyruvate production and subsequent acetyl-CoA availability for TCA cycle flux

This model does not refute that there are Ca^{2+}-sensitive matrix dehydrogenases, but it does suggest that they are not rate limiting and thus are unimportant for controlling overall flux through the entire mitochondrial OXPHOS pathway. This is consistent with our observations in Chapters 2 and 3. There is some evidence that this model may be applicable specifically in photoreceptors, since retinas from mice lacking expression of Aralar have been reported to have significantly greater dark-dependent metabolic defects than those we observed in $MCU^{-/-}$ retinas in **Figure 3.5** (Du et al., 2016b). However, this model is still in its infancy, based entirely on *ex vivo* experiments, and is not without criticism (Gellerich et al., 2020; Rutter et al., 2020). It should be thoroughly tested *in viv*o before it is accepted as the explanation for the mild-to-nonexistent metabolic phenotypes resulting from loss of MCU.

Photoreceptor function does not depend on MCU

Increasing MCU expression ~100-fold resulted in altered activities of Ca^{2+}-sensitive reactions in both the mitochondria and cytosol (**Chapter 2**). However, the extremely mild phenotypes exhibited by $MCU^{-/-}$ photoreceptors show that fraction of mitochondrial Ca^{2+} uptake mediated specifically by MCU plays no role in modulating photoreceptor activity (**Chapter 3**). It is important to emphasize that we cannot conclude with absolute finality that mitochondrial Ca^{2+} uptake plays no role at all in modulating photoreceptor activity, since the sustained mitochondrial Ca^{2+} uptake exhibited by $MCU^{-/-}$ photoreceptors (**Figure 3.2**) might still be physiologically important, although it has slower kinetics than what would be required to meaningfully modulate the photoresponse.

The residual mitochondrial Ca^{2+} uptake we observe in $MCU^{-/-}$ cones is not the first evidence for an alternative mitochondrial Ca^{2+} uptake pathway in a neuronal cell type. The first clue that neurons might have an MCU-independent Ca^{2+} uptake pathway came from the observation that PDH phosphatase could be stimulated by elevated cytosolic Ca^{2+} in $MCU^{-/-}$ cortical neurons (Nichols et al., 2016). An independent group then observed that mitochondria isolated from $MCU^{-/-}$ brains maintain some mitochondrial Ca^{2+} uptake, while mitochondria isolated from other tissues from the same animals do not (Hamilton et al., 2018). The report from Hamilton et al. fits most closely with our observation that mitochondrial clusters from MCU$^{-/-}$ zebrafish still take up Ca^{2+} (**Figure 3.2D**). An important difference between these findings and our results is that Ru360 was able to strongly inhibit the residual Ca^{2+} uptake in brain mitochondria, while we saw that Ru360 had no influence on the residual Ca^{2+} uptake in cone mitochondria (**Figure 3.2D-F**) (Hamilton et al., 2018).

Identification of the putative alternative mitochondrial Ca^{2+} uptake pathway in photoreceptors and other neurons will be challenging. It would be ideal to first rule out other mitochondrial proteins with known Ca^{2+}-transport abilities, such as the Ca^{2+}/H^+ exchanger Letm1 and the mitochondrial Na^+/Ca^{2+} exchanger (Smets et al., 2004; Tsai et al., 2014). If known mitochondrial Ca^{2+} transporters can be ruled out, photoreceptor mitochondria could be selectively purified using a tissue-specific MITO-tag mouse and an unbiased mass spectrometry approach could be attempted to identify a novel, neuron-specific Ca^{2+} transporter (Bayraktar et al., 2019).

Succinate in the retinal ecosystem

In the second half of this dissertation, the metabolic adaptations made by photoreceptors and RPE cells in response to the very different levels of O_2 they are exposed to in the vertebrate eye are explored. The key findings which highlight the relationship between O_2 tension and metabolism in the retina and RPE are:

1. There is significant flux through the reverse SDH pathway in retinas
2. Eyecups import succinate, possibly through a noncanonical succinate transporter
3. Retinas export succinate via MCT1 and do not express the eyecup succinate importer

Retinas reduce fumarate to succinate

In **Figure 4.6**, we quantitatively establish that retinas rely heavily on reversal of SDH activity to maintain a large portion of their succinate pool. Under normal conditions, reversal of the canonical SDH reaction and the subsequent reduction of fumarate to succinate would be a problematic drain on ETC reducing power since electrons that could be used to generate a proton gradient are instead exiting the ETC early. However, the ability to reverse canonical SDH activity would be an asset to cells in the absence of oxygen, since the use of fumarate as an electron acceptor can sustain proton pumping at complex I, allowing ATP synthesis to continue to some degree.

In **Figure 4.8A-C**, we show a link between O_2 tension, low COXIV expression, and reversal of SDH. However, it is very likely the photoreceptors possess additional undiscovered molecular adaptations which facilitate reversal of SDH. While limited CIV expression appears to contribute to maintaining a reduced QH_2 pool (**Figure 4.8**), there are clues that this is not the only adaptation driving reversal of SDH. The correlation we observed between amount of reverse SDH activity and pO_2 preconditioning in **Figure 4.8C** was imperfect, indicating there may be other variables modulating reversal of SDH in retinas. Furthermore, the observed low expression of COXIV in retinal lysate by western blot (**Figure 4.8A)** does not necessarily match histochemistry reporting high CIV activity in mouse and zebrafish photoreceptors (Giarmarco et al., 2020; Rueda et al., 2016). Since we showed that modulating activity of CI can also influence reversal of SDH in **Figure 4.8G-I**, an alternative hypothesis that should be further explored is that instead of only low COXIV expression, retinas may instead have a mismatch of CI and CIV expression and/or activity. If CI activity were much greater than CIV activity, the influx of electrons to the ETC would be greater than the efflux. This would result in an overly reduced QH_2 pool which could drive the SDH reversal we observe in retinas.

There may be uncharacterized succinate transporters

There remains a significant unanswered question regarding the molecular identity of the succinate importer in eyecups. We initially hypothesized that a member of the Slc13 family of sodium-coupled dicarboxylate transporters was the most likely candidate, and some features of succinate uptake in eyecups (like sensitivity to inhibition by certain dicarboxylates) are eerily similar to characteristics of NaDC1 and NaDC3 (**Figure 5.3D**).

However, the sustained uptake of succinate in the absence of sodium effectively rules out a sodium-linked transporter (**Figure 5.3E**).

A consistent observation made in all experiments where eyecup tissue was supplied with succinate is an increase in the rates of fumarate and malate export (**Figure 4.3D and 4.3E**). It is possible that this occurs due to increased synthesis resulting from succinate anaplerosis. However, an alternative explanation is that the putative succinate importer acts as a dicarboxylate exchanger. A candidate family of transporters which should be further investigated with this in mind are the Slc22 family of Organic Anion Transporters (OATs). OATs are most well studied in the kidney, where they utilize a dicarboxylate gradient produced by sodium-coupled dicarboxylate carriers to couple import of organic anions with export of a dicarboxylate. This facilitates filtration of organic anions out of the blood so they can be extruded in urine (Nigam et al., 2015).

Outside of the kidney, OATs can be found in barrier epithelium cells in several different tissues, and OAT1 and OAT3 expression are reported in the retinal pigment epithelium (Lee et al., 2015). OAT1 and OAT3 have millimolar affinities for succinate, although it is unclear if the dicarboxylates fumarate or malate are able to substitute for the larger organic anions usually exchanged by OATs (Kaufhold et al., 2011). In an experiment too preliminary to include in this thesis, the OAT inhibitor probenecid was ineffective at reducing succinate import in eyecups. However, this hypothesis needs to be more stringently tested before OATs can be fully discounted as the eyecup succinate importers.

MCT1-mediated succinate transit in ocular tissues is one-way

We find that succinate travels in a one-way circuit in the vertebrate eye: retinas exclusively export succinate and do not effectively import it, and eyecups exclusively import succinate and do not normally export it (**Chapter 4, Chapter 5**). While we do not conclusively identify the succinate importer in eyecups, we find evidence that MCT1 is the transporter which exports a portion of succinate in retinas (**Figures 5.5** and **5.6**).

Future work should focus on 1) characterizing this transit in intact tissues, and 2) determining why retina-to-RPE succinate delivery is important for ocular health.

Obtaining *in vivo* evidence of a metabolite cycle between different tissues is a huge challenge. For example, even the relatively famous neuronal-astrocyte lactate shuttle is still debated by some due to weak *in vivo* evidence (Díaz-García et al., 2017; Mächler et al., 2016). We have taken the initial steps to test the existence of succinate/malate exchange *in vivo* by performing experiments where we infuse ^{13}C-metabolites prior to euthanizing mice. This has provided preliminary validation that retinas in a living mouse exhibit reverse SDH activity and reduce fumarate to succinate. Now that we have identified the retinal succinate exporter as MCT1, we can use this to our advantage in designing experiments to specifically test if RPE cells in eyecups import succinate produced in the retina. For example, we could infuse a retina-specific MCT1$^{-/-}$ mouse with ^{13}C-malate and determine if less m4 succinate accumulates in eyecup tissue. This would be promising evidence that the retina feeds the RPE with succinate in a living animal.

At the end of **Chapter 4**, we hypothesized that succinate exported from the retina might have the role of enhancing O_2 consumption in the RPE to protect the retina from O_2 damage. We attempted to test this hypothesis by determining if secondary cone death (caused in part by oxidative damage) in two retinitis pigmentosa mouse models was reduced by supplementing mouse drinking water with 2% sodium succinate (Komeima et al., 2006; Punzo et al., 2012; Shen et al., 2005). We found that succinate was ineffective in rescuing either rod or cone visual function in Rho$^{P23H/+}$ or Rd10$^{-/-}$ mice. However, succinate was recently shown to prolong visual function in a Pde6α preclinical mouse model of autosomal recessive retinitis pigmentosa (Rowe et al., 2021). Supplementing other TCA cycle metabolites (citrate and α-ketoglutarate) resulted in a similar degree of rescue in this study. Since citrate and α-ketoglutarate are not as effective at stimulating RPE oxygen consumption as succinate, it is likely that the mechanism of rescue observed by succinate is not through the "O_2 shield" mechanism we hypothesized. Notably, in communication with Rowe et al. we learned they also attempted to rescue degeneration in Rho$^{P23H/+}$ mice with succinate and replicated our result that it was ineffective. This indicates succinate might not rescue a “general” symptom of retinitis pigmentosa (such as oxidative stress-induced secondary cone death) but may instead ameliorate a specific problem in retinitis pigmentosa caused by Pde6α mutation.

By identifying the retinal succinate exporter, we hoped we would be able to harness it to study the role of succinate exchange in the retinal ecosystem by enhancing or decreasing its expression. Unfortunately, the canonical role of MCT1 as a lactate and pyruvate transporter is fundamental to retinal health and it would be difficult to parse any succinate-specific phenotype from disruptions caused by inhibition of lactate and pyruvate transport. However, this general strategy may still be pursued once the RPE succinate importer has been identified.

References

Adijanto, J., and Philp, N.J. (2012). The SLC16A family of monocarboxylate transporters (MCTs)-physiology and function in cellular metabolism, pH homeostasis, and fluid transport (Elsevier).

Adijanto, J., Du, J., Moffat, C., Seifert, E.L., Hurley, J.B., and Philp, N.J. (2014). The retinal pigment epithelium utilizes fatty acids for ketogenesis implications for metabolic coupling with the outer retina. J. Biol. Chem. *289*, 20570–20582.

Ames, A., Li, Y.Y., Heher, E.C., and Kimble, C.R. (1992). Energy metabolism of rabbit retina as related to function: High cost of Na+ transport. J. Neurosci. *12*, 840–853.

Andersen, C.L., Jensen, J.L., and Ørntoft, T.F. (2004). Normalization of real-time quantitative reverse transcription-PCR data: a model-based variance estimation approach to identify genes suited for normalization, applied to bladder and colon cancer data sets. Cancer Res. *64*, 5245–5250.

Andrienko, T.N., Pasdois, P., Pereira, G.C., Ovens, M.J., and Halestrap, A.P. (2017). The role of succinate and ROS in reperfusion injury – A critical appraisal. J. Mol. Cell. Cardiol. *110*, 1–14.

Ban, Y., and Rizzolo, L.J. (2000). Regulation of glucose transporters during development of the retinal pigment epithelium. Dev. Brain Res. *121*, 89–95.

Barnes, S., and Kelly, M.E.M. (2002). Calcium channels at the photoreceptor synapse. Adv. Exp. Med. Biol. *514*, 465–476.

Baughman, J.M., Perocchi, F., Girgis, H.S., Plovanich, M., Belcher-Timme, C.A., Sancak, Y., Bao, X.R., Strittmatter, L., Goldberger, O., Bogorad, R.L., et al. (2011). Integrative genomics identifies MCU as an essential component of the mitochondrial calcium uniporter. Nature *476*, 341–345.

Baumgartner, H.K., Gerasimenko, J. V., Thorne, C., Ferdek, P., Pozzan, T., Tepikin, A. V., Petersen, O.H., Sutton, R., Watson, A.J.M., and Gerasimenko, O. V. (2009). Calcium elevation in mitochondria is the main Ca2+ requirement for mitochondrial permeability transition pore (mPTP) opening. J. Biol. Chem. *284*, 20796–20803.

Bayraktar, E.C., Baudrier, L., Özerdem, C., Lewis, C.A., Chan, S.H., Kunchok, T., Abu-Remaileh, M., Cangelosi, A.L., Sabatini, D.M., Birsoy, K., et al. (2019). MITO-Tag Mice enable rapid isolation and multimodal profiling of mitochondria from specific cell types in vivo. Proc. Natl. Acad. Sci. U. S. A. *116*, 303–312.

Beutner, G., Sharma, V.K., Giovannucci, D.R., Yule, D.I., and Sheu, S.S. (2001). Identification of a ryanodine receptor in rat heart mitochondria. J. Biol. Chem. *276*, 21482–21488.

Bisbach, C.M., Hass, D.T., Robbings, B.M., Rountree, A.M., Sadilek, M., Sweet, I.R., and Hurley, J.B. (2020). Succinate Can Shuttle Reducing Power from the Hypoxic Retina to the O2-Rich Pigment Epithelium. Cell Rep. *31*, 107606.

Brockerhoff, S.E. (2017). Genome Editing to Study Ca2+ Homeostasis in Zebrafish Cone Photoreceptors. In Precision Medicine, CRISPR, and Genome Engineering: Moving from Association to Biology and Therapeutics, S.H. Tsang, ed. (Cham: Springer International Publishing), pp. 91–100.

Brown, S., Muhamad, N., C Pedley, K., and C Simcock, D. (2014). The Kinetics of Enzyme Mixtures. Mol. Biol. Res. Commun. *3*, 21–32.

Campochiaro, P.A., and Mir, T.A. (2018). The mechanism of cone cell death in Retinitis Pigmentosa. Prog. Retin. Eye Res. *62*, 24–37.

Cascarano, J., Ades, I.Z., and O'Connor, J.D. (1976). Hypoxia: A succinate-fumarate electron shuttle between peripheral cells and lung. J. Exp. Zool. *198*, 149–153.

Chen, Y., Song, X., Ye, S., Miao, L., Zhu, Y., Zhang, R.-G., and Ji, G. (2013). Structural insight into enhanced calcium indicator GCaMP3 and GCaMPJ to promote further improvement. Protein Cell *4*, 299–309.

Chidlow, G., Wood, J.P.M., Graham, M., and Osborne, N.N. (2005). Expression of monocarboxylate transporters in rat ocular tissues. Am. J. Physiol. - Cell Physiol. *288*, 416–428.

Chinchore, Y., Begaj, T., Wu, D., Drokhlyansky, E., and Cepko, C.L. (2017). Glycolytic reliance promotes anabolism in photoreceptors. Elife *6*, 1–3.

Chinopoulos, C. (2019). Succinate in ischemia: Where does it come from? Int. J. Biochem. Cell Biol. *115*, 105580.

Chouchani, E.T., Pell, V.R., Gaude, E., Aksentijević, D., Sundier, S.Y., Robb, E.L., Logan, A., Nadtochiy, S.M., Ord, E.N.J., Smith, A.C., et al. (2014). Ischaemic accumulation of succinate controls reperfusion injury through mitochondrial ROS. Nature *515*, 431–435.

Chouchani, E.T., Pell, V.R., James, A.M., Work, L.M., Saeb-Parsy, K., Frezza, C., Krieg, T., and Murphy, M.P. (2016). A unifying mechanism for mitochondrial superoxide production during ischemia-reperfusion injury. Cell Metab. *23*, 254–263.

Cohen, L.H., and Noell, W.K. (1960). Glucose Catabolism of Rabbit Retina before and after Development of Visual Function. J. Neurochem. *5*, 253–276.

Cooper, L.L., Hansen, R.M., Darras, B.T., Korson, M., Dougherty, F.E., Shoffner, J.M., and Fulton, A.B. (2002). Rod Photoreceptor Function in Children With Mitochondrial Disorders. Arch. Ophthalmol. *120*, 1055.

Cordes, T., Lucas, A., Divakaruni, A.S., Murphy, A.N., Cabrales, P., and Metallo, C.M. (2020). Itaconate modulates tricarboxylic acid and redox metabolism to mitigate reperfusion injury. Mol. Metab. *32*, 122–135.

Csordás, G., Golenár, T., Seifert, E.L., Kamer, K.J., Sancak, Y., Perocchi, F., Moffat, C., Weaver, D., Perez, S.D.L.F.,

Bogorad, R., et al. (2013). MICU1 controls both the threshold and cooperative activation of the mitochondrial Ca2+ uniporter. Cell Metab. *17*, 976–987.
Curtis, N.J., Mooney, L., Hopcroft, L., Michopoulos, F., Whalley, N., Zhong, H., Murray, C., Logie, A., Revill, M., Byth, K.F., et al. (2017). Pre-clinical pharmacology of AZD3965, a selective inhibitor of MCT1: DLBCL, NHL and Burkitt's lymphoma anti-tumor activity. Oncotarget *8*, 69219–69236.
DeLuca, H., and Engstrom, G. (1961). Calcium Uptake by Rat Kidney Mitochondria. *47*, 1744–1750.
Denton, R.M. (2009). Regulation of mitochondrial dehydrogenases by calcium ions. Biochim. Biophys. Acta - Bioenerg. *1787*, 1309–1316.
Denton, R.M., Randle, P.J., and Martin, B.R. (1972). Stimulation by Calcium Ions of Pyruvate Dehydrogenase Phosphate Phosphatase. J. Exp. Biol. *128*, 161–163.
Denton, R.M., McCormack, J.G., and Edgell, N.J. (1980). Role of calcium ions in the regulation of intramitochondrial metabolism. Effects of Na+, Mg2+ and ruthenium red on the Ca2+-stimulated oxidation of oxoglutarate and on pyruvate dehydrogenase activity in intact rat heart mitochondria. Biochem. J. *190*, 107–117.
Díaz-García, C.M., Mongeon, R., Lahmann, C., Koveal, D., Zucker, H., and Yellen, G. (2017). Neuronal Stimulation Triggers Neuronal Glycolysis and Not Lactate Uptake. Cell Metab. *26*, 361-374.e4.
Doonan, P.J., Chandramoorthy, H.C., Hoffman, N.E., Zhang, X., Cárdenas, C., Shanmughapriya, S., Rajan, S., Vallem, S., Chen, X., Foskett, J.K., et al. (2014). LETM1-dependent mitochondrial Ca2+ flux modulates cellular bioenergetics and proliferation. FASEB J. *28*, 4936–4949.
Du, J., Cleghorn, W.M., Contreras, L., Lindsay, K., Rountree, A.M., Chertov, A.O., Turner, S.J., Sahaboglu, A., Linton, J., Sadilek, M., et al. (2013a). Inhibition of mitochondrial pyruvate transport by Zaprinast causes massive accumulation of aspartate at the expense of glutamate in the retina. J. Biol. Chem. *288*, 36129–36140.
Du, J., Cleghorn, W., Contreras, L., Linton, J.D., Chan, G.C.-K., Chertov, A.O., Saheki, T., Govindaraju, V., Sadilek, M., Satrústegui, J., et al. (2013b). Cytosolic reducing power preserves glutamate in retina. Proc. Natl. Acad. Sci. *110*, 18501–18506.
Du, J., Cleghorn, W., Contreras, L., Linton, J.D., Chan, G.C.-K., Chertov, A.O., Saheki, T., Govindaraju, V., Sadilek, M., Satrustegui, J., et al. (2013c). Cytosolic reducing power preserves glutamate in retina. Proc. Natl. Acad. Sci. *110*, 18501–18506.
Du, J., Linton, J.D., and Hurley, J.B. (2015). Probing Metabolism in the Intact Retina Using Stable Isotope Tracers (Elsevier Inc.).
Du, J., Yanagida, A., Knight, K., Engel, A.L., Vo, A.H., Jankowski, C., Sadilek, M., Tran, V.T.B., Manson, M.A., Ramakrishnan, A., et al. (2016a). Reductive carboxylation is a major metabolic pathway in the retinal pigment epithelium. Proc. Natl. Acad. Sci. *113*, 14710–14715.
Du, J., Rountree, A., Cleghorn, W.M., Contreras, L., Lindsay, K.J., Sadilek, M., Gu, H., Djukovic, D., Raftery, D., Satrústegui, J., et al. (2016b). Phototransduction Influences Metabolic Flux and Nucleotide Metabolism in Mouse Retina. J. Biol. Chem. *291*, 4698–4710.
Ehinger, J.K., Piel, S., Ford, R., Karlsson, M., Sjövall, F., Frostner, E.Å., Morota, S., Taylor, R.W., Turnbull, D.M., Cornell, C., et al. (2016). Cell-permeable succinate prodrugs bypass mitochondrial complex i deficiency. Nat. Commun. *7*, 1–8.
Fain, G.L., Matthews, H.R., Cornwall, M.C., and Koutalos, Y. (2001). Adaptation in vertebrate photoreceptors. Physiol. Rev. *81*, 117–151.
Flicker, D., Sancak, Y., Mick, E., Goldberger, O., and Mootha, V.K. (2019). Exploring the In Vivo Role of the Mitochondrial Calcium Uniporter in Brown Fat Bioenergetics. Cell Rep. *27*, 1364-1375.e5.
Fukuda, R., Zhang, H., Kim, J. whan, Shimoda, L., Dang, C. V., and Semenza, G.L.L. (2007). HIF-1 Regulates Cytochrome Oxidase Subunits to Optimize Efficiency of Respiration in Hypoxic Cells. Cell *129*, 111–122.
Gage, G.J., Kipke, D.R., and Shain, W. (2012). Whole animal perfusion fixation for rodents. J. Vis. Exp. 1–9.
Gellerich, F.N., Szibor, M., Gizatullina, Z., Lessmann, V., Schwarzer, M., Doenst, T., Vielhaber, S., and Kunz, W.S. (2020). Reply to Rutter et al.: The roles of cytosolic and intramitochondrial Ca21 and the mitochondrial Ca21-uniporter (MCU) in the stimulation of mammalian oxidative phosphorylation. J. Biol. Chem. *295*, 10507.
George, R.L., Huang, W., Naggar, H.A., Smith, S.B., and Ganapathy, V. (2004). Transport of N-acetylaspartate via murine sodium/dicarboxylate cotransporter NaDC3 and expression of this transporter and aspartoacylase II in ocular tissues in mouse. Biochim. Biophys. Acta - Mol. Basis Dis. *1690*, 63–69.
Gherardi, G., Nogara, L., Ciciliot, S., Fadini, G.P., Blaauw, B., Braghetta, P., Bonaldo, P., De Stefani, D., Rizzuto, R., and Mammucari, C. (2018). Loss of mitochondrial calcium uniporter rewires skeletal muscle metabolism and substrate preference. Cell Death Differ.
Giarmarco, M.M., Cleghorn, W.M., Sloat, S.R., Hurley, J.B., and Brockerhoff, S.E. (2017a). Mitochondria maintain distinct Ca $^{2+}$ pools in cone photoreceptors. J. Neurosci. *37*, 2689–16.
Giarmarco, M.M., Cleghorn, W.M., Sloat, S.R., Hurley, J.B., and Brockerhoff, S.E. (2017b). Mitochondria maintain distinct Ca2+ pools in cone photoreceptors. J. Neurosci. *37*, 2689–16.
Giarmarco, M.M., Cleghorn, W.M., Hurley, J.B., and Brockerhoff, S.E. (2018). Preparing fresh retinal slices from adult zebrafish for ex vivo imaging experiments. J. Vis. Exp. *2018*, 1–11.
Giarmarco, M.M., Brock, D.C., Robbings, B.M., Cleghorn, W.M., Tsantilas, K.A., Kuch, K.C., Ge, W., Rutter, K.M., Parker, E.D., Hurley, J.B., et al. (2020). Daily mitochondrial dynamics in cone photoreceptors. Proc. Natl. Acad. Sci.

U. S. A. *117*, 28816–28827.
Glancy, B., and Balaban, R.S. (2012). Role of Mitochondrial Ca $^{2+}$ in the Regulation of Cellular Energetics. Biochemistry *51*, 2959–2973.
Griffiths, E.J., and Rutter, G.A. (2009). Mitochondrial calcium as a key regulator of mitochondrial ATP production in mammalian cells. BBA - Bioenerg. *1787*, 1324–1333.
Halestrap, A.P. (2012). The monocarboxylate transporter family-Structure and functional characterization. IUBMB Life *64*, 1–9.
Halestrap, A.P. (2013). Monocarboxylic Acid Transport. Compr. Physiol. *3*, 1611–1643.
Hamilton, J., Brustovetsky, T., Rysted, J.E., Lin, Z., Usachev, Y.M., and Brustovetsky, N. (2018). Deletion of mitochondrial calcium uniporter incompletely inhibits calcium uptake and induction of the permeability transition pore in brain mitochondria. J. Biol. Chem. *293*, 15652–15663.
Han, J.Y.S., Kinoshita, J., Bisetto, S., Bell, B.A., Nowak, R.A., Peachey, N.S., and Philp, N.J. (2020). Role of monocarboxylate transporters in regulating metabolic homeostasis in the outer retina: Insight gained from cell-specific Bsg deletion. FASEB J. *34*, 5401–5419.
Hems, R., Stubbs, M., and Krebs, H.A. (1968). Restricted permeability of rat liver for glutamate and succinate. Biochem. J. *107*, 807–815.
Hoang, Q. V., Linsenmeier, R.A., Chung, C.K., and Curcio, C.A. (2002). Photoreceptor inner segments in monkey and human retina: Mitochondrial density, optics, and regional variation. Vis. Neurosci. *19*, 395–407.
Hochachka, P.W., Owen, T.G., Allen, J.F., and Whittow, G.C. (1975). Multiple end products of anaerobiosis in diving vertebrates. Comp. Biochem. Physiol. -- Part B Biochem. *50*, 17–22.
Hoffman, N.E., Chandramoorthy, H.C., Shamugapriya, S., Zhang, X., Rajan, S., Mallilankaraman, K., Gandhirajan, R.K., Vagnozzi, R.J., Ferrer, L.M., Sreekrishnanilayam, K., et al. (2013). MICU1 motifs define mitochondrial calcium uniporter binding and activity. Cell Rep. *5*, 1576–1588.
Holmström, K.M., Pan, X., Liu, J.C., Menazza, S., Liu, J., Nguyen, T.T., Pan, H., Parks, R.J., Anderson, S., Noguchi, A., et al. (2015). Assessment of cardiac function in mice lacking the mitochondrial calcium uniporter. J. Mol. Cell. Cardiol. *85*, 178–182.
Hsu, S.C., and Molday, R.S. (1991). Glycolytic enzymes and a GLUT-1 glucose transporter in the outer segments of rod and cone photoreceptor cells. J. Biol. Chem. *266*, 21745–21752.
Huang, Gudi, R., Wu, P., Harris, R. a, Hamilton, J., and Popov, K.M. (1998). Isoenzymes of Pyruvate Dehydrogenase Phosphatase. Biochemistry *273*, 17680–17688.
Huang, W., Wang, H., Kekuda, R., Fei, Y.J., Friedrich, A., Wang, J., Conway, S.J., Cameron, R.S., Leibach, F.H., and Ganapathy, V. (2000). Transport of N-acetylaspartate by the Na+-dependent high-affinity dicarboxylate transporter NaDC3 and its relevance to the expression of the transporter in the brain. J. Pharmacol. Exp. Ther. *295*, 392–403.
Hutto, R.A., Bisbach, C.M., Abbas, F., Brock, D.C., Cleghorn, W.M., Parker, E.D., Bauer, B.H., Ge, W., Vinberg, F., Hurley, J.B., et al. (2020). Increasing Ca2+ in photoreceptor mitochondria alters metabolites, accelerates photoresponse recovery, and reveals adaptations to mitochondrial stress. Cell Death Differ. *27*, 1067–1085.
Jakob, R., Beutner, G., Sharma, V.K., Duan, Y., Gross, R.A., Hurst, S., Jhun, B.S., O-Uchi, J., and Sheu, S.S. (2014). Molecular and functional identification of a mitochondrial ryanodine receptor in neurons. Neurosci. Lett. *575*, 7–12.
Jeon, C.J., Strettoi, E., and Masland, R.H. (1998). The major cell populations of the mouse retina. J Neurosci *18*, 8936–8946.
Jiang, D., Zhao, L., Clish, C.B., and Clapham, D.E. (2013). Letm1, the mitochondrial Ca2+/H+ antiporter, is essential for normal glucose metabolism and alters brain function in Wolf-Hirschhorn syndrome. Proc. Natl. Acad. Sci. U. S. A. *110*.
Jolly, W.W., Wilhelm, D.D., and Harris, R.A. (1979). Assessment of tissue and cell damage by succinate oxidation. J. Mol. Cell. Cardiol. *11*, 485–500.
Kanow, M.A., Giarmarco, M.M., Jankowski, C.S., Tsantilas, K., Engel, A.L., Du, J., Linton, J.D., Farnsworth, C.C., Sloat, S.R., Rountree, A., et al. (2017). Biochemical adaptations of the retina and retinal pigment epithelium support a metabolic ecosystem in the vertebrate eye. Elife *6*, e28899.
Kaufhold, M., Schulz, K., Breljak, D., Gupta, S., Henjakovic, M., Krick, W., Hagos, Y., Sabolic, I., Burckhardt, B.C., and Burckhardt, G. (2011). Differential interaction of dicarboxylates with human sodium-dicarboxylate cotransporter 3 and organic anion transporters 1 and 3. Am. J. Physiol. - Ren. Physiol. *301*.
Kekuda, R., Wang, H., Huang, W., Pajor, A.M., Leibach, F.H., Devoe, L.D., Prasad, P.D., and Ganapathy, V. (1999). Primary structure and functional characteristics of a mammalian sodium- coupled high affinity dicarboxylate transporter. J. Biol. Chem. *274*, 3422–3429.
Kennedy, B.N., Alvarez, Y., Brockerhoff, S.E., Stearns, G.W., Sapetto-Rebow, B., Taylor, M.R., and Hurley, J.B. (2007). Identification of a Zebrafish Cone Photoreceptor–Specific Promoter and Genetic Rescue of Achromatopsia in the *nof* Mutant. Investig. Opthalmology Vis. Sci. *48*, 522.
Kim, J.H., Lee, S.-R., Li, L.-H., Park, H.-J., Park, J.-H., Lee, K.Y., Kim, M.-K., Shin, B.A., and Choi, S.-Y. (2011). High Cleavage Efficiency of a 2A Peptide Derived from Porcine Teschovirus-1 in Human Cell Lines, Zebrafish and Mice. PLoS One *6*, e18556.
Knoll, A.H., Bergmann, K.D., and Strauss, J. V. (2016). Life: The first two billion years. Philos. Trans. R. Soc. B Biol. Sci. *371*.

Kolb, H., Strauss, O., and Fu, Y. (2012). Webvision.

Komeima, K., Rogers, B.S., Lu, L., and Campochiaro, P.A. (2006). Antioxidants reduce cone cell death in a model of retinitis pigmentosa. Proc. Natl. Acad. Sci. U. S. A. *103*, 11300–11305.

Korenbrot, J.I., and Rebrik, T.I. (2002). Tuning outer segment Ca2+ homeostasis to phototransduction in rods and cones. Adv. Exp. Med. Biol. *514*, 179–203.

Krebs, H. (1927). On the Metabolism of the Retina. Biochem. Z. *189*, 57–59.

Kremers, G.-J., Goedhart, J., van den Heuvel, D.J., Gerritsen, H.C., and Gadella, T.W.J. (2007). Improved Green and Blue Fluorescent Proteins for Expression in Bacteria and Mammalian Cells. Biochemistry *46*, 3775–3783.

Krizaj, D., and Copenhagen, D.R. (1998). Compartmentalization of calcium extrusion mechanisms in the outer and inner segments of photoreceptors. Neuron *21*, 249–256.

Krizaj, D., and Copenhagen, D.R. (2002). Calcium regulation in photoreceptors. Front. Biosci. *7*, d2023–d2044.

Kruse, S.E., Watt, W.C., Marcinek, D.J., Kapur, R.P., Schenkman, K.A., and Palmiter, R.D. (2008). Mice with Mitochondrial Complex I Deficiency Develop a Fatal Encephalomyopathy. Cell Metab. *7*, 312–320.

Kushnir, M.M., Komaromy-Hiller, G., Shushan, B., Urry, F.M., and Roberts, W.L. (2001). Analysis of dicarboxylic acids by tandem mass spectrometry. High-throughput quantitative measurement of methylmalonic acid in serum, plasma, and urine. Clin. Chem. *47*, 1993–2002.

Kwong, J.Q., Lu, X., Correll, R.N., Schwanekamp, J.A., Vagnozzi, R.J., Sargent, M.A., York, A.J., Zhang, J., Bers, D.M., and Molkentin, J.D. (2015). The Mitochondrial Calcium Uniporter Selectively Matches Metabolic Output to Acute Contractile Stress in the Heart. Cell Rep. *12*, 15–22.

Kwong, J.Q., Huo, J., Bround, M.J., Boyer, J.G., Schwanekamp, J.A., Ghazal, N., Maxwell, J.T., Jang, Y.C., Khuchua, Z., Shi, K., et al. (2018). The mitochondrial calcium uniporter underlies metabolic fuel preference in skeletal muscle. JCI Insight *3*.

Lamb, T.D., and Pugh Jr, E.N. (1992). A Quantitative Account of the Activation Steps Involved in Phototransduction in Amphibian Photoreceptors. J. Physiol. Chabre *449*, 719–758.

Land, M. (2019). Eyes to See: The Astonishing Variety of Eyes in Nature (Oxford University Press).

Lee, J., Shahidullah, M., Hotchkiss, A., Coca-Prados, M., Delamere, N.A., and Pelis, R.M. (2015). A renal-like organic anion transport system in the ciliary epithelium of the bovine and human eye. Mol. Pharmacol. *87*, 697–705.

Lewis, C.A., Parker, S.J., Fiske, B.P., Mccloskey, D., Gui, D.Y., Green, C.R., Vokes, N.I., Feist, A.M., Heiden, M.G. Vander, and Metallo, C.M. (2014). Article Tracing Compartmentalized NADPH Metabolism in the Cytosol and Mitochondria of Mammalian Cells. 253–263.

Li, S., Chen, D., Sauvé, Y., McCandless, J., Chen, Y.J., and Chen, C.K. (2005). Rhodopsin-iCre transgenic mouse line for Cre-mediated rod-specific gene targeting. Genesis *41*, 73–80.

Linsenmeier, R.A. (1986). Effects of light and darkness on oxygen distribution and consumption in the cat retina. J. Gen. Physiol. *88*, 521–542.

Linsenmeier, R.A. (2004). Oxygen distribution and consumption in the cat retina during normoxia and hypoxemia. J. Gen. Physiol. *99*, 177–197.

Linsenmeier, R.A., and Yancey, C.M. (1989). Effects of hyperoxia on the oxygen distribution in the intact cat retina. Investig. Ophthalmol. Vis. Sci. *30*, 612–618.

Linsenmeier, R.A., and Zhang, H.F. (2017). Retinal oxygen: from animals to humans. Prog. Retin. Eye Res. *58*, 115–151.

Lombardi, A.A., Gibb, A.A., Arif, E., Kolmetzky, D.W., Tomar, D., Luongo, T.S., Jadiya, P., Murray, E.K., Lorkiewicz, P.K., Hajnóczky, G., et al. (2019). Mitochondrial calcium exchange links metabolism with the epigenome to control cellular differentiation. Nat. Commun. *10*.

Luongo, T.S., Lambert, J.P., Yuan, A., Zhang, X., Gross, P., Song, J., Shanmughapriya, S., Gao, E., Jain, M., Houser, S.R., et al. (2015). The Mitochondrial Calcium Uniporter Matches Energetic Supply with Cardiac Workload during Stress and Modulates Permeability Transition. Cell Rep. *12*, 23–34.

Ma, E.Y., Lewis, a, Barabas, P., Stearns, G., Suzuki, S., Krizaj, D., and Brockerhoff, S.E. (2013). Loss of Pde6 reduces cell body Ca(2+) transients within photoreceptors. Cell Death Dis. *4*, e797.

MacDonald, M.J., Fahien, L.A., Mertz, R.J., and Rana, R.S. (1989). Effect of esters of succinic acid and other citric acid cycle intermediates on insulin release and inositol phosphate formation by pancreatic islets. Arch. Biochem. Biophys. *269*, 400–406.

Mächler, P., Wyss, M.T., Elsayed, M., Stobart, J., Gutierrez, R., Von Faber-Castell, A., Kaelin, V., Zuend, M., San Martín, A., Romero-Gómez, I., et al. (2016). In Vivo Evidence for a Lactate Gradient from Astrocytes to Neurons. Cell Metab. *23*, 94–102.

Makino, C.L., Dodd, R.L., Chen, J., Burns, M.E., Roca, A., Simon, M.I., and Baylor, D.A. (2004). Recoverin Regulates Light-dependent Phosphodiesterase Activity in Retinal Rods. J. Gen. Physiol. *123*, 729–741.

Mallilankaraman, K., Cárdenas, C., Doonan, P., Harish, C., Irrinki, K.M., Golenár, T., Csordás, G., Yang, J., Müller, M., Miller, R., et al. (2013). MCUR1 is an Essential Component of Mitochondrial Ca2+ Uptake that Regulates Cellular Metabolism. *14*, 1336–1343.

Mammucari, C., Gherardi, G., Zamparo, I., Raffaello, A., Boncompagni, S., Chemello, F., Cagnin, S., Braga, A., Zanin, S., Pallafacchina, G., et al. (2015a). The Mitochondrial Calcium Uniporter Controls Skeletal Muscle Trophism InVivo. Cell Rep. *10*, 1269–1279.

Mammucari, C., Gherardi, G., Zamparo, I., Raffaello, A., Boncompagni, S., Sandri, M., Stefani, D. De, Protasi, F., Lanfranchi, G., and Rizzuto, R. (2015b). The Mitochondrial Calcium Uniporter Controls Skeletal Muscle Trophism In Vivo. Cell Rep. *10*, 1269–1279.

Mammucari, C., Raffaello, A., Vecellio Reane, D., and Rizzuto, R. (2016). Molecular structure and pathophysiological roles of the Mitochondrial Calcium Uniporter. Biochim. Biophys. Acta - Mol. Cell Res. *1863*, 2457–2464.

Mammucari, C., Raffaello, A., Vecellio Reane, D., Gherardi, G., De Mario, A., and Rizzuto, R. (2018). Mitochondrial calcium uptake in organ physiology: from molecular mechanism to animal models. Pflügers Arch. - Eur. J. Physiol. 1165–1179.

Matthews, H.R., and Fain, G.L. (2003). The effect of light on outer segment calcium in salamander rods. J. Physiol. *552*, 763–776.

McCormack, J.G., and Denton, R.M. (1979). The effects of calcium ions and adenine nucleotides on the activity of pig heart 2-oxoglutarate dehydrogenase complex. Biochem. J. *180*, 533–544.

McCormack, J.G., Halestrap, A.P., and Denton, R.M. (1990). Role of calcium ions in regulation of mammalian intramitochondrial metabolism. Physiol. Rev. *70*, 391–425.

McCurley, A.T., Callard, G. V, Eisen, J., Huggett, J., Dheda, K., Bustin, S., Zumla, A., Bustin, S., Bustin, S., Dheda, K., et al. (2008). Characterization of housekeeping genes in zebrafish: male-female differences and effects of tissue type, developmental stage and chemical treatment. BMC Mol. Biol. *9*, 102.

Mendez, A., Burns, M.E., Sokal, I., Dizhoor, A.M., Baehr, W., Palczewski, K., Baylor, D.A., and Chen, J. (2001). Role of guanylate cyclase-activating proteins (GCAPs) in setting the flash sensitivity of rod photoreceptors. Proc. Natl. Acad. Sci. *98*, 9948–9953.

Millard, P., Letisse, F., Sokol, S., and Portais, J.C. (2012). IsoCor: Correcting MS data in isotope labeling experiments. Bioinformatics *28*, 1294–1296.

Mills, E.L., Pierce, K.A., Jedrychowski, M.P., Garrity, R., Winther, S., Vidoni, S., Yoneshiro, T., Spinelli, J.B., Lu, G.Z., Kazak, L., et al. (2018). Accumulation of succinate controls activation of adipose tissue thermogenesis. Nature *560*, 102–106.

Mills, E.L., Harmon, C., Jedrychowski, M.P., Xiao, H., Garrity, R., Tran, N. V., Bradshaw, G.A., Fu, A., Szpyt, J., Reddy, A., et al. (2021). UCP1 governs liver extracellular succinate and inflammatory pathogenesis. Nat. Metab. *3*, 604–617.

Miyadera, H., Shiomi, K., Ui, H., Yamaguchi, Y., Masuma, R., Tomoda, H., Miyoshi, H., Osanai, A., Kita, K., and Omura, S. (2003). Atpenins, potent and specific inhibitors of mitochondrial complex II (succinate-ubiquinone oxidoreductase). Proc. Natl. Acad. Sci. *100*, 473–477.

Murphy, E., Pan, X., Nguyen, T., Liu, J., Holmström, K.M., and Finkel, T. (2014). Unresolved questions from the analysis of mice lacking MCU expression. Biochem. Biophys. Res. Commun. *449*, 384–385.

Nakatani, K., and Yau, K.-W. (1988). Calcium and light adaptation in retinal rods and cones. Nature *334*, 69–71.

Nakatani, K., Chen, C., Yau, K.-W., and Koutalos, Y. (2002). Calcium and Phototransduction. In Photoreceptors and Calcium, W. Baehr, and K. Palczewski, eds. (Boston, MA: Springer US), pp. 1–20.

Nichols, M., Elustondo, P.A., Warford, J., Thirumaran, A., Pavlov, E. V, and Robertson, G.S. (2016). Global ablation of the mitochondrial calcium uniporter increases glycolysis in cortical neurons subjected to energetic stressors. J. Cereb. Blood Flow Metab. 0271678X16682250.

Nickla, D.L., and Wallman, J. (2010). The multifunctional choroid. Prog. Retin. Eye Res. *29*, 144–168.

Nigam, S.K., Bush, K.T., Martovetsky, G., Ahn, S.Y., Liu, H.C., Richard, E., Bhatnagar, V., and Wu, W. (2015). The organic anion transporter (OAT) family: A systems biology perspective. Physiol. Rev. *95*, 83–123.

Okawa, H., Sampath, A.P., Laughlin, S.B., and Fain, G.L. (2008). ATP Consumption by Mammalian Rod Photoreceptors in Darkness and in Light. Curr. Biol. *18*, 1917–1921.

Ovens, M.J., Davies, A.J., Wilson, M.C., Murray, C.M., and Halestrap, A.P. (2010). AR-C155858 is a potent inhibitor of monocarboxylate transporters MCT1 and MCT2 that binds to an intracellular site involving transmembrane helices 7-10. Biochem. J. *425*, 523–530.

Padnick-Silver, L., and Linsenmeier, R.A. (2002). Quantification of in vivo anaerobic metabolism in the normal cat retina through intraretinal pH measurements. Vis. Neurosci. *19*, 793–806.

Paillard, M., Csordás, G., Huang, K.-T., Várnai, P., Joseph, S.K., and Hajnóczky, G. (2018). MICU1 Interacts with the D-Ring of the MCU Pore to Control Its Ca2+ Flux and Sensitivity to Ru360. Mol. Cell *72*, 1–8.

Pajor, A.M. (1995). Sequence and functional characterization of a renal sodium/dicarboxylate cotransporter. J. Biol. Chem. *270*, 5779–5785.

Pajor, A.M. (1996). Molecular cloning and functional expression of a sodium-dicarboxylate cotransporter from human kidney. Am. J. Physiol. *270*.

Pajor, A.M. (2006). Molecular properties of the SLC13 family of dicarboxylate and sulfate transporters. Pflugers Arch. Eur. J. Physiol. *451*, 597–605.

Pajor, A.M. (2014). Sodium-coupled dicarboxylate and citrate transporters from the SLC13 family. Pflugers Arch. Eur. J. Physiol. *466*, 119–130.

Pajor, A.M., and Sun, N. (1996). Characterization of the rabbit renal Na+-dicarboxylate cotransporter using antifusion protein antibodies. Am. J. Physiol. - Cell Physiol. *271*, 808–816.

Pajor, A.M., and Sun, N.N. (2000). Molecular cloning, chromosomal organization, and functional characterization of a sodium-dicarboxylate cotransporter from mouse kidney. Am. J. Physiol. - Ren. Physiol. *279*, 482–490.

Pajor, A.M., Gangula, R., and Yao, X. (2001). Cloning and functional characterization of a high-affinity Na+/dicarboxylate cotransporter from mouse brain. Am. J. Physiol. - Cell Physiol. *280*, 1215–1223.

Pan, X., Liu, J., Nguyen, T., Liu, C., Sun, J., Teng, Y., Fergusson, M.M., Rovira, I.I., Allen, M., Springer, D.A., et al. (2013). The physiological role of mitochondrial calcium revealed by mice lacking the mitochondrial calcium uniporter. Nat. Cell Biol. *15*, 1464–1472.

Patron, M., Checchetto, V., Raffaello, A., Teardo, E., VecellioReane, D., Mantoan, M., Granatiero, V., Szabò, I., DeStefani, D., and Rizzuto, R. (2014). MICU1 and MICU2 finely tune the mitochondrial Ca2+ uniporter by exerting opposite effects on MCU activity. Mol. Cell *53*, 726–737.

Patron, M., Granatiero, V., and Espino, J. (2018). MICU3 is a tissue-specific enhancer of mitochondrial calcium uptake. Cell Death Differ.

Payen, V.L., Mina, E., Van Hée, V.F., Porporato, P.E., and Sonveaux, P. (2020). Monocarboxylate transporters in cancer. Mol. Metab. *33*, 48–66.

Perkins, G.A., Ellisman, M.H., and Fox, D.A. (2003). Three-dimensional analysis of mouse rod and cone mitochondrial cristae architecture: Bioenergetic and functional implications. Mol. Vis. *9*, 60–73.

Perocchi, F., Gohil, V.M., Girgis, H.S., Bao, X.R., McCombs, J.E., Palmer, A.E., and Mootha, V.K. (2010a). MICU1 encodes a mitochondrial EF hand protein required for Ca(2+) uptake. Nature *467*, 291–296.

Perocchi, F., Gohil, V.M., Girgis, H.S., Bao, X.R., McCombs, J.E., Palmer, A.E., and Mootha, V.K. (2010b). MICU1 encodes a mitochondrial EF hand protein required for Ca2+uptake. Nature *467*, 291–296.

Philp, N.J., Yoon, H., and Lombardi, L. (2001). Mouse MCT3 gene is expressed preferentially in retinal pigment and choroid plexus epithelia. Am. J. Physiol. - Cell Physiol. *280*, 1319–1326.

Philp, N.J., Ochrietor, J.D., Rudoy, C., Muramatsu, T., and Linser, P.J. (2003). Loss of MCT1, MCT3, and MCT4 expression in the retinal pigment epithelium and neural retina of the 5A11/basigin-null mouse. Investig. Ophthalmol. Vis. Sci. *44*, 1305–1311.

Piao, L., Li, Y., Kim, S.J., Byun, H.S., Huang, S.M., Hwang, S.K., Yang, K.J., Park, K.A., Won, M., Hong, J., et al. (2009). Association of LETM1 and mrpl36 contributes to the regulation of mitochondrial ATP production and necrotic cell death. Cancer Res. *69*, 3397–3404.

Plovanich, M., Bogorad, R.L., Sancak, Y., Kamer, K.J., Strittmatter, L., Li, A.A., Girgis, H.S., Kuchimanchi, S., De Groot, J., Speciner, L., et al. (2013a). MICU2, a Paralog of MICU1, Resides within the Mitochondrial Uniporter Complex to Regulate Calcium Handling. PLoS One *8*, e55785.

Plovanich, M., Bogorad, R.L., Sancak, Y., Kamer, K.J., Strittmatter, L., Li, A.A., Girgis, H.S., Kuchimanchi, S., De Groot, J., Speciner, L., et al. (2013b). MICU2, a Paralog of MICU1, Resides within the Mitochondrial Uniporter Complex to Regulate Calcium Handling. PLoS One *8*.

Prag, H.A., Gruszczyk, A. V, Huang, M.M., Beach, T.E., Young, T., Tronci, L., Nikitopoulou, E., Mulvey, J.F., Ascione, R., Hadjihambi, A., et al. (2020). Mechanism of succinate efflux upon reperfusion of the ischaemic heart. Cardiovasc. Res.

Preibisch, S., Saalfeld, S., and Tomancak, P. (2009). Globally optimal stitching of tiled 3D microscopic image acquisitions. Bioinformatics *25*, 1463–1465.

Pugh, E.N., Nikonov, S., and Lamb, T.D. (1999). Molecular mechanisms of vertebrate photoreceptor light adaptation. Curr. Opin. Neurobiol. *9*, 410–418.

Punzo, C., Xiong, W., and Cepko, C.L. (2012). Loss of daylight vision in retinal degeneration: Are oxidative stress and metabolic dysregulation to blame? J. Biol. Chem. *287*, 1642–1648.

Ramamurthy, V., Niemi, G.A., Reh, T.A., and Hurley, J.B. (2004). Leber congenital amaurosis linked to AIPL1: A mouse model reveals destabilization of cGMP phosphodiesterase. Proc. Natl. Acad. Sci. U. S. A. *101*, 13897–13902.

Rasmussen, T.P., Wu, Y., Joiner, M.A., Koval, O.M., Wilson, N.R., Luczak, E.D., Wang, Q., Chen, B., Gao, Z., Zhu, Z., et al. (2015). Inhibition of MCU forces extramitochondrial adaptations governing physiological and pathological stress responses in heart. Proc. Natl. Acad. Sci. *112*, 9129–9134.

Reddy, A., Bozi, L.H.M., Yaghi, O.K., Mills, E.L., Xiao, H., Nicholson, H.E., Paschini, M., Paulo, J.A., Garrity, R., Laznik-Bogoslavski, D., et al. (2020). pH-Gated Succinate Secretion Regulates Muscle Remodeling in Response to Exercise. Cell *183*, 62-75.e17.

Renner, K., Bruss, C., Schnell, A., Koehl, G., Becker, H.M., Fante, M., Menevse, A.N., Kauer, N., Blazquez, R., Hacker, L., et al. (2019). Restricting Glycolysis Preserves T Cell Effector Functions and Augments Checkpoint Therapy. Cell Rep. *29*, 135-150.e9.

Reyes-Reveles, J., Dhingra, A., Alexander, D., Bragin, A., Philp, N.J., and Boesze-Battaglia, K. (2017). Phagocytosis-dependent ketogenesis in retinal pigment epithelium. J. Biol. Chem. *292*, 8038–8047.

Richardson, K.C., Jarett, L., and Finke, E.H. (1960). Embedding in Epoxy Resins for Ultrathin Sectioning in Electron Microscopy. Stain Technol. *35*, 313–323.

Rowe, A.A., Patel, P.D., Gordillo, R., and Wert, K.J. (2021). Replenishment of TCA cycle intermediates provides photoreceptor resilience against neurodegeneration during progression of retinitis pigmentosa. JCI Insight *6*.

Rueda, E.M., Johnson, J.E., Giddabasappa, A., Swaroop, A., Brooks, M.J., Sigel, I., Chaney, S.Y., Fox, D.A., and Fox, D.A. (2016). The cellular and compartmental profile of mouse retinal glycolysis, tricarboxylic acid cycle, oxidative phosphorylation, and ~P transferring kinases. Mol. Vis. *22*, 847–885.

Rutter, G.A., and Denton, R.M. (1988). Regulation of NAD+-linked isocitrate dehydrogenase and 2-oxoglutarate dehydrogenase by Ca2+ ions within toluene-permeabilized rat heart mitochondria. Interactions with regulation by adenine nucleotides and NADH/NAD+ ratios. Biochem. J. *252*, 181–189.
Rutter, G.A., McCormack, J.G., Halestrap, A.P., and Denton, R.M. (2020). The roles of cytosolic and intramitochondrial Ca2+ and the mitochondrial Ca2+-uniporter (MCU) in the stimulation of mammalian oxidative phosphorylation. J. Biol. Chem. *295*, 10506.
Sakurai, K., Chen, J., and Kefalov, V.J. (2011). Role of guanylyl cyclase modulation in mouse cone phototransduction. J. Neurosci. *31*, 7991–8000.
Sakurai, K., Chen, J., Khani, S.C., and Kefalov, V.J. (2015). Regulation of Mammalian Cone Phototransduction by Recoverin and Rhodopsin Kinase. J. Biol. Chem. *290*, 9239–9250.
Sancak, Y., Markhard, A.L., Kitami, T., Kovács-Bogdán, E., Kamer, K.J., Udeshi, N.D., Carr, S.A., Chaudhuri, D., Clapham, D.E., Li, A.A., et al. (2013a). EMRE is an essential component of the mitochondrial calcium uniporter complex. Science *342*, 1379–1382.
Sancak, Y., Markhard, A.L., Kitami, T., Kovács-bogdán, E., Kamer, K.J., Udeshi, N.D., Carr, S.A., Chaudhuri, D., Clapham, D.E., Li, A.A., et al. (2013b). EMRE Is an Essential Component of the Mitochondrial Calcium Uniporter Complex. Science (80-.). *147*, 1379–1382.
Sánchez-Chávez, G., Peña-Rangel, M.T., Riesgo-Escovar, J.R., Martínez-Martínez, A., and Salceda, R. (2012). Insulin Stimulated-Glucose Transporter Glut 4 Is Expressed in the Retina. PLoS One *7*, 1–7.
Sapieha, P., Sirinyan, M., Hamel, D., Zaniolo, K., Joyal, J.S., Cho, J.H., Honoré, J.C., Kermorvant-Duchemin, E., Varma, D.R., Tremblay, S., et al. (2008). The succinate receptor GPR91 in neurons has a major role in retinal angiogenesis. Nat. Med. *14*, 1067–1076.
Sasaki, S., Futagi, Y., Ideno, M., Kobayashi, M., Narumi, K., Furugen, A., and Iseki, K. (2016). Effect of diclofenac on SLC16A3/MCT4 by the Caco-2 cell line. Drug Metab. Pharmacokinet. *31*, 218–223.
Schindelin, J., Arganda-Carreras, I., Frise, E., Kaynig, V., Longair, M., Pietzsch, T., Preibisch, S., Rueden, C., Saalfeld, S., Schmid, B., et al. (2012). Fiji: An open-source platform for biological-image analysis. Nat. Methods *9*, 676–682.
Schmitt, E.A., and Dowling, J.E. (1999). Early retinal development in the zebrafish, Danio rerio: light and electron microscopic analyses. J. Comp. Neurol. *404*, 515–536.
Schneider, C.A., Rasband, W.S., and Eliceiri, K.W. (2012). NIH Image to ImageJ: 25 years of image analysis. Nat. Methods *9*, 671–675.
Schwarzländer, M., Logan, D.C., Fricker, M.D., and Sweetlove, L.J. (2011). The circularly permuted yellow fluorescent protein cpYFP that has been used as a superoxide probe is highly responsive to pH but not superoxide in mitochondria: Implications for the existence of superoxide “flashes.” Biochem. J. *437*, 381–387.
Shen, J., Yang, X., Dong, A., Petters, R.M., Peng, Y.W., Wong, F., and Campochiaro, P.A. (2005). Oxidative damage is a potential cause of cone cell death in retinitis pigmentosa. J. Cell. Physiol. *203*, 457–464.
Smets, I., Caplanusi, A., Despa, S., Molnar, Z., Radu, M., VandeVen, M., Ameloot, M., and Steels, P. (2004). Ca2+ uptake in mitochondria occurs via the reverse action of the Na+/Ca2+ exchanger in metabolically inhibited MDCK cells. Am. J. Physiol. - Ren. Physiol. *286*, 784–794.
Sonoda, S., Spee, C., Barron, E., Ryan, S.J., Kannan, R., and Hinton, D.R. (2009). A protocol for the culture and differentiation of highly polarized human retinal pigment epithelial cells. Nat. Protoc. *4*, 662–673.
Stearns, G., Evangelista, M., Fadool, J.M., and Brockerhoff, S.E. (2007). A Mutation in the Cone-Specific pde6 Gene Causes Rapid Cone Photoreceptor Degeneration in Zebrafish. J. Neurosci. *27*, 13866–13874.
De Stefani, D., Raffaello, A., Teardo, E., Szabó, I., and Rizzuto, R. (2011). A forty-kilodalton protein of the inner membrane is the mitochondrial calcium uniporter. Nature *476*, 336–340.
De Stefani, D., Patron, M., and Rizzuto, R. (2015). Structure and function of the mitochondrial calcium uniporter complex. Biochim. Biophys. Acta - Mol. Cell Res. *1853*, 2006–2011.
Stone, J., van Driel, D., Valter, K., Rees, S., and Provis, J. (2008). The locations of mitochondria in mammalian photoreceptors: Relation to retinal vasculature. Brain Res. *1189*, 58–69.
Swarup, A., Samuels, I.S., Bell, B.A., Han, J.Y.S., Du, J., Massenzio, E., Abel, E.D., Boesze-battaglia, K., Peachey, N.S., Philp, N.J., et al. (2019). Modulating GLUT1 expression in retinal pigment epithelium decreases glucose levels in the retina : impact on photoreceptors and Müller glial cells. 121–133.
Sweet, I.R., Khalil, G., Wallen, A.R., Steedman, M., Schenkman, K.A., Reems, J.A., Kahn, S.E., and Callis, J.B. (2002). Continuous measurement of oxygen consumption by pancreatic islets. Diabetes Technol. Ther. *4*, 661–672.
Sweet, I.R., Cook, D.L., DeJulio, E., Wallen, A.R., Khalil, G., Callis, J., and Reems, J.A. (2004). Regulation of ATP/ADP in Pancreatic Islets. Diabetes *53*, 401–409.
Szibor, M., Gizatullina, Z., Gainutdinov, T., Endres, T., Debska-Vielhaber, G., Kunz, M., Karavasili, N., Hallmann, K., Schreiber, F., Bamberger, A., et al. (2020). Cytosolic, but not matrix, calcium is essential for adjustment of mitochondrial pyruvate supply. J. Biol. Chem. *295*, 4383–4397.
Szikra, T., and Krizaj, D. (2007). Intracellular organelles and calcium homeostasis in rods and cones. Vis. Neurosci. *24*, 733–743.
Tang, R., Dodd, A., Lai, D., McNabb, W.C., and Love, D.R. (2007). Validation of zebrafish (Danio rerio) reference genes for quantitative real-time RT-PCR normalization. Acta Biochim. Biophys. Sin. (Shanghai). *39*, 384–390.

Tomar, D., Jaña, F., Dong, Z., Quinn, W.J., Jadiya, P., Breves, S.L., Daw, C.C., Srikantan, S., Shanmughapriya, S., Nemani, N., et al. (2019). Blockade of MCU-Mediated Ca 2+ Uptake Perturbs Lipid Metabolism via PP4-Dependent AMPK Dephosphorylation. Cell Rep. *26*, 3709-3725.e7.
Tsai, M.F., Jiang, D., Zhao, L., Clapham, D., and Miller, C. (2014). Functional reconstitution of the mitochondrial Ca2+/H+ antiporter letm1. J. Gen. Physiol. *143*, 67–73.
Vandesompele, J., De Preter, K., Pattyn, F., Poppe, B., Van Roy, N., De Paepe, A., and Speleman, F. (2002). Accurate normalization of real-time quantitative RT-PCR data by geometric averaging of multiple internal control genes. Genome Biol. *3*, 0034.1–0034.11.
Vijayasarathy, C., Damle, S., Prabu, S.K., Otto, C.M., and Avadhani, N.G. (2003). Adaptive changes in the expression of nuclear and mitochondrial encoded subunits of cytochrome c oxidase and the catalytic activity during hypoxia. Eur. J. Biochem. *270*, 871–879.
Villefranc, J.A., Amigo, J., and Lawson, N.D. (2007). Gateway compatible vectors for analysis of gene function in the zebrafish. Dev. Dyn. *236*, 3077–3087.
Vinberg, F., and Kefalov, V. (2015). Simultaneous ex vivo functional testing of two retinas by in vivo electroretinogram system. J. Vis. Exp. *2015*, 1–7.
Vinberg, F., and Kefalov, V.J. (2018). Investigating the Ca2+-dependent and Ca2+-independent mechanisms for mammalian cone light adaptation. Sci. Rep. *8*, 15864.
Vinberg, F., Kolesnikov, A. V., and Kefalov, V.J. (2014). Ex vivo ERG analysis of photoreceptors using an in vivo ERG system. Vision Res. *101*, 108–117.
Vinberg, F., Wang, T., Molday, R.S., Chen, J., and Kefalov, V.J. (2015). A new mouse model for stationary night blindness with mutant Slc24a1 explains the pathophysiology of the associated human disease. Hum. Mol. Genet. *24*, 5915–5929.
Vinberg, F., Wang, T., De Maria, A., Zhao, H., Bassnett, S., Chen, J., and Kefalov, V.J. (2017). The Na+/Ca2+, K+ exchanger NCKX4 is required for efficient cone-mediated vision. Elife *6*.
Vinberg, F., Chen, J., and Kefalov, V.J. (2018). Regulation of calcium homeostasis in the outer segments of rod and cone photoreceptors. Prog. Retin. Eye Res. 0–1.
Voigt, A.P., Whitmore, S.S., Lessing, N.D., DeLuca, A.P., Tucker, B.A., Stone, E.M., Mullins, R.F., and Scheetz, T.E. (2020). Spectacle: An interactive resource for ocular single-cell RNA sequencing data analysis. Exp. Eye Res. *200*, 108204.
Wang, L., Tornquist, P., and Bill, A. (1997a). Glucose metabolism of the inner retina in pigs in darkness and light. Acta Physiol. Scand. *160*, 71–74.
Wang, L., TORNQUIST, P., and Bill, A. (1997b). Glucose metabolism in pig outer retina in light and darkness. Acta Physiol. Scand. *160*, 75–81.
Winkler, B.S. (1981). Glycolytic and oxidative metabolism in relation to retinal function. J. Gen. Physiol. *77*, 667–692.
Winkler, B.S. (1995). A quantitative assessment of glucose metabolism in the isolated rat retina. Les Semin. Ophtalmol. d'IPSEN *6*, 79–96.
Winkler, B.S., Starnes, C.A., Twardy, B.S., Brault, D., and Taylor, R.C. (2008). Nuclear Magnetic Resonance and Biochemical Measurements of Glucose Utilization in the Cone-Dominant Ground Squirrel Retina AND. Invest. Ophthalmol. Vis. Sci. *49*, 4613–4619.
Woodruff, M.L., Sampath, A.P., Matthews, H.R., Krasnoperova, N. V., Lem, J., and Fain, G.L. (2002). Measurement of cytoplasmic calcium concentration in the rods of wild-type and transducin knock-out mice. J. Physiol. *542*, 843–854.
Wu, J.Y., Huang, T.W., Hsieh, Y.T., Wang, Y.F., Yen, C.C., Lee, G.L., Yeh, C.C., Peng, Y.J., Kuo, Y.Y., Wen, H.T., et al. (2020). Cancer-Derived Succinate Promotes Macrophage Polarization and Cancer Metastasis via Succinate Receptor. Mol. Cell *77*, 213-227.e5.
Xu, R., Ritz, B.K., Wang, Y., Huang, J., Zhao, C., Gong, K., Liu, X., and Du, J. (2020). The retina and retinal pigment epithelium differ in nitrogen metabolism and are metabolically connected. J. Biol. Chem. *295*, jbc.RA119.011727.
Yam, M., Engel, A.L., Wang, Y., Zhu, S., Hauer, A., Zhang, R., Lohner, D., Huang, J., Dinterman, M., Zhao, C., et al. (2019). Proline mediates metabolic communication between retinal pigment epithelial cells and the retina. J. Biol. Chem. *294*, 10278–10289.
Young, R.W., and Bok, D. (1969). Participation of the retinal pigment epithelium in the rod outer segment renewal process. J. Cell Biol. *42*, 392–403.
Yu, D.Y., and Cringle, S.J. (2006). Oxygen distribution in the mouse retina. Investig. Ophthalmol. Vis. Sci. *47*, 1109–1112.
Yu, D.Y., Cringle, S.J., Su, E.N., and Yu, P.K. (2000). Intraretinal oxygen levels before and after photoreceptor loss in the RCS rat. Investig. Ophthalmol. Vis. Sci. *41*, 3999–4006.
Yu, D.Y., Cringle, S.J., and Su, E.N. (2005). Intraretinal oxygen distribution in the monkey retina and the response to systemic hyperoxia. Investig. Ophthalmol. Vis. Sci. *46*, 4728–4733.
Zhang, J., Wang, Y.T., Miller, J.H., Day, M.M., Munger, J.C., and Brookes, P.S. (2018). Accumulation of Succinate in Cardiac Ischemia Primarily Occurs via Canonical Krebs Cycle Activity. Cell Rep. *23*, 2617–2628.
Zhao, C., Wilson, M.C., Schuit, F., Halestrap, A.P., and Rutter, G.A. (2001). Expression and distribution of lactate/monocarboxylate transporter isoforms in pancreatic islets and the exocrine pancreas. Diabetes *50*, 361–366.